# Probing Interactions in Ytterbium Fermi Gases and Mixtures Using the Optical Clock Transition

**Dissertation**
**zur Erlangung des Doktorgrades**
**an der Fakultät für Mathematik, Informatik und Naturwissenschaften**
**Fachbereich Physik**
**der Universität Hamburg**

**vorgelegt von**
**Benjamin Abeln**

**Hamburg**
**2021**

| | |
|---|---|
| Gutachter/innen der Dissertation: | Prof. Dr. Klaus Sengstock<br>Prof. Dr. Andreas Hemmerich |
| Zusammensetzung der Prüfungskommission: | Prof. Dr. Klaus Sengstock<br>Prof. Dr. Andreas Hemmerich<br>Prof. Dr. Ludwig Mathey<br>Prof. Dr. Roman Schnabel<br>Prof. Dr. Henning Moritz |
| Vorsitzende/r der Prüffungskommision: | Prof. Dr. Ludwig Mathey |
| Datum der Disputation: | 14.10.2021 |
| Vorsitzende/r des Fach-Promotionsausschusses PHYSIK: | Prof. Dr. Wolfgang Hansen |
| Leiter des Fachbereichs PHYSIK | Prof. Dr. Günter H. W. Sigl |
| Dekan der Fakultät MIN | Prof. Dr. Heinrich Graener |

# Abstract

Ultracold quantum gases in optical lattices constitute a versatile tool for quantum simulation of strongly correlated many-body systems. Alkaline earth(like) elements such as strontium or ytterbium possess an ultranarrow optical transition from the electronic ground state $^1S_0$ to the metastable state $^3P_0$ that might serve as a frequency standard for time-keeping. High-resolution spectroscopy on the optical 'clock' transition is a powerful analysis tool and allows to resolve interaction-induced energy shifts in a lattice system. The population of the metastable state $^3P_0$ can conveniently be controlled by the means of resonant clock laser light and due to its long lifetime, it can be regarded as an additional degree of freedom for quantum simulation and might be used to realize multi-band Hubbard models.

In this thesis I present spectroscopic measurements mainly conducted with ytterbium quantum gases and Fermi-Fermi mixtures of both fermionic isotopes $^{171}$Yb and $^{173}$Yb. We coherently address the metastable state $^3P_0$ using a clock-laser at 578 nm characterized by a narrow laser linewidth of approximately one Hertz. By performing clock-spectroscopy in a 3D magical optical lattice at 759 nm we are able to drive intra- and interband transitions and reach a maximum resolution of 26.7(2.4) Hz for a non-band changing transition. The high spectroscopic resolution allows resolving shifts of the clock transition that are induced by interactions between atom pairs. We determine interisotope interorbital interactions in ytterbium Fermi-Fermi mixtures and directly proof the $SU(2) \otimes SU(6)$ symmetry of the interactions.

In two spin component gases of $^{171}$Yb the antisymmetry required for the two-particle wave function of two indistinguishable fermions can be realized by a orbitally symmetric spin singlet or an orbitally antisymmetric spin triplet state. Both states are characterized by their own molecular potentials giving rise to an interorbital spin-exchange interaction that spectroscopically is characterized and found to be antiferromagnetic. The antiferromagnetic spin-exchange interaction together with the vanishingly small ground state interaction renders $^{171}$Yb a promising candidate for quantum simulation of Kondo lattice type physics in state-dependent optical lattices. Using $^{171}$Yb in both orbital states a state-dependent optical 1D lattice at wavelength of $\lambda_{\mathrm{SDL}} = 660\,\mathrm{nm}$ is characterized. In a first set of measurements, we observe spin-exchange dynamics in the state-dependent optical lattice which can be considered a first step towards quantum simulation of multi-band Hubbard models.

# Zusammenfassung

Ultrakalte Atome in optischen Gittern stellen ein vielseitiges Werkzeug zur Quantensimulation stark korrelierter Vielteilchensysteme dar. Erdalkali bzw. erdalkaliähnliche Elemente wie Strontium oder Ytterbium besitzen einen ultraschmalen optischen Übergang vom elektronischen Grundzustand $^1S_0$ zum metastabilen Zustand $^3P_0$, welcher sich als Frequenzstandard zur Zeitmessung eignet. Hochauflösende Spektroskopie auf dem optischen "Uhren-Übergang" ist eine sensible Analysemethode, die es ermöglicht Energiedifferenzen, die durch die Wechselwirkung mehrerer Atome in einem optischen Gitter induziert werden, zu messen. Die Besetzung des metastabilen Zustands kann durch resonantes Laserlicht zuverlässig kontrolliert werden. Aufgrund der langen radiativen Lebensdauer stellt der metastabile Zustand einen zusätzlichen Freiheitsgrad dar, der für die Quantensimulation von multiband Hubbard Modellen oder die Realisierung dissipativer System genutzt werden kann. In dieser Arbeit präsentiere ich spektroskopische Messungen die mit Fermigasen und Fermi-Fermimischungen beider fermionischer Ytterbium Isotope $^{171}$Yb und $^{173}$Yb durchgeführt wurden. Mit Hilfe eines Uhrenlasers, der eine Laserlinien-Halbwertsbreite von etwa einem Hz aufweist, wird der metastabile Zustand kohärent angeregt. In einem dreidimensionalen optischen Gitter bei der magischen Wellenlänge $\lambda_{\mathrm{mag}} = 759\,\mathrm{nm}$ können Intra- und Interbandübergänge zwischen verschiedenen Bloch-Bändern getrieben werden. Für einen Intrabandübergang wird eine maximale spektroskopische Auflösung erreicht, die einer spektroskopischen Halbwertsbreite von $26.7(2.4)\,\mathrm{Hz}$ entspricht. Unter Ausnutzung der hohen spektroskopischen Auflösung werden interisotop Zweiteilchenwechselwirkungen in Ytterbium Fermi-Fermimischungen charakterisiert und die der Wechselwirkung zugrunde liegende $\mathrm{SU}(2) \otimes \mathrm{SU}(6)$ Symmetrie direkt gezeigt. Interorbitale Paare von zwei $^{171}$Yb Atomen mit gegensätzlichem Spin können entweder durch einen symmetrischen orbitalen und antisymmetrischen Spinzustand oder antisymmetrischen orbitalen und Symmetrischen Spinzustand beschrieben werden. Die Spinaustauschwechselwirkung zwischen dem Spinsingulett und Spintriplettzustand wird ebenfalls spektroskopisch vermessen und als antiferromagnetisch identifiziert. Aufgrund der antiferromagnetischen Spinaustauschwechselwirkung und der verschwindend geringen Grundzustandswechselwirkung ist $^{171}$Yb ein vielversprechender Kandidat für die Quantensimulation von Kondo-Gitterphysik in zustandsabhängigen optischen Gittern. Mit Hilfe von $^{171}$Yb in beiden orbitalen Zuständen wird ein zustandsabhängiges Gitter bei einer Wellenlänge von $\lambda_{\mathrm{SDL}} = 660\,\mathrm{nm}$ charakterisiert. In einem ersten Schritt in Richtung der Quantensimulation von multiband Hubbardmodellen wird Spinaustauschdynamik im zustandsabhängigen Gitter beobachtet.

## Publikationen

Im Rahmen der vorliegenden Arbeit sind die folgenden wissenschaftlichen Veröffentlichungen entstanden.

## Publications

The following research articles have been published in the course of this thesis.


[1] K. Sponselee, L. Freystatzky, B. Abeln, M. Diem, B. Hundt, A. Kochanke, T. Ponath, B. Santra, L. Mathey, K. Sengstock and C. Becker, *"Dynamics of ultracold quantum gases in the dissipative Fermi-Hubbard model"*, Quantum Science and Technology 4(1):14002 (2018).

[2] B. Abeln, K. Sponselee, M. Diem, N. Pintul, K. Sengstock and C. Becker, *"Interorbital interactions in an $SU(2)\otimes SU(6)$-symmetric Fermi-Fermi mixture"*, Phys. Rev. A 103:033315 (2021)

# Contents

# Introduction

Since the first realization of Bose-Einstein condensates (BEC) with dilute gases of ultracold neutral atoms in 1995 [3, 4], soon followed by the creation of degenerate Fermi gases in 1999 [5], the ultracold quantum gas community has grown rapidly and developed into a diverse field of research, covering metrology, ultracold chemistry, quantum simulation and quantum information, to name only a few examples.
A main interest of modern physics is to understand the behavior of quantum many-body systems. Reducing the complexity of the system under research to an extent that allows for a microscopic understanding is generally a promising road to understanding the more complex problem. In many cases, simple models reveal fundamental physical concepts that can also be applied to the more complex problems. - Although generally nature is more complicated than the two-body problem, the hydrogen atom or the two-level system, these models increased our understanding of nature tremendously. Yet, understanding the interplay of many of those well understood microscopic systems remains extremely challenging. The physical properties of many interacting particles significantly differ from the single particle behavior and many-body phenomena such as the emergence of high $T_\mathrm{C}$ super conductivity in cuprates [6, 7] or spin-liquids in frustrated magnets [8, 9] are subjects of on-going research. Understanding these phenomena might lead to technical innovations of great social benefit, and therefore is not purely of large scientific interest. To address the questions raised by the behavior of certain materials such as high $T_\mathrm{C}$ super conductors, theoreticians came up with strongly simplified models such as the Fermi-Hubbard [10] or the Kondo-lattice model [11–13] which are believed to contain all the ingredients necessary to explain the yet not understood phenomenon. However, solving even these strongly simplified models remains challenging as the exponential growth of the Hilbert space with increasing system size is inherent to all quantum mechanical many-body systems and cannot be overcome, thus rendering the simulation of a many-body system on a classical computer an intractable mathematical problem.

To address this problem Richard Feynman in the 1980s suggested to simulate the system of interest using devices that themselves obey the laws of quantum mechanics, instead of using classical computers [14–16]. Universal digital quantum computers, that could be programmed to simulate an arbitrary quantum system [17], would require an enormous degree of experimental control and because of that are yet out of reach [18]. However, over the last decades large progress has been made in the field of so-called analog quantum simulation [18, 19].
The central idea is to transfer the concept of reducing complexity to the experimental domain by building an experimental apparatus that allows to create and observe a quantum system that is made up from well understood and controllable constituents, and represents a good approximation of the theory under study. Then, by experimentally tuning the model parameters the phase diagram of the underlying model can be mapped out.

Ultracold atoms in optical lattices represent such a well controlled experimental platform in many respects [20, 21]. Quantum gas experiments benefit from long coherence times and many of the system parameters can be conveniently controlled using laser light and magnetic fields. The idea to use ultracold quantum gases in optical lattice potentials formed by interfering laser beams to simulate Hubbard physics emerged as early as 1998 [22]. In a fascinating experiment the observation of the paradigmatic super-fluid to Mott insulator transition [23] [24] demonstrated the capability of the ultracold atomic platform for quantum simulation and initiated a vast growth of the quantum gas community.
Since then, a variety of different lattice geometries has been realized ranging from simple cubic lattices [24] to super lattices [25], triangular and honeycomb lattices [26, 27] or Kagome lattices [28]. In remarkable experiments intriguing phenomena like fermionic band insulation [29], artificial magnetic fields [30], frustration [31], the Haldane [32] and Harper-Hofstadter model [33–35]) or the Berry curvature could be studied [36]. While in the beginning observables were restricted to momentum space using time of flight techniques, experimental and technological advances lead to the development of quantum gas microscopes, capable of resolving single atoms in a 2D-plane of an optical lattice [37, 38]. This rather new development allows to directly measure correlations. A long standing goal was reached by the direct observation of antiferromagnetic order in a system of ultracold fermions in an optical lattice [39].
An even more recent development are micro-trap arrays, that allow to trap, detect and manipulate single atoms and assemble defect-free geometries atom by atom [40, 41]. Making use of Rydberg excitation and blockade these systems have been used to demonstrate the entanglement of a large number of particles [42] or to study the SSH model [43] and spin liquids [44].

The most common elements used in the quantum gas community are alkali elements such as lithium, sodium, potassium and in particular rubidium, with a single $s$-shell electron, and hence a hydrogen-like level structure. Typical dipole transitions for the alkali elements show linewidths on the order of several MHz. The van-der-Waals interaction in ultracold gases is a short-range interaction often modeled as contact interaction, and hence substantially differs from the coulomb interaction between electrons. Different experimental approaches aim at the creation of long range interactions to overcome this limitation using polar molecules [45] or elements with a large magnetic moment such as chromium [46], dysprosium [47] or erbium [48]. In recent experiments dipolar quantum gases have been used to study the formation of quantum droplets caused by competing repulsive and attractive interactions [49, 50].

Alkaline earth (like) elements such as strontium and ytterbium have two outer $s$-shell electrons and hence feature a helium-like level scheme with a spin singlet and a spin triplet manifold. The transitions from the singlet ground state to the triplet state are only weakly allowed and show small linewidths. For the doubly dipole forbidden transition ${}^1S_0 \rightarrow {}^3P_0$, these are far below one Hz [51]. Optical lattices at a so-called magic wavelength[52], as well as the invention of the optical frequency comb [53] enabled the development of a new type of optical lattice clock [54], using the optical ${}^1S_0 \rightarrow {}^3P_0$ transition of alkaline earth (like) elements such as strontium or ytterbium as frequency standard. State-of-the-art optical lattice clocks outperform current frequency standards [55, 56]. Most optical lattice clocks load a one-dimensional magic lattice directly from a MOT and do not require quan-

tum degenerate gases. Yet the combination of high precision spectroscopy and ultracold quantum gases of alkaline earth (like) elements in optical lattices are highly interesting for quantum simulation applications. On the one hand, high precision spectroscopy comprises a powerful tool for the analysis of interaction induced shifts in optical lattices [2, 57–63], on the other hand the lifetime of the long-lived metastable state exceeds the typical experimental timescale and hence can be used as an additional degree of freedom for quantum simulation [64–66]. A peculiarity of fermionic alkaline earth (like) elements is the SU($\mathcal{N}$) symmetry [67] (with $N = I + 1/2$, where $I$ denotes the nuclear spin) of ground- and excited-state atoms that causes an interorbital spin-exchange interaction, that has been spectroscopically characterized [2, 57–62, 68]. A novel kind of interorbital Feshbach resonance allows to tune the interaction between ground and metastable state atoms [69, 70] and has been used to create orbital Feshbach molecules [71], and might allow to study exotic superfluidity [72–74]. Particle losses due to strong inelastic collisions of excited-state atoms allow to engineer dissipative Hubbard systems[1, 75] that might prove useful for the preparation of highly entangled quantum states [1, 76]. Mixtures of ytterbium atoms in different orbital states have been proposed for quantum simulation of multi-band Hubbard models such as the Kondo lattice model, using state-dependent optical potentials to realize systems of localized atoms in the excited state and itinerant atoms in the ground state that interact via the interorbital spin-exchange interaction [64–66]. First experiments with $^{173}$Yb (nuclear spin $I = 5/2$) [77] and very recently with $^{171}$Yb (with nuclear spin $I = 1/2$) (see ref. [78] and this thesis) studied spin-exchange dynamics in state-dependent lattices.
Fermi-Fermi mixtures of $^{171}$Yb-$^{173}$Yb have been proposed for the simulation of two-flavor symmetry-locking phases [79, 80], which might yield valuable insights for high energy physics.
In the course of this thesis a variety of experiments have been performed that exploit the above-mentioned properties of ultracold ytterbium atoms. We employ high precision spectroscopic methods to study interacting Fermi gases and Fermi-Fermi mixtures of $^{171}$Yb and $^{173}$Yb. We characterize SU(2) $\otimes$ SU(6) symmetric interisotope interorbital interactions between $^{171}$Yb and $^{173}$Yb and determine the interorbital spin-exchange interaction of $^{171}$Yb. Furthermore as a step towards quantum simulation of Kondo-lattice physics we study spin-exchange dynamics for a gas of $^{171}$Yb in a state dependent optical lattice.

This thesis is organized as follows:

Section one is dedicated to fundamental properties of the element ytterbium for the operation of a quantum gas machine, the experimental setup and experimental techniques. I present the experimental apparatus in its current form and especially focus on changes that have been made over the course of this thesis.

In section two I describe the creation of ytterbium Fermi-Fermi mixtures and Fermi gases of $^{171}$Yb via sympathetic cooling with $^{173}$Yb and present characterization measurements.

Section three is dedicated to clock spectroscopy in a magic optical lattice. I establish a

theoretical framework for understanding clock spectroscopy in the framework of the ytterbium experiment and present measurements of intra- and interband transitions. The current spectroscopy setup allows for a Fourier limited resolution of $\Gamma_{\mathrm{FWHM}} \leq 26.7(2.4)\,\mathrm{Hz}$. Combining clock spectroscopy and band mapping techniques, we directly probe the dispersion relation of the lattice and observe the quasimomentum transfer caused by the excitation process.

In section four I characterize two-particle interaction induced shifts of the clock transition for Fermi-Fermi mixtures of $^{171}$Yb and $^{173}$Yb as well as in two spin component mixtures of $^{171}$Yb employing the spectroscopic techniques presented in the previous section. The total antisymmetric wave function required for two indistinguishable particles in the case of the two-spin mixture of $^{171}$Yb gives rise to an interorbital spin-exchange interaction, that we find to be antiferromagnetic. The spin-exchange interaction $V_{\mathrm{ex}}$ is a crucial parameter for possible simulation of Kondo-lattice physics.

In section five a state-dependent optical lattice at a wavelength of $\lambda = 660\,\mathrm{nm}$ is characterized using gases of $^{171}$Yb in both orbital states. In a first step towards quantum simulation of Kondo-lattice-type physics, we prepare an interorbital mixture in different $m_F$ states and observe spin-exchange dynamics.

# 1. Experimental Setup and Methods

In the ytterbium experiment, we create quantum degenerate gases and mixtures of different ytterbium isotopes. We perform high-precision spectroscopy on the optical clock transition to resolve interaction-induced energy shifts and aim at quantum simulation and quantum state preparation using the metastable state $^3P_0$ as an experimental degree of freedom. The ytterbium quantum gas project started more than ten years ago. The first PhD students S. Dörscher [81] and A.Thobe [82] started setting up the ytterbium quantum gas machine. Later the team was joined by B. Hundt [83], A. Kochanke [84] and T. Ponath [85]. The initial setup is described in [86] as well as in the doctoral theses of A. Thobe and S. Dörscher. Over the years, the apparatus has been constantly modified and improved. The evolution of the technical setup can be followed in the PhD theses of the aforementioned people as well as several bachelor, master and diploma theses [87–97]. Based on preparatory work by A. Kochanke [84] and the author [91], the experimental apparatus has been modified to allow for simultaneous trapping and cooling of two different isotopes enabling to create and manipulate quantum degenerate Fermi-Fermi mixtures of $^{171}$Yb and $^{173}$Yb and single isotope gases of $^{171}$Yb. In the following, I will first give an overview of the most important physical properties of the element ytterbium relevant for the operation of a quantum gas experiment and then describe the experimental apparatus in its current form, as it has been used for the measurements presented in this theses.

Dipole trap frequencies and spin preparation have been characterized by K. Sponselee, M. Diem and the author. The here presented measurements have been conducted by K. Sponselee and the author and data analysis has been performed by the author. The phase noise measurements of the clock laser have been performed and analyzed by the author. Further details on the experimental apparatus can be found in the doctoral theses of K. Sponselee[98] and M. Diem [99].

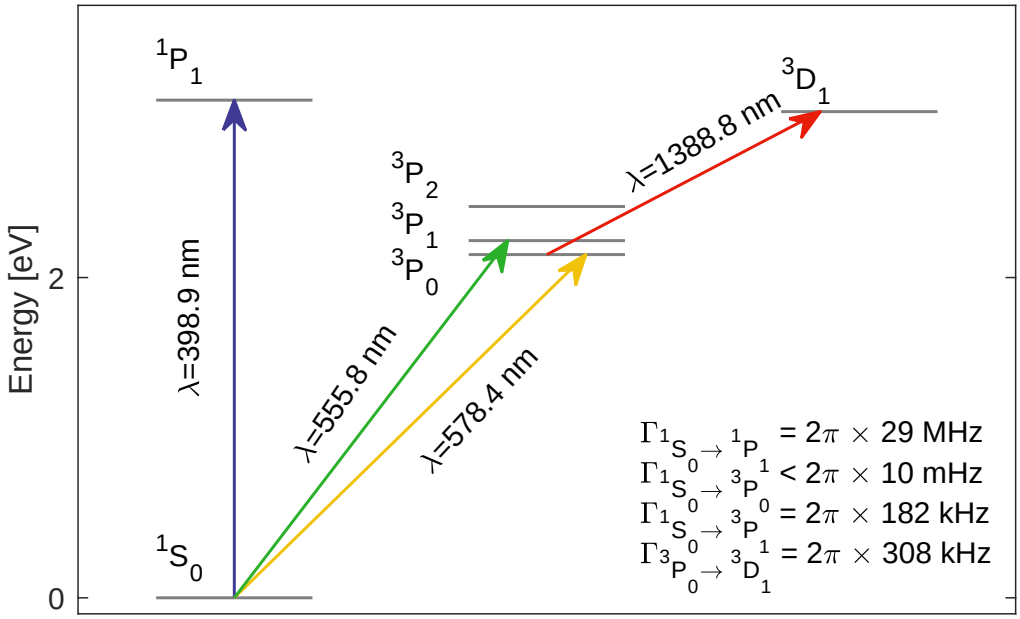


**Figure 1.1.:** Reduced level scheme for neutral ytterbium. Shown are the transitions resonantly addressed in the experiment. All energies and wavelengths according to ref. [100]. Linewidths according to refs. [101–104].

## 1.1. Properties of Ytterbium

Ytterbium is a rare earth element. With an atomic number of 70 it can be found next to the last element of the lanthanide series in the periodic table. It features as many as seven stable isotopes. The even isotopes $^{168}$Yb,$^{170}$Yb,$^{172}$Yb,$^{174}$Yb and $^{176}$Yb have a nuclear spin of $I = 0$ and obey bosonic statistics, whereas odd isotopes $^{171}$Yb, with $I = 1/2$ and $^{173}$Yb, with $I = 5/2$ obey fermionic statistics. Table 1.1 shows the natural abundances of the stable isotopes. The electronic configuration of ytterbium [Xe]$4f^{14}6s^2$ features filled $4f$- and

| $^{168}$Yb | $^{170}$Yb | $^{171}$Yb | $^{172}$Yb | $^{173}$Yb | $^{174}$Yb | $^{176}$Yb |
|---|---|---|---|---|---|---|
| 0.126 % | 3.023 % | 14.216 % | 21.754 % | 16.098 % | 31.896 % | 12.887 % |

**Table 1.1.:** Natural abundances of the stable isotopes of ytterbium according to ref. [105].

$6s$-shells. Due to the two $s$-shell valence electrons ytterbium shows similarities to alkaline-earth elements e.g. strontium. Therefore ytterbium is often called an alkaline-earth like element. The level structure of ytterbium depicted in figure 1.2 features a singlet and triplet manifold as known from other two-electron elements such as helium. The ground state is characterized by a vanishing electronic angular momentum $J = 0$ and thus carries an almost vanishing, purely nuclear magnetic moment. Referring to the selection rules for dipole radiation, so called intercombination transitions from the spin singlet to the

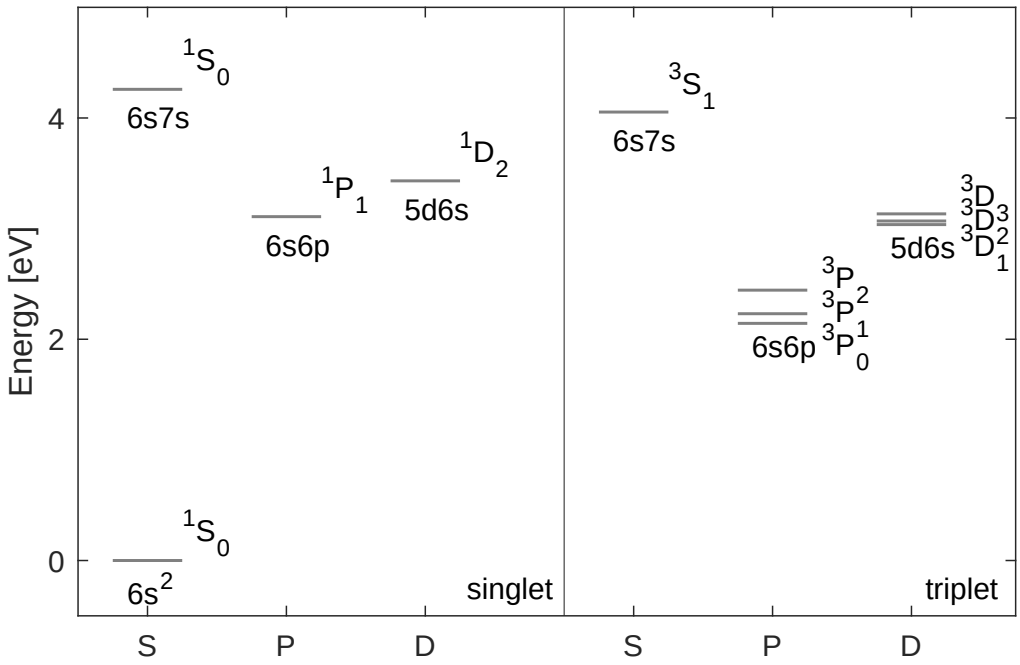


**Figure 1.2.:** Electronic level scheme for neutral ytterbium. Shown are the lowest lying states with a filled $4f$ shell according to ref. [100].

spin triplet manifold are electric dipole forbidden, as $\Delta S \neq 0$. However, due to the large mass of ytterbium, $LS$ coupling is not perfectly realized and state mixing weakly enables transitions from the $^1S_0$ ground state to the state $^3P_1$. For fermionic isotopes additional hyperfine mixing caused by the hyperfine interaction enables the doubly dipole forbidden transitions $^1S_0 \rightarrow {}^3P_{0,2}$ [51, 102, 106]. For bosonic isotopes, to enable the $^1S_0 \rightarrow {}^3P_0$ transition, state mixing has to be induced by applying a dc-magnetic field [107, 108].
In the experiment we resonantly address the transitions $^1S_0 \rightarrow {}^1P_1$ at $\lambda = 399\,\mathrm{nm}$, $^1S_0 \rightarrow {}^3P_0$ at $\lambda = 578\,\mathrm{nm}$, $^1S_0 \rightarrow {}^3P_1$ at $\lambda = 556\,\mathrm{nm}$ and $^3P_0 \rightarrow {}^3D_1$ at $\lambda = 1389\,\mathrm{nm}$, shown in the reduced level scheme depicted in fig. 1.1. The corresponding linewidths are summarized in table 1.2. The small natural linewidth of the $^1S_0 \rightarrow {}^3P_0$ transition of $\Gamma/2\pi < 10\,\mathrm{mHz}$ [102], combined with the small sensitivity to magnetic fields due to the vanishing electronic angular momentum of the initial and final state render this transition well suited to serve as a frequency standard [102] and ytterbium-based optical lattice clock experiments are operated at metrological institutes around the world [55, 109, 110].

Apart from the optical transitions that are well suited for high-precision spectroscopy, another outstanding feature of ytterbium is its large mass. Ytterbium is the heaviest element for which quantum degeneracy has been achieved so far. Therefore ytterbium is an interesting candidate for experiments aiming at studying mass-dependent or mass-imbalance dependent phenomena such as Efimov physics [111].
Laser trapping and cooling of ytterbium have been pioneered by the Kyoto group. The vanishing magnetic moment prevents the use of magnetic traps, and thus quantum degeneracy has to be achieved by evaporative cooling in all-optical traps. Bose-Einstein

| transition | $\Gamma/2\pi$ | reference |
|---|---|---|
| $^1S_0 \rightarrow {}^1P_1$ | 29.1 MHz | [101] |
| $^1S_0 \rightarrow {}^3P_0$ | $< 10$ mHz | [102] |
| $^1S_0 \rightarrow {}^3P_1$ | 182 kHz | [103] |
| $^3P_0 \rightarrow {}^3D_1$ | 308 kHz | [104] |

**Table 1.2.:** Natural linewidths of the transitions, resonantly addressed in the experiment. Note that the values for the clock transition are obtained by *ab initio* calculations, while the other values are based on the experimental observation of lifetimes.

| | $^{168}$Yb | $^{170}$Yb | $^{171}$Yb | $^{172}$Yb | $^{173}$Yb | $^{174}$Yb | $^{176}$Yb |
|---|---|---|---|---|---|---|---|
| $^{168}$Yb | 251.9(3.4) | 117.0(1.5) | 89.2(1.7) | 65(2) | 38.6(2.5) | 2.5(3.4) | -360(30) |
| $^{170}$Yb | | 63(2) | 36.5(2.5) | -2.1(3.6) | -81(7) | -520(50) | 209.4(2.3) |
| $^{171}$Yb | | | -3(4) | -84(7) | -580(60) | 429(13) | 114(15) |
| $^{172}$Yb | | | | -600(60) | 417.6(1.3) | 200.5(2.3) | 106.2(1.5) |
| $^{173}$Yb | | | | | 199(2) | 138.7(1.5) | 79.7(1.9) |
| $^{174}$Yb | | | | | | 104(15) | 54.4(2.3) |
| $^{176}$Yb | | | | | | | -24(4) |

**Table 1.3.:** Inter and intraisotope $s$-wave scattering lengths in units of Bohr radii $a_0 = 5.29177210903 \times 10^{-11}$ m, according to ref. [118].

condensation of the bosonic isotope $^{174}$Yb has first been achieved in 2003 [112]. Since then, degeneracy has been reached for multiple isotopes, including both fermionic isotopes and different isotope mixtures [113–115].
In the ultracold regime, interactions in quantum gases are restricted to $s$-wave scattering, characterized by the $s$-wave scattering length $a$. For alkali elements such as potassium and lithium, magnetic Feshbach resonances allow to tune the interaction parameter over a broad range enabling studies of e.g. the BEC-BCS crossover [116, 117]. Due to the purely nuclear angular momentum ytterbium only weakly couples to magnetic fields. Therefore there are no magnetic Feshbach resonances and thus the interaction parameter is fixed. However, the different ytterbium isotopes feature largely different $s$-wave scattering lengths, and thus choosing a particular element allows a limited choice of interaction strength. Table 1.3 shows intra- and interisotope s-wave scattering lengths obtained by two-color photo association [118].
Repulsive scattering lengths of the most abundant bosonic and fermionic isotopes $^{174}$Yb and $^{173}$Yb of $^{174}a = 104(15)\,a_0$ and $^{173}a = 199(2)\,a_0$, respectively allow for effective evaporative cooling in single isotope gases. Due to the almost vanishing s-wave scattering length of $^{171}a = -3(4)\,a_0$ reaching quantum degeneracy for $^{171}$Yb requires sympathetic cooling via a second isotope or element and therefore is technically more demanding. On the other hand, the vanishing s-wave interaction of $^{171}$Yb is interesting for quantum

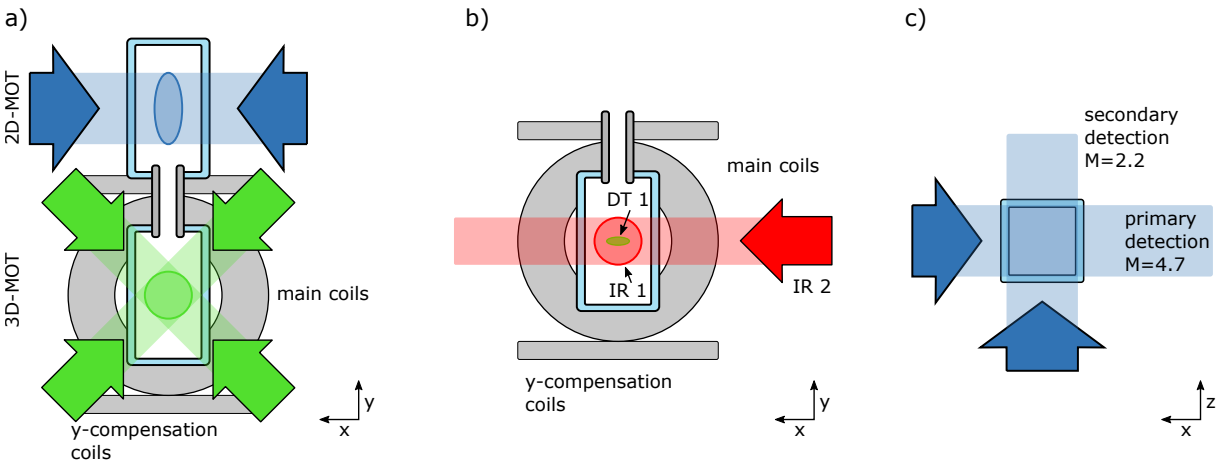


**Figure 1.3.:** Schematic of MOT, dipole trap and detection beams. Panel a) depicts the 2D/3D-MOT configuration. Atoms are initially trapped and cooled in the upper glass cell in a 2D-MOT on the blue ${}^1S_0 \rightarrow {}^1P_1$ transition. Subsequently the atoms are further cooled in a 3D-MOT on the ${}^1S_0 \rightarrow {}^3P_1$ transition in the lower glass cell. Panel b) shows the bichromatic dipole trap formed by three high power beams at $\lambda_{\mathrm{DT1}} = 532\,\mathrm{nm}$ and $\lambda_{\mathrm{IR1,IR2}} = 1064\,\mathrm{nm}$ labeled as DT1,IR1 and IR2. Panel c) shows the imaging beams of the primary detection along $x$-direction with a magnification of $M = 4.7$ and the secondary detection along $z$-direction with a magnification of $M = 2.2$. The main coils are operated either in Helmholtz or anti-Helmholtz configuration to create a quantization axis or a gradient field for the 3D-MOT, the $y$-compensation coils are used to set the quantization axis for clock spectroscopy and spin detection. 2D-MOT coils and compensation coils in $x$- and $z$-direction are omitted for clarity.

simulation applications[64].

## 1.2. Magneto Optical Trapping

The heart of the ytterbium experiment is a vacuum apparatus that consists of an upper and a lower glass cell. A dispenser in the upper glass cell is heated to a temperature of approximately 700 K [81] and emits ytterbium, serving as atom source. To separate the experimental environment from the atom source and minimize interaction with the background gas, the upper glass cell and the lower glass cell are connected via a differential pumping stage. As a consequence the pressure in the lower glass cell is about $p_{\mathrm{lower}} < 1 \times 10^{-11}\,\mathrm{mbar}$ while in the upper glass cell the pressure is usually about $p_{\mathrm{upper}} \sim 1 \times 10^{-10}\,\mathrm{mbar}$.
First, the atoms are trapped and cooled in a 2D-magneto optical trap (MOT) [119] on the ${}^1S_0 \rightarrow {}^1P_1$ transition. Due to the broad linewidth of $\Gamma = 2\pi \times 29\,\mathrm{MHz}$ [101] the 2D-MOT features a high trapping velocity. On the other hand the corresponding Doppler temperature of $T_{\mathrm{D}} \approx 0.7\,\mathrm{mK}$ is rather high. Aided by a pushing beam pointing at the 2D-MOT trapping region at an angle from above, atoms are transferred into the lower glass cell, where they are confined in a 3D-MOT, operated on the intercombination line ${}^1S_0 \rightarrow {}^3P_1$. The 2D/3D-MOT configuration is schematically shown in fig. 1.3 a) As the narrow linewidth of $\Gamma = 2\pi \times 182\,\mathrm{kHz}$ [103] corresponds to a small capture velocity, the frequency of the MOT beams is broadened by applying a saw-tooth shaped frequency

modulation at $f_{\mathrm{mod}} \approx 200\,\mathrm{kHz}$ to allow for a larger MOT detuning and to increase the capture velocity [86]. To reach MOT temperatures close to the Doppler temperature of $T_{\mathrm{D}} = 4.4\,\mu\mathrm{K}$ the MOT is compressed by simultaneously reducing laser broadening, MOT-detuning and MOT-power, resulting in typical final MOT temperatures of $T_{\text{3D-MOT}} \sim 20\,\mu\mathrm{K}$.
The single isotope MOT performances for both fermionic isotopes $^{171}$Yb and $^{173}$Yb as well as the most abundant bosonic isotope $^{174}$Yb have been characterized by A. Kochanke [84] and the author in the course of his master's thesis [91]. In the past, especially the 2D-MOT for $^{173}$Yb has been an experimental bottle neck. Due to a narrow hyperfine splitting of the $^1S_0 \leftrightarrow {}^1P_1$ transition the detuning of the 2D-MOT laser with respect to the 2D-MOT $F = 5/2 \rightarrow F = 7/2$ transition of $\Delta_{\text{2D-MOT}} \approx -1.2\,\Gamma_{399}$ is comparable to the detuning with respect to the $F = 5/2 \rightarrow F = 3/2$ transition, but of opposite sign. Therefore loading of $^{173}$Yb is diminished and the 2D-MOT settings for $^{173}$Yb are rather unconventional. Polarization and alignment of the 2D-MOT beams significantly differ from the settings optimal for $^{171}$Yb and $^{174}$Yb. First attempts to avoid experimental difficulties caused by the narrow hyperfine splitting by operating the 2D-MOT on the $5/2 \rightarrow 5/2$ as proposed in [96, 120] did not succeed.
The MOT loading rates have been improved by increasing the available 2D-MOT power by exchanging the 2D-MOT laser. This allows to operate the 2D-MOT closer to the saturation intensity which increases the robustness of the 2D-MOT performance. Nevertheless, the $^{173}$Yb 2D-MOT still is very sensitive to misalignment and therefore, the 2D-MOT settings for all other isotopes are a compromise to allow for optimal MOT loading rates of $^{173}$Yb. Typically we achieve loading rates of $3 \times 10^6\,\mathrm{s}^{-1}$ for $^{171}$Yb, $2 \times 10^6\,\mathrm{s}^{-1}$ for $^{173}$Yb and more than $3 \times 10^6\,\mathrm{s}^{-1}$ for $^{174}$Yb.
To create mixtures of both fermionic isotopes, we subsequently load atoms from the 2D-MOT into an uncompressed bi-chromatic 3D-MOT. To do so, the frequency of the 2D-MOT laser is chirped in the experimental cycle to account for the isotope shift of the 2D-MOT transition $\Delta_{{}^1P_1} = 244\,\mathrm{MHz}$. After 3D-MOT loading, the 3D-MOT is compressed simultaneously for both isotopes as described above.

## 1.3. Dipole Traps

The almost vanishing magnetic moment of ytterbium in the electronic ground state prevents the use of magnetic traps. Instead, trapping potentials are created by high power, red detuned laser beams. The optical dipole potential is determined by the complex polarizability $\alpha$ and the intensity $I$ of the laser beam [121]. The dipole potential can be written as [121]:

$$U_{\mathrm{dip}} = -\frac{1}{2\epsilon_0 c}\,\mathrm{Re}\{\alpha\} I, \tag{1.1}$$

where $\epsilon_0$ denotes the vacuum permittivity and $c$ the speed of light. For a two level system this expression can be simplified to [121]:

$$U_{\mathrm{dip}} = \frac{3\pi c^2}{2\omega_0^3}\frac{\Gamma}{\Delta} I, \tag{1.2}$$

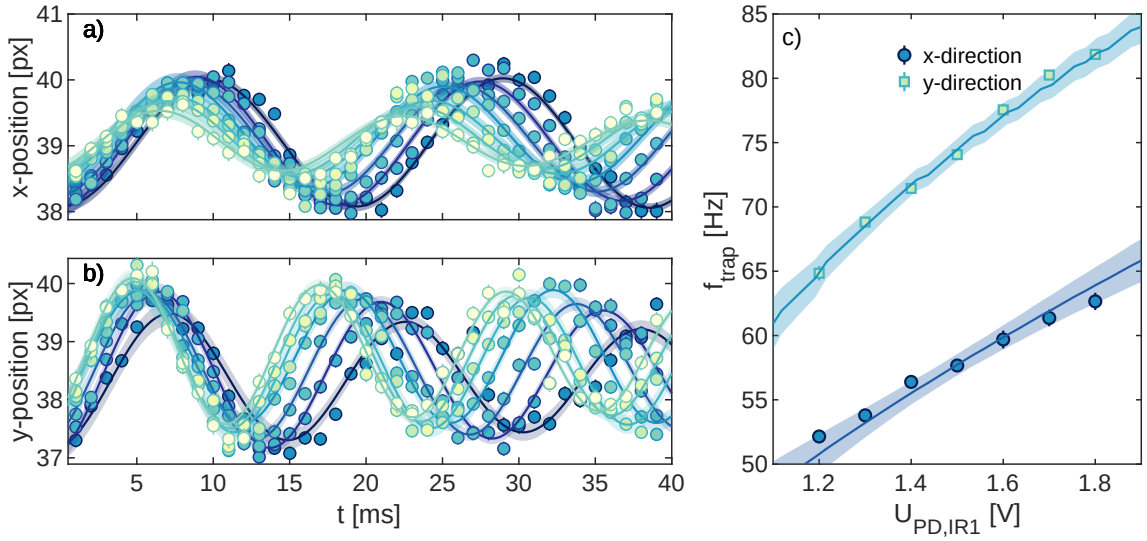


**Figure 1.4.:** Center of mass oscillations in the IR dipole trap. Center off mass oscillations of an $^{174}$Yb BEC excited by displacing the atoms inside the IR trap using a misaligned lattice beam. Panel a) and b) show the observed center of mass oscillations in the $x$- and $y$-directions, for increasing power of IR1 indicated by colors from light to dark, solid lines indicate a fit of a damped sine, where shaded areas represent the 95% confidence interval of the fit. Each data point corresponds to a single measurement. Panel c) shows the trapping frequencies obtained from the fits in panel a) and b). Errorbars (mostly smaller than the marker size) indicate fit uncertainties. The solid lines indicate a combined fit of the trapping frequencies as a function of the power in the IR1 and IR2 beams, see main text for more details. The edges in the fit for the frequencies in y-direction are caused by the discretization of the trapping potential in the course of the fitting routine.

where $\omega_0$ denotes the resonance frequency, $\Gamma$ the linewidth of the transition and $\Delta = \omega - \omega_0$ the detuning. The photon scattering rate is given by [121]:

$$\Gamma_{\text{scat}} = \frac{\Gamma}{\Delta} U_{\text{dip}}. \tag{1.3}$$

Hence to create an attractive potential and simultaneously minimize photon scattering, it is desirable to use high-power laser beams that are far-red detuned with respect to the resonance. In the experiment after the MOT stage the pre-cooled atoms are loaded into a bi-chromatic optical dipole trap, schematically shown in figure 1.3 b). The combined dipole trap consists of a single beam at $\lambda_{\text{DT1}} = 532\,\text{nm}$ with a maximum power of $P_{\text{DT1,max}} \approx 14\,\text{W}$, referred to as DT1 and a crossed dipole trap at $\lambda_{\text{IR1,2}} = 1064\,\text{nm}$ formed by two intersecting beams referred to as IR1 and IR2[1], with a maximum power of $P_{\text{IR1}} \approx 1\,\text{W}$ and $P_{\text{IR2}} \approx 10\,\text{W}$. While DT1 is tightly focused (with waists $w_{y,\text{DT1}} = 18\,\mu\text{m}$ and $w_{x,\text{DT1}} = 29\,\mu\text{m}$) and therefore allows for large trapping frequencies and effective evaporative cooling, the IR-traps feature larger waists ($w_{x,\text{IR1}} = 52\,\mu\text{m}$ $w_{y,\text{IR1}} = 51\,\mu\text{m}$ $w_{y,\text{IR2}} = 67\,\mu\text{m}$ $w_{z,\text{IR1}} = 227\,\mu\text{m}$) to improve the loading of the lowest band of the optical lattice. To reach quantum degeneracy, the power of DT1 is exponentially decreased to

[1]Light for DT1 is provided by a Coherent Verdi V 18, while for the IR traps light is provided by an Innolight Mephisto MOPA

zero within a time of $t_{\mathrm{DT1,evap}} = 6\,\mathrm{s}$. Subsequently, in a second evaporation stage the power of IR1 and IR2 is exponentially decreased by approximately 85% and 30% respectively within $t_{\mathrm{IR,evap}} = 3\,\mathrm{s}$. The final IR trap powers are adapted to obtain an optimal performance in terms of particle number and temperature. The trapping potential of the crossed optical dipole trap at the lowest order can be approximated by an harmonic oscillator that is characterized by an oscillator frequency $\omega_{\mathrm{ho}}$.
To characterize the dipole trap potential, we excite center of mass oscillations that occur at the characteristic frequencies of the dipole trap by displacing the atoms using a misaligned lattice beam. Fig. 1.4 a) and b) show a measurement of the dipole trap frequencies $\omega_x$ and $\omega_y$ as a function of the final power of IR1. We fit the data using a model of the dipole trap, assuming Gaussian beams with the respective waists, intersecting in the horizontal plane at $x = 0$ and $z = 0$ and offset in the vertical direction by half a waist of IR2. This allows to determine the third trapping frequency $\omega_z$. As shown in fig. 1.4 the fits describe the data well, however fitting the trapping frequencies is rather tricky and requires a careful choice of the start parameters. Deviations of the trapping frequencies in the vertical direction from the fit might indicate a small misalignment of the beams. At the final IR trap depth, the dipole trap is characterized by a geometrical mean of the trapping frequencies $\bar{\omega} = \sqrt[3]{\omega_x\omega_y\omega_z}$ of typically $\bar{\omega} \approx 40\,\mathrm{Hz}$ to $\bar{\omega} \approx 50\,\mathrm{Hz}$. More details on the dipole trap setup can be found in refs. [83, 84].

## 1.4. Detection

We use standard absorption imaging on the blue ${}^1S_0 \rightarrow {}^1P_1$ transition to detect atoms after time of flight [122]. As indicated in fig. 1.3 c), two different imaging systems allow to either image along the $x$- or the $z$- direction. The main detection along the $x$-axis has a magnification of $M = 4.7$ and uses an EMCCD camera[2] optimized for detecting blue light. The other detection setup features a magnification of $M = 2.2$ and uses a CCD camera [3]. We take a series of four images: one absorption image and one reference image, with and without atoms, as well as two dark images, without any detection light. These four images are processed to achieve a two-dimensional map of the optical density[122] which is used for further data processing. Atoms prepared in the metastable state ${}^3P_0$ are dark to the 399 nm detection light. To image atoms in the ground and excited state in a single experimental run, we first take an absorption image of the ground-state atoms and subsequently remove residual ground-state atoms from the field of sight using a pulse of resonant blue light from the other imaging direction. Afterwards we shine in a pulse of light at a wavelength of 1389 nm to pump the excited-state atoms to the state ${}^3D_1$ that subsequently decays to the ground state ${}^1S_0$ via the state ${}^3P_1$. In this way the atoms that have been excited initially are repumped to the ground state with a theoretical efficiency of the 97.5% [84] and finally are imaged on the reference picture. Ground and excited state populations are spatially separated as the excited state atoms undergo typically a 3 ms longer time of flight. Having direct access to the populations of both electronic states allows to compute an excited state fraction and thus reduce the effect of shot-to-shot particle number fluctuations. The repump process does not preserve the $m_F$ state and

[2] Andor, iXon 3A-DU888-DC-QBB

[3] PCO Pixelfly

therefore it is not possible to resolve the spin population of the excited state using the OSG technique after repumping. Yet, a spin-selective detection for the excited state would be a valuable add-on and preparatory work for the implementation of a spin-selective detection has already been done by setting up a frequency stabilization for a 1389 nm laser [123].

## 1.5. Spin Resolved Detection and Spin Manipulation

The fermionic isotopes of ytterbium carry a spin of $I = 1/2$ ($^{171}$Yb) and $I = 5/2$ ($^{173}$Yb). For many experiments, it is desirable to work with atoms in certain $m_F$ states. Therefore, it is necessary on the one hand to access the spin information and on the other hand to be able to manipulate the population of the different $m_F$ states.
Spin resolved imaging can be achieved by applying a spin-dependent force spatially separating the atomic cloud. For alkali elements this can be achieved by applying magnetic fields whereas for ytterbium due to the purely nuclear magnetic moment, this is inconvenient. Instead, the spin-dependent force is created optically, using a so-called optical Stern-Gerlach (OSG) technique [124, 125]. Shortly after the atoms are released from the trapping potential, during time of flight (TOF), we shine in a $\sigma^-$-polarized beam that is 1.4 GHz blue detuned with respect to the $^1S_0, F = 5/2 \rightarrow {}^3P_1, F = 7/2$ transition of $^{173}$Yb and that has a power of $P \approx 35$ mW. In the vicinity of the resonance, the ac-polarizability is spin-dependent and, thus the atoms experience a spin-dependent dipole force, spatially separating the atomic cloud into its spin components. Due to spatial restrictions, the beam hits the atoms under an angle of approximately 11° with respect to the horizontal plane. Therefore, the quantization axis has to be turned using the $y$-compensation coils to ensure the OSG beam is purely $\sigma^-$-polarized. Further details on the optical setup and the spin-dependent potentials can be found in [84]. To manipulate the $m_F$ state of the atoms we use resonant optical pumping on the $^1S_0 \rightarrow {}^3P_1$ transition. A magnetic field of typically $B = 18$ G is applied along the $z-$ axis to provide a Zeeman splitting sufficiently large to address individual $m_F$ states on the 182 kHz broad $^1S_0 \rightarrow {}^3P_1$ transition. We use the MOT beams on the $z$-axis to either shine in resonant $\sigma^+$ or $\sigma^-$ polarized light to depopulate a certain $m_F$- state and pump the atoms to a state with a higher or lower $m_F$ quantum number. By applying a series of individual pulses shifted in frequency, atoms can be prepared in a certain spin configuration. The upper panel of fig. 1.5, shows a spin-resolved absorption image of a six spin component gas of $^{173}$Yb. The lower panels show images of gases prepared in a single $m_\mathrm{F}$ state. A small fraction of atoms is pumped to states with lower $m_F$ number by off-resonant scattering of $\sigma^-$ polarized OSG photons and therefore some atoms are detected between the positions that correspond to different $m_F$ states. Spin detection and manipulation for $^{171}$Yb is done analogously. We use the same OSG beam for both isotopes, since at $\Delta = 1.4$ GHz with respect to the $^1S_0, F = 5/2 \rightarrow {}^3P_1, F = 7/2$ of $^{171}$Yb it provides a sufficiently large differential polarizability for both $m_F$ states to resolve the spin populations. The transition of $^1S_0, F = 1/2 \rightarrow {}^3P_1, F = 3/2$ used for the 3D-MOT of $^{171}$Yb is only detuned by $\Delta = -2.67(14)$ MHz [126] with respect to the $^1S_0, F = 5/2 \rightarrow {}^3P_1, F = 5/2$ transition of $^{173}$Yb. Therefore when working with Fermi-Fermi mixtures we first apply optical pumping for $^{171}$Yb, which unintentionally affects the spin population of $^{173}$Yb, and only afterwards perform optical pumping for $^{173}$Yb, which does not affect the spin population of $^{171}$Yb.

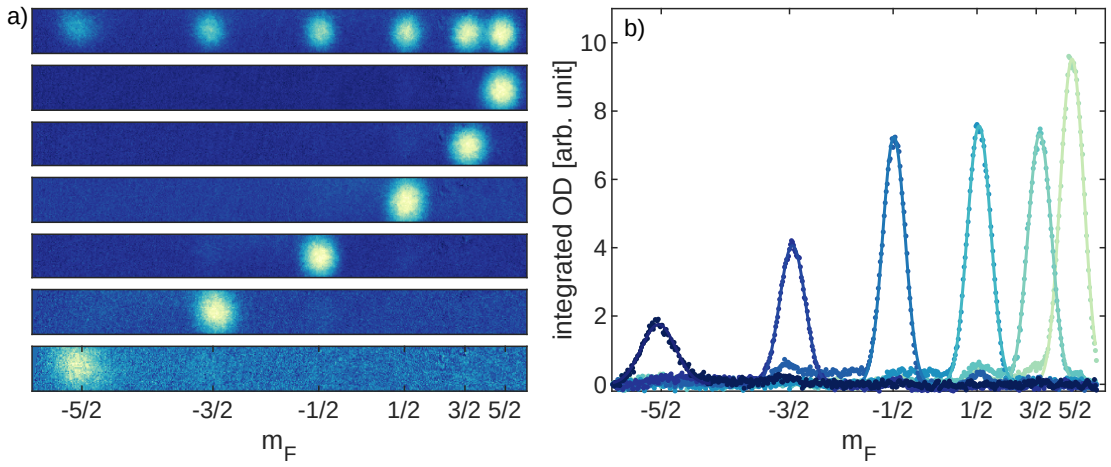


**Figure 1.5.:** Spin detection and manipulation using the optical Stern Gerlach technique and optical pumping. The first row of panel a) shows an OSG picture of a six spin mixture of $^{173}$Yb. In rows two to seven optical pumping has been applied to prepare the atoms in a single $m_F$ state. Panel b) shows the integrated OD corresponding to the single spin images from panel b). Solid lines indicate fits using a 1D Fermi profile

In this way a proper spin preparation for both isotopes is achieved. Hence, by the means of optical pumping various spin configurations for gases of both fermionic isotopes and Fermi-Fermi mixtures can be prepared.

## 1.6. Optical Lattices for Ytterbium Atoms in Different Orbital States

Tailored optical lattice potentials pave the way for quantum simulation of solid-state physics with ultracold atoms. Fueled by the observation of the paradigmatic super-fluid to Mott insulator transition [24], quantum simulation of Hubbard models with ultracold atoms in optical lattices gained much attention. The more recent measurements of topologic quantities of Bloch bands in hexagonal optical lattices [36, 127] and the direct observation of antiferromagnetic ordering in a quantum gas microscope [128] underlines the capacity of ultracold gases in optical lattices for quantum simulation.
Optical lattices at a so-called magic wavelength, characterized by an equal polarizability $\alpha_g = \alpha_e$ for atoms in ground and excited states, have been a breakthrough for metrology, paving the way for optical lattice clocks with unprecedented accuracy [52, 55]. On the other hand, state-dependent lattices, with $\alpha_e/\alpha_g \gg 1$ have been proposed for quantum simulation of multi-band Hubbard models as e.g. the Kondo-Lattice model[64–66]. In the following, I will briefly introduce optical lattices. A comprehensive discussion of optical lattices in the context of ultracold atoms, can be found in ref. [129]. A general discussion of lattice physics can be found in many textbooks such as ref. [130].

The simplest possible optical lattice is formed by two lattice beams intersecting under an angle $\theta$ with equal frequencies, $\omega_1 = \omega_2$ and wavevectors $|\boldsymbol{k}_1| = |\boldsymbol{k}_2|$. The intensity distribution of a laser beam coupled out of an optical fiber and propagating in $z$ direction

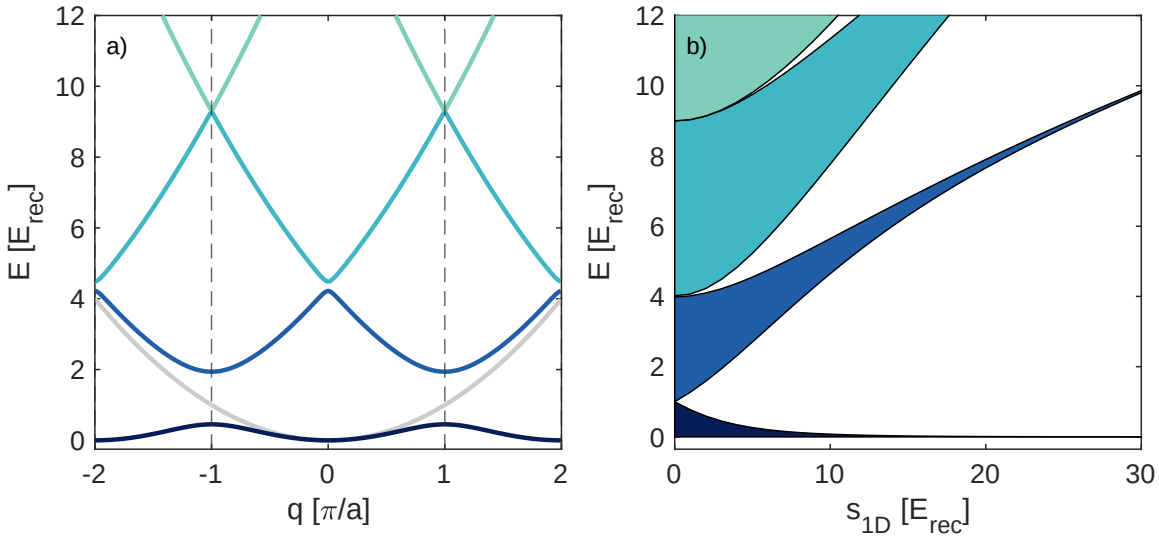


**Figure 1.6.:** Band structure of a one dimensional lattice. Panel a) shows the dispersion relation of the four lowest bands (indicated by colors from dark blue to light green) for a lattice depth of $V_{\text{lat}} = 3\,E_{\text{rec}}$. For comparison, the dispersion relation of a free particle is shown in light gray. Dashed vertical lines indicate the edges of the first Brillouin zone. Panel b) shows energy spectrum of the four lowest bands as a function of the lattice depth. Energies are given with respect to the minimum energy of the lowest band at the specific lattice depth.

$I(r, z)$ usually is well approximated by a Gaussian beam [131]. In the vicinity of the axis of propagation, $r \ll w_0$, (where $r$ denotes the radial position and $w_0$ the waist of the beam), and close to the waist $z \ll z_{\text{R}}$ (where $z_{\text{R}}$ denotes the Rayleigh range) the electric field can be well approximated in terms of plane waves:

$$E_{1,2}(\boldsymbol{r}, t) = E_0 e^{i(\omega t + \boldsymbol{k}_{1,2}\boldsymbol{r})} \tag{1.4}$$

The sum of both $E_1$ and $E_2$ reads:

$$E_1(\boldsymbol{r}, t) + E_2(\boldsymbol{r}, t) = E_0 e^{i(\omega t + \boldsymbol{k}_1\boldsymbol{r})} + E_0 e^{i(\omega t + \boldsymbol{k}_2\boldsymbol{r})}. \tag{1.5}$$

The dipole potential is proportional to the intensity $I(\boldsymbol{r}) = |E_1 + E_2|^2$ that is given by:

$$I(\boldsymbol{r}) = 4E_0^2 \cos^2\left(\frac{1}{2}(\boldsymbol{k}_1 - \boldsymbol{k}_2)\boldsymbol{r}\right) \tag{1.6}$$

The wave vectors have the same absolute value $k = |\boldsymbol{k}_1| = |\boldsymbol{k}_2|$ and hence one can write:

$$\boldsymbol{k}_{\text{lat}} = \boldsymbol{k}_1 - \boldsymbol{k}_2 = |k|\sqrt{2 - 2\cos(\theta)}\hat{\boldsymbol{e}}_{k_{\text{lat}}}, \tag{1.7}$$

where $\hat{\boldsymbol{e}}_{k_{\text{lat}}}$ denotes the unit vector in the direction of $k_{\text{lat}}$. Eq. The dipole potential an atom experiences, is proportional to the intensity $V_{\text{lat}} \sim I(\boldsymbol{r})$ and using eq. 1.6 and eq. 1.7 it can be rewritten as:

$$V_{\text{lat}}(\boldsymbol{r}) = V_0 \cos^2(\boldsymbol{k}_{\text{lat}}\boldsymbol{r}). \tag{1.8}$$

The resulting periodic optical lattice potential is described by a Bravais lattice with primitive lattice vector $\boldsymbol{a} = \pi/k_{\mathrm{lat}}\hat{\boldsymbol{e}}_{\mathrm{lat}}$ and reciprocal lattice vector $\boldsymbol{G} = \pi/|a|\hat{\boldsymbol{e}}_{\mathrm{lat}}$. The lattice Hamiltonian is given by:

$$\mathcal{H}_{\mathrm{lat}} = \frac{\boldsymbol{p}}{2m} + V_{\mathrm{lat}}(\boldsymbol{r}), \tag{1.9}$$

and obeys $\mathcal{H}_{\mathrm{lat}}(\boldsymbol{r}) = \mathcal{H}_{\mathrm{lat}}(\boldsymbol{r} + \boldsymbol{R})$, where $\boldsymbol{R}$ denotes a Bravais lattice vector. According to Bloch's theorem the eigenstates of the lattice Hamiltonian eq. 1.9 are given by Bloch states of the form [130]:

$$\psi^n_{\boldsymbol{q}}(\boldsymbol{r}) = e^{i\boldsymbol{q}\boldsymbol{r}} u^n_{\boldsymbol{q}}(\boldsymbol{r}), \tag{1.10}$$

where the function $u^n_{\boldsymbol{q}}(\boldsymbol{r})$ obeys the same periodicity as the Hamiltonian $u^n_q(\boldsymbol{r} + \boldsymbol{R}) = u^n_{\boldsymbol{q}}(\boldsymbol{r})$. The momentum $\boldsymbol{p}$ is not a good quantum number anymore and is replaced by the quasimomentum $\boldsymbol{q}$. The eigenergies $E^n(\boldsymbol{q})$ form discrete bands labeled by the band index $n \in \mathbb{N}$. Both, the eigenergies and the eigenstates obey the symmetry $E^n(\boldsymbol{q} + \boldsymbol{G}) = E^n(\boldsymbol{q})$ and $\psi^n_{\boldsymbol{q}+\boldsymbol{G}}(\boldsymbol{r}) = \psi^n_{\boldsymbol{q}}(\boldsymbol{r})$ and the quasimomentum hence is only defined up to a vector of the reciprocal lattice $\boldsymbol{G}$. Figure 1.6 a) shows the three lowest bands for a $V_{\mathrm{lat}} = 3\,E_{\mathrm{rec}}$ deep lattice potential. As the lattice depth increases the bandwidth decreases and the band gap increases.

The Bloch wave functions describe particles delocalized over the lattice. Often, especially in deep lattice potentials it is more instructive to describe the system in terms of a localized basis. The Wannier functions constitute an alternative set of eigenstates, describing particles localized at individual lattice sites, and are connected to the Bloch wave functions via [132] :

$$w^n_{\boldsymbol{R_i}}(\boldsymbol{r} - \boldsymbol{R}_i) = \frac{1}{\sqrt{N}} \sum_q e^{-i\boldsymbol{q}\boldsymbol{R}_i} \psi^n_{\boldsymbol{q}}(\boldsymbol{r}). \tag{1.11}$$

Here $\boldsymbol{R_i}$ denotes a lattice vector while $N$ is the number of primitive cells and the sum goes over $q$ in the first Brillouin zone.

Hubbard models [10] describe the dynamics of interacting particles in a lattice using the tight binding approximation [130] and are commonly used to describe ultracold atoms in optical lattices: Atoms reside at individual lattice sites, can hop to neighboring lattice sites and interact with other atoms at the same lattice site. Tunneling and interaction are characterized by energies $t$ and $U$. Tunneling is restricted to nearest neighbor hopping and interactions are restricted to on-site interactions, long range interaction and higher-order tunneling processes are neglected.

The Fermi Hubbard Hamiltonian describing spin 1/2 atoms in a lattice, in second quantization is given by [10]:

$$\mathcal{H}_{\mathrm{FH}} = t \sum_{\langle i,j\rangle,\sigma} \left( c^\dagger_{i,\sigma} c_{j,\sigma} + c^\dagger_{i,\sigma} c_{j,\sigma} \right) + U \sum_i n_{i,\sigma} n_{i,\sigma'}, \tag{1.12}$$

where $c^\dagger_{i,\sigma}$ and $c_{i,\sigma}$ denote the fermionic creation and annihilation operators creating or annihilating an atom of spin $\sigma$ at lattice site $i$, respectively, whereas $n_{i,\sigma}$ and $n_{i,\sigma'}$ denote the fermionic number operators. The tunneling energy $t$ is determined by the wavefunction overlap of neighboring lattice sites $\boldsymbol{R}_i$ and $\boldsymbol{R}_j$ and is given by the matrix element [133]:

$$t = \int w^*_{\boldsymbol{R}_i}(\boldsymbol{r})\, \mathcal{H}\, w_{\boldsymbol{R}_j}(\boldsymbol{r})\, d\boldsymbol{r}, \tag{1.13}$$

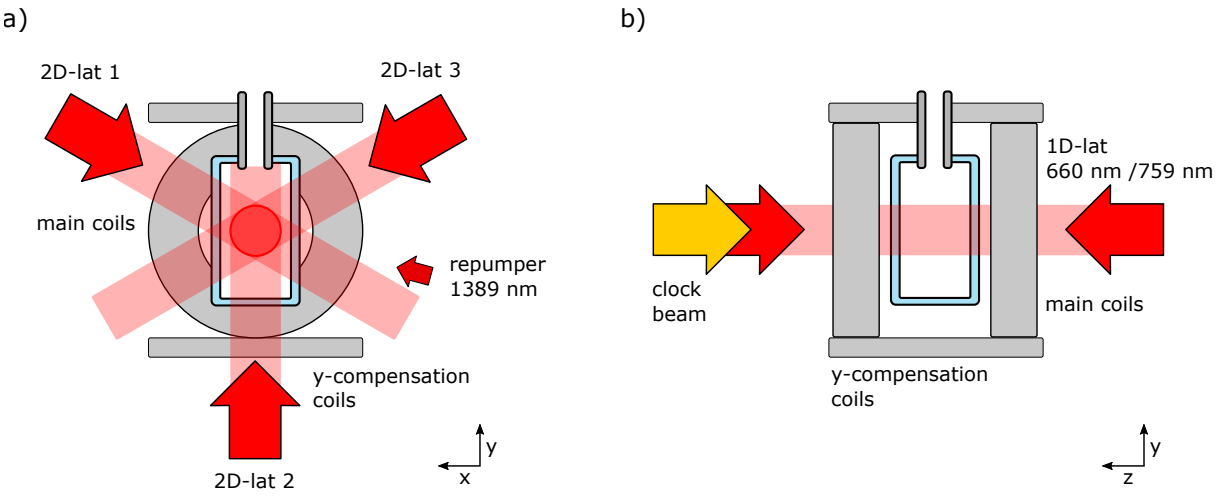


**Figure 1.7.:** Schematic of the lattice and spectroscopy setup. Panel a) shows the three beams forming the 2D lattice in the vertical plane. An out-of-plane polarization of the lattice beams corresponds to a triangular lattice geometry while an in plane polarization corresponds to a honeycomb lattice. Throughout this thesis we use a triangular 2D lattice. A beam of light at $\lambda = 1389\,\text{nm}$ is used to transfer atoms from the metastable state $^3P_0$ to the ground state $^1S_0$ via excitation to the state $^3D_1$ and subsequent radiative decay. Panel b) shows the 1D lattice at either $\lambda_{\text{1D,mag}} = 759\,\text{nm}$ or $\lambda_{\text{1D,SDL}} = 660\,\text{nm}$ that is superimposed with the clock spectroscopy beam at $\lambda_{\text{clock}} = 578\,\text{nm}$.

whereas the Hubbard on-site interaction parameter $U$ is given by [133]:

$$U = g \int |w_{\boldsymbol{R}}(\boldsymbol{r})|^4 \, d\boldsymbol{r}. \tag{1.14}$$

In the limit of $s$-wave interactions, the interaction strength $g$ is determined by:

$$g = \frac{4\pi\hbar^2 a}{m}, \tag{1.15}$$

where $a$ denotes the $s$-wave scattering length, $m$ the atomic mass and $\hbar$ the reduced Planck constant.
Combining 1D-lattices in $x$, $y$ and $z$-directions a three-dimensional simple cubic lattice potential can be realized. There are various schemes to realize more sophisticated lattice geometries as e.g. honeycomb lattices or superlattices (see e.g. ref. [129] for a comprehensive review of different optical lattice types for ultracold atom experiments). At the ytterbium experiment, we use a one-dimensional lattice along the $z$-axis and a triangular lattice in the vertical $x-y$ plane, that is formed by three interfering beams intersecting under an angle of 120 degrees with a linear polarization out-of-plane, as described in [26]. Figure 1.7 shows the lattice-beam configuration at the experimental glass cell. Note that by turning the polarization of the 2D-lattice beams the lattice potential can be transformed into a honeycomb lattice. However, for all experiments presented in this thesis the 2D-lattice potential is restricted to a triangular geometry. The 1D-lattice along the $z$-axis is superimposed with the clock laser beam, used to excite atoms to the metastable state $^3P_0$. For the spectroscopic measurements presented in this thesis, the 2D-lattice is used as a confining potential, holding the atoms against gravity. Therefore, the triangular geometry is not of further importance but has to be accounted for when calculating

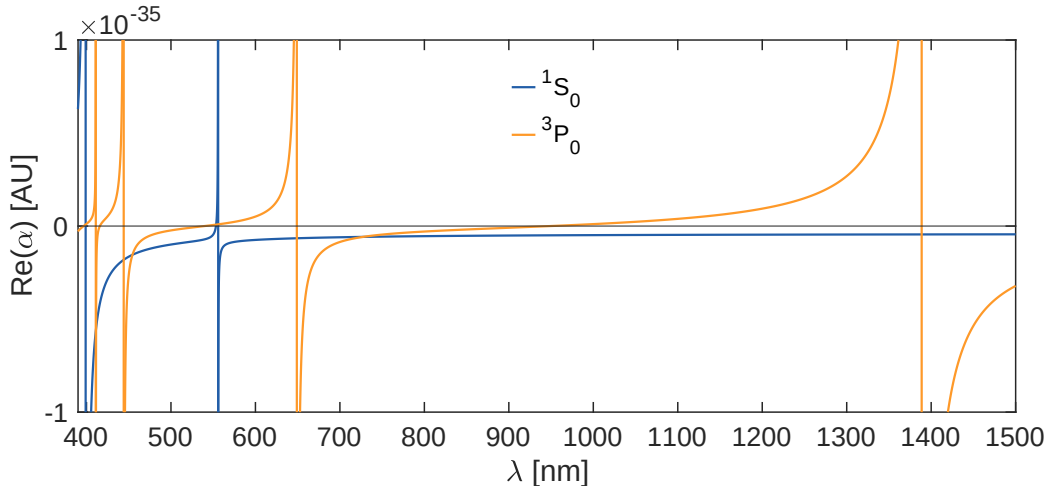


**Figure 1.8.:** Polarizability of the ${}^1S_0$ and ${}^3P_0$ states according to a calculation presented in [81], taking into account the most prominent known transitions. While the predicted value of the magic wavelength significantly deviates from experimentally determined value of $\lambda_{\text{mag}} = 759$nm [108, 134, 135]. The computed polarizabilities are expected to better agree with the experiment close to resonances. More accurate, relativistic many-body calculations of static and dynamic polarizabilities for the states ${}^1S_0$ and ${}^3P_0$ can be found in [136].

Wannier integrals necessary to determine Hubbard on-site interactions.

The light shift $\Delta E$ that an atom in initial state $i$ experiences, when interrogated by a laser beam at wavelength $\lambda$, can be obtained by means of perturbation theory and is given by [121]:

$$\Delta E_i = \sum_{j \neq i} \frac{|\langle j|\mathcal{H}_{\text{int}}|i\rangle|^2}{\mathcal{E}_i - \mathcal{E}_j}, \tag{1.16}$$

where $\langle j|\mathcal{H}_{\text{int}}|i\rangle$ denotes the matrix transition element for initial state $i$ and final state $j$. The corresponding eigenenergies are denoted by $\mathcal{E}_{i,j}$ and the sum goes over all possible final states with $i \neq j$. As for different states $i$, the final states $j$ are generally different, the dipole potential depends on the electronic state of the atom. Therefore at a given lattice laser wavelength the lattice depth in general differs for atoms in the ground state ${}^1S_0$ and the excited state ${}^3P_0$ in. Figure 1.8 shows a calculation of polarizabilities for ground and metastable state atoms according to ref. [81]. At certain wavelengths the polarizabilities are equal which therefore are referred to as magic wavelengths. Optical lattices operated at a magic wavelength have been a major breakthrough for metrology enabling high-resolution spectroscopy [52], free of differential ac-stark shifts. Ytterbium has a magic wavelength at $\lambda_{\text{mag}} = 759\,\text{nm}$ [108, 134, 135]. The precise values experimentally determined for different ytterbium isotopes are summarized in tab. 1.4. In the lab a Ti:Sa laser[4] provides about 3.5 W of light at the magic wavelength, that is used for the one and two dimensional lattices. Further details on the magic lattice setup can be found in [83, 84, 137]. While for high-resolution spectroscopy it is crucial to work at the magic wavelength a state dependent lattice, that is deep for atoms in the metastable state and shallow for ground state, atoms offers intriguing possibilities for

[4] Coherent MBR 110

| isotope | $\nu_{\mathrm{mag}}$ | reference |
|---|---|---|
| $^{174}$Yb | 394.799 475(35) THz | [108] |
| $^{171}$Yb | 394.798 329(10) THz | [134] |
| $^{173}$ Yb | 394.82(2) THz | [135] |

**Table 1.4.:** Experimentally determined magic lattice frequencies for different ytterbium isotopes.

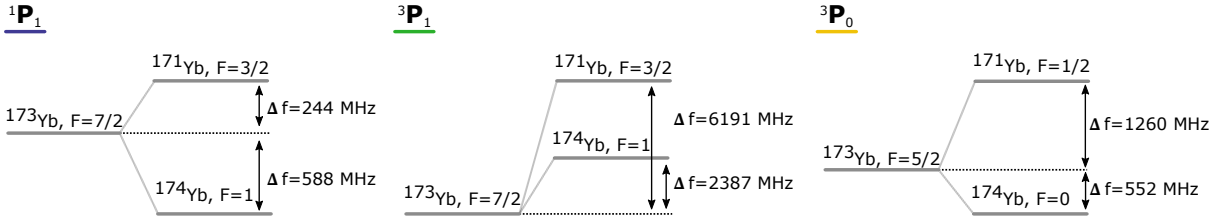


**Figure 1.9.:** Isotope Shifts for the MOT and clock transitions for $^{171}$Yb and $^{174}$Yb relative to $^{173}$Yb, as reported in refs. [126, 134, 138–140]. Distances are not to scale.

quantum simulation applications[64–66]. A solid state laser[5] provides about 500 mW of light at $\lambda_{\mathrm{SDL}} = 660\,\mathrm{nm}$ that is used to create a state dependent 1D-lattice (SDL) along the $z$-direction, characterized by a ratio of lattice depths for ground and excited state atoms of $V_{\mathrm{lat,e}}/V_{\mathrm{lat,g}} \approx 5.55(32)$. The SDL is characterized in sec. 5. Further details on the optical setup of the state dependent lattice can be found in refs. [84, 90].

## 1.7. Laser Systems

In the ytterbium lab we use a multitude of lasers at several different wavelengths. While the optical lattices and dipole traps have low to moderate requirements concerning frequency stability as they all are operated in the far-detuned regime, the near-resonant and resonant light used for magneto optical trapping, imaging and clock spectroscopy demands active frequency stabilization. The absolute stability requirements are very different as the linewidths of the relevant transitions $^1S_0 \rightarrow {}^1P_1$, $^1S_0 \rightarrow {}^3P_1$ and $^1S_0 \rightarrow {}^3P_0$ vary about 9 orders of magnitude between $\Gamma_{^1P_1} = 2\pi \times 29\,\mathrm{MHz}$, $\Gamma_{^3P_1} = 2\pi \times 182\,\mathrm{kHz}$ and $\Gamma_{^3P_0} < 2\pi \times 10\,\mathrm{mHz}$ [101–103]. Additionally the isotope shifts between $^{171}$Yb and $^{173}$Yb (see fig. 1.9) require to span a broad frequency range of up to 6.2 GHz. The laser systems used in the ytterbium lab have in large parts been designed and set up prior to my time as PhD student at the experiment. Therefore, detailed discussions of design considerations and technical implementations can be found in ref. [82, 84, 85, 91].
However, during the past years, some of the laser systems have been modified and improved. In the following, I will discuss the laser systems providing light for resonant addressing of the $^1P_1$, $^3P_1$ and $^3P_0$ states. I will focus on recent modifications and frequency stabilizations schemes, as a profound understanding is necessary to operate the lab.

[5] Cobolt Flamenco

### 1.7.1. Frequency Stabilization in the Ytterbium Laboratory

There are different ways to achieve frequency stability. Typically it is a good choice to use Doppler-free saturation spectroscopy (see e.g. [141]) on transitions of interest to create an error signal that can be used to lock the laser. For rubidium, a compact spectroscopy setup can be realized using vapor cells. However, the low vapor pressure of ytterbium prohibits the use of vapor cells. Instead, an oven has to be used to create an atom beam that can be used for spectroscopy. In the early days of the experiment a beam apparatus has been utilized to perform spectroscopy and stabilize lasers on the blue and green transitions ${}^1S_0 \rightarrow {}^1P_1$ and ${}^1S_0 \rightarrow {}^3P_1$ [82]. Unfortunately, the achieved frequency stability was not satisfactory for a reliable and stable operation of the experiment.
Another way to achieve frequency stability is to utilize a resonance of an optical resonator as a frequency reference and use the Pound-Drever-Hall (PDH) technique to create an error signal for frequency stabilization [142, 143]. The PDH technique provides an error signal with a high signal-to-noise ratio and a steep slope, well-suited for frequency stabilization and laser linewidth narrowing. A resonator possesses an infinite number of equally spaced resonances, that can be used for frequency stabilization. While this offers flexibility in terms of frequencies the laser can be stabilized to, stabilizing the laser to a particular absolute frequency e.g. close to a particular atomic transition requires knowledge of the laser frequency up to a free spectral range (FSR). The resolution of a wavelength meter is sufficient to resolve the free spectral range of a 10 cm long cavity with a free spectral range of $\Delta_{\mathcal{FSR}} \approx 1.5\,\mathrm{GHz}$, and thus can conveniently be used to solve the first problem. To achieve long term stability it is necessary to isolate the resonator from environmental disturbances such as pressure and temperature fluctuations in a vacuum chamber. By manufacturing the resonator from materials that feature a zero crossing of the coefficient of thermal expansion and actively stabilizing the cavity's temperature to the temperature of the zero crossing the effect of temperature fluctuations can be minimized.
In the laboratory, three different resonators are used to stabilize lasers on the blue, green and yellow transitions. To bridge isotope shifts, for ${}^{171}$Yb, ${}^{173}$Yb and ${}^{174}$Yb of up to $\sim 6.2\,\mathrm{GHz}$ (see fig. 1.9), we employ offset locking techniques to transfer the stability achieved by the PDH frequency locking to other lasers operated at the desired frequencies.

#### Frequency Stabilization according to Pound, Drever and Hall

In the following, I will briefly introduce the Pound-Drever-Hall frequency stabilization according to ref. [144].

Consider a resonator consisting of two mirrors with reflectivities $r_1, r_2$ placed at a distance of $L$. The resonance condition is then given by $\lambda = 2L/n$, with $n \in \mathbb{N}$. The resonances are equally spaced in frequency, seperated by a free spectral range (FSR) $\Delta_{\mathrm{FSR}} = c/2L$, where $c$ denotes the speed of light. The linewidth of the resonance is determined by the finesse $\mathcal{F}$ that is given by the reflectivity of the mirrors. For $r = r_1 = r_2$ it reads: $\mathcal{F} = \pi\sqrt{r}/(1-r)$.
To realize a closed feedback cycle for frequency stabilization it is crucial to be able to

analyze whether the actual frequency is below or above the desired frequency. Assuming an incoming electric field of $E_{\text{in}} = E_0 \cdot e^{i\omega t}$ the reflected electric field can be expressed as $E_{\text{ref}} = F(\omega)E_{\text{in}}$, where $F(\omega)$ denotes the complex reflection coefficient given by [144]:

$$F(\omega) = \frac{r\left(e^{\frac{i\omega}{\Delta_{\text{FSR}}}} - 1\right)}{1 - r^2 e^{\frac{i\omega}{\Delta_{\text{FSR}}}}}. \tag{1.17}$$

Scanning the frequency across the cavity resonance, one observes a phase shift of $2\pi$ and a dip in the reflected intensity as the resonator becomes transparent on resonance. While the reflected intensity is symmetric, with respect to the resonance and therefore does not allow to identify whether the actual frequency is red or blue detuned, the phase of the light is antisymmetric around the resonance frequency. It therefore allows to unambiguously identify whether the actual frequency is blue or red detuned with respect to the resonance and thus can be used to apply a negative feedback loop. The Pound-Drever-Hall technique utilizes interference between a carrier and sidebands obeying a fixed phase relation with respect to the carrier to access the phase information of the reflected light and create an error signal that can be used for frequency stabilization.
We typically use electro optical modulators (EOMs) to modulate the phase of the light and create sidebands. Assuming a light frequency $\omega$ and a modulation frequency $\Omega$ the modulated electric field can be described by[144]:

$$E(t) = E_0 \cdot e^{i\omega t + i\beta \sin \Omega t}. \tag{1.18}$$

Here $E_0$ denotes the amplitude of the electric field while $\beta$ represents the modulation depth. Equation 1.18 can be rewritten in terms of Bessel functions $J_k(\beta)$ as [144]:

$$E(t) = E_0 \left( J_0(\beta) e^{i\omega t} + \sum_{k=1} J_k(\beta) e^{(\omega + k\Omega)t} + \sum_{k=1} (-1)^k J_k(\beta) e^{(\omega - k\Omega)t} \right), \tag{1.19}$$

where $k$ denotes the order of the Bessel function. Measuring the reflected intensity[144]:

$$\begin{aligned} P_{\text{ref}} &= P_{\text{c}} |F(\omega)|^2 + P_{sb}(|F(\omega + \Omega)|^2 + |F(\omega - \Omega)|^2) \\ &+ 2\sqrt{P_{\text{c}} P_{\text{sb}}}(\text{Re}\{F(\omega)F^*(\omega + \Omega) - F(\omega)F^*(\omega - \Omega)\}) \cos \Omega t \\ &+ 2\sqrt{P_{\text{c}} P_{\text{sb}}}(\text{Im}\{F(\omega)F^*(\omega + \Omega) - F(\omega)F^*(\omega - \Omega)\}) \sin \Omega t \end{aligned} \tag{1.20}$$

and demodulating the signal at the modulation frequency $\Omega$ yields the Pound, Drever and Hall error signal. Analyzing the amplitude of the error signal as a function of the modulation depth yields an optimum modulation depth of $\beta = 1.08$. Figure 1.10 shows a schematic PDH frequency stabilization setup. An EOM is used to create sidebands at a frequency $\Omega$. Subsequently, the light passes an optical diode and is coupled into the resonator. Light back-reflected from the resonator is reflected by the optical diode and directed onto a photodiode. To create the error signal, the photodiode signal is demodulated at the modulation frequency $\Omega$ using the same (or another phase stable) RF-source that is used for the creation of the sidebands. Finally, the error signal is fed into a frequency control circuit e.g. a PID controller that is used to apply negative feedback to the frequency of the laser. For an external cavity diode laser (ECDL) this can be achieved e.g. by modulating the laser diode current.

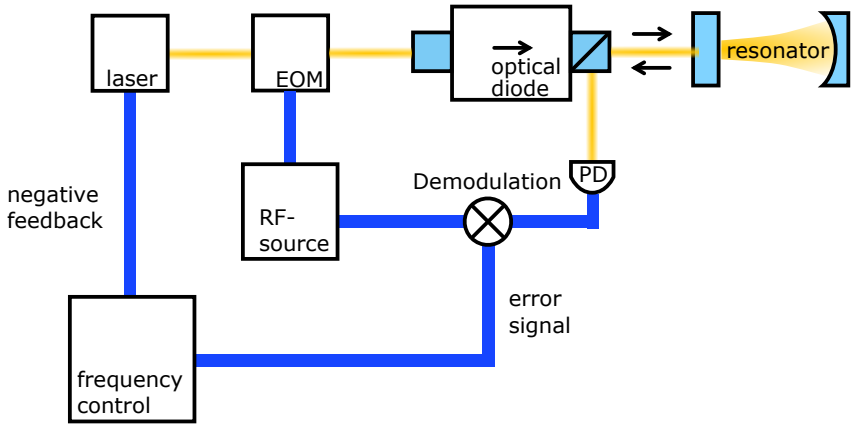


**Figure 1.10.:** Schematic PDH frequency stabilization setup. See main text for a detailed description.

## 1.7.2. Blue Laser System

### Master Laser

A frequency-doubled diode laser[6] provides up to 300 mW of light at 399 nm for imaging and the 2D-MOT push beam and serves as a master laser for the blue transition. Over the course of this thesis the entire setup has been rebuilt by the author.
As mentioned earlier, the previously-used atom beam spectroscopy did not yield a sufficiently good error signal to allow for reliable frequency stabilization of the imaging laser. Therefore we decided to use an optical resonator as a frequency reference instead. Over the course of his bachelor thesis M. Hagenah (who was co-supervised by the author) built a resonator using a Zerodur spacer with glued mirrors that have been coated in house [97]. As it turned out, the drift of the resonance was too large to be compensated for using AOMs. Therefore, we decided to switch to a commercial resonator system[7] based on a resonator with mirrors optically contacted to the spacer, both made out of ULE glass. The custom-made multichroic coatings of the mirrors yield a finesse of $\sim 3000$ for 798 nm, 1285 nm and 1389 nm. Therefore, different lasers can simultaneously be referenced to the resonator. We lock the fundamental mode of the blue master laser at $\lambda = 798$ nm to the resonator, whose temperature is stabilized to the CTE zero crossing of the ULE spacer to improve the long-term frequency stability. The setup used for frequency stabilization is schematically shown in fig. 1.11. A resonant free space EOM [8] creates sidebands at $\sim 20$ MHz. The frequency of the light is shifted by approximately 80 MHz by an AOM in double pass configuration (omitted in fig. 1.11) and then is coupled into a one-to-two, 50:50 fiber splitter. A fiber collimator with a de-adjusted lens is used to focus the outcoupled beam onto the incoupling facette of the resonator and couple light into the cavity. Back-reflected light is coupled back into the fiber splitter. The intensity of the reflected light is measured at the remaining port of the fiber coupler using a home-built photodiode. The measured signal is fed into a PDH-detection unit[9], (also used to drive the EOM) to create an error signal that is finally fed into a control circuit[10] that imposes

[6] Toptica Photonics DL-TA-SHG pro
[7] Stable Laser Systems
[8] Qubig EO-20-M3-VIS
[9] Qubig EO-20-L3-IR
[10] Toptica FALC 110

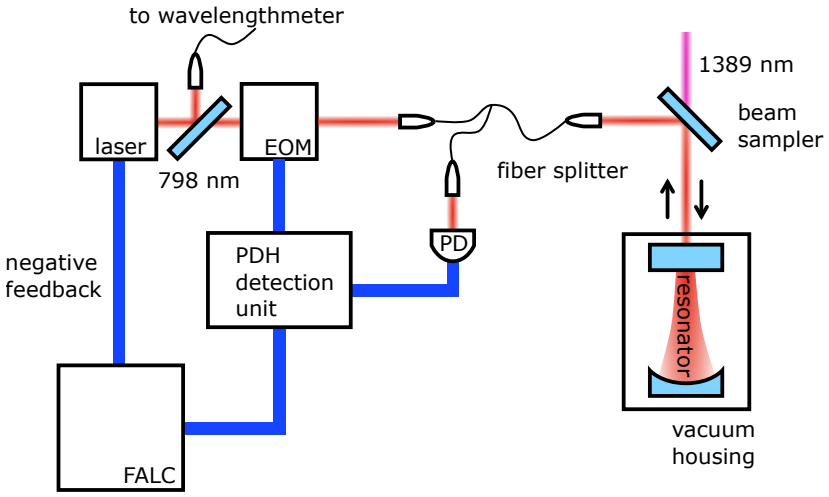


**Figure 1.11.:** Frequency stabilization setup for the blue master laser.

negative feedback onto the diode current and piezo voltage of the ECDL laser. A fiber splitter allows to built a compact setup that apart from the outcoupler does not require any further mode-matching or polarizing optics. However, to simultaneously achieve a good cavity mode match and a high fiber coupling efficiency for the back-reflected light requires careful adjustment and positioning of the fiber outcoupler. A beam sampler in front of the cavity allows to superimpose light at 798 nm and 1389 nm, and to use the cavity as a frequency reference for both wavelengths. An analogue setup used to stabilize a laser at the repump wavelength 1389 nm has been built over the course of the master's thesis of N. Pintul [123]. To distinguish between different transversal cavity modes we observe the beam profile of light transmitted through the resonator using a simple commercial camera. To choose the correct cavity resonance for frequency stabilization, the frequency of the laser is monitored using a wavelength meter.
Changing the frequency stabilization to the cavity-based setup vastly increased the stability of the experiment. The experiment can be operated unsupervised for many hours and overnight and therefore the data acquisition time could be drastically increased.

The blue master laser is stabilized at a detuning of $\Delta \approx -160\,\mathrm{MHz}$ with respect to the ${}^1S_0 \rightarrow {}^3P_1$ transition of ${}^{173}\mathrm{Yb}$ and provides resonant and near-resonant light used for absorption imaging of two different isotopes and the 2D-MOT push-beam. Therefore the isotope shift has to be bridged using AOMs. The laser system features three independent branches for $x$- and $y$-axis imaging and the 2D-MOT push beam as shown in fig. 1.12. Each branch again is divided into two different branches. One is shifted by $+160\,\mathrm{MHz}$ to the resonance of ${}^{173}\mathrm{Yb}$ using an 80 MHz AOM in double pass configuration. The other can either be shifted to the resonance of ${}^{171}\mathrm{Yb}$ or ${}^{174}\mathrm{Yb}$ by $\Delta_f = +404\,\mathrm{MHz}$ or $\Delta_f = -428\,\mathrm{MHz}$, respectively, using a 200 MHz AOM in double pass configuration. The two branches subsequently are superimposed again employing a 50:50 beamsplitter and finally the light is coupled into a single-mode optical fiber guiding light to the main experiment.

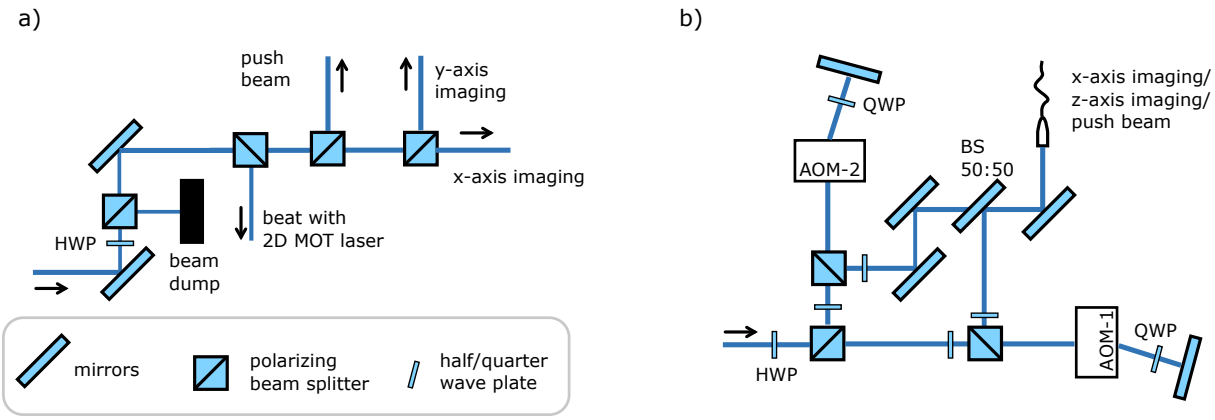


**Figure 1.12.:** Blue master laser system. Panel a) schematically shows the different branches of the blue master laser system. The laser's output power is split up into four different branches, used to offset lock the 2D-MOT laser, imaging along $x$- and $z$-direction and for the 2D-MOT pushing beam. Panel b) schematically depicts one of the three branches used for $x$- and $y$-axis imaging and 2D-MOT beam. Each branch is again split up into two different branches, the frequency of the light is shifted to the resonance of the different isotopes using an 80 MHz AOM (AOM-1) and an 200 MHz AOM (AOM-2) in double pass configuration, respectively. Subsequently, the two branches are superimposed again, and light is coupled into an optical fiber, guiding light to the main experiment. The AOMs allow for fast switching and enable double isotope imaging by changing the frequency of the imaging light for absorption and reference image.

## 2D-MOT Laser

Due to the broad linewidth of the ${}^1S_0 \rightarrow {}^1P_1$, reaching the saturation intensity of $I_{\text{sat}} = \pi hc\Gamma/3\lambda^3 \approx 60\,\text{mW/cm}^2$ requires a lot of power. The pointing stability of the MOT beams can be increased by using fiber coupled telescopes, though for light in the blue part of the optical spectrum this is difficult. Scattering processes as e.g. Rayleigh scattering are more likely ($\propto 1/\lambda^4$) for shorter wavelengths, and the fiber coupling efficiency is decreased compared to higher wavelengths eg. in the infrared. Due to solarization, the optical fibers degrade [145] and have to be exchanged regularly. Therefore, the 2D-MOT laser system has been built as a free-space setup, avoiding fiber associated losses but with deteriorated pointing stability. In the past the 2D-MOT performance especially for the fermionic isotope ${}^{173}$Yb has been the bottle neck of the experiment, partly due to the 2D-MOT laser power being limited to $P_{\text{2D-MOT laser}} \approx 300\,\text{mW}$, yielding a mean intensity of $I_{\text{mean}} < 0.5\,I_{\text{sat}}$ in the 2D-MOT beams. Exchanging the 2D-MOT laser by a new high power version with an output power of up to 1.5 W, allowed to increase the mean intensity of the 2D-MOT beams and to reach saturation intensity. Thereby the effect of power fluctuations could be decreased. Due to different sizes of the new laser's housing, the 2D-MOT laser setup has been rebuilt by B. Santra, K. Sponselee, and the author over the course of this work. A detailed description of the optical setup can be found in the doctoral thesis of K. Sponselee [98].
The frequency of the 2D-MOT laser is referenced to the master laser using an offset lock based on a digital phase detector [146] and using the locking electronics of the laser [11]. The

[11] Toptica DLC locking option

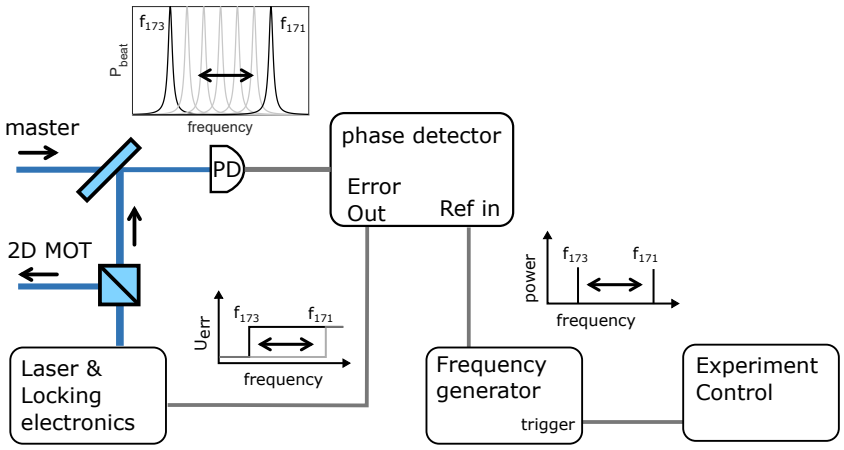


**Figure 1.13.:** Offset locking scheme for the 2D-MOT laser. A portion of the light emitted by the 2D-MOT laser is superimposed with light emitted from the master laser, that is stabilized to a resonance of a cavity (see sec. 1.7.2). The beat signal is measured with a photo diode and fed into a phase detector [146], where it is compared to a reference signal from a frequency generator. The error signal is fed to a PID controller applying negative feedback to the laser diode current and piezo voltage of the ECDL laser. The frequency generator performs a frequency sweep triggered by the experiment control to switch between a 2D-MOT of $^{173}$Yb and $^{171}$Yb.

frequency stabilization setup is schematically shown in figure 1.13. A beat note between the blue master laser and the 2D-MOT laser is detected using a fast photodiode[12]. The signal is amplified and fed into a home-built phase detection circuitry based on ref. [146]. The beat note is compared to a reference signal generated by a frequency generator [13] and internally multiplied by a factor of $n = 25$. The digital, step-function-shaped, error signal is fed to the laser driving electronics and used to lock the laser using an internal PID circuitry. While the digital error signal restricts the frequency stability of the lock, the frequency of the 2D-MOT laser can conveniently be changed by the isotope shift within the experimental cycle by applying a frequency chirp to the reference signal of the phase detector, as schematically shown in figure 1.13. In this way subsequent loading of different isotopes into the bi-chromatic 3D-MOT can be realized.

### 1.7.3. Green Laser System

The green laser system for the bi-chromatic 3D-MOT has been designed over the course of the master's thesis of the author [91] and has been set up mainly by A. Kochanke [84]. Since then the setup has been extended by an additional laser[14] and some components of the locking setup have been changed. In the following, I will therefore describe the green laser system in its current form.

The setup is schematically shown in fig. 1.14 a). Light is provided by three different frequency-doubled lasers referred to as green master laser[15], green laser[16]-2 and green

[12] Hamamatsu G4176-03
[13] Keysight 33600A Series Waveform Generator
[14] Toptica DL-TA-SHG Pro
[15] Toptica Photonics DL-BoosTA-SHG Pro
[16] Toptica Photonics DL-TA-SHG Pro

laser[17]-3. The green master laser provides light for the 3D-MOT of $^{173}$Yb and the OSG beam used for spin-resolved imaging of both fermionic isotopes. An additional branch of the laser system might be used for photoassociation (PA) spectroscopy in the future. Green-laser-2 provides 3D-MOT light for $^{171}$Yb or $^{174}$Yb while green-laser-3 provides light for a Raman setup described in ref. [99, 147].
The frequency of the green master laser is referenced to a high-finesse resonator, referred to as cavity-2, whereas green-laser-2 and green-laser-3 are referenced to the green master laser employing offset-locking techniques. Cavity-2 is part of the clock laser setup and can be used to characterize the linewidth of the clock laser in self-heterodyne measurements[82, 85]. Designed for a wavelength of $\lambda = 578\,\mathrm{nm}$ the coating of the cavity mirrors is broad enough to allow being used as a frequency reference for the green master laser. The cavity length of $L = 7.5\,\mathrm{cm}$ yields a free spectral range of $\Delta_{\mathrm{FSR}} \approx 2\,\mathrm{GHz}$. The resonator spacer is made of ULE glass, while the the cavity mirrors are made of silica. Due to technical limitations it is not possible to stabilize the temperature of the resonator at the temperature of the CTE zero crossing of $T_{\mathrm{CTE,zero}} = -26(2)\,^{\circ}\mathrm{C}$ [137]. Instead, the resonator is stabilized to a temperature of $T_{\mathrm{work}} = 0.59\,^{\circ}\mathrm{C}$ [137] and the frequency stability of the cavity-2 setup is diminished. Therefore, the frequency of the green master laser has to be adjusted on a daily basis to compensate for drifts of the cavity setup. The frequency of the green master laser is stabilized to $\Delta \approx +400\,\mathrm{MHz}$ with respect to the MOT transition of $^{173}$Yb. Beat notes between the green master laser and green-laser-2 and green-laser-3 are measured via photodiodes(PD) PD-1 and PD-2 and are used to offset lock green-laser-2 and green-laser-3. Green-laser-2 is referenced to the master laser using an offset locking technique as described in ref. [148], whereas green-laser-3 is referenced to the green master laser using a commercial phase detection and locking unit [18]. In this way the frequency of green-laser-2 and green-laser-3 can be tuned over a wide range and the isotope shifts between $^{171}$Yb, $^{173}$Yb and $^{174}$Yb can be easily bridged.
The optical setup used for PDH frequency stabilization of cavity-2 is similar to the clock laser locking setup described in ref. [82] and is schematically shown in fig. 1.14 b). AOM-1 and AOM-2 are used to shift the frequency of the green master laser light to the cavity resonance. Light is coupled into an optical fiber delivering light onto a breadboard on a vibration-isolation platform, which is located inside a wooden box to reduce sound. EOM-1 creates sidebands at approximately 20 MHz used for PDH-frequency stabilization. Light is coupled into the optical resonator, and an optical isolator is used to spatially filter light back-reflected from the resonator and direct it onto PD-4. The power transmitted through the cavity is monitored using PD-5 whereas PD-3 is used to stabilize the laser power guided onto the vibration isolation platform.
Over the course of this thesis the non-resonant EOM[19] that previously had been used to create sidebands as well as the driving and error detection electronics have been replaced by a resonant free-space EOM[20] and a commercial PDH detection unit[21]. In this way an optimal modulation depth of $\beta = 1.08$ is reached and the frequency lock's stability could be improved. Additionally, the photodiode used for the PDH detection has been replaced by a fast home-built photodiode.

[17] Menlo Systems Orange One
[18] Menlo Systems Syncro
[19] Linos PM-25
[20] Qubig EO-20-M3-VIS
[21] Qubig ADU

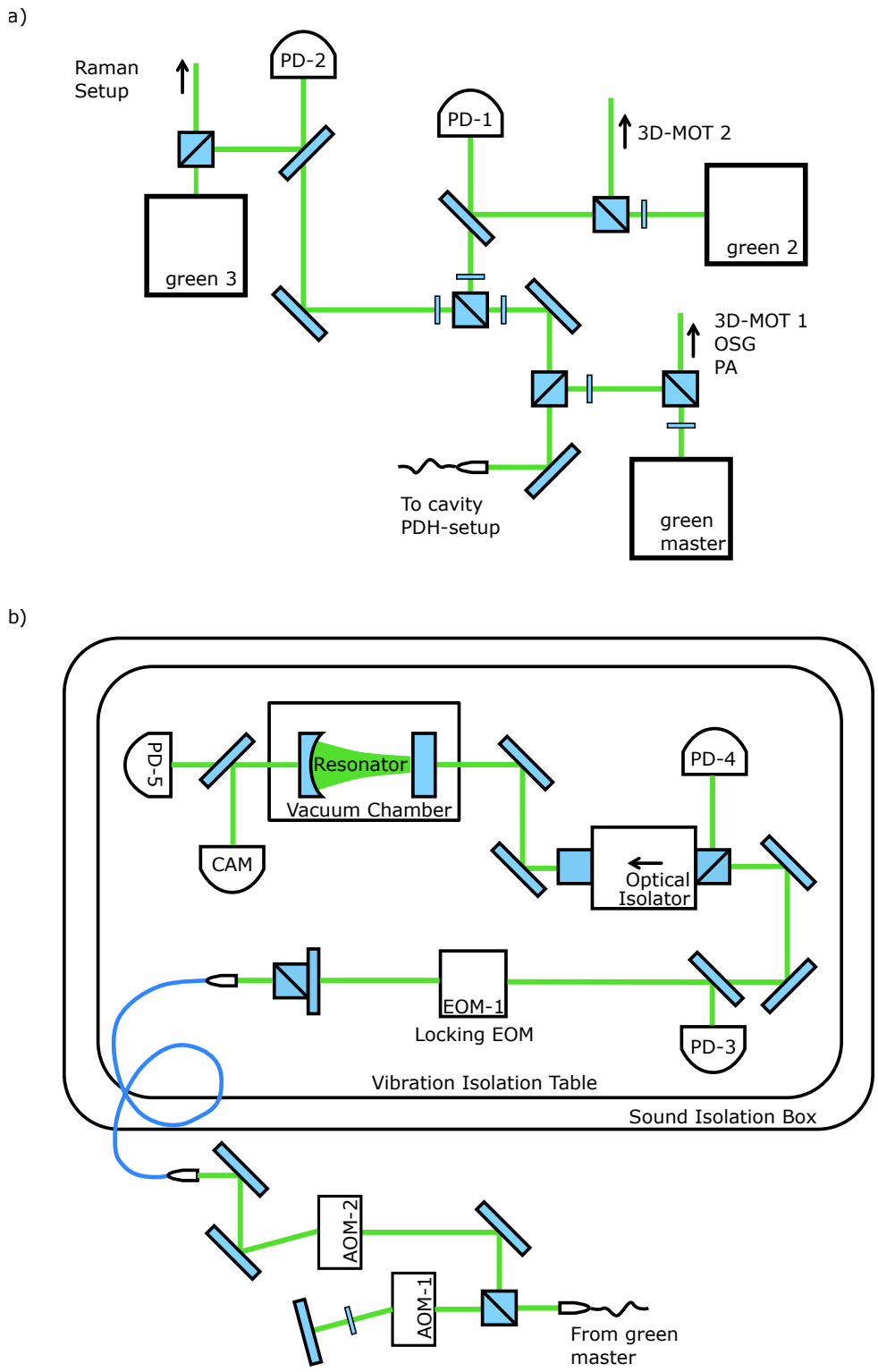


**Figure 1.14.:** Green laser system. The lasers and the cavity are located on two different optical tabels. Panel a) schematically shows the green laser system. Panel b) shows the PDH locking setup for cavity-2. See main text for detailed description.

The detunings necessary for MOTs and OSG are set by one or multiple AOMs in single- or double-pass configuration, (omitted in fig. 1.14). Light is guided to the main experiment using optical fibers. A home-built 'fiber cluster' is used to superimpose two beams at the different MOT frequencies and to divide the available power into four branches used for the four 3D-MOT beams [91]. Frequency broadening as described earlier in this section is achieved by modulating the driving frequency of the MOT AOMs at a modulation frequency of $f_{\text{broadening}} \approx 200\,\text{kHz}$. To compress the MOT and achieve low temperatures, central frequency, modulation depth and the amplitude of the RF-drive are simultaneously ramped in two subsequent steps. Given the modulation frequency of 200 kHz, to implement these ramps with a digital RF source is not straightforward. Therefore, the AOM driving signal is generated by an analog RF source, which however is prone to long-term frequency drifts and shows a slow frequency response. For spin preparation we switch to a digital RF-source (using an RF-switch) to assure frequency reproducibility and stability for the short optical pumping pulses. However, a replacement of the analog driving electronics by a FPGA-controlled digital RF source might yield an improved MOT performance.

## 1.7.4. Clock Laser System

One of the main goals of the ytterbium experiment is to use high-resolution spectroscopy on the ultra-narrow clock transition ${}^1S_0 \rightarrow {}^3P_0$ to observe e.g. interaction induced energy shifts. While the linewidth of the clock transition has been estimated to be below 10 mHz [102], the linewidth of a free-running diode laser is typically on the order of $\sim 10-100$ kHz, limiting the spectroscopic resolution. The linewidth of a laser is related to its frequency-noise characteristics and can be reduced by stabilizing the laser to an external frequency reference [149]. In practice, this is achieved by frequency locking a laser to an optical resonator using the Pound-Drever-Hall technique [143]. Reaching laser linewidths of one Hertz or below requires a high degree of frequency noise suppression and is technically demanding. However, state-of-the-art lasers stabilized to cryogenically-cooled single-crystal silicon resonators reach a sub-10 mHz linewidth [150, 151].
The clock laser system initially has been designed and set up by A. Thobe [82] as well as T. Rützel[87] and J. Carstens [88]. Later on, the high-finesse resonator has been exchanged to improve the stability of the cavity system, and large parts of the locking setup have been rebuilt to reduce residual amplitude modulation (RAM) by T. Ponath [85]. The short-time linewidth has been characterized to 1 Hz within two seconds [85].
Over the course of this thesis, the setup has been adapted to enable addressing the clock transition of both fermionic isotopes ${}^{171}$Yb and ${}^{173}$Yb. Also, the former analog fiber noise cancellation has been exchanged by an all-digital solution developed in the research group [152]. In the following, I will present the clock laser system in its current form.
Figure 1.15 schematically shows the complete clock laser system. It can be divided into three functional subsystems used for frequency stabilization, fiber noise cancellation and control of the spectroscopy beam.

### Frequency Stabilization

The clock laser is stabilized to a high-finesse optical resonator using the PDH technique introduced earlier. The plano-concave resonator[22] has a length of $L \approx 7.5$ cm, yielding a free spectral range of $\Delta_{\mathrm{FSR}} = 1.934(3)$ GHz [85]. The football-shaped cavity spacer and the mirror substrates are both made of ULE glass that features a CTE zero crossing close to room temperature. The resonator has been characterized by T. Ponath, finding a finesse of $\mathcal{F} = 216.9(4) \times 10^3$ corresponding to a resonance linewidth of $\Gamma_{\mathrm{res}} = 8.92(1)$ kHz [85]. The CTE zero crossing has been found at a temperature of $T_{\mathrm{CTE\text{-}zc}} = 32.3(1)\,^{\circ}$C [85]. The cavity is vertically mounted and isolated from thermal radiation by two gold-coated copper heat shields. The resonator and heat shields are placed in a vacuum chamber operated at a pressure of $p \sim 10^{-8}$ mBar. The outer heat shield is stabilized to the temperature of the CTE zero crossing using a thermo-electric cooler (TEC) and a home-built TEC-driver[23]. The vacuum setup and the heat shields are described in [82, 87, 88]. To isolate the cavity from low-frequency noise, the vacuum housing is placed on a breadboard on a vibration-isolation table[24] that is surrounded by a wooden box revetted with acoustic isolation foam.

[22] Advanced Thin Films ATF-6030
[23] based on: Wavelength Electronics WTC3243
[24] MinusK 150BM-1

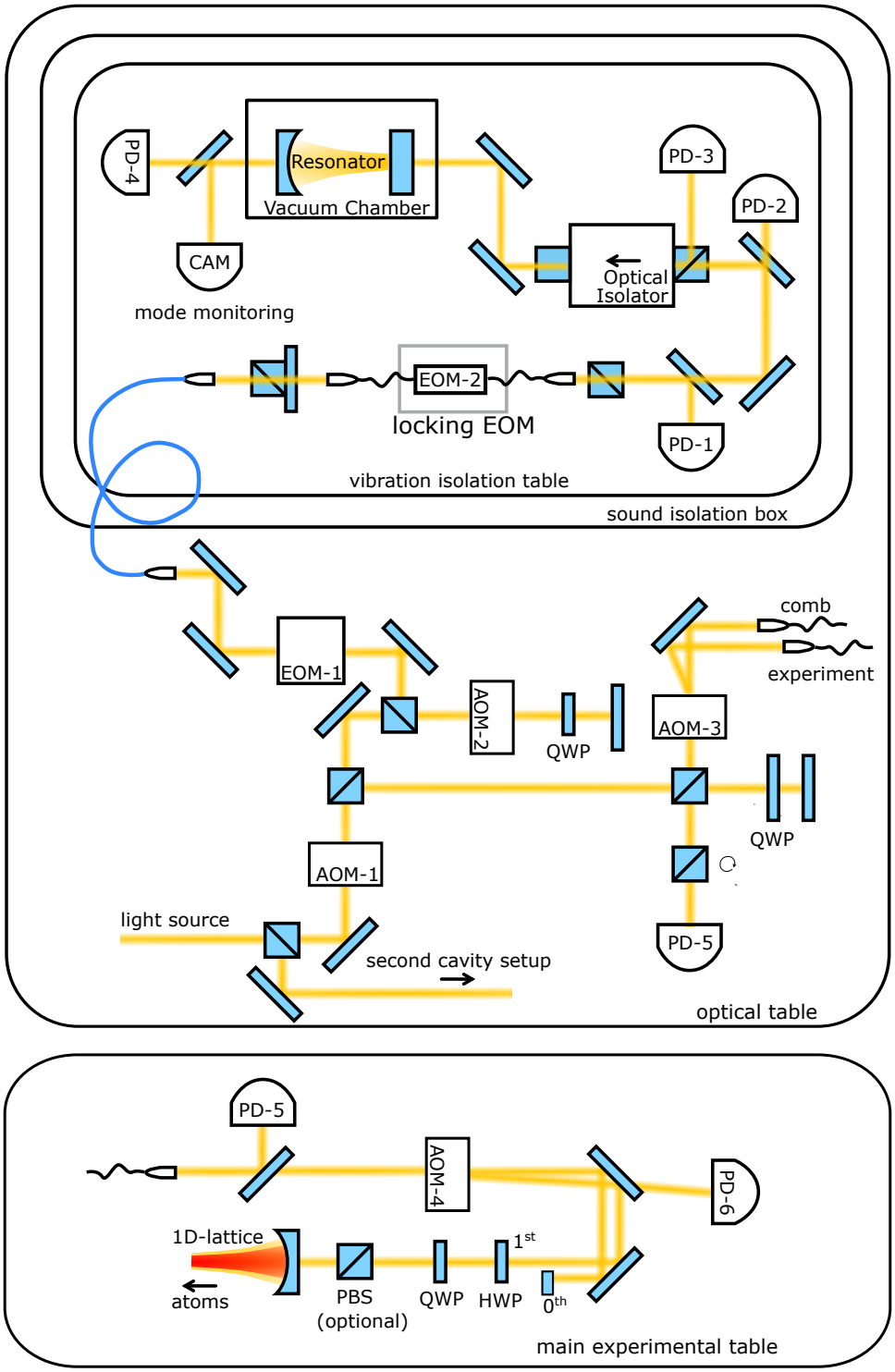


**Figure 1.15.:** Illustration of the optical setup of the clock laser system. Beam shaping optics, and some mirrors and waveplates have been omitted for clarity. See main text for a detailed description.

Figure 1.15 schematically shows the clock laser system. A frequency-doubled diode laser[25] provides up to 300 mW of light at $\lambda_{\text{clock}} = 578\,\text{nm}$. The output power is divided

[25] Toptica DL-TA-SHG pro

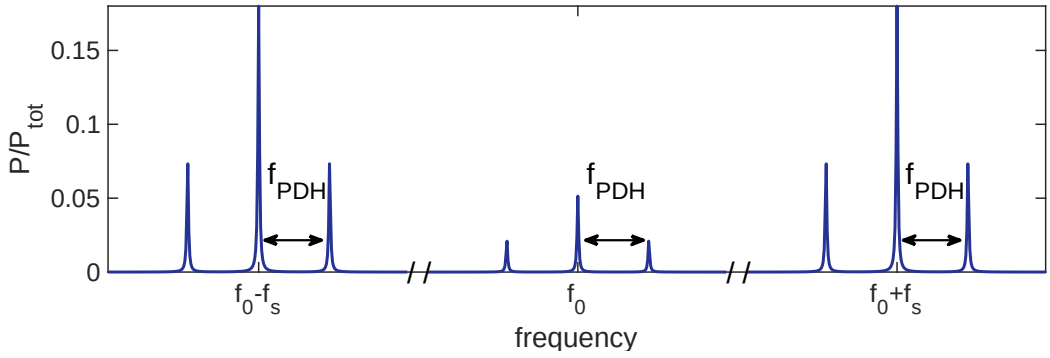


**Figure 1.16.:** Double-sideband modulation of the clock beam, modulation at a frequency of $f_s$ at a modulation depth of $\beta_s = 1.84$ and $f_{PDH}$ at modulation depth $\beta_{PDH} = 1.08$.

into two branches for cavity-1 and cavity-2, respectively. Here only the cavity-1 branch is discussed. The beam passes through AOM-1, AOM-2 and EOM-1 and is subsequently coupled into an optical fiber that is fed through the wooden box and guides light onto the vibration-isolation platform. A fiber coupled EOM[26] (EOM-2) is used to create sidebands at $f_{mod} = 17.8\,\mathrm{MHz}$ at a modulation depth of $\beta = 1.08$. To reduce residual amplitude modulation (RAM) the EOM is temperature stabilized [85]. The power on the vibration isolation table is measured using photodiode PD-1[27] and regulated using AOM-2 (alternatively, the power transmitted through the cavity can be regulated using PD-4, see ref. [85]). The light that is back-reflected from the incoupling mirror is directed onto an avalanche photodiode [28] using an optical isolator. The measured signal is demodulated at the modulation frequency $f_{\mathrm{mod}}$ using an RF-mixer [29]. The resulting error signal is fed into a fast control circuitry [30], to impose negative feedback to the clock laser frequency. Fast feedback is induced by modulating the frequency of AOM-1, while slow feedback is induced using the piezo voltage of the ECDL.
The clock transition of $^{171}$Yb is shifted by $\Delta_{171} = -1.26\,\mathrm{GHz}$ with respect to the clock transition of $^{173}$Yb [140]. Since the cavity provides an absolute frequency reference, to address the clock transition of $^{171}$Yb the isotope shift has to be accounted for by shifting the laser frequency. To do so we employ a dual sideband modulation scheme[153], schematically depicted in fig. 1.16. As the isotope shift is larger than half the free spectral range $\Delta_{171} > 0.5\Delta_{\mathrm{FSR}}$ it is useful to lock the laser to a higher-lying resonance to reduce the necessary frequency shift to $f_s = \Delta_{171} - \Delta_{\mathrm{FSR}}$. EOM-1 is used to create sidebands at $\pm f_s = 674\,\mathrm{MHz}$. By locking the upper sideband to the cavity resonance the laser frequency is shifted close to the $^{171}$Yb clock transition. A residual detuning can be accounted for by changing the frequency of AOM-3. While for an optimal PDH-signal the modulation depth of EOM-2 should be $\beta_{\mathrm{PDH}} = 1.08$, to obtain maximum power in the first sidebands the modulation depth of EOM-1 should be $\beta_s = 1.84$. Applying the dual-sideband modulation only 18% of the overall power ends up in the resonant sideband. To achieve the same locking performance and the same intra-cavity power as for

[26] Jenoptik PM594 with PM APC fibres
[27] Thorlabs PDA-36
[28] Femto HCA-S with Si APD Detector, customized model
[29] Mini-Circuits ZAD-3+
[30] Toptica Photonics FALC110

the single-sideband modulation scheme the overall laser power has to be increased by a factor of approximately three. EOM-1 is a resonant free space EOM[31] with tunable resonance frequency. To achieve a modulation index of $\beta_s \sim 1.8$ at a modulation frequency of $f_s = 674\,\mathrm{MHz}$ the EOM is driven by an RF signal with a power of $P_{\mathrm{drive}} = 35\,\mathrm{dBm}$. Thermal lensing, caused by the EOM crystal changes the beam parameters and thus affects the efficiency of the subsequent fiber coupling. To avoid misalignment when switching between the clock laser frequency of $^{171}$Yb and $^{173}$Yb, we therefore continously drive the EOM and only change the overall beam power when switching between isotopes. Note that the non-temperature controlled EOM-1 is subject to RAM. Therefore, to reduce RAM-related noise, it would be desirable to apply the double-sideband modulation using solely EOM-2. Serrodyne frequency shifting [154–156] could be an intriguing alternative to the double sideband modulation scheme and might reduce noise caused by undesirable light on the avalanche photodiode. However, the generation of a high quality saw-tooth signal necessary for serrodyne scheme at the modulation frequency $f_s$ might be challenging.

### Spectroscopy Branch

Behind AOM-1 a large part of the laser light is picked up and passes through AOM-3. The $0^{\mathrm{th}}$ diffraction order of AOM-3 is coupled into a fiber that guides to a frequency comb setup that allows measuring the clock laser's frequency. The $1^{\mathrm{st}}$ diffraction order is coupled into a fiber that guides to the main experiment. The clock laser power on the main experimental table is stabilized using AOM-3 and PD-6, while the spectroscopy beam is switched on and off by switching the RF drive of AOM-4 using a high isolation RF-switch [32] with fast switching characteristics. The switching AOM is operated with low RF-power resulting in a small diffraction efficiency. This way, pointing instabilities can be reduced, and on the other hand, the power of the beat note used for fiber-noise cancellation is only weakly reduced when the spectroscopy beam is switched on. By using different AOMs for switching and intensity regulation we avoid a deformation of the rectangular shaped clock pulse used for clock due to the transient behaviour of the intensity regulation. The frequency of the spectroscopy beam is set by changing the driving frequency of AOM-2 via the experimental control software. Thus frequency, intensity and length of the spectroscopy pulses are controlled by three individual AOMs.
The first diffraction order of AOM-4 passes through a half-wave and a quarter-wave plate as well as an optional polarizing beamsplitter used to set the desired polarization of the spectroscopy beam. The clock laser beam is superimposed with the 1D-lattice using the same concave mirror that is used to retro reflect the 1D-lattice beam. At the position of the atoms the spectroscopy beam has a waist of $w_{0,\mathrm{clock}} = 100\,\mu\mathrm{m}$. The $0^{\mathrm{th}}$ diffraction order of AOM-4 is back-reflected into the fiber and used for fiber noise cancellation using AOM-3. PD-6 directly monitors the power in the spectroscopy beam measuring the residual transmission of the 1st diffraction order of AOM-4 behind a steering mirror. All acousto optic modulators except for the locking AOM-1 are operated using digital RF sources sharing a common clock signal that is locked to a GPS referenced oven-controlled crystal oscillator. This way, differential drifts of the AOM frequencies are avoided. How-

[31] Qubig EO-T990K3-VIS

[32] Mini-Circuits ZASWA-2-50DR

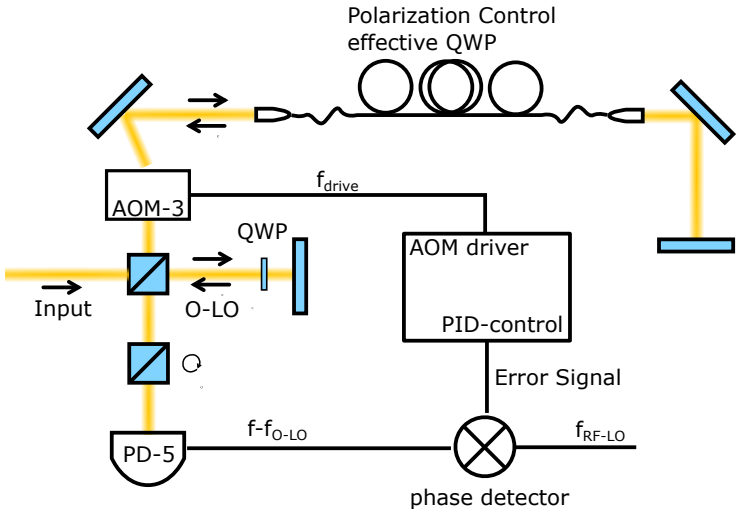


**Figure 1.17.:** Optical setup for fiber noise detection and cancellation in the clock-spectroscopy branch. See main text for a detailed description.

ever, the absolute frequency of the clock laser is determined by the cavity's resonance frequency, which is subject to fluctuations. To compensate for a slow linear drift caused by a slow shrinking of the cavity spacer, the driving frequency of AOM-2 is chirped by about 10 kHz/day (see sec. 3.5 for an analysis of the clock laser frequency drifts).

### Fiber Induced Noise Cancellation

A non-polarization maintaining single-mode optical fiber is used to conveniently guide light from the clock laser system to the main experiment. However, the fiber is sensitive to vibrations and induces low-frequency phase noise deteriorating the coherence properties of the clock laser light [157]. To reduce the effect of fiber-induced phase noise, we use homodyne detection to measure fiber related noise and employ active feedback to suppress it by up to 40 dB.

The setup for the fiber-induced noise cancellation is shown in fig. 1.17. The input beam is split into two branches. One acting as a probe beam and the other as a local oscillator (LO). The probe beam passes AOM-3 in single-pass configuration and is coupled into an optical fiber. Stress is induced to the fiber, so that it acts as an effective quarter-wave plate, turning the polarization of the light. The light is coupled out of the fiber, back-reflected and again passes the fiber, now possessing a polarization turned by 90 degrees compared to the input beam. The frequency of the light is again shifted by the AOM and superimposed with the local oscillator on the beam splitter. To achieve a common polarization between probe and LO beam, a polarizing beam splitter rotated by 45 degrees is used. Finally PD-5 measures a beat between the probe and the LO beam at twice the driving frequency of the AOM. The phase difference between the beat signal and an RF-signal at twice the driving frequency of AOM-3, is measured using a phase detector[33]. The resulting error signal is fed to a digital PID controler, applying negative feedback

[33]Mini-Circuits ZRPD-1

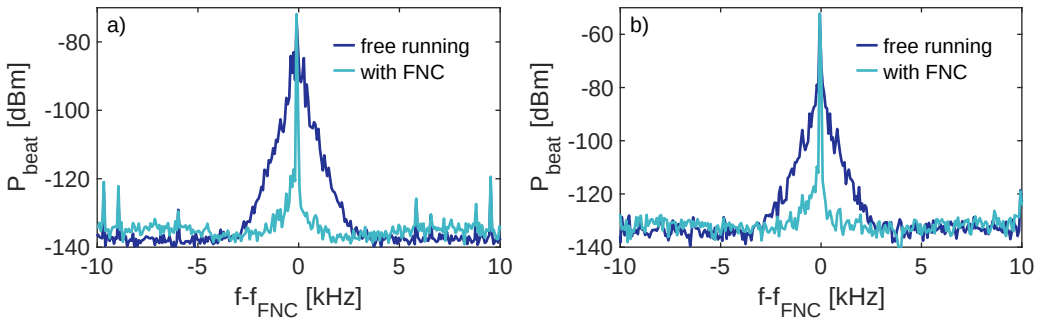


**Figure 1.18.:** Spectra of the homodyne photodiode (PD-5) signal, with and without active fiber noise cancellation. In panel a) the clock laser is locked to the resonance of $^{171}$Yb, while in panel b) it is locked to the resonance of $^{173}$Yb.

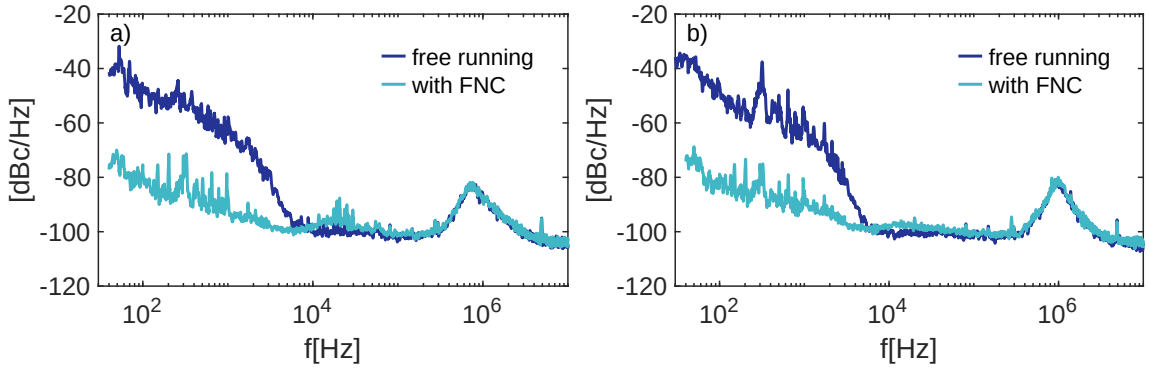


**Figure 1.19.:** Phase noise measurement of the homodyne signal. The phase noise of the free-running system is depicted in dark blue, while the phase noise of the actively stabilized system is depicted in light blue. Panel a) shows the data obtained for the clock laser system locked to the resonance of $^{171}$Yb. Panel b) shows the data obtained for the clock laser locked to the resonance of $^{173}$Yb. The active fiber-noise cancellation reduces phase noise by up to more than 40 dB for frequencies $\lesssim$ 5 kHz. Servo bumps at $\sim$ 10 kHz and $\sim$ 800 kHz in panel a) and at $\sim$ 10 kHz and $\sim$ 1 MHz in panel b) indicate the regulation bandwidth of the active fiber noise cancellation and the PDH frequency stabilization of the clock laser, respectively.

to the phase of the AOM driving signal. Figure 1.18 shows homodyne spectra with and without active fiber noise cancellation, whereas fig. 1.19 shows the corresponding phase noise. The active FNC suppresses phase noise by up to 40 dB for frequencies $\lesssim$ 5 kHz. Servo bumps at frequencies of $\sim$ 10 kHz and $\sim$ 1 MHz indicate the regulation bandwidth of the active fiber noise cancellation and the PDH frequency stabilization, respectively.

## 1.8. Summary

In this chapter, I gave an overview of the experimental apparatus in its current form and described methods used for the measurements presented in the following chapters. The apparatus allows to prepare quantum degenerate gases and mixtures of $^{171}$Yb, $^{173}$Yb, whereas creating Bose-Einstein condensates of $^{174}$Yb requires only a few quick changes. A

3D-lattice at the magic wavelength of $\lambda_{\text{mag}} = 759$, and a clock laser 578 nm, characterized by a laser linewidth on the 1 Hz level (within two seconds), allows for high-resolution spectroscopy on the clock transition ${}^1S_0 \rightarrow {}^3P_0$. A state-dependent lattice at $\lambda_{\text{SDL}} = 660\,\text{n}m$ allows to study orbital mixtures with different mobility properties for ground- and excited-state atoms. By increasing the 2D-MOT power and stabilizing the blue master laser to an optical resonator, the stability and reliability of the apparatus could be significantly improved, which allowed to vastly increase the data acquisition time. Further technical improvements such as replacing cavity-2 by another resonator with a CTE zero-crossing close to room temperature or replacing the analog RF sources used for the 3D-MOT broadening might yield a further increase of the experiment's stability and therefore be reasonable.

# 2. Ytterbium Quantum Gases and Fermi-Fermi Mixtures

We routinely create quantum degenerate gases of $^{171}$Yb, $^{173}$Yb, $^{174}$Yb as well as Fermi-Fermi mixtures of $^{171}$Yb and $^{173}$Yb. The creation of single isotope gases of $^{173}$Yb and $^{174}$Yb with the experimental apparatus is described extensively in the theses of the doctoral theses of S. Dörscher, A. Thobe, B. Hundt and A. Kochanke [81–84].
Due to its particular scattering properties, namely a vanishingly small $s$-wave interaction [118], $^{171}$Yb is subject of various proposals for quantum simulation of the Kondo lattice model [64–66]. The small $s-$wave scattering length, however, prevents direct evaporative cooling of single isotope gases of $^{171}$Yb. To reach quantum degeneracy, therefore, it requires sympathetic cooling with another species[114, 115]. Based on preparatory work of A. Kochanke and the author, over the course of this thesis, the apparatus has been modified to enable simultaneous magneto-optical trapping of two different ytterbium isotopes and subsequent evaporation, allowing to create quantum degenerate gases of $^{171}$Yb and Fermi-Fermi Mixtures of $^{171}$Yb and $^{173}$Yb.
In the following I will present characterization measurements for Fermi-Fermi mixtures of $^{171}$Yb and $^{173}$Yb.

Fermi gases and Fermi-Fermi mixtures with $^{171}$Yb have been characterized by K. Sponselee, M. Diem and the author. The here presented measurements have been conducted by K. Sponselee and the author. Data analysis has been performed by the author.

## 2.1. Fermi-Fermi Mixtures of $^{171}$Yb and $^{173}$Yb

For cold gases, quantum degeneracy typically is achieved by first employing laser cooling in a MOT, eventually followed by a sub-Doppler laser cooling stage and subsequent evaporative cooling. Although Bose-Einstein condensation using laser cooling only has been demonstrated [158], evaporative cooling remains the most commonly used technique.
Evaporative cooling relies on removing the hottest atoms of a gas that subsequently thermalizes via collisions at a lower temperature and can be achieved by continuously decreasing the depth of the trap [159]. In the low temperature regime interactions are limited to $s$-wave collisions characterized by the s-wave scattering length. For the bosonic isotope $^{174}$Yb the scattering lengths of $a = 104(15)\,a_0$ allows to efficiently employ evaporative cooling to reach quantum degeneracy. For identical fermions $s$-wave collisions are prohibited, thus limiting evaporative cooling for fermionic gases to mixtures of atoms in different e.g. $m_F$ states [5]. The $s$-wave scattering length $a = 199(2)\,a_0$ allows for an effective evaporative cooling of spin mixtures of $^{173}$Yb while the almost vanishing scattering length of $a = -3(4)\,a_0$ for $^{171}$Yb prevents evaporative cooling. This limitation can

be overcome by so-called sympathetic cooling, employing a buffer gas of another species that interacts with the $^{171}$Yb atoms via collisions to cool the sample. Sympathetic cooling has been demonstrated for various different systems [160, 161] and sympathetic cooling of $^{171}$Yb with a different ytterbium isotope has been demonstrated either using $^{174}$Yb [113, 114] or $^{173}$Yb as coolant [115], reaching quantum degeneracy in the latter case.
To create quantum degenerate gases of $^{171}$Yb we subsequently load $^{171}$Yb and $^{173}$Yb into the bi-chromatic MOT operated on the $^1S_0 \rightarrow {}^3P_1$ line. After MOT compression both species are loaded into the dipole trap. In a first evaporation stage the power of the green dipole trap DT1 is exponentially ramped down. Afterwards we apply resonant optical pumping first for $^{171}$Yb, then for $^{173}$Yb, to prepare a certain spin configuration. After spin preparation the atoms are cooled to quantum degeneracy in a second evaporation stage, exponentially reducing the power of the IR traps. By varying the MOT loading times for the different isotopes, while keeping the overall MOT loading time constant we can tune the isotope ratio $N_{171}/(N_{171}+N_{173})$ from a pure gas of $^{173}$Yb to an almost pure gas of $^{171}$Yb, as shown in fig. 2.1. Unwanted residual $^{173}$Yb atoms might be removed after evaporation by a resonant blast pulse of imaging light. Note that in the measurement we used loading times for $^{173}$Yb of $t_{\mathrm{load},^{173}\mathrm{Yb}} \geq 3\,\mathrm{s}$. For smaller loading times the number of $^{171}$Yb atoms goes down as expected for a non interacting Fermi-gas. To systematically characterize the different Fermi-Fermi mixtures, we determine the particle numbers and temperatures for both isotopes. In order to obtain the temperature of the gases a 2D-Fermi profile $n_{\mathrm{2D}}(x,y)$ is fitted to the optical density distribution obtained from absorption images, given by[162]:

$$n_{\mathrm{2D}}(x,y) = n_{\mathrm{2D},0}\frac{\mathrm{Li}_2\left(\pm\varphi\exp\left[-\left(\frac{x^2}{R_x^2}+\frac{y^2}{R_y^2}\right)\frac{\mathrm{Li}_1(-\varphi)}{\mathrm{Li}_0(-\varphi)}\right]\right)}{\mathrm{Li}_2(\pm\varphi)}, \tag{2.1}$$

to obtain the fugacity $\varphi$. Here $\mathrm{Li}_n$ denotes the polylogarithm of $n^{\mathrm{th}}$ order, $n_{\mathrm{2D},0}$ denotes the amplitude $R_x$ and $R_y$ denote the radii in $x$- and $y$-directions. The degeneracy parameter given by the quotient of the temperature $T$ and the Fermi temperature $T_{\mathrm{F}}$ can be determined using the fugacity via [162]:

$$\frac{T}{T_{\mathrm{F}}} = \left[-6\mathrm{Li}_3\left(-\varphi\right)\right]^{-1/3}, \tag{2.2}$$

and is shown in panel 2.1 b). Given the trapping frequencies $\omega_i$ of the trapping potential the temperature of the cloud can be determined using [162]:

$$T = \frac{m\omega_i^2}{2k_B\varphi}\frac{R_i^2}{1+\omega_i^2 t_{\mathrm{TOF}}^2}. \tag{2.3}$$

Panel 2.1 c) shows the average of the temperature obtained for the different axes using eq. 2.3. While we observe different degeneracy parameters for both isotopes, note that the absolute temperatures of both gases for a certain dipole trap depth are very similar, indicating that the gases are in thermal equilibrium. Figure 2.1 d)-e) shows the same measurement but for a mixture of a two spin component gas of $^{171}$Yb and a spin polarized gas of $^{173}$Yb. Comparing figures 2.1 a)-c) and 2.1 d)-e) we find a similar behavior of the atom numbers and temperatures. We reach final atom numbers for $^{171}$Yb comparable to the

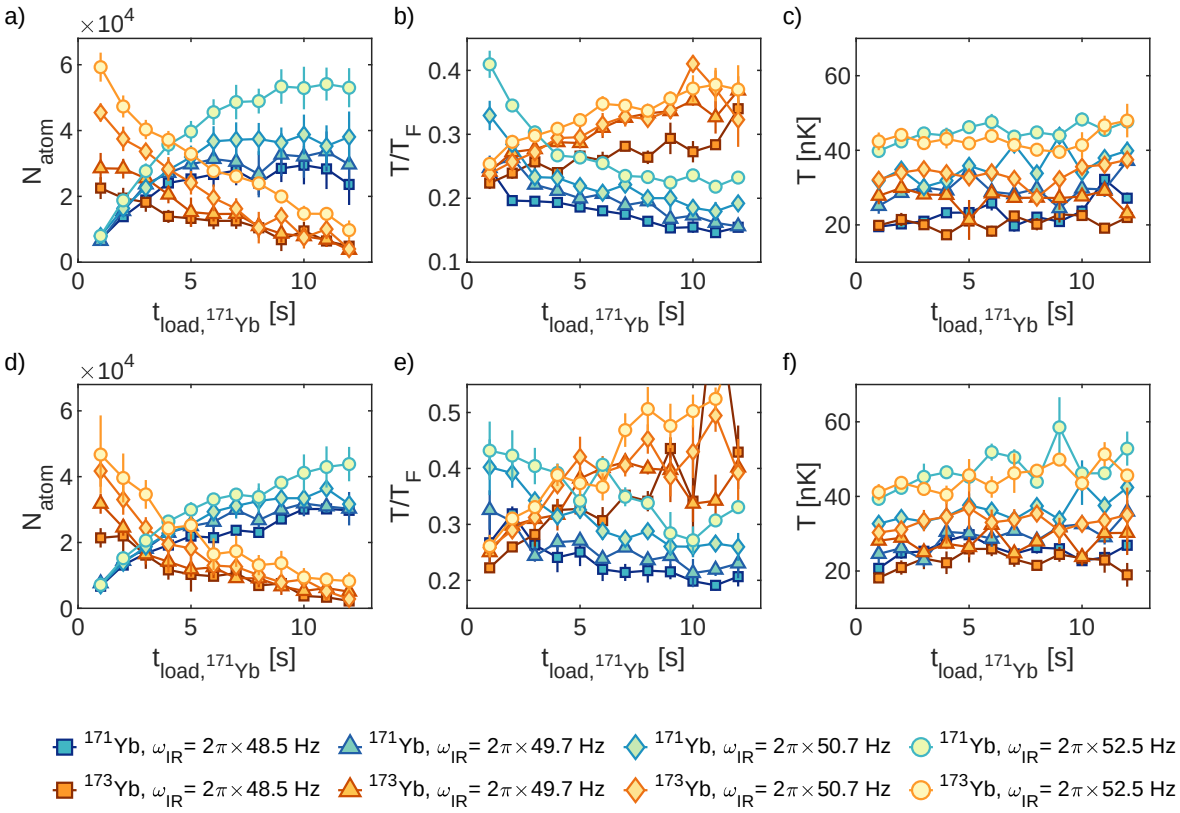


**Figure 2.1.:** Atom numbers a) [d)] and degeneracy parameter $T/T_\mathrm{F}$ b) [e)] and temperatures c) [f)] for doubly spin polarized mixtures of $^{171}$Yb in the $m_F = -1/2$ and $^{173}$Yb in the $m_F = 5/2$ state [for a two spin component mixture of $^{171}$Yb and a spin polarized gas of $^{173}$Yb in the $m_F = 5/2$ state] as a function of the $^{171}$Yb MOT loading time $t_{\mathrm{load},^{171}\mathrm{Yb}}$. To keep the total MOT loading time constant, we adjust $t_{\mathrm{load},^{173}\mathrm{Yb}}$ according to $t_{\mathrm{load},^{173}\mathrm{Yb}} = 15\,\mathrm{s} - t_{\mathrm{load},^{171}\mathrm{Yb}}$. Colors from bright to dark denote a decreasing final power of IR1 corresponding to smaller trapping frequencies that can be characterized by the goeometric mean $\omega_\mathrm{IR} = \sqrt[3]{\omega_x\omega_y\omega_z}$. Data points show the weighted average of up to three measurements, with error bars indicating the standard deviation of the mean.

doubly spin polarized mixtures, while the final number of $^{173}$Yb atoms ceases at smaller $^{171}$Yb loading times. The degeneracy parameter for $^{171}$Yb is significantly increased compared to the doubly spin-polarized gasdegeneracy parameter for the two spin component gas of $^{171}$Yb. For a two spin component gas one actually expects an increased degeneracy parameter as for the same number of particles the fermi energy decreases.
The data shown in fig. 2.1 has been obtained using single isotope absorption imaging. Yet, the imaging system, (see sec. 1.7.2) allows to quickly switch between imaging light that is resonant for $^{171}$Yb and $^{173}$Yb. Therefore, in analogy to the double imaging technique used to access the orbital state population during spectroscopy (see sec. 1.4) it allows imaging one isotope on the absorption image and the other isotope on the reference image. However, due to the different frequencies of the imaging light in the two shots, the images show increased fringes. Combining double isotope imaging and the optical Stern

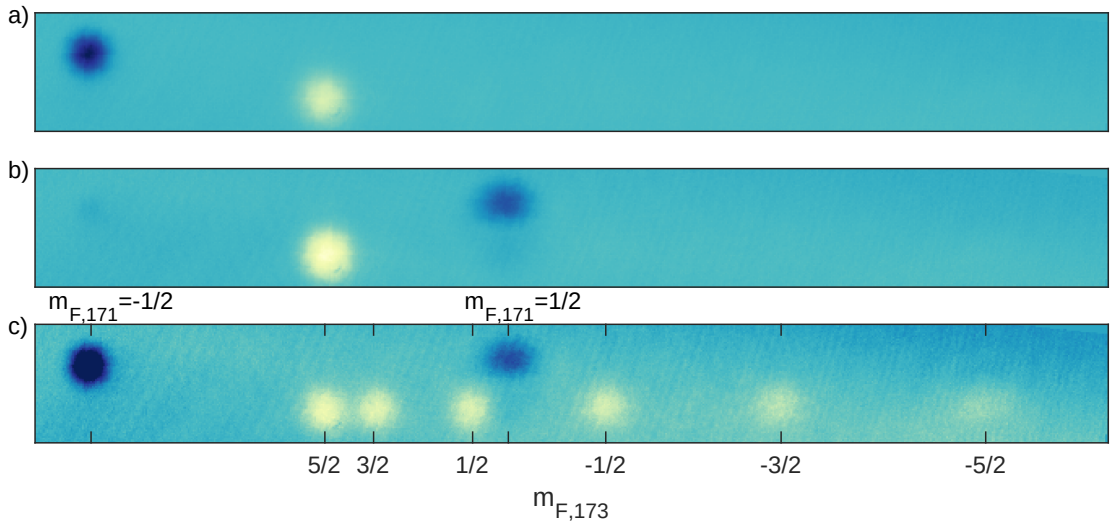


**Figure 2.2.:** OSG absorption images for ytterbium Fermi-Fermi mixtures in different spin configurations. Panel a) ( b) )shows a mixture of $^{171}$Yb and $^{173}$Yb prepared in $m_F = -1/2$ ($m_F = +1/2$) and $m_F = 5/2$ respectively. Panel c) shows a mixture containing all two and six $m_F$ states of $^{171}$Yb and $^{173}$Yb,respectively. Colors from bright to dark denote an increasing optical density, computed according to [122]. $^{171}$Yb is imaged on the first image and $^{173}$Yb on the second image of the imaging sequence. Therefore clouds of $^{171}$Yb appear in dark color while clouds of $^{173}$Yb appear in bright color, as due to the image processing the sign of the OD is reversed. To increase the visibility of the different $m_F$ components of $^{173}$Yb the maximum of the colorscale has been cut in panel c). The shown images are the average of ten individual absorption images.

Gerlach technique allows to directly resolve the spin population for both isotopes in a single shot, as shown in fig. 2.2 for two different doubly spin-polarized mixtures and a mixture containing atoms in all $m_F$-states for both isotopes.

To characterize the performance of the double isotope imaging to the standard single isotope imaging during the measurement presented in fig. 2.1 for each loading time and IR trap value we took three individual images: two standard single isotope absorption images and one image using the double isotope imaging technique. Figure 2.3 shows a comparison of particle numbers and temperatures obtained in single and double isotope imaging for subsequently taken pictures. Each data point represents a single measurement. The atom numbers determined from absorption images using the double imaging technique are very similar. The temperatures determined for $^{171}$Yb are comparable, while the temperatures determined for $^{173}$Yb deviate and systematically appear higher in double imaging. $^{171}$Yb is imaged on the first and $^{173}$Yb on the second image, therefore we attribute the higher temperatures to heating caused by the first imaging pulse. The isotope shift is only on the order of $10\,\Gamma_{^1P_0}$ therefore the $^{171}$Yb imaging light is off resonant for $^{171}$Yb but it is not far detuned either. The temperature predominantly affects the wings of the momentum distribution, hence the region where the signal to noise ratio is smallest. In addition the double isotope imaging technique decreases the signal-to-noise ratio, as the background corrections gets more difficult. Hence, to obtain reliable temperature single isotope imaging should be used. In summary the characterization measurements show

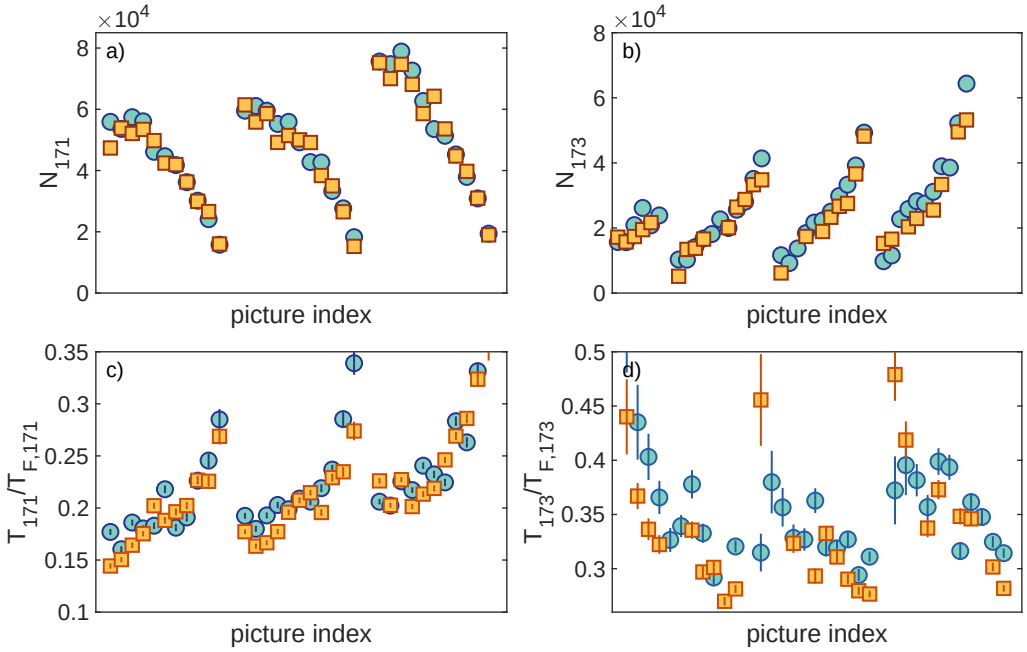


**Figure 2.3.:** Characterization of the double isotope imaging. Shown is part of the data of the measurement shown in fig. 2.1. Blue circles denote data obtained by double imaging, red squares denote data obtained by single isotope imaging for otherwise the same experimental settings. Panels a) and d) show atom numbers panel for $^{171}$Yb and $^{171}$Yb, respectively. Panel c) and d) show the degeneracy parameters $T/T_F$ obtained by fitting a 2D Fermi profile [162] to the optical density distribution of the $^{171}$Yb and $^{173}$Yb atoms, respectively. Each data point corresponds to a single image error bars denote the uncertainties in determining the degeneracy parameter from the fitted 2D-Fermi profile.

that it is possible to determine meaningful particle numbers obtained for both isotopes and temperatures for the gas imaged first using the double imaging technique. Temperatures obtained for the gas imaged second tend to be unreliable due to heating that occurs during the imaging process. Note however, that under the assumption that both gases are in thermal equilibrium it is sufficient to determine only the temperature for one isotope.

## 2.2. Conclusion and Outlook

In this chapter I presented characterization measurements for Fermi-Fermi mixtures of $^{171}$Yb-$^{173}$Yb respectively quantum gases of $^{171}$Yb. With our experimental apparatus we are able to create either pure gases of $^{171}$Yb or mixtures of both fermionic isotopes at various mixing ratios with $N_{171,173} \approx$ (10-40) $\times 10^3$ atoms and typical temperatures of $T \approx (0.15\text{-}0.35)\, T_\mathrm{F}$. By removing residual $^{173}$Yb atoms using resonant imaging light clean spin polarized and balanced gases of only $^{171}$Yb can be prepared and particle numbers are typically $N_{171} \approx (20-40) \times 10^3$ atoms and temperatures about $T \approx (0.15-0.3)\, T_\mathrm{F}$. Compared to gases of pure $^{173}$Yb with typically $N_{173} \approx 80 \times 10^3$ and similar temperatures, the mixtures and gases of $^{171}$Yb are smaller. For most experiments however, it is desirable only to load the lowest band of the optical lattice and in the past an atom number of

$N \sim 2 \times 10^4$ atoms has been a good working point to achieve an efficient loading of the lowest band [84]. Although there might be room for improvement by optimizing e.g. the evaporation ramps the achieved performance in terms of particle numbers is sufficient for most experiments. A comparison between single isotope and double isotope absorption imaging shows that particle numbers and temperatures obtained by the different imaging techniques are comparable, yet the single isotope imaging produces more reliable results. On the other hand double isotope imaging yields good enough results to get a valid impression of the prepared Fermi-Fermi mixture and reduces the number of images needed to characterize the system by a number of two, which is especially relevant for long measurement series, and allows to increase data acquisition. In the future the imaging could be improved by increasing the total number of images taken in the detection sequence to allow for individual reference images for both isotopes.

# 3. Probing the Clock Transition

The most outstanding feature of alkaline earth (like) elements, such as strontium and ytterbium, in the context of cold gases is the existence of a triplet manifold $^3P_{0,1,2}$ that is accessible from the singlet ground state $^1S_0$ via an optical transition. In the case of pure LS coupling these intercombination transitions are dipole or even doubly dipole forbidden as $\Delta S \neq 0$ and for $^1S_0 \rightarrow {}^3P_{0,2}$ $\Delta j \neq \pm 1$. For heavy elements LS coupling is not perfectly realized and a small admixture of the state $^1P_1$ to the triplet states enables the optical transition, resulting in narrow linewidths [51, 106]. Especially the transition $^1S_0 \rightarrow {}^3P_0$ is of interest. Due to the ultra-narrow linewidth, that for ytterbium has been calculated to be $\Gamma < 10\,\mathrm{mHz}$ [102], it is well suited to serve as a frequency standard. Apart from its use as an optical frequency standard high precision spectroscopy on the optical 'clock' transition $^1S_0 \rightarrow {}^3P_0$ can be used to resolve small energy shifts and therefore is a versatile analysis tool for quantum simulation. The long natural lifetime allows to employ the metastable state $^3P_0$ as an additional degree of freedom that could be used for quantum simulation of multi-band Hubbard models such as the Kondo lattice model [64, 65]. These applications require a precise experimental control over the optical excitation process. Therefore, a detailed understanding of the underlying physics is crucial.
In this chapter a theoretical model of the excitation process based on the paradigmatic two-level system is introduced. Later-on, the motional degree of freedom is included into the description, and the excitation of atoms trapped in a magic optical lattice potential is discussed. Finally, the effects of decoherence and spontaneous decay are discussed in terms of the density matrix formalism. Along the discussion of the excitation process I will present spectroscopic measurements employing (mainly) spin polarized gases of $^{171}$Yb and $^{173}$Yb in a magic optical lattice.
A description of the two-level system can be found in many textbooks as for example ref. [163] or ref. [164]. A compact introduction of the density matrix formalism can be found in ref. [165]. In ref. [166] the authors describe the theory of damped Rabi Oscillations in terms of a two-level system that is coupled to a thermal bath. For the description of the two-level system in sec. 3.1 and sec. 3.3 I follow the notation and argumentation of ref. [164].

Measurements presented in sec. 3.2.2 and sec. 3.5 have been conducted by M. Diem, K. Sponselee and the author, data analysis has been performed by the author. Measurements presented in sec. 3.3 and 3.2.1 have been conducted by K. Sponselee and the author. Data analysis has been performed by the author. Theory plots presented in this chapter have been made by the author.

## 3.1. Two-Level System

Consider a single two-level system with states $|g\rangle$ and $|e\rangle$ and corresponding eigenenergies $\mathcal{E}_g = 0$ and $\mathcal{E}_e = \hbar\omega_0$ representing the ground state ${}^1S_0$ and the metastable state ${}^3P_0$. The non-interacting Hamiltonian is given by:

$$\mathcal{H}_0 = \hbar\omega_0 \, |e\rangle\langle e| \tag{3.1}$$

In the presence of an electromagnetic field:

$$\boldsymbol{E} = \frac{1}{2}\boldsymbol{\varepsilon} E_0 \left(e^{i\omega t} + e^{-i\omega t}\right), \tag{3.2}$$

with amplitude $E_0$, frequency $\omega$ and polarization vector $\boldsymbol{\varepsilon}$, the states are coupled via the electric dipole interaction. The Hamiltonian of the system can be written as:

$$\mathcal{H} = \mathcal{H}_0 + \mathcal{H}_{\text{int}}, \tag{3.3}$$

where the interaction part of the Hamiltonian $\mathcal{H}_{\text{int}}$ is given by:

$$\mathcal{H}_{\text{int}} = \langle e|\mathbf{d}|g\rangle \, \mathbf{E} \, |e\rangle\langle g| + \langle g|\mathbf{d}|e\rangle \, \mathbf{E} \, |g\rangle\langle e| \,. \tag{3.4}$$

Here, $\mathbf{d}$ denotes the electric dipole operator. The matrix element $\langle g|\mathbf{d}|e\rangle$ can be expressed in terms of the Rabi frequency:

$$\Omega := -\frac{\langle g|\mathbf{d}|e\rangle \, E_0}{\hbar}. \tag{3.5}$$

Using the definition of the Rabi frequency eq. 3.5 and applying the rotating wave approximation, the interaction Hamiltonian reads:

$$\mathcal{H}_{\text{int}} = \frac{\hbar\Omega}{2} \left(e^{i\omega t} \, |g\rangle\langle e| + e^{-i\omega t} \, |e\rangle\langle g|\right). \tag{3.6}$$

The time evolution of the system is governed by the Schrödinger equation $i\hbar\partial_t \, |\psi\rangle = \mathcal{H} \, |\psi\rangle$. For a state $|\psi\rangle = c_g(t) \, |g\rangle + c_e(t) \, |e\rangle$, one finds:

$$\partial_t c_g \, |g\rangle + \partial_t c_e \, |e\rangle = -i\omega_0 c_e \, |e\rangle + i\frac{\Omega}{2} e^{i\omega t} c_e \, |g\rangle - i\frac{\Omega}{2} e^{-i\omega t} c_g \, |e\rangle \tag{3.7}$$

Projecting out the states $|g\rangle$ and $|e\rangle$ and applying the rotating frame transformation $\tilde{c}_e = c_e e^{i\omega t}$, one finds the two coupled differential equations:

$$\partial_t c_g = \frac{-i\Omega}{2} \tilde{c}_e \tag{3.8}$$

$$\partial_t \tilde{c}_e = i\Delta \tilde{c}_e - i\frac{\Omega}{2} c_g \tag{3.9}$$

Here, the detuning $\Delta := \omega - \omega_0$ is introduced. For an atom initially in the ground state, characterized by $c_g(0) = 1$ and $\tilde{c}_e(0) = 0$, the solution of the differential equations

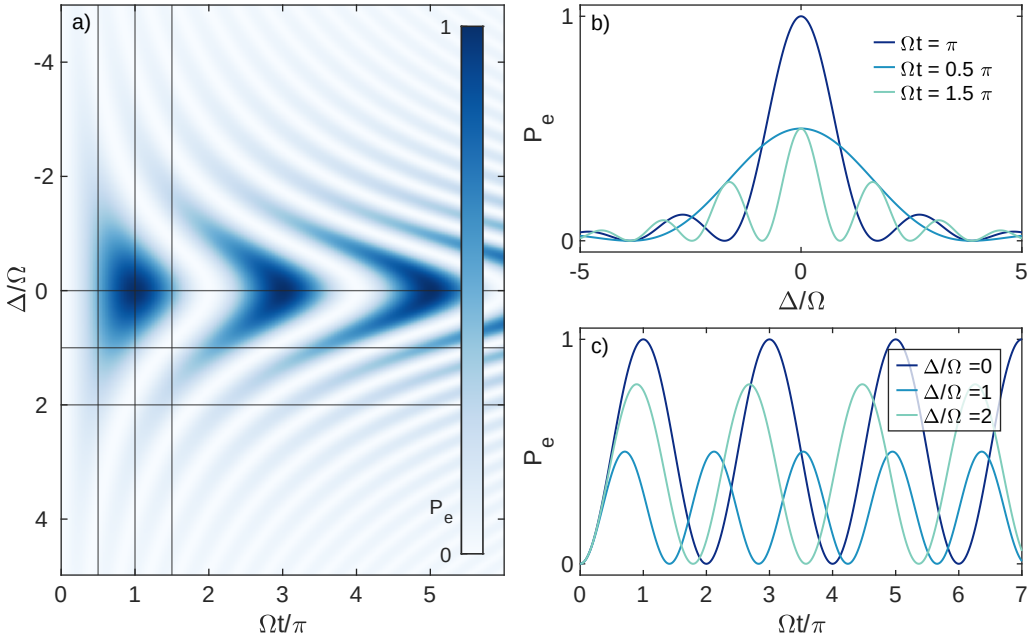


**Figure 3.1.:** Rabi oscillations in a two level system. Panel a) shows the excitation probability $P_e$ as a function of the detuning and interrogation time. Light to dark colors indicate an increasing excitation probability. Vertical (horizontal) lines indicate the position of the cuts shown in panel b) ( panel c) ). Panel b) shows spectra for different interrogation times. Panel c) shows Rabi oscillations for different detunings.

eqs. 3.8-3.9 is given by:

$$c_g(t) = e^{i\Delta t/2}\left[\cos\left(\frac{\tilde{\Omega}t}{2}\right) - \frac{i\Delta}{\tilde{\Omega}}\sin\left(\frac{\tilde{\Omega}t}{2}\right)\right] \tag{3.10}$$

$$\tilde{c}_e(t) = -ie^{i\Delta t/2}\frac{\Omega}{\tilde{\Omega}}\sin\left(\frac{\tilde{\Omega}t}{2}\right) \tag{3.11}$$

where $\tilde{\Omega} = \sqrt{\Omega^2 + \Delta^2}$ denotes the effective Rabi frequency. The probability to find an atom in the excited state is given by $P_e = |c_e|^2$ with:

$$P_e(t) = \frac{\Omega^2}{\tilde{\Omega}^2}\sin^2\left(\frac{\tilde{\Omega}t}{2}\right). \tag{3.12}$$

Figure 3.1 a) shows eq. 3.12 as a function of the interrogation time $t$ and detuning $\Delta$. On resonance $\Delta = 0$ the excitation probability oscillates at the bare Rabi frequency $\Omega$ and one observes a complete population transfer from the ground state $|g\rangle$ to the excited state $|e\rangle$. The excitation probability reaches its maximum at $t = (2n-1)\pi/\tilde{\Omega}$ with $n \in \mathbb{N}$. In the following, pulses that meet the condition $t_\pi = \pi/\Omega$ are called $\pi$-pulses. For increasing detuning $\Delta$ the effective Rabi frequency $\tilde{\Omega}$ increases, while the amplitude of the Rabi oscillation decreases, as shown in fig. 3.1 c). Figure 3.1 b) shows spectra calculated for different interrogation times $t$. The spectroscopic lineshape significantly changes for

different interrogation times. For $t = \pi/\Omega$ the central peak reaches $P_e = 1$, while for increasing interrogation time the side lobes of the sinc$^2$ become more prominent.
From an experimentalist's point of view the figures of merit for spectroscopy typically are high contrast and high spectroscopic resolution. As pointed out before, the highest contrast is achieved using $\pi$-pulses ($t = \pi/\Omega$), while the spectroscopic linewidth $\Gamma_{\mathrm{FWHM}}$ (full width at half maximum) depends on the Rabi frequency and for $t = \pi/\Omega$ can be approximated by $\Gamma_{\mathrm{FWHM}} \approx 1.6\,\Omega/2\pi$. Hence, the resolution increases with decreasing Rabi frequency. Experimentally the Rabi frequency can be conveniently controlled by changing the power of the spectroscopy beam. For ytterbium at a given intensity $I$ the Rabi frequency can be estimated by $\Omega \approx 77\,\mathrm{Hz}\sqrt{I}$, with $[I] = \mathrm{mW\ cm^{-2}}$ [167].

## 3.2. Spectroscopy in a Magic Optical Lattice

So far, we have considered a two-level system without motional degrees of freedom. Real atoms in the lab framework, of course, move and have to obey energy and momentum conservation.
Consider a photon at wavelength $\lambda_{\mathrm{phot}}$ and an atom of mass $m$ at velocity $\boldsymbol{v}$. The atom's momentum can be expressed as $\boldsymbol{p}_{\mathrm{atom}} = \hbar\boldsymbol{k}_{\mathrm{atom}}$, where $k_{\mathrm{atom}} = 2\pi/\lambda_{\text{de Broglie}}$ is determined by the de Broglie wavelength of the atom $\lambda_{\text{de Broglie}} = h/mv$. The momentum of the photon is given by $\boldsymbol{p}_{\mathrm{phot}} = \hbar\boldsymbol{k}_{\mathrm{phot}}$, where $k_{\mathrm{phot}} = 2\pi/\lambda_{\mathrm{phot}}$ is determined by the wavelength of the photon. Momentum conservation for an optical excitation process can then be expressed as:

$$\boldsymbol{p}'_{\mathrm{atom}} = \boldsymbol{p}_{\mathrm{atom}} + \boldsymbol{p}_{\mathrm{phot}}. \tag{3.13}$$

Here $\boldsymbol{p}_{\mathrm{atom}}$ denotes the atom's momentum in the initial state, while $\boldsymbol{p}'_{\mathrm{atom}}$ denotes the atom's momentum in the excited state. Energy conservation requires that the energy of the excited atom $E'_{\mathrm{atom}}$ is the sum of the atom's energy prior to the excitation $E_{\mathrm{atom}}$ and the photon's energy $E_{\mathrm{phot}}$:

$$E'_{\mathrm{atom}} = E_{\mathrm{atom}} + E_{\mathrm{phot}}. \tag{3.14}$$

The energy of the atom is the sum of an internal part $E_{\mathrm{int,g/e}}$, describing the electronic state of the atom, and a kinetic part, that for a free particle is given by the dispersion relation:

$$E_{\mathrm{kin}} = \frac{\hbar^2 k^2}{2m}. \tag{3.15}$$

The energy of the photon is given by $E_{\mathrm{phot}} = \hbar\omega$. Using these definitions one can rewrite eq. 3.14:

$$\frac{\hbar^2}{2m}(\boldsymbol{k}_{\mathrm{atom}} + \boldsymbol{k}_{\mathrm{phot}})^2 + E_{\mathrm{int,e}} = \frac{\hbar^2}{2m}\boldsymbol{k}^{\boldsymbol{2}}_{\mathrm{atom}} + E_{\mathrm{int,g}} + \hbar\omega. \tag{3.16}$$

Solving eq. 3.16 for the photons's energy $\hbar\omega$ yields:

$$\hbar\omega = \hbar\boldsymbol{v}_{\mathrm{atom}}\boldsymbol{k}_{\mathrm{phot}} + \frac{\hbar^2\boldsymbol{k}^2_{\mathrm{phot}}}{2m} + \hbar\omega_0, \tag{3.17}$$

where we have used the definition of the atomic resonance frequency $\omega_0 = (E_{\mathrm{int,e}} - E_{\mathrm{int,g}})/\hbar$, and the de Broglie wavelength. Equation 3.17 explicitly shows that the transition frequency is shifted by the photon recoil energy $E_{\mathrm{rec}} = \hbar^2\boldsymbol{k}^2_{\mathrm{phot}}/2m$ (in our case

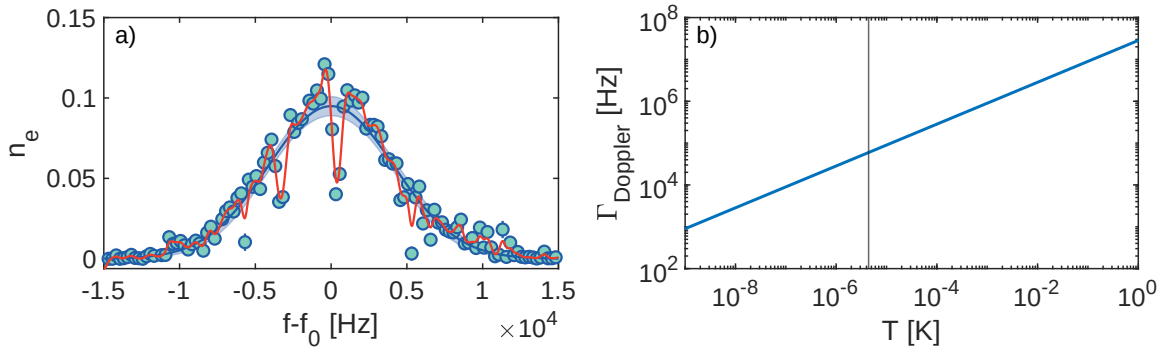


**Figure 3.2.:** Doppler broadening of the ${}^1S_0 \rightarrow {}^3P_0$ transition. a) Spectrum of the ${}^1S_0 \rightarrow {}^3P_0$ transition obtained for N $\sim 50 \times 10^3$ atoms in a shallow optical lattice at a lattice depth of $s_{1D} \approx 1\,E_{rec}$. The blue line denotes a Gaussian fit with the shaded area representing the 95% confidence interval. The red line shows a spline fit to the data to guide the eye, and emphasize the band gaps that begin to open at $f - f_0 \approx -3$ kHz and $f - f_0 \approx 1$ kHz. The overall lineshape is well described by a Gaussian, indicating that the transition is motionally broadened. A Gaussian fit yields a linewidth of $\Gamma_{\text{Doppler}} \approx 10$ kHz and corresponding a temperature of $T \approx 120$ nK. b) Doppler broadening $\Gamma_{\text{Doppler}}$ for a thermal gas as a function of the temperature $T$. The vertical line indicates the Doppler temperature of the ${}^1S_0 \rightarrow {}^3P_1$ MOT of $T_{\text{Doppler}} = 4.4\,\mu$K

$E_{\text{rec,clock}} \approx h \times 3.5$ kHz) and the Doppler shift $\hbar \boldsymbol{v}_{\text{atom}} \boldsymbol{k}_{\text{phot}}$.
Experimentally, we usually probe ensembles of several thousand atoms that obey a certain momentum distribution. In the thermal regime, the momentum distribution of a free gas is described by a Maxwell-Boltzmann distribution while in the quantum degenerate regime the momentum distribution is given by a Fermi-Dirac or Bose-Einstein distribution for Fermions or Bosons, respectively. As every velocity experiences a different Doppler shift the spectral linewidth of the transition is broadened. The so-called Doppler-broadened linewidth (full width at half maximum) $\Gamma_{\text{Doppler}}$ of a thermal gas is a function of the temperature $T$ and given by [168]:

$$\Gamma_{\text{Doppler}} = \frac{f_0}{c}\sqrt{\frac{k_B T}{m} 8\log(2)}. \tag{3.18}$$

Here $f_0$ denotes the resonance frequency, $c$ the speed of light and $k_B$ the Boltzmann constant. For a gas of Ytterbium atoms that is cooled to the Doppler temperature $T_{\text{Doppler}} \approx 4.4\mu K$ in the ${}^3\text{P}_1$ MOT, this yields a linewidth of $\Gamma_{\text{Doppler}} \approx 60$ kHz which is still orders of magnitude too large for metrological applications.
By further cooling the atoms employing sub-Doppler laser cooling techniques or evaporative cooling schemes, the linewidth can be further reduced. However, the lowest reachable temperatures are limited and even at temperatures as low as $T = 1$ nK the spectroscopic linewidth (assuming for simplicity a thermal distribution) is still limited to $\Gamma_{\text{Doppler}} \sim 10^2$ Hz as can be seen in Figure 3.2 b).
In 2003 Katori et al. [52] proposed a scheme for an optical lattice clock based on the ${}^1S_0 \rightarrow {}^3P_0$ transition of ${}^{87}$Sr, employing an optical lattice at a 'magic' trapping wavelength $\lambda_{\text{magic}}$ to overcome Doppler broadening and the differential ac-light shift induced by the optical trap. Optical lattice clocks based on alkaline earth(like) atoms in magic

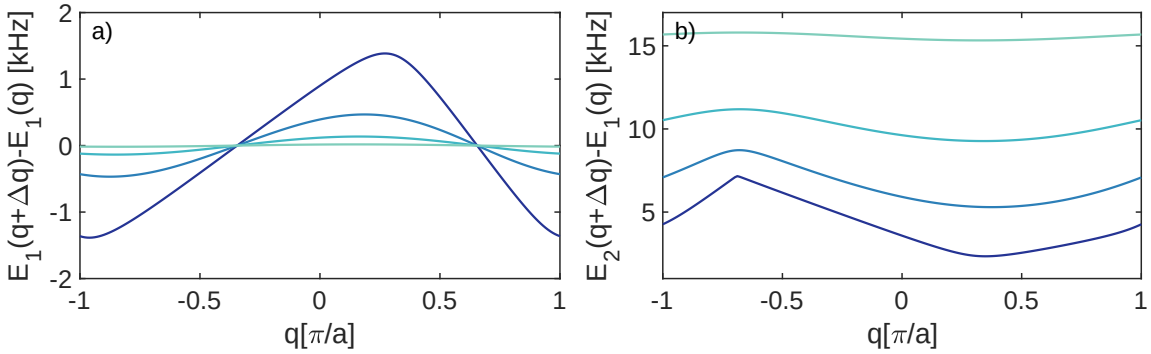


**Figure 3.3.:** Spectroscopic dispersion relation for a quasimomentum transfer of $\Delta q = -1.31$ a) for the intraband transition $n = 1 \rightarrow n = 1$, and b) for the interband transition $n = 1 \rightarrow n = 2$, colors from dark to light indicate an increasing lattice depth of $s_{1D} = (1, 5, 10, 20)\, E_{\mathrm{rec}}$.

optical lattices nowadays reach an unprecedented stability of $10^{-18}$ [55, 56] and might become the next time standard.
As the magical optical lattice is a prerequisite for high-resolution spectroscopy, it is necessary to understand the excitation process in the presence of a lattice potential. The lattice consists of interfering laser beams forming a periodic intensity landscape. Due to the optical dipole force the atoms experience a potential $V_{\mathrm{lat}}$ that is proportional to the light intensity $I(\boldsymbol{r})$ and the real part of the complex polarizability $\alpha(\lambda)$:

$$V_{\mathrm{lat}} \sim \mathrm{Re}(\alpha(\lambda)) I(\boldsymbol{r}). \tag{3.19}$$

As described previously in sec. 1.6, in general the complex polarizability $\alpha(\lambda)$ differs for atoms in different electronic states. Here, we focus on the particular case of an optical lattice at a so-called 'magic' wavelength for which the differential polarizability $\Delta\alpha = \alpha_{\mathrm{e}}(\lambda) - \alpha_{\mathrm{g}}(\lambda)$ vanishes. As described in sec. 1.6, in a periodic potential the momentum $\boldsymbol{p}$ is replaced by the quasimomentum $\boldsymbol{q}$, which is only defined up to a reciprocal lattice vector. The dispersion relation of the free particle $E(\boldsymbol{k}) = \hbar^2 \boldsymbol{k}^2 / 2m$ is replaced by a bandstructure $E_n(\boldsymbol{q})$ that depends on the depth of the potential, the lattice geometry and the band index $n \in \mathbb{N}$. In the following, the description is restricted to one-dimensional lattices and therefore given in terms of scalar values instead of vectors.
Due to the non-zero photon momentum the clock excitation process in an optical lattice is associated with a finite quasimomentum transfer of $\Delta q$. The frequency corresponding to the transition of a ground-state atom in band $n = i$ to an excited state in band $n' = j$ therefore is given by:

$$\omega_{i,j}(q) = \frac{1}{\hbar} \left( E_{j,e}(q + \Delta q) - E_{i,g}(q) + E_{\mathrm{int,e}} - E_{\mathrm{int,g}} \right) \tag{3.20}$$

and in particular is a function of the quasi momentum. Here, the subscripts $e, g$ refer to the energies for the ground- and excited-state atom, respectively. At the magic wavelength ground- and excited-state atoms, however, experience the same light shift, and thus the lattice potentials for ground- and excited-state atoms are the same at a given quasimomentum $E_{i,g}(q) = E_{i,g}(q)$. For a one-dimensional lattice the momentum transfer

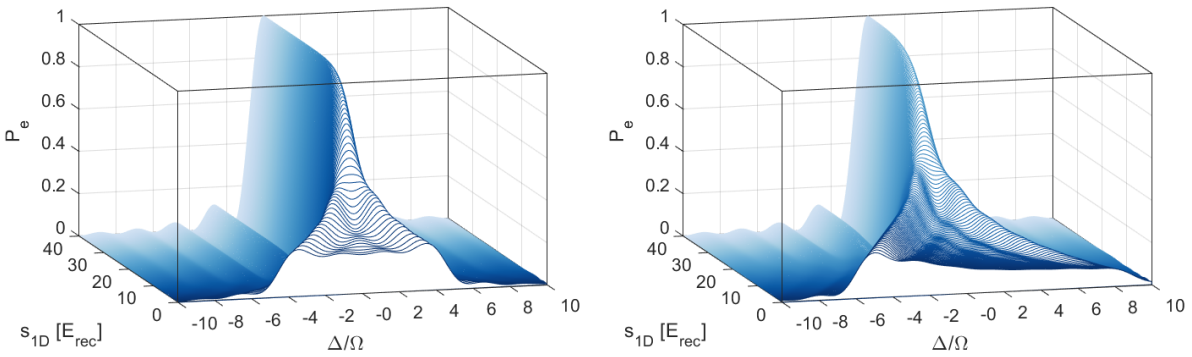


**Figure 3.4.:** Spectra obtained for $1 \times 10^3$ atoms equally spaced in quasimomentum space, as a function of lattice depth $s_{1D}$. The left panel shows the line shape obtained for a transition where initial and final band are the same $n = 1 \rightarrow n' = 1$, with $\Omega_{11} = 2\pi \times 330\,\text{Hz}$. The right panel shows the line shapes obtained for a transition from the first to the second band $n = 1 \rightarrow n = 2$ with $\Omega_{12} = 2\pi \times 330\,\text{Hz}$. Here, the quasimomentum-dependent coupling strength, caused by the different Franck-Condon overlap has not been taken into account. (For an analysis including the $q$ dependence of the Rabi frequency see ref.[82] and ref.[170]

$\Delta \boldsymbol{k}_{\text{phot}}$ associated with an optical excitation results in a quasimomentum transfer of [169]:

$$\Delta q = \frac{\lambda_{\text{lat}}}{\lambda_{\text{clock}}} \cos(\theta), \tag{3.21}$$

where $\theta$ denotes the angle between the photon's wave vector and the lattice vector. With $\lambda_{\text{clock}} = 578\,\text{nm}$ and $\lambda_{\text{magic}} = 759\,\text{nm}$ and a clock laser beam superimposed with the lattice one finds $\Delta q = \pm 1.31$. Figure 3.3 a) and b) show the spectroscopic dispersion relation $E_{i,j}(q) = E_{j,e}(q + \Delta q) - E_{i,g}(q)$ for the transitions $n = 1 \rightarrow n' = 1$ and $n = 1 \rightarrow n' = 2$ for $\Delta q = -1.31$ at different 1D lattice depths $s_{1D}$. Due to the quasimomentum transfer the spectroscopic bands are asymmetric with respect to $q = 0$. As the lattice depth increases the bands flatten and in the limit of $s_{1D} \rightarrow \infty$ the transition frequency is independent of the quasimomentum and the spectroscopic linewidth is free of motional broadening. To understand how the optical lattice affects the spectroscopic signal let us assume a filled first Brillouin zone, with $N$ atoms equally spaced in quasimomentum space. Corresponding to eq. 3.20, at a given clock laser frequency $\omega$ the detuning is a function of the quasimomentum $\Delta(q, i, j) = \omega - \omega_{i,j}(q)$. The excitation probability $p_e(\Omega, \Delta(q), t_{\text{int}})$ of an atom at quasimomentum $q$ for a given clock laser frequency $\omega$, Rabi frequency $\Omega$ and interrogation time $t_{\text{int}}$ can be computed using eq. 3.12. The main experimental observable, the excited-state fraction, for a certain transition is then given by:

$$n_{\text{e},i,j} = \frac{1}{N} \sum_{n=1}^{N} p_e(\Omega, \Delta(q_n, i, j), t_{\text{int}}). \tag{3.22}$$

In general, the Rabi frequency $\Omega$ depends on the quasimomentum $q$. However, in the tight binding regime the Rabi frequency varies only slowly within the Brillouin zone and the approximation is justified [170, 171]. For very shallow lattices the Franck-Condon [172] factor strongly depends on the quasimomentum and therefore eq. 3.22 does not describe the spectroscopic response correctly. A calculation of the excitation probabilities

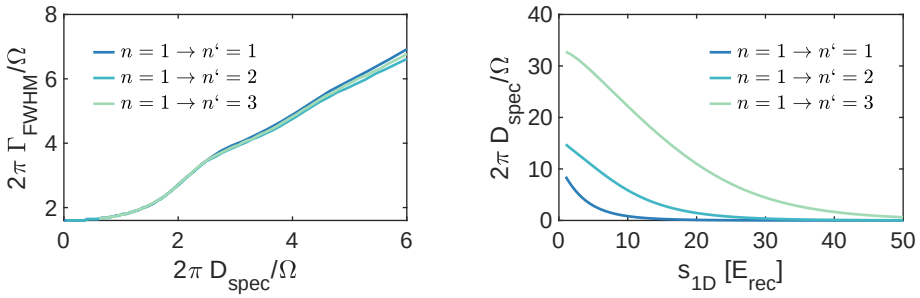


**Figure 3.5.:** Left: Spectroscopic linewidth $\Gamma_{\mathrm{FWHM}}$ as a function of the width of the spectroscopic dispersion relation $D_{\mathrm{spec}}$, both in units of the Rabi frequency $f_{\mathrm{Rabi}} = 330\,\mathrm{Hz}$ for transitions with $n = 1 \rightarrow n' \in \{1, 2, 3\}$. Right: width of the spectroscopic dispersion relation $D_{\mathrm{spec}}$ over $f_{\mathrm{Rabi}} = 330\,\mathrm{Hz}$ as a function of the lattice depth for transitions with $n = 1 \rightarrow n' \in \{1, 2, 3\}$.

including the quasimomentum-dependent Franck-Condon factors can be found in ref.[82]. Figure 3.4 shows the spectroscopic lineshapes of the intraband transitions $n = 1 \rightarrow n' = 1$ (fig. 3.4 a) ) and the interband transition $n = 1 \rightarrow n' = 2$ (fig. 3.4 b) ) for a Rabi frequency of $\Omega_{11} = \Omega_{12} = 2\pi \times 330\,\mathrm{Hz}$ and interrogation time of $t_{\mathrm{int}} = \pi/\Omega$ as a function of the 1D lattice depth, according to eq. 3.22. For small lattice depths the spectroscopic features are broadened and the maximum of the excited state fraction decreases. At the edges of the spectroscopic feature the excited state fraction is enhanced, which can be connected to Van-Hove singularities in the density of states [169, 171]. With increasing lattice depth the spectroscopic feature narrows, the maximum of the excited-state fraction increases and the lineshape transforms into a $\mathrm{sinc}^2$ determined by the interrogation time and the Rabi frequency. In contrast to the spectroscopic feature of the $n = 1 \rightarrow n' = 1$ transition, the spectroscopic feature of the $n = 1 \rightarrow n' = 2$ transition shows an asymmetry at small lattice depths and the transformation into a $\mathrm{sinc}^2$ occurs at higher lattice depths. Figure 3.5 a) shows the numerically obtained linewidth $\Gamma_{\mathrm{FWHM}}$ as a function of the width of the spectroscopic dispersion relation $D_{\mathrm{spec}}$ (in units of Hertz) over the Rabi frequency $\Omega = 2\pi \times 330\,\mathrm{Hz}$. For a ratio of $2\pi D_{\mathrm{spec}}/\Omega \gtrsim 3$ the spectroscopic linewidth is determined by $D_{\mathrm{spec}}$ which itself is determined by the lattice depth as shown in fig. 3.5 b). For a ratio $2\pi D_{\mathrm{spec}}/\Omega \lesssim 0.1$ the linewidth is Fourier limited and reaches a minimum of $\Gamma_{\mathrm{FWHM}} \approx 1.6\Omega/2\pi$.
Using these relations one can estimate the minimal Fourier limited linewidth reachable at a given lattice depth. For example at a lattice depth of $s_{1D} = 50\,E_{\mathrm{rec}}$, the bandwidth of the spectroscopic dispersion relation for an intraband transition $n = 1 \rightarrow n' = 1$ is $D_{\mathrm{spec}} < 0.5\,\mathrm{Hz}$. Fourier limitation is reached for Rabi frequencies of $\Omega \gtrsim 2\pi \times 5\,\mathrm{Hz}$, resulting in an estimated minimal Fourier limited linewidth of $\Gamma_{\mathrm{FWHM}} \gtrsim 8\,\mathrm{Hz}$.

### 3.2.1. Clock Spectroscopy in a Shallow Optical Lattices

To probe the spectroscopic response as a function of the lattice depth, we prepare a spin-polarized gas of $^{171}$Yb predominantly in the lowest band of the optical lattice and take spectra for different 1D lattice depths. We detect atoms in the ground and the

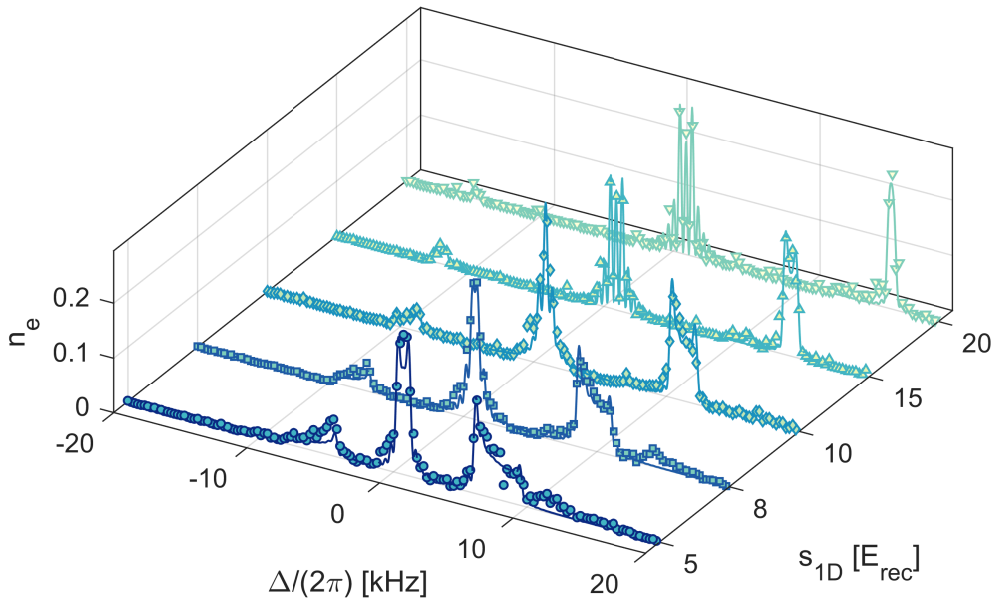


**Figure 3.6.:** Sideband spectroscopy on the $^1S_0 \rightarrow {}^3P_0$ transition for $N \sim 50 \times 10^3$ atoms using pulses of $t_{\text{int}} = 2.55\,\text{ms}$ at a Rabi frequency for the intraband transition of $\Omega \approx 2\pi \times 330\,\text{Hz}$. Shown is the excited-state fraction as a function of the detuning $\Delta$ for different depths of the 1D lattice $s_{1\text{D}}$. The 2D lattice depth was set to $s_{2\text{D}} \approx 17\,E_{\text{rec}}$. Solid lines denote fits of eq. 3.22 to the intraband transition (blue) and the interband transitions (green). The maximum amplitude of the spectroscopic signal, the resonance frequency and the Rabi frequency are used as fitting parameters. The amplitude of the red sideband, that is reduced compared to the blue sideband indicates that atoms are predominantly loaded into the lowest band.

excited state and use bandmapping to observe the population of the different bands with momentum resolution.

Figure 3.2 a) shows a spectrum for a lattice depth of $s_{1D} = 1E_{\text{rec}}$. Although bandgaps at $f - f_0 \approx -3\,\text{kHz}$ and $f - f_0 \approx 1\,\text{kHz}$ are already visible, the overall lineshape is still well described by a Gaussian, as one would expect for a Doppler broadened line. Figure 3.6 shows spectra for lattice depths between $s_{1\text{D}} = 5\,E_{\text{rec}}$ and $s_{1\text{D}} = 20\,E_{\text{rec}}$. Several distinct spectroscopic features correspond to intra- and interband transitions, respectively. We identify the central feature as the intraband transition $n = 1 \rightarrow n' = 1$, whereas the features to the left and right are identified as the red and blue sidebands $n = 2 \rightarrow n' = 1$ and $n = 1 \rightarrow n' = 2$, respectively. For this particular measurement, the evaporation ramp has been stopped at an early stage to load a significant fraction of atoms into the second band and demonstrate the existence of the red sideband. Nonetheless, the red sideband has a lower weight than the blue sideband, indicating that the atoms are predominantly loaded into the lowest band of the optical lattice. Comparing the spectroscopic response of the sidebands and evaluating bandmapping images, it is estimated that about 15% to 30% of the atoms are loaded into the second band. Typically, we work at lower particle numbers and temperatures and try to avoid populating higher bands. The Rabi frequency of the intraband transition $\Omega_{12}$ is estimated to be reduced by a factor of 0.38

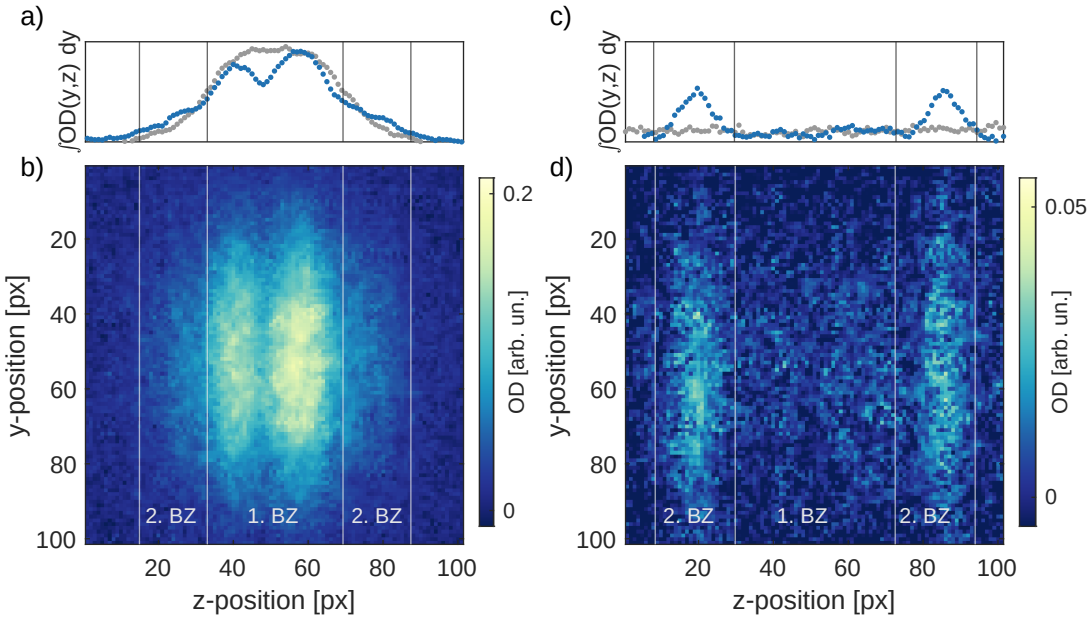


**Figure 3.7.:** Momentum resolved clock spectroscopy in a $s_{1D} = 15\,E_{\text{rec}}$ deep 1D-lattice. By resonantly driving the clock transition, atoms at a certain quasimomentum $q$ are removed from the first Brillouin zone of the ground state atoms and reappear in the second Brillouin zone of the excited state atoms. Panels b) and d) show absorption images of ground- and excited-state atoms after the 1D lattice has been ramped down exponentially within $t_{\text{BM}} = 0.5\,\text{ms}$ and a time of flight for a gas of $^{171}$Yb. False colors from bright to dark indicate an increasing optical density. Vertical lines indicate the Brillouin zones corresponding to the Bloch bands of the 1D lattice. Panel a) and b) show the optical density (OD) integrated along the y-direction. Blue dots correspond to the images shown in panel c) and d). For comparison grey dots show the integrated OD for an off-resonant clock laser pulse.

compared to the Rabi frequency of the intraband transition [84] of $\Omega_{11} \approx 2\pi \times 330\,\text{Hz}$. Therefore, to increase the spectroscopic contrast of the first sideband, we used pulse times of $t_{\text{int}} = 2.55\,\text{ms}$ with $\Omega_{11} t > \pi$, however, yet not meeting the $\pi$ pulse condition of the interband transition $\Omega_{12} t < \pi$. As the lattice depth increases, the distance between the intra- and interband features increases, whereas the widths of the spectroscopic features decrease as the bands flatten out.
The spectra are modelled by the sum of the intraband transition and the first red and blue sidebands:

$$P_{\text{e}} = c_1\, n_{\text{e},11} + c_2, n_{\text{e},21} + c_1\, n_{\text{e},12}. \tag{3.23}$$

Here, $n_{\text{e},11}$,$n_{\text{e},21}$ and $n_{\text{e},12}$ describe the spectroscopic response of the non-band changing transition and the sidebands, respectively, according to eq. 3.22. The coefficients $c_1$ and $c_2$ denote the relative population of the first and second band and $c_1 + c_2 = 1$ is assumed. We fit eq. 3.23 to the data, leaving the Rabi frequencies and the resonance frequencies of the different transitions as well as the relative population as free parameters. Although, the transitions $n = 1 \rightarrow n' = 3$, $n = 2 \rightarrow n' = 2$ and $n = 2 \rightarrow n' = 3$ as well as the quasimomentum-dependence of the Rabi frequency have been omitted, the fit reasonably

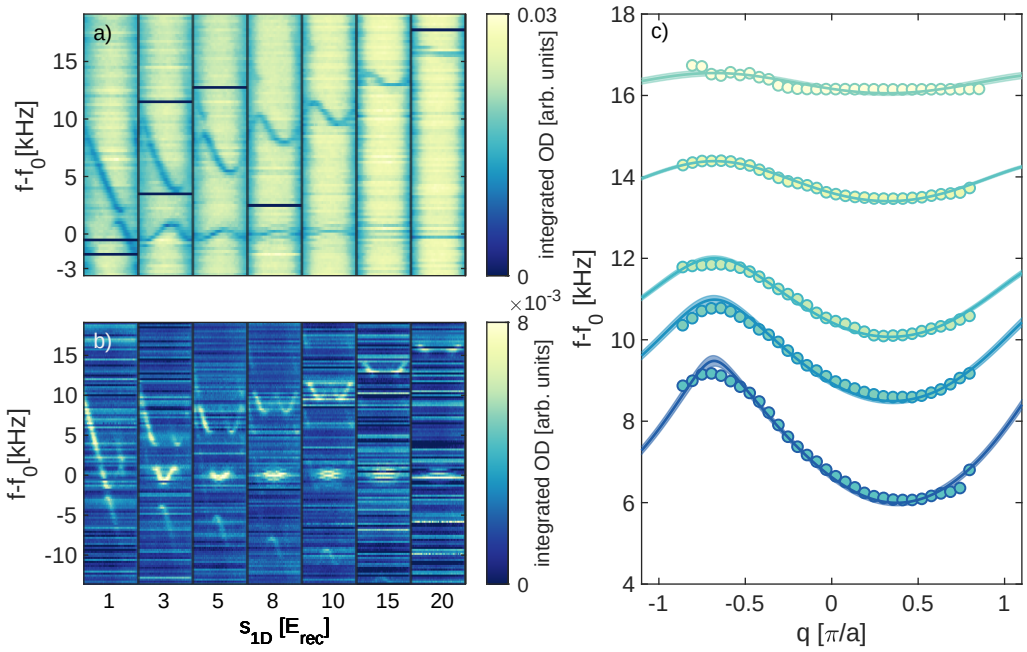


**Figure 3.8.:** Quasimomentum resolved clock spectroscopy for different 1D lattice depths $s_{1D}$ (same dataset as in Figure 3.6). Each row of panel a) (panel b)) shows the optical density integrated along axes perpendicular to the 1D-lattice, obtained from absorption images of ground-state (excited-state atoms) after the lattice potential has been exponentially ramped down in $t_{BM} = 0.5\,\text{ms}$ and time of flight. Each row is normalized to the total number of atoms. Every row corresponds to a single spectroscopic measurement with another detuning of the clock laser. The horizontal position denotes the quasimomentum. Colors from bright to dark represent an increasing integrated optical density. While for the panel a) only the first Brillouin zone is depicted, panel b) shows the first, the second and a small part of the third Brillouin zone. From left to right the 1D lattice depth increases. Panel c) shows the quasimomentum resolved resonance frequencies obtained from fitting the holes in the first Brillouin zone of the ground state atoms corresponding, to the $n = 1 \rightarrow n' = 2$ interband transition for $s_{1D} = 5, 8, 10, 15, 20\,E_{rec}$. Solid lines indicate a fit of the spectroscopic dispersion relation according to eq. 3.20, assuming a quasimomentum transfer of $\Delta q = -1.31$ and leaving the lattice depth as a fitting parameter. Data is shown for $-0.8 < q < 0.8$ only, because the determination of the resonance frequency is unreliable at the edges of the Brillouin zone. Frequencies are given with respect to the resonance frequency of the intraband transition.

describes the observed lineshapes.

Up to now, we have used the excited-state fraction $n_e$, which is an integral over all quasimomenta, as a spectroscopic observable. Combining double imaging and bandmapping allows to directly resolve the quasimomentum-dependence of the clock transition frequency. Figure 3.7 shows absorption images after time of flight and band mapping with and without driving a transition from the first into the second band. Atoms that are transferred to the excited state disappear in the Brillouin zone of the ground-state atoms at the corresponding quasimomentum $q_{\text{initial}}$ and reappear in the Brillouin zone of the excited-state atoms, shifted by quasimomentum transfer $\Delta q$ associated with the excitation process at $q_{\text{final}} = q_{\text{initial}} + \Delta q_{\text{photon}}$. Figure 3.8 a) and b) show quasimomentum-resolved spectra for intra- and interband transitions. Figure 3.8 a) shows the optical density integrated along

the direction perpendicular to the lattice in the first Brillouin zone of the ground-state atoms as a function of the clock laser frequency. Panels from left to right show spectra for an increasing 1D lattice depth. Three distinct features are visible corresponding to the intraband transition $n = 1 \rightarrow n' = 1$ and the first two blue sidebands $n = 1 \rightarrow n' = 2$ and $n = 1 \rightarrow n' = 3$. While the frequency of the intraband transition does not shift as the lattice depth increases, the resonance frequency of the interband transitions increases as the band gaps grow for an increasing lattice depth. At $s_{1\mathrm{D}} = 1\,E_{\mathrm{rec}}$ a band gap between the first and the second band is visible, while the band gap between the second and the third band is only resolved at higher lattice depths. (The third band is only barely visible at the left edge of the Brillouin-zone). As the lattice depth increases, the bands flatten and the resonance frequency of the transitions does not depend on the quasimomentum. Figure 3.8 b) shows the first, second and a part of the third Brillouin zone for atoms in the excited state. Atoms that disappeared in the first Brillouin zone of the ground-state reappear either in the same Brillouin zone for an intraband transition or in a higher Brillouin zone for the blue sidebands. Below the resonance frequency of the intraband transition, the first red sideband can be observed. Here, atoms are removed from the second Brillouin zone of the ground-state atoms, which is not shown in fig. 3.8 a) and reappear in the first Brillouin zone of the excited state atoms (momentum resolved clock spectra showing the first and the second Brillouin zone for ground and excited state atoms are shown in App. A ).
For small lattice depths of $s_{1D} = 1\,E_{\mathrm{rec}}$ and $s_{1D} = 3\,E_{\mathrm{rec}}$, the excitation strength for intra- and interband transitions strongly depends on the quasimomentum $q$, which can be associated to a strong $q$-dependence of the Franck-Condon factor and is in qualitative agreement with the calculations presented in ref. [82]. At higher lattice depths, where the tight-binding approximation is well justified, the excitation strength does not vary over the Brillouin zone.
Fig. 3.8 c) shows the $q$-dependent resonance frequency of the blue sideband for lattice depths between $s_{1\mathrm{D}} = 5\,E_{\mathrm{rec}}$ and $s_{2\mathrm{D}} = 20\,E_{\mathrm{rec}}$, extracted from the spectra shown in panel a). We fit eq. 3.20 to the data, assuming $\Delta q = -1.31$ and leaving the lattice depth as a free parameter. At small lattice depths of $s_{1\mathrm{D}} = 5\,E_{\mathrm{rec}}$ and $s_{1\mathrm{D}} = 8\,E_{\mathrm{rec}}$ the data shows systematic deviations from the fit at the edges of the Brillouin zone. This could possibly be caused by the harmonic confinement of the 2D-lattice, which, compared to the 1D-lattice depth, is more significant at small 1D-lattice depths and which has been neglected in the description of the system. Errors in determining the quasimomentum could as well play a significant role. However, the reason for the observed deviations remains an open question that requires further measurements. For an increasing lattice depth $s_{1\mathrm{D}} = 5\,E_{\mathrm{rec}}$ and $s_{1\mathrm{D}} = 8\,E_{\mathrm{rec}}$ the deviations become smaller. At $s_{1\mathrm{D}} = 20\,E_{\mathrm{rec}}$ the spectroscopic resolution is not sufficient to resolve the curvature of the spectroscopic band anymore and therefore, the resonance positions extracted from the momentum resolved spectra appear as straight line for a large part of the Brillouin zone. Clock spectroscopy in shallow optical lattices thus allows to resolve the quasimomentum-dependence of the resonance frequency and has therefore been extensively discussed in the context of synthetic spin orbit coupling with optical lattice clocks and synthetic dimensions [169, 171, 173].

### 3.2.2. Clock Spectroscopy in a Deep Optical Lattice

Due to the quasimomentum transfer associated with the excitation the spectroscopic resolution in shallow lattices is limited by the width of the Bloch bands. To obtain a maximal spectroscopic resolution, the motional and internal degrees have to be decoupled, which can be achieved in deep optical lattices, where the bands essentially are flat. The decoupling of motional and internal degrees of freedom is typically characterized by the so-called Lamb-Dicke parameter $\eta$. For an atom in a harmonic potential it is given by [174]:

$$\eta = \sqrt{\frac{\omega_{\mathrm{rec}}}{\omega_{\mathrm{trap}}}} \tag{3.24}$$

where $\omega_{\mathrm{rec}}$ and $\omega_{\mathrm{trap}}$ denote the recoil frequency associated with the optical excitation and the trapping frequency, respectively. The Lamb-Dicke parameter decreases with increasing trapping frequency and in a deep lattice the Lamb-Dicke regime, characterized by $\eta^2 \ll 1$ [174] is reached. In the Lamb-Dicke regime coupling to higher or lower vibrational states is suppressed and the Rabi frequencies for exciting the next higher or lower vibrational state $n+1$ or $n-1$ are given [175]:

$$\Omega_{n,n+1} = \Omega\eta\sqrt{n+1} \tag{3.25}$$

$$\Omega_{n,n-1} = \Omega\eta\sqrt{n}, \tag{3.26}$$

Therefore, working in deep optical lattices allows to probe the clock transition free of detrimental Doppler and recoil effects [54]. At a typical working depth of the 1D-lattice of $s_{1\mathrm{D}} = 50\,E_{\mathrm{rec}}$, the Lamb-Dicke parameter corresponds to $\eta^2 = 0.12$. Taking into account the available lattice laser power it has been estimated that a lattice depth of $s_{1\mathrm{D}} = 150\,E_{\mathrm{rec}}$ corresponding to $\eta^2 \approx 0.07$ [82, 84] can be reached.

To probe the achievable spectroscopic linewidth, we prepare a spin polarized gas of $N \sim 10 \times 10^3$ atoms $^{173}$Yb in a deep magic lattice at $s_{1\mathrm{D}} = 60\,E_{\mathrm{rec}}$ and $s_{2\mathrm{D}} = 25\,E_{\mathrm{rec}}$, corresponding to a Lamb-Dicke parameter $\eta^2 = 0.11$. We take spectra of the $n = 1 \rightarrow n' = 1$ transition and step by step reduce the Rabi frequency while increasing the interrogation time to fulfill the $\pi$-pulse condition. The obtained spectra are shown in fig. 3.9. Fitting eq. 3.12 to the data yields the Rabi frequencies $\Omega$. The linewidth $\Gamma_{\mathrm{FWHM}}$ is numerically obtained from the fitted spectra. The linewidth of $\Gamma_{\mathrm{FWHM}} = 26.7(2.4)\,\mathrm{Hz}$ observed at a Rabi frequency of $\Omega = 2\pi \times 10(6)\,\mathrm{Hz}$ using pulses with a length of $t_{\mathrm{pulse}} = 34\,\mathrm{ms}$, is the smallest spectroscopic linewidth measured at the ytterbium experiment so far. The visibility of small side-lobes of the sinc$^2$ indicates that the linewidth is still limited by the interaction time and therefore we conclude that it is Fourier-limited. Note that we compensated for a linear drift of the clock cavity resonance during the experiment by applying a frequency ramp to an AOM in the clock laser setup and, *a posteriori*, by analyzing the residual linear drift using the resonance frequencies measured in several clock spectra.

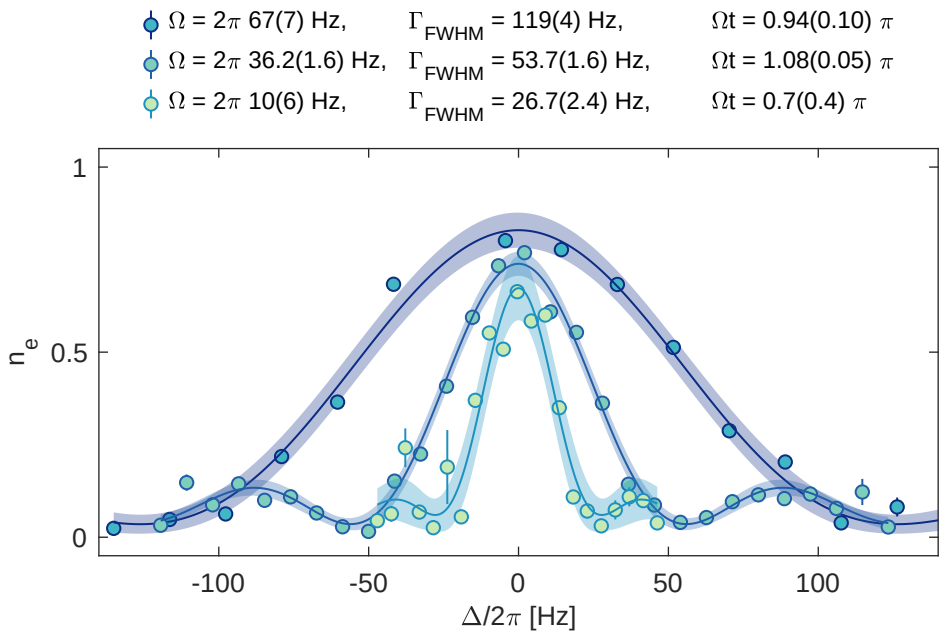


**Figure 3.9.:** High-resolution spectroscopy with spin polarized gases of $10 \times 10^3$ atoms of $^{173}$Yb in a deep optical lattice at $s_{1D} = 60\, E_{rec}$ and $s_{2D} = 25\, E_{rec}$. Shown is the excited state fraction as a function of the clock laser detuning. Every data point represents a single measurement. Error bars indicate the uncertainty of the determination of the excited state fraction. Colors from light to dark indicate an increasing Rabi frequency $\Omega$. Solid lines represent a best fit according to eq. 3.12 for a fixed pulse time $t$ of $t = 7\,$ms, $t = 15\,$ms and $t = 34\,$ms. The legend lists Rabi frequencies, the spectroscopic linewidths $\Gamma_{FWHM}$ and the parameter $\Omega t$ obtained from the fits. Shaded areas show the 95% confidence interval of the fit.

## 3.3. Optical Bloch Equations

Up to now, we have used a single particle description to analyze the spectroscopic measurements. In the experiment we usually work with a cloud of approximately (1-4) $\times 10^4$ atoms, thus working with many almost identical copies of the same simple two-level system simultaneously. The statistical properties of an ensemble of quantum systems can conveniently be described in terms of the density matrix (see e.g. ref. [165] for an introduction of the density operator).
Consider an ensemble of $N$ subsystems. If all $N$ subsystems are in the same state $\psi_i$, the state of the ensemble is referred to as a pure state and the expectation value of the observable $A$ is given by:

$$\langle A \rangle = \langle \psi_i | A | \psi_i \rangle \,. \tag{3.27}$$

In the more general case, where the quantum states of the individual subsystems are not identical, the state of the ensemble is referred to as a mixed state. The expectation value of $A$ is then given by

$$\langle A \rangle = \sum_i p_i \, \langle \psi_i | A | \psi_i \rangle \,, \tag{3.28}$$

were $p_i$ denotes the probability of an arbitrary subsystem to be in the state $\psi_i$. The density matrix describing the ensemble is defined as:

$$\rho = \sum_i p_i \left|\psi_i\right\rangle \left\langle\psi_i\right| , \tag{3.29}$$

and allows to write the expectation value as:

$$\langle A \rangle = \mathrm{tr}(\rho A). \tag{3.30}$$

Given the density matrix of a system, it is straightforward to distinguish between pure and mixed states, as $\mathrm{tr}(\rho^2) = 1$ for pure states and $\mathrm{tr}(\rho^2) < 1$ for mixed states.
For the two level system the density matrix is given by:

$$\rho = \begin{pmatrix} \rho_{ee} & \rho_{eg} \\ \rho_{ge} & \rho_{gg} \end{pmatrix} = \begin{pmatrix} c_e c_e^* & c_e c_g^* \\ c_e^* c_g & c_g c_g^* \end{pmatrix} \tag{3.31}$$

The diagonal elements of the density matrix describe the population of the states $|g\rangle$ and $|e\rangle$. Non-zero off-diagonal elements indicate a coherent superposition of different quantum states (therefore, they are usually referred to as 'coherences').
The time evolution of the density matrix is governed by the Von-Neumann equation[165]:

$$\partial_t \rho = -\frac{i}{\hbar} \left[\mathcal{H}, \rho\right] . \tag{3.32}$$

Using the two-level Hamiltonian, derived earlier in sec. 3.1 to describe the atom-light interaction, and applying the rotating frame transformation:

$$\tilde{\rho}_{ee} = \rho_{ee},\ \tilde{\rho}_{gg} = \rho_{gg},\ \tilde{\rho}_{ge} = \rho_{ge} e^{-i\omega t},\ \tilde{\rho}_{eg} = \tilde{\rho}_{ge}^*, \tag{3.33}$$

the Von-Neumann equation yields four coupled differential equations[164]:

$$\partial_t \rho_{ee} = i\frac{\Omega}{2} \left(\tilde{\rho}_{eg} - \tilde{\rho}_{ge}\right) \tag{3.34}$$

$$\partial_t \rho_{gg} = -i\frac{\Omega}{2} \left(\tilde{\rho}_{eg} - \tilde{\rho}_{ge}\right) \tag{3.35}$$

$$\partial_t \tilde{\rho}_{ge} = -i\Delta\tilde{\rho}_{ge} - i\frac{\Omega}{2} \left(\rho_{ee} - \rho_{gg}\right) \tag{3.36}$$

$$\partial_t \tilde{\rho}_{ge} = i\Delta\tilde{\rho}_{eg} + i\frac{\Omega}{2} \left(\rho_{ee} - \rho_{gg}\right) . \tag{3.37}$$

that are known as the 'optical Bloch equations' (OBE) [176] and describe the time evolution of the ensemble.
The density matrix of the two-level system can be expressed in terms of the Pauli matrices $\sigma_i$:

$$\sigma_x = \begin{pmatrix} 0 & 1 \\ 1 & 0 \end{pmatrix}, \sigma_y = \begin{pmatrix} 0 & -i \\ i & 0 \end{pmatrix}, \sigma_z = \begin{pmatrix} 1 & 0 \\ 0 & -1 \end{pmatrix}, \tag{3.38}$$

as together with the identity matrix $\mathbb{1}$ they form a basis for the space of Hermitian $2 \times 2$ matrices. The density matrix can thus be written as [165]:

$$\tilde{\rho} = \frac{1}{2} \left(\mathbb{1} + \boldsymbol{s} \cdot \boldsymbol{\sigma}\right) . \tag{3.39}$$

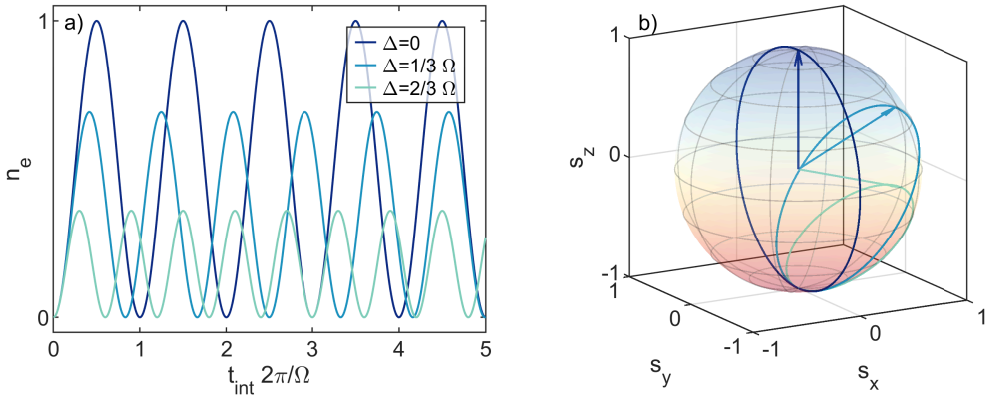


**Figure 3.10.:** Rabi oscillations in the Bloch sphere representation. Panel a) shows the excited-state fraction $n_e$ as a function of the interrogation time $t_{\text{int}}$ for different detunings $\Delta$ as indicated by different colors. Panel b) shows the time evolution of the Bloch vector during the Rabi oscilllations shown in panel a). Circles indicate the orbit of the Bloch vector and arrows denote the Bloch vector after an interogation time of $t_{\text{int}} = \pi/\tilde{\Omega}$. Different colors indicate different detunings $\Delta$.

The vector $\boldsymbol{s}$ is called Bloch vector and is given by:

$$\boldsymbol{s} = \begin{pmatrix} s_x \\ s_y \\ s_z \end{pmatrix} = \begin{pmatrix} \rho_{\text{eg}} + \rho_{\text{ge}} \\ i(\rho_{\text{eg}} - \rho_{\text{ge}}) \\ \rho_{ee} - \rho_{gg} \end{pmatrix}. \tag{3.40}$$

The $x$- and $y$-components of the Bloch vector are determined by the in- and out-of-phase components of the coherences, while the $z$-component is determined by the population difference of the two states.
According to the optical Bloch equations 3.34-3.37, the time evolution of the Bloch vector is given by [164]:

$$\partial_t \boldsymbol{s} = (\Omega \boldsymbol{e}_x - \Delta \boldsymbol{e}_z) \times \boldsymbol{s}. \tag{3.41}$$

The vectors $\boldsymbol{e}_x$ and $\boldsymbol{e}_z$ denote the unit vectors in $x$- and $z$-direction, respectively. To gain a more intuitive understanding of the quantum state of the ensemble and its time evolution, it is beneficial to visualize the Bloch vector. Figure 3.10 b) shows the time evolution of the Bloch vector for Rabi oscillations at different detunings as described by eq. 3.41. The tip of the Bloch vector is bound to the Bloch sphere and precesses around the direction of the vector $\boldsymbol{\Omega} = \Omega \boldsymbol{e}_x - \Delta \boldsymbol{e}_z$. On resonance $\Delta = 0$ the precession orbit lies in the $y - z$ plane and the precession frequency $\tilde{\Omega}$ is given by the bare Rabi frequency $\Omega$, whereas for increasing detuning $|\Delta| > 0$ the precession orbit tilts into the $x$-direction, its radius decreases and the precession frequency $\tilde{\Omega}$ increases.

Thus far, the description is analog to the single particle two-level system discussed before. However, up to now we have only considered a closed quantum system, that does not suffer from dissipation and decoherence. Experimentally decoherence and dissipation usually occur as damping and one typically strives to minimize the effects of decoherence. Nevertheless, this is only possible to a certain degree and for example the coupling of a system to the vacuum is inevitable.
To take into account spontaneous emission and decoherence, the optical Bloch equations

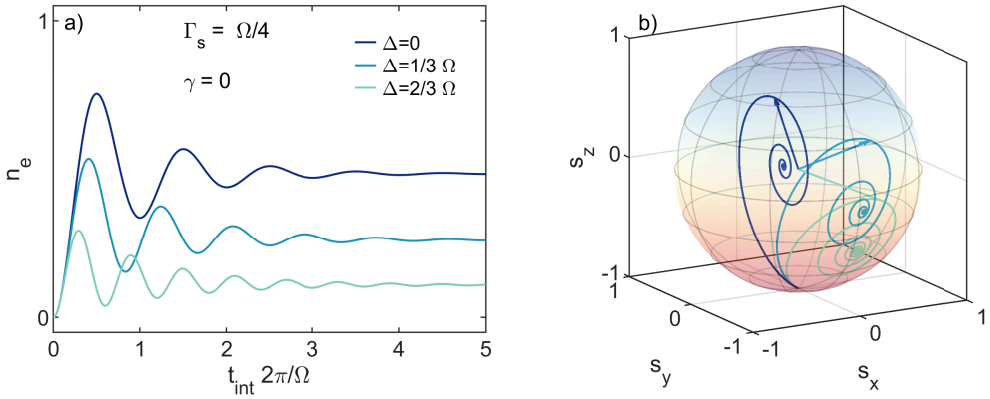


**Figure 3.11.:** Time evolution of the two-level system obtained by numerically solving the damped optical Bloch equations, taking into account spontaneous emission at a rate of $\Gamma_s = \Omega/4$. Panel a) shows the excited-state fraction $n_e$ as a function of the interrogation time $t_{\text{int}}$ for different detunings $\Delta$ as indicated by the color. Panel b) shows the time evolution of the Bloch vector for different detunings $\Delta$ indicated by color. The straight lines show the time evolution for $t_{\text{int}} = 0$ to $t_{\text{int}} = 5 \times 2\pi/\Omega$. Arrows show the Bloch vector at $t_{\text{int}} = \pi/\tilde{\Omega}$.

have to be modified by some additional terms. In refs. [166, 177] the authors derive the time evolution of the density matrix, considering a two-level system coupled to a (thermal) bath, taking into account different internal and external relaxation channels. Here, we will focus on spontaneous decay and dephasing only and omit particle loss as a source of relaxation. The time evolution of the density matrix then is given by [164]:

$$\partial_t \rho_{ee} = i\frac{\Omega}{2}\left(\tilde{\rho}_{eg} - \tilde{\rho}_{ge}\right) - \Gamma_s \rho_{ee} \tag{3.42}$$

$$\partial_t \rho_{gg} = -i\frac{\Omega}{2}\left(\tilde{\rho}_{eg} - \tilde{\rho}_{ge}\right) + \Gamma_s \rho_{ee} \tag{3.43}$$

$$\partial_t \tilde{\rho}_{ge} = -\left(\gamma_\perp + i\Delta\right)\tilde{\rho}_{ge} - i\frac{\Omega}{2}\left(\rho_{ee} - \rho_{gg}\right) \tag{3.44}$$

$$\partial_t \tilde{\rho}_{ge} = -\left(\gamma_\perp - i\Delta\right)\tilde{\rho}_{eg} + i\frac{\Omega}{2}\left(\rho_{ee} - \rho_{gg}\right). \tag{3.45}$$

Due to spontaneous emission atoms in the excited state $|e\rangle$ decay into the ground state $|g\rangle$ at a rate $\Gamma_s$ given by the natural linewidth of the transition. This is described by the $\mp\Gamma\rho_{ee}$ terms in eq. 3.42 and eq. 3.43. The terms $\gamma_\perp\tilde{\rho}_{ge}$ and $\gamma_\perp\tilde{\rho}_{eg}$ in equations eq. 3.44 and eq. 3.45, describe the decay of the coherences or, in other words, the decay of the transversal (with respect to the $z$-axis) component of the Bloch vector. The coefficient $\gamma_\perp$ is given by [164]:

$$\gamma_\perp = \frac{\Gamma_s}{2} + \gamma, \tag{3.46}$$

where the coefficient $\gamma$ takes into account decoherence caused e.g. by laser phase noise or collisions (see ref. [178] for a study of collisional dephasing in an optical lattice clock experiment). Figure 3.11 shows the time evolution of the driven two-level system taking into account spontaneous emission at a rate of $\Gamma_s = \Omega/4$ for different detunings $\Delta$. Figure 3.11 a) shows the excited-state fraction $n_e$ as a function of the interrogation time $t_{\text{int}}$

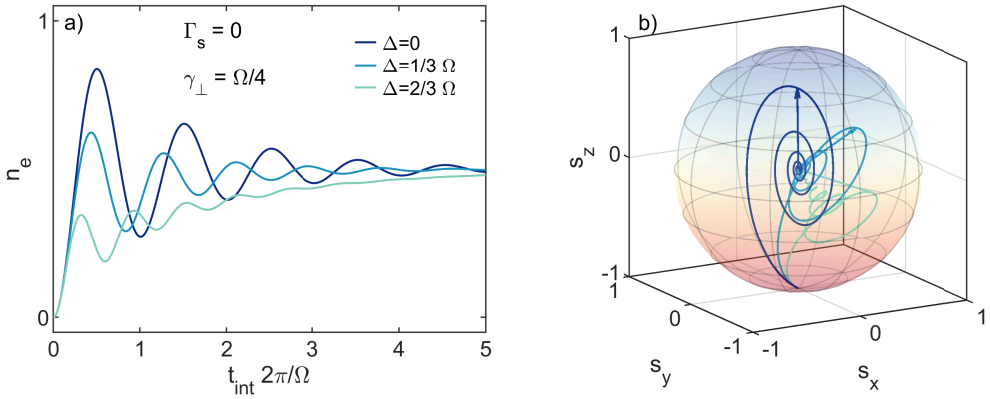


**Figure 3.12.:** Time evolution of the two-level system obtained by numerically solving the damped optical Bloch equations taking into account decoherence at a rate of $\gamma_\perp = \Omega/4$. Panel a) shows the excited-state fraction $n_e$ as a function of the interrogation time $t_{\text{int}}$ for different detunings $\Delta$ as indicated by the color. Panel b) shows the time evolution of the Bloch vector for different detunings $\Delta$. The straight lines show the time evolution for $t_{\text{int}} = 0$ to $t_{\text{int}} = 5 \times 2\pi/\Omega$. Arrows show the Bloch vector at $t_{\text{int}} = \pi/\tilde{\Omega}$.

for different detunings $\Delta$. The spontaneous emission damps the Rabi oscillation and in the limit of a large interrogation time the excited-state fraction approaches a finite value that depends on the detuning $\Delta$. Figure 3.11 b) shows the corresponding time evolution of the Bloch vector. Due to spontaneous emission the length of the Bloch vector is reduced over time, and the precession orbits observed in the resonant case are transformed into spirals. Figure 3.12 shows the time evolution of the two-level system under the assumption of purely transversal decoherence, that could be realized by e.g. laser phase noise. Figure 3.12 a) shows the excited-state fraction $n_e$ as a function of the interrogation time $t_{\text{int}}$. The purely transversal decay leads to a damping of the oscillations, however, in the limit of long interrogation times the excited-state fraction approaches $n_e = 0.5$, independent of the detuning.

Spontaneous decay and transversal damping not only affect the the appearance of the Rabi oscillations, but as well the spectroscopic lineshape. Figure 3.13 a) shows lineshapes computed for pulse times of $t_{\text{int}} = \pi/\Omega$ for purely spontaneous decay ($\Gamma_s \geq 0$ and $\gamma_\perp = \Gamma_s/2$.) Figure 3.13 b) shows the lineshapes for purely transversal decay $\gamma_\perp \geq 0$. As the damping increases, in both cases the maximum of the excited-state fraction $n_e$ decreases while the linewidth $\Gamma_{\text{FWHM}}$ increases. The decrease of the spectroscopic contrast is stronger for purely spontaneous decay, the increase in linewidth and the change of the lineshape is stronger for purely transversal decay. For both cases considered in the limit of strong damping the side lobes of the sinc$^2$ wash out and the lineshape transforms into a Lorentzian. In the limit of $\Omega \gg \gamma_\perp$ and $\Omega \gg \Gamma_s$ the spectroscopic linewidth approaches $\Gamma_{\text{FWHM}} \approx 1.6\Omega/2\pi$, and hence is fully determined by the excitation pulse - the linewidth is 'Fourier' limited.

Considering the theoretical linewidth of the $^1S_0 \rightarrow ^3P_0$ transition of ytterbium of $\Gamma < 2\pi \times 10\,\text{mHz}$ [102], the effect of the spontaneous decay on the spectroscopic linewidth is negligible, and hence neglected in data analysis. Note, however, that the lifetime of atoms in the metastable state in the magic optical lattice is on the order of $\tau \approx 4\,\text{s}$, and

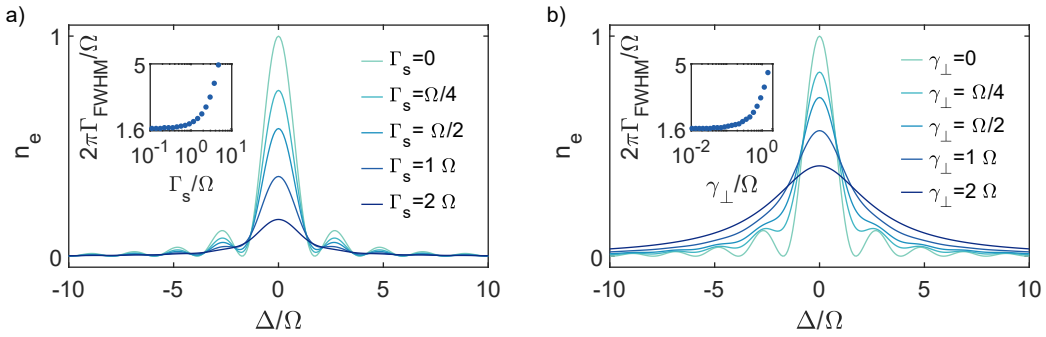


**Figure 3.13.:** Spectroscopic line shapes obtained from numerically solving the damped optical Bloch equations for a) purely spontaneous decay and b) purely transversal decay. Colors from light to dark indicate an increasing damping coefficient $\Gamma_s$ or $\gamma_\perp$, respectively. Insets show the spectroscopic linewidths $\Gamma_{FWHM}$ as function of the damping $\Gamma_s$ and $\gamma_\perp$, respectively

thus significantly smaller than the lifetime associated with spontaneous decay (see sec. 5). To probe the coherence properties of the system, we prepare a gas of spin-polarized $^{173}$Yb in a deep optical lattice, drive the clock transition and observe Rabi flopping. As there is no double occupancy due to the Pauli principle (also doubly occupied sites would be shifted in energy), one can preclude interaction-induced dephasing [178]. Nonetheless, the possible sources of decoherence are manifold. They include for example, laser phase noise, fluctuations of the lattice laser wavelength, fluctuations of the magnetic fields, and the inhomogeneity of the spectroscopy beam. Figure 3.14 a) to c) show Rabi oscillations for different $m_F$ states of $^{173}$Yb, driven with $\pi$ polarized clock laser light at the same intensity. Each panel shows two different measurements. Due to a drift of the clock laser frequency over the course of the measurement, both measurements have been recorded at different detunings. Therefore, Rabi flopping occurs at different effective Rabi frequencies $\tilde{\Omega}$. To account for the linear drift of the clock laser, after each Rabi oscillation measurement we take spectra and determine the resonance positions, which subsequently are used to perform an *a posteriori* drift compensation and to determine the time-dependent detuning during the Rabi oscillation measurement. Panels d) to f) show the spectra after the drift compensation has been applied (to account for different Rabi frequencies of the clock transition, for different $m_F$ states the pulse length has been adapted to fulfill the $\pi$-pulse condition). Frequencies are denoted with respect to the resonance frequencies obtained from a sinc$^2$ fit and vertical lines indicate the detuning at which the Rabi oscillations have been recorded. The width of the vertical lines indicates the drift over the course of the Rabi oscillation sequence.

Whereas the drift of approximately $\Delta_{\text{drift}} \approx 15\,\text{Hz}$ over the course of the Rabi oscillation measurement is small compared to the observed linewidths of the $m_F = 5/2$ and $m_F = 3/2$ transitions with $\Gamma_{m_F=5/2}/\Delta_{\text{drift}} \approx 20$ and $\Gamma_{m_F=3/2}/\Delta_{\text{drift}} \approx 13$, the drift of approximately $\Delta_{\text{drift}} \approx 20\,\text{Hz}$ over the course of the Rabi oscillation measurement of the $m_F = 1/2$ transition is comparable to the Rabi frequency with $\Gamma_{m_F=1/2}/\Delta_{\text{drift}} \approx 3$, and therefore significantly affects the Rabi oscillation measurements. To account for the drift, we fit the numerically obtained solutions of the damped optical Bloch equations to the data, using a time dependent detuning $\Delta(t)$, as obtained from the drift analysis, and use the Rabi frequencies $\Omega$, the damping rate $\gamma_\perp$ and the amplitude of the oscillations as fit pa-

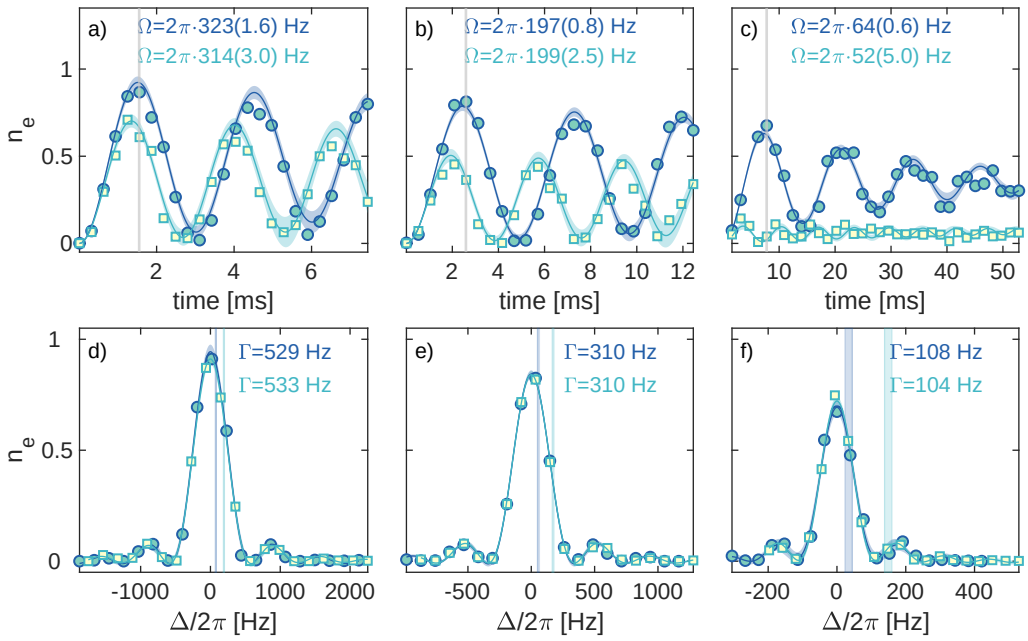


**Figure 3.14.:** Rabi Oscillations ( panels a) to c) ) and spectra ( panels d) to f) ) of the clock transition for different $m_F$ states of $^{173}$Yb, taken at the same clock laser intensity. Panels a) and d) show data for $m_F = 5/2$, panels b) and e) for $m_F = 3/2$ and panels c) and f) for $m_F = 1/2$. Vertical lines in panels a) to c) indicate the pulse times $t_{clock}$ used for the spectra in panels d) to f). Panels a) to f) show two data sets each indicated by different colors. The spectra are used to analyze the clock laser drift and perform an *a posteriori* linear drift compensation. Therefore, the detuning during the Rabi oscillation measurements becomes time dependent. Vertical shaded areas in panels d) to f) indicate the range of the drift of the detuning during the Rabi oscillations in panels a) to c). Solid lines indicate fits using numerical solutions of the damped optical Bloch equations assuming an negligible spontaneous decay and setting $\Gamma_s = 0$. Shaded areas indicate 95 % confidence intervals of the fits. The spectroscopic linewidths specified in panels d)-f) is the numerically determined linewidth at full width at half maximum.

rameters. The fits are shown in fig. 3.14 a) to c) and show good agreement with the data. The Rabi frequencies of the $m_F = 1/2$ and $m_F = 3/2$ transitions are reduced with respect to the Rabi frequency of the $m_F = 5/2$ transition. The obtained values are in excellent agreement with the expected spin-dependence caused by the Clebsch-Gordan coefficients for the different transitions, which are given by $c_{CG,5/2} = -\sqrt{35}/7$, $c_{CG,5/2} = -3\sqrt{35}/35$ and $c_{CG,1/2} = -\sqrt{35}/35$ (see ref. [92]). From the fits we obtain an average transversal damping rate of $\bar{\gamma}_\perp = 2\pi \times 5(1)\,\mathrm{Hz}$. A transversal decoherence of this order of magnitude is in good qualitative agreement with the so far smallest observed spectroscopic linewidth of $\Gamma_{\mathrm{FWHM}} = 26.7(2.4)\,\mathrm{Hz}$.

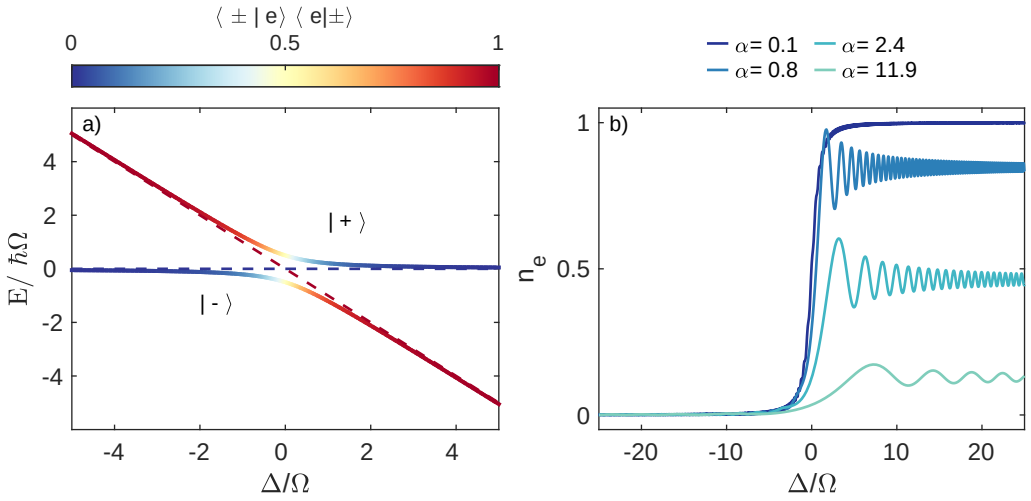


**Figure 3.15.:** Panel a) shows the spectrum of the two-level system as a function of the detuning $\Delta$. Dashed lines correspond to the eigenenergies of the bare states whereas solid lines show the dressed eigenstates of the coupled two-level system. The colors of the lines indicate the projection of the dressed state onto the bare excited state $|e\rangle$. Panel b) shows the transfer efficiency from ground to excited state of a $50\,\Omega$ broad RAP for different sweep velocities, characterized by $\alpha = \partial_t \Delta/\Omega^2$.

## 3.4. Excited State Preparation Using a Rapid Adiabatic Passage

High-fidelity excited-state preparation using $\pi-$ pulses requires an exact knowledge of the Rabi and the resonance frequency. The Rabi frequency can conveniently be controlled by means of an intensity regulation, whereas keeping the clock laser on resonance for a long time is experimentally rather challenging as the clock laser frequency undergoes linear and non-linear drifts due to the limited stability of the reference cavity (see sec. 3.5). Increasing the Rabi frequency improves the stability, as compared to the spectroscopic linewidth the drift becomes smaller. However, the achievable Rabi frequency is limited by the available laser power. Another option for excited-state preparation is to invoke state transfer using a rapid adiabatic passage (RAP). The RAP is a commonly used technique that allows for a high-fidelity state transfer and, at the same time, is technically easy to implement and robust against experimental imperfections such as drifts of the excitation laser frequency. In the following, I will briefly introduce the theory of the rapid adiabatic passage. A detailed discussion of the RAP can be found in various textbooks as e.g. ref.[163]. Here, I follow the notation and argumentation of ref. [164].

Let us again consider a coupled two-level system, which in the rotating wave approximation, is described by the Hamiltonian [164]:

$$\mathcal{H} = \hbar \begin{pmatrix} 0 & \frac{\Omega}{2} \\ \frac{\Omega}{2} & -\Delta \end{pmatrix}. \tag{3.47}$$

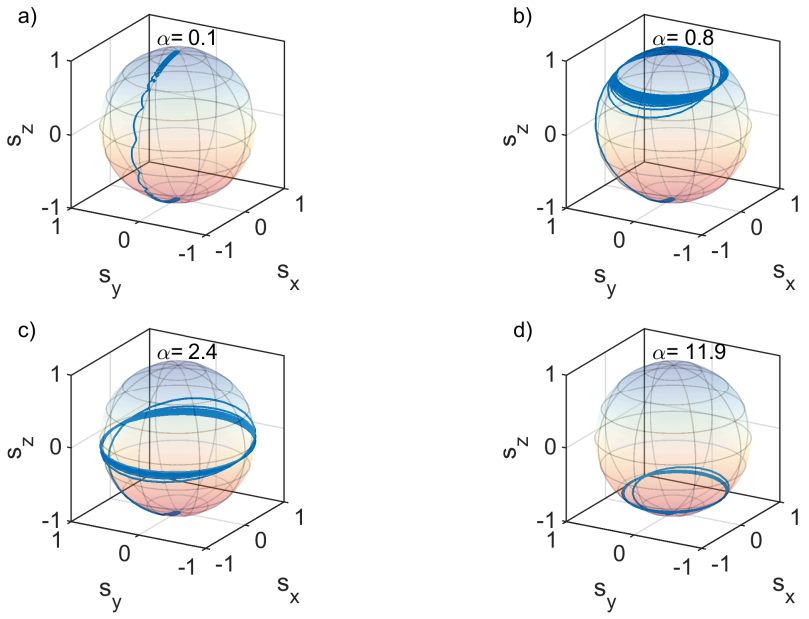


**Figure 3.16.:** Time evolution of the Bloch vector during a frequency chirp from $\Delta_{\text{initial}} = -25\,\Omega$ to $\Delta_{\text{final}} = 25\,\Omega$, characterized by $\alpha = \partial_t \Delta/\Omega^2$. For $\alpha > 0$ the state transfer from ground to excited state is incomplete and decreases for an increasing value $\alpha$.

Diagonalizing the Hamiltonian yields the dressed or adiabatic states $|\pm\rangle$ and new eigenenergies $E_\pm$. The new eigenstates can be expressed in terms of the uncoupled states [164]:

$$|+\rangle = \sin\theta\,|g\rangle + \cos\theta\,|e\rangle \tag{3.48}$$

$$|-\rangle = \cos\theta\,|g\rangle - \sin\theta\,|e\rangle\,, \tag{3.49}$$

with the mixing angle $\theta$ defined by[164]:

$$\tan(2\theta) = -\frac{\Omega}{\Delta}. \tag{3.50}$$

The corresponding eigenenergies are given by [164]:

$$E_\pm = -\frac{\hbar\Delta}{2} \pm \frac{\hbar\tilde{\Omega}}{2}. \tag{3.51}$$

Figure 3.15 a) shows the eigenenergies of the dressed states $|\pm\rangle$ as a function of the detuning $\Delta$, showing a so-called 'avoided crossing´. The color coding illustrates the projection of the dressed states onto the excited state. In the limit of $\Delta \to -\infty$ the $|+\rangle$ state is given by the ground state, while in the limit of $\Delta \to \infty$ it is given by the excited state. The idea of the RAP is to chirp the detuning from a large negative value to a large positive value slowly enough to ensure that the atom stays in the same adiabatic state, thereby flipping its diabatic state from ground to excited state or vice versa. If the detunings are changed too quickly, the atom will tunnel through the gap of the avoided crossing and ends up in the other adiabatic state, not flipping its diabatic state. This is

know as a Landau-Zener transition and the probability of a transition $|\pm\rangle \rightarrow |\mp\rangle$ is given by the Landau-Zener formula[164]:

$$P_{\mathrm{LZ}} = \exp\left(-\frac{\pi\Omega^2}{2|\partial_t\Delta|}\right). \tag{3.52}$$

In the limit of $\Omega^2 \gg |\partial_t\Delta|$, the state population adiabatically follows the dressed state and is therefore transferred to the excited state. On the other hand, in the limit $\Omega^2 \ll |\partial_t\Delta|$, the population tunnels across the gap to the other dressed state and therefore stays in the ground state. Figure 3.15 a) shows the excited state fraction as a function of the detuning for different values of $\alpha = \partial_t\Delta/\Omega^2$. As the chirp velocity$v_{\mathrm{chirp}} = \partial_t\Delta$ increases compared to the Rabi frequency, the state transfer becomes incomplete. The chirp velocity experimentally can be conveniently controlled and therefore a fast RAP can be used to prepare samples with a certain ratio of ground and excited state atoms. Fig. 3.16 depicts the rapid adiabatic passage for different values of $\alpha = \partial_t\Delta/\Omega^2$ in the Bloch sphere representation.

## 3.5. Drifts of the Clock Laser Frequency

The stability of the clock laser relies on the stability of the length of the high finesse resonator that it is locked to (see sec. 1.7.4). The cavity spacer is placed inside a vacuum chamber and stabilized to the temperature of the CTE zero crossing of the spacer to minimize fluctuations due to temperature instability.
Nonetheless, the clock laser frequency is subject to drifts that can be described by a linear and a non-linear component. Due to material creep, the length of ULE made cavities slowly shrinks, and thereby causes a drift of the cavity's resonance frequency that is characterized by fractional frequency drift rates of $\dot{\Delta f}/f_0$ of typically $10^{-16}/s$ to $10^{-17}/s$ and shows day-to-day fluctuations on the order of $10^{-17}/s$ [179, 180]. On a timescales of days to weeks, the drift associated to material creep can be well described by a linear model [85] and in the experiment, we *a priori* compensate for a linear drift by continuously applying a slow frequency chirp to the RF-drive of an AOM in the clock laser system. A residual linear drift might be compensated for, *a posteriori*, when analyzing the spectroscopic data. Nevertheless, it is more convenient to account for the linear drift directly by the *a priori* drift compensation, as otherwise the frequency windows used for spectroscopy have to be constantly adapted. To quantify the drift of the clock laser frequency and to find the right settings of the linear drift compensation, it is necessary to measure the clock laser frequency against the atomic resonance on a timescale of many hours or ideally days. Figure 3.17 shows a measurement of the atomic clock resonance over the course of 17 hours. Figure 3.17 a) shows exemplary spectra obtained for a spin balanced gas of $^{171}$Yb at different magnetic fields. Two distinct spectroscopic features correspond to atoms at singly occupied lattice sites in either $m_F = 1/2$ or $m_F = -1/2$. The spectra are fitted by the sum of two sinc$^2$ functions according to eq. 3.12 to determine the resonance positions $f_\downarrow$ and $f_\uparrow$. Given the resonance positions of the two $m_F$ states the actual magnetic field $B$ can be calibrated according to $B = (f_\uparrow - f_\downarrow) / (-399.0(1)\,\mathrm{Hz/G})$ [68]. The clock laser detuning with respect to th the clock resonance frequency $f_0$ (at zero

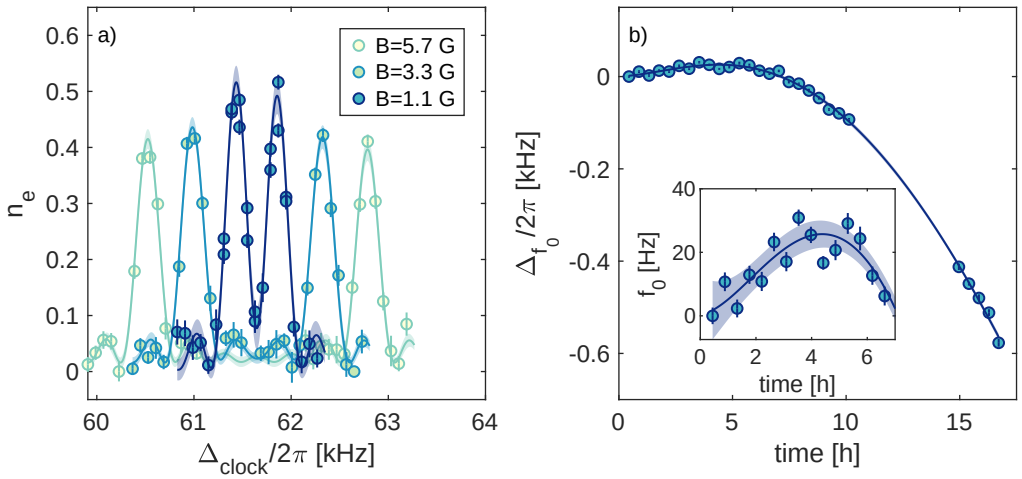


**Figure 3.17.:** Analysis of the clock laser frequency drifts. Panel a) shows spectra of a two spin component gas of $^{171}$Yb at different magnetic fields. Atoms are excited using pulses of clock laser light with a pulse length of $t_{\text{pulses}} = 3.2\,\text{ms}$ at a Rabi frequency of $\Omega = 2\pi \times 153(3)\,\text{Hz}$. Data points represent single measurements with error bars representing the uncertainty of the excited-state fraction. The two spectroscopic features correspond to atoms at singly occupied lattice sites in the $m_F = \pm 1/2$ and are fitted using the sum of two sinc$^2$ functions, indicated by solid lines. Shaded areas represent the 95% confidence intervals of the fits. Panel b) shows the clock laser detuning with respect to the clock resonance frequency at zero magnetic field $\Delta_{f_0} = -1/2(f_\uparrow + f_\downarrow)$, obtained from spectra as shown in panel a) measured over the course of 17 hours. Detunings are given with respect to the first data point of the measurement. Each data point corresponds to the resonance frequency obtained from a single spectrum. Error bars indicate the propagated fit uncertainty. Due to technical reasons, no data was recorded between $t \approx 10\,\text{h}$ and $t \approx 15\,\text{h}$.

magnetic field) $\Delta_{f_0} = f_{\text{laser}} - f_0$ is obtained by:

$$\Delta_{f_0} = -1/2(f_\uparrow + f_\downarrow). \tag{3.53}$$

Figure 3.17 b) shows $\Delta_{f_0}$ measured over the course of 17 hours. The drift shows a distinct time dependence, that is be modeled by:

$$\Delta_{f_0}(t) = \Delta_{f_0,0} + \Delta_{\text{drift,lin}}(t) + \Delta_{\text{comp}}(t) + \Delta_{\text{drift,non-lin}}(t). \tag{3.54}$$

Here $\Delta_{f_0,0}$ describes $\Delta_{f_0}$ at $t = 0$, the linear drift of the cavity is $\Delta_{\text{drift,lin}}(t) = c_{\text{lin}}t$ and $\Delta_{\text{comp}}(t) = c_{\text{comp}}t$ denotes the *a priori* linear drift compensation applied during the measurement and has been set to $\Delta_{\text{comp}}(t) = -0.1632\,\text{Hz/s}\cdot t$. The non-linear drift is described by $\Delta_{\text{drift,non-lin}}(t)$. While for the first seven hours of the measurement, shown in the inset of fig. 3.17 b), the measured detunings are characterized by an RMS of 9 Hz, for longer time scales the measured detuning $\Delta_{f_0}$ continously increases. In a prior measurement, correlations between temperature fluctuations on the order of $\Delta T = \pm 50\,\text{mK}$, measured on the outer side of the vacuum chamber of the cavity-1 setup, and drifts of the cavity resonance frequency on the order of 1 kHz have been found [85]. Therefore, we associate the large drift observed in fig. 3.17 to a response of the cavity to a temperature change. According to ref. [85] close to the temperature of the CTE zero $T_{\text{CTE,ZC}}$ crossing, the shift

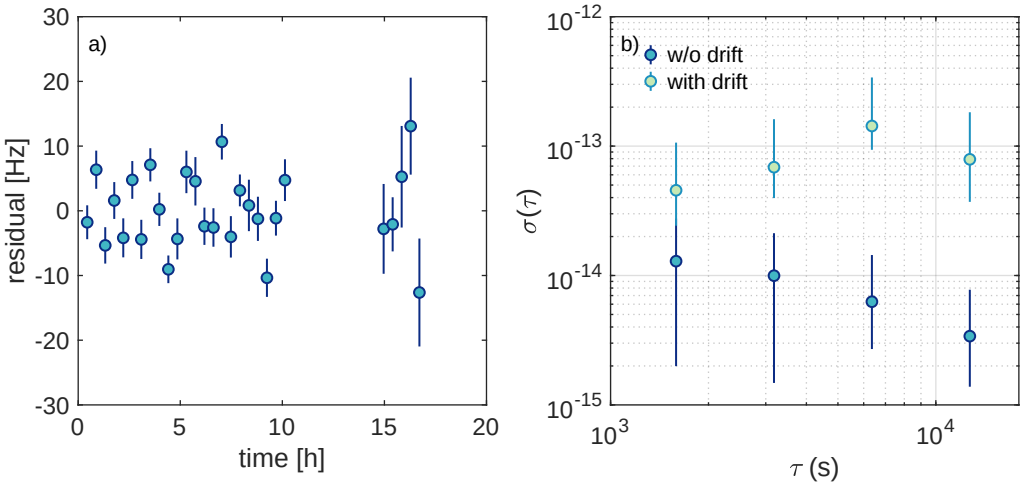


**Figure 3.18.:** Residual drift of the clock laser frequency. Panel a) shows residuals of the fit used to describe the measured clock laser detuning at the atomic resonance $\Delta_{f_0}$, presented in fig. 3.17.Panel b) shows the overlapped Allan deviation of the fractional frequency as a fucntion of averaging time $\tau$ for the data shown in fig. 3.17 and the residuals after subtraction of systematic drifts (see text for details). The Allan deviations have been computed using ref.[181].

of the resonance frequency caused by a change of temperature can be described by:

$$\Delta\nu(t) \propto -(T_{\mathrm{cav}}(t) - T_{\mathrm{CTE,ZC}})^2 \tag{3.55}$$

Using an exponential ansatz for the time dependence of the cavity temperature $T(t) = \Delta T e^{-(t-t_0)/\tau}$, the time-dependent shift of the resonance frequency has the form [85]:

$$\Delta\nu(t) = c_1 e^{-2(t-t_0)/\tau} + c_2 e^{-(t-t_0)/\tau} + \nu_0 \tag{3.56}$$

We fit eq. 3.54 to the measured data, using eq. 3.56 as an ansatz for the non-linear drift $\Delta_{\mathrm{drift,non\text{-}lin}}(t)$. We obtain the linear and non-linear drift coefficients $c_{\mathrm{lin}}$ and $c_{\mathrm{nlin}}$ as well as the time constant $\tau$. The fit is shown in fig. 3.17 b), whereas the residuals of the fit are shown in fig. 3.18. The data is well described by the fit and the residuals show an RMS of 6 Hz. The linear drift rate of the cavity resonance is determined to be $c_{\mathrm{lin}} = 0.1168(8)$ Hz/s, which yields a frequency drift of 10.1(1) kHz/day. Given the absolute frequency of the clock transition[1] [134] this corresponds to a fractional frequency drift of $\Delta\dot{\nu}/\nu = 2.2 \times 10^{-16}/s$. In a previous measurement, shortly after the rebuilt of the cavity-1 setup in September 2016, the linear drift of the cavity resonance has been characterized and found to be $c_{\mathrm{lin}} = 0.318(1)$ Hz/s. The measurement presented here, has been conducted in October 2019, and hence indicates a reduction of the linear drift by a factor of approximately 0.4 over the course of three years. The time constant of the temperature equillibration $\tau_{\mathrm{cav}}$ here is found to be $\tau_{\mathrm{cav}} = 10.31(15)$h. Figure 3.18 b) shows the overlapping Allan deviation (see e.g. ref. [182] for a detailed description of the Allan deviation) calculated for the frequency data shown in fig. 3.17 before and after the subtraction of systematic drifts. The Allan deviation increases for the uncorrected data

[1] Here we assume for simplicity that the measured frequency corresponds to the bare atomic transition.

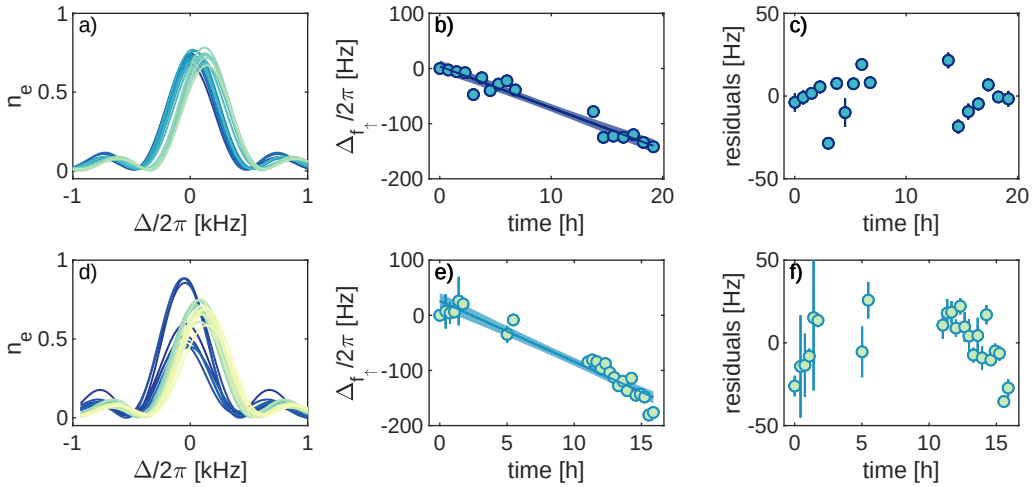


**Figure 3.19.:** Long-term measurement of the resonance frequency $f_\uparrow$ of the $|g,\uparrow\rangle \rightarrow |e,\uparrow\rangle$ at a magnetic field of $B = 16.5\,\mathrm{G}$. Panel a) and c) shows fits of spectra recorded on two different days over the course 20 and 17 hours, respectively Panel b) and d) shows the clock laser detuning at the resonance obtained from the individual spectra shown in panel a) and c) as a function of time. Solid lines indicate fits of a linear model, with shaded areas representing 95% confidence intervals of the fits. The residuals of the fits are shown in panels c) and f).

for increasing averaging time, while for the data that has been corrected for a systematic drift shown in fig. 3.18 a) the Allan deviation decreases from $\sigma = 1.3 \times 10^{-14}$ at an averaging time of $\tau = 1590\,\mathrm{s}$ to $\sigma = 3.4 \times 10^{-15}$ at an averaging time of $\tau = 12720\,\mathrm{s}$. However, the data set is small, and therefore these values should be taken with care. Due to the long cycle time of the experiment ( in this measurement $t_{\mathrm{cycle}} = 53\,\mathrm{s}$), it takes about half an hour to record a single spectrum. In comparison, atomic lattice clocks do not require evaporative cooling and the experimental cycle is much faster. In ref.[183] cycle times of $t_{\mathrm{cycle}} < 0.5\,\mathrm{s}$ are reported, which allow acquiring 100 times more data in the same time. Figure 3.19 a) to c) and d) to f) shows two different long-term measurements of the $m_F = +1/2$ resonance frequency. The measurements have been conducted several weeks after the measurement presented in fig. 3.17 and in the meantime care has been taken to keep the clock laser in lock as much as possible and to minimize disturbances to the cavity setup. The *a priori* drift compensation has been set to $\Delta_{\mathrm{comp}}(t) = -0.1118\,\mathrm{Hz/s}\,t$. Fig. 3.19 a) (d)) shows the fits of 17 (36) spectra recorded over the course of approximately 20 (17) hours. Fig. 3.19 b) (e)) shows the clock laser detuning at the resonance frequency $f_\uparrow$of the $|g,\uparrow\rangle \rightarrow |e,\uparrow\rangle$ transition, obtained from the fits of the spectroscopic feature shown in panel a) (d)) as a function of time. The detuning increases over time and a linear increase is fitted to the data as indicated by the different colors in fig. 3.19 b). We obtain residual linear drift rates of $c_{\mathrm{lin,res}} = -0.0021(1)\,\mathrm{Hz/s}$ for the data shown in panel b) and $c_{\mathrm{lin,res}} = -0.0031(4)\,\mathrm{Hz/s}$ for the data shown in panel e), indicating that the drift is overcompensated by the *a priori* drift compensation. The measured residual drift rates correspond to total linear drifts of $c_{\mathrm{lin,res}} = 0.1097(1)\,\mathrm{Hz/s}$ and $c_{\mathrm{lin,res}} = 0.1087(1)\,\mathrm{Hz/s}$, respectively. The values are comparable to the linear drift of $c_{\mathrm{lin,res}} = 0.1168(8)\,\mathrm{Hz/s}$ found in the previously presented measurement and reflect the day-to-day fluctuations of

the drift rate. The measured values are in good agreement with the fluctuations of the fractional drift rate on the order of $10^{-17}/s$ expected according to ref. [180]. The residuals of the fits shown in fig. 3.19 c) and fig. 3.19 f) are characterized by an RMS of 12 Hz and 16 Hz, respectively.
To summarize, we have found that the clock laser frequency is subject to linear and non-linear drifts. A linear drift can be associated with a slow length change of the resonator caused by material aging. Temperature fluctuations cause non-linear drifts. On the timescale of days the clock laser frequency might drift non-linearly over several 100 Hz or more. However, on the time scale of a few up to 20 hours, the observed drift often is well approximated by a linear ansatz. Depending on the cycle time of the experiment and the desired span and resolution, it typically takes 20 to 45 minutes to record a single spectrum. After subtraction of systematic drifts, on this timescale we find residual non-linear fluctuations that are characterized by an RMS on the order of 10 Hz. Given the absolute frequency of the clock transition $\nu_{\mathrm{clock},171} = 518\,295\,836\,590\,865.2(0.7)$ Hz [134] this corresponds to an RMS of the fractional frequency on the $10^{-14}$ level. Constant monitoring and logging of the temperature of the cavity vaccum chamber could lead to a better understanding of the non-linear short-term and long-term drifts, and an improvement of the temperature stability would increase the frequency stability of the clock laser. On the other hand, the ultimate road to achieving better frequency stability is to actively stabilize the clock laser to the atomic resonance. Such an atomic clock operation constitutes a long-term goal, requiring online data evaluation of spectroscopic measurements and an almost entirely autonomous experiment operation.

## 3.6. Conclusion

In this chapter, I introduced the theoretical framework that allows describing clock spectroscopy on the ${}^1S_0 \rightarrow {}^3P_0$ transition in a magic optical lattice. The description starts with a simple two-level system and is extended to include damping due to spontaneous decay and decoherence. I have presented spectroscopic measurements with spin-polarized ytterbium gases of ${}^{171}$Yb and ${}^{173}$Yb in a magic optical lattice, driving either intra- or interband transitions. In a deep optical lattice, a minimal spectroscopic resolution, characterized by a spectroscopic linewidth of $\Gamma_{\mathrm{FWHM}} = 26.7(2.4)\,\mathrm{Hz}$, is reached. Combining clock spectroscopy and bandmapping techniques, the spectroscopic dispersion relation in shallow optical lattice is observed directly. The data analysis shows good agreement between the observed spectroscopic lineshapes and a simple model combining a two-level system with the dispersion relation of an optical lattice. High-fidelity excited-state preparation can be achieved using a rapid adiabatic passage. Finally, the frequency of the cavity-stabilized clock laser has been measured against the atomic resonance. An analysis of the observed frequency drift yields a linear drift of approximately 110 mHz/s, that is associated with material aging. After the subtraction of a systematic drift, fluctuations of the clock laser frequency show an RMS on the level of 10 to 20 Hz, corresponding to an RMS of the fractional frequency of $10^{-14}$.

# 4. Clock Spectroscopy of Interacting Fermi Gases and Fermi-Fermi Mixtures

In the previous section, I presented spectroscopic measurements conducted mainly with spin-polarized ytterbium quantum gases on the ${}^1S_0 \rightarrow {}^3P_0$ clock transition. A spectroscopic linewidths on the order of $\Gamma_{\mathrm{FWHM}} \sim 30\,\mathrm{Hz}$ has been achieved and the lattice system was characterized by the means of clock spectroscopy.
Spin-polarized gases in optical lattices are non-interacting, as the Pauli principle precludes any double occupancy. Adding a second species realized by either another spin component or another isotope or element lifts this restriction and allows for double occupancy. Atoms at the same lattice site interact via $s$-wave scattering and therefore experience an energy shift according to the Hubbard on-site interaction $U$. The intra- and interisotope s-wave interactions of ytterbium atoms in the ground state ${}^1S_0$ have been studied using two-color photo-association in early experiments of the Kyoto group [118]. Here, we study interorbital two-body interactions between atoms in the ground and excited state. In comparison clock resonance frequency of atoms at singly occupied lattice sites, the resonance that corresponds to the excitation of an atom that resides at a doubly occupied lattice site is shifted by $\Delta f = (U_{eg} - U_{gg})/h$. High precision clock spectroscopy allows resolving and characterizing these interaction shifts.
While atom pairs of different isotopes constitute two distinguishable Fermions, pairs of the same isotope constitute two indistinguishable Fermions and therefore require a totally antisymmetric wave-function that can be realized by either an orbital symmetric spin singlet or an orbital antisymmetric spin triplet state. Each of those states is characterized by its own molecular potential, giving rise to an interorbital spin-exchange interaction. Here we study interorbital interactions of atom pairs in interacting doubly spin-polarized Fermi-Fermi mixtures of ${}^{171}$Yb and ${}^{173}$Yb and two spin component gases Fermi of ${}^{171}$Yb. Whereas interorbital spin-exchange interactions have previously been studied in gases of ${}^{173}$Yb [57, 58] and ${}^{87}$Sr [61, 184] it has rather recently been studied in ${}^{171}$Yb [2, 62, 68].

This section is divided into two parts. In sec. 4.1 I will present measurements of interorbital interisotope interactions in Fermi-Fermi mixtures of ${}^{171}$Yb and ${}^{173}$Yb. We directly show the $\mathrm{SU}(2) \otimes \mathrm{SU}(6)$ symmetry of the interaction and characterize the lifetimes of the interorbital interisotope pairs.
In sec. 4.2 I will present measurements of interorbital interactions in two spin-component gases of ${}^{171}$Yb. The direct and spin-exchange part of the interorbital interaction is spectroscopically determined and we confirm its antiferromagnetic nature, which has been observed in recent experiments by the Kyoto and Munich group [62, 68].

The measurements of the interorbital interisotope interactions have been performed and analyzed by K. Sponselee and the author. A first series of measurements has been conducted by K. Sponselee, M. Diem, N. Pintul and the author.
A first series of measurements of the spin-exchange interaction in $^{171}$Yb has been conducted and analyzed by K. Sponselee, M. Diem and the author. The final measurements shown here have been conducted by K. Sponselee and M. Diem and the author with the help of N. Pintul. Data analysis has been performed by K. Sponselee and the author.

The main results of this chapter have been published in [2].

## 4.1. Interorbital Interactions in an Ytterbium Fermi-Fermi Mixture with SU(2) ⊗ SU(6) Symmetry

Over the past decades mixtures of ultracold atomic gases realized by atoms in different hyperfine states [185–188], different isotopes [114, 189–191], different elements[192–198] and different orbital states [57, 184, 199] have been used to study intriguing physics such as the formation of hetero-nuclear [195] and dipolar molecules [200–202], polaronic quasi-particles [203–206] or interaction-induced insulating phases [200, 207–211] and quantum magnetism [128, 212, 213]. For quantum simulations of solid-state models it is usually desirable to work with (effective) spin 1/2 systems to mimic the behavior of electrons. Ultracold atoms, however, are not restricted to spin 1/2 systems and therefore allow to study high spin systems. Ultracold gases of $^{40}$K with ($F = 9/2$) have been used to observe spin changing dynamics[214, 215], while for alkaline earth(like) elements such as ytterbium ( with $I = 5/2$ for$^{173}$Yb) and strontium ($I = 9/2$ for $^{87}$Sr) the ground state s-wave interaction shows a SU($\mathcal{N} = 2I + 1$) symmetry, characterized by the absence of spin changing collisions. Fermi-Fermi mixtures of $^{171}$Yb and $^{173}$Yb as first realized by the Kyoto group [115] exhibit an exotic SU(2) ⊗ SU(6) symmetry and might be useful to study two-flavor symmetry locking phases [79, 80].
Here we study elastic and inelastic interorbital interactions of Fermi-Fermi gases of $^{171}$Yb-$^{173}$Yb. Therefore we prepare doubly spin polarized gases of typically $N_{171/173} \approx (10 - 40) \times 10^3$ atoms at temperatures of $T \approx (0.25 - 0.55)T_F$ in a magical optical lattice. By the means of resonant optical pumping we prepare different spin configurations, that are in the following denoted as $|g, m_{F,171}; g, m_{F,173}\rangle$.

### 4.1.1. Elastic Interactions

To probe the elastic interorbital interactions we perform spectroscopy on the clock transition of $^{171}$Yb or $^{173}$Yb, using rectangular $\pi$ pulses of $t_{\text{pulse}} = 1.6\,\text{ms}$ or $t_{\text{pulse}} = 1.55\,\text{ms}$ that yield a Fourier limited spectroscopic linewidth of $\Gamma_{\text{FWHM}} \approx 500\,\text{Hz}$ and $\Gamma_{\text{FWHM}} \approx 516\,\text{Hz}$, respectively. Figure 4.1 a) shows exemplary spectra of doubly spin-polarized gases prepared in the $|g, -1/2; g, 5/2\rangle$ configuration, for spectroscopy on the clock transition of $^{171}$Yb for different 1D-lattice depths. The three different observed spectroscopic features are attributed to single atoms of $^{171}$Yb, interacting interisotope pairs excited to the state $|e, -1/2; g, 5/2\rangle$ and single atoms of $^{171}$Yb that are excited to the second band of the optical lattice. The resonance frequency of the blue sideband depends on the lattice depth and is used to determine $s_{1\text{D}}$ for each individual spectrum. The interaction induced energy shift of the interorbital interisotope pairs can be expressed in terms of Hubbard on-site interactions:

$$\Delta^{171}_{173}U_{eg} = {}^{171}_{173}U_{eg} - {}^{171}_{173}U_{gg} \tag{4.1}$$

and

$$\Delta^{171}_{173}U_{ge} = {}^{171}_{173}U_{ge} - {}^{171}_{173}U_{gg}. \tag{4.2}$$

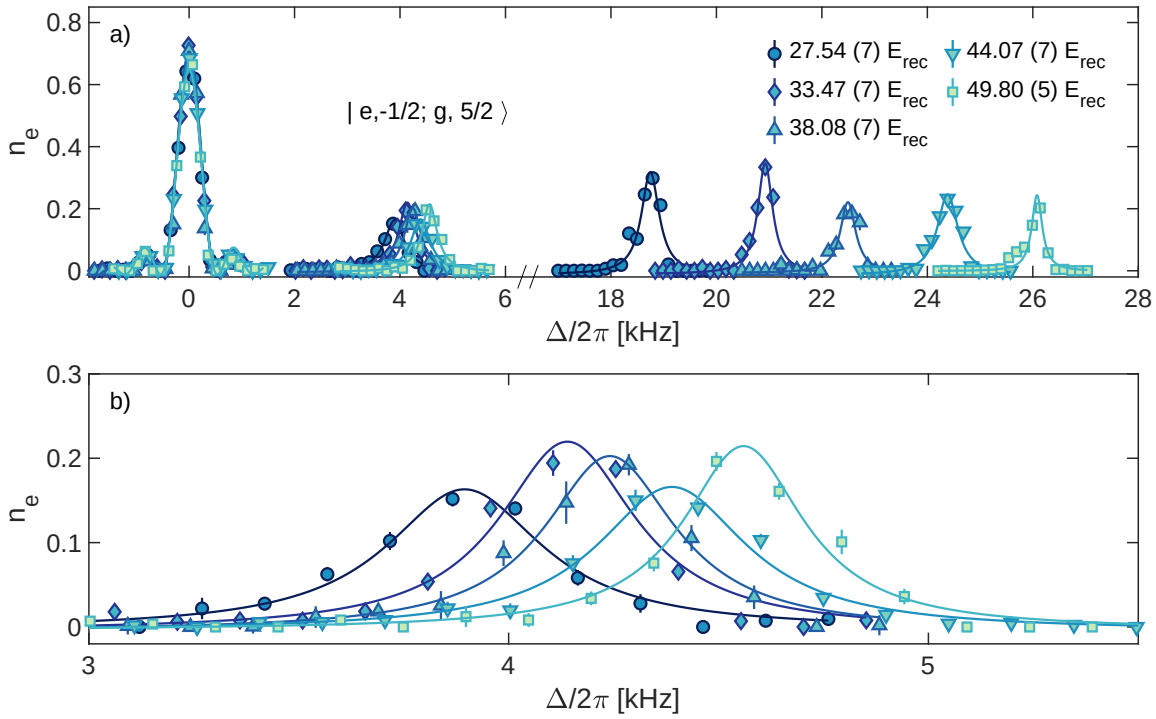


**Figure 4.1.:** Clock spectra of an interacting Fermi-Fermi mixture for different 1D lattice depths driving the clock transition of $^{171}$Yb. Panel a) shows a complete spectrum with three spectroscopic features corresponding to singly occupied lattice sites, doubly occupied sites shifted by the interorbital interisotope interaction and singly occupied lattice sites that are excited to the second Bloch band of the 1D-lattice. Panel b) shows the interorbital interisotope interaction feature in detail a detailed view. Frequencies are given with respect to the non-band changing transition of single atoms. The frequency offset of the blue motional sideband is used to determine the lattice depth of the 1D-lattice. Solid lines indicate fits using a sinc$^2$ model for the non band changing transition and Lorentzians otherwise. The non-band changing single particle resonance is used for an *a posteriori* drift compensation. The 2D-lattice was operated at a depth of$s_{2D} = 16.971(15)\, E_{rec}$, whereas a magnetic field of $B = 8.8\,$G was applyed in the vertical direction. The figure is adapted from the published version [2]. ©2021 American Physical Society.

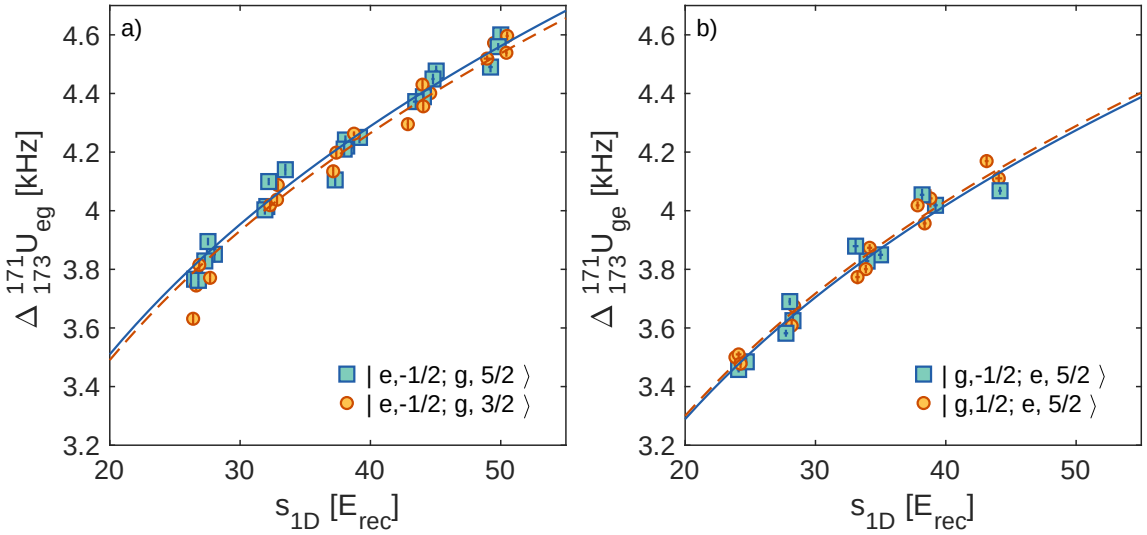


**Figure 4.2.:** Interorbital interisotope interaction shift $\Delta^{171}_{173}U_{\mathrm{eg}}$ (panel a)) and $\Delta^{171}_{173}U_{\mathrm{ge}}$ (panel b)) as a function of the 1D lattice depths. Solid and dashed lines respectively show fits of equation 4.3 to the data leaving the inte-orbital interisotope $s$- wave scattering lengths as a free parameter. Every data point represents the interaction shift obtained from a single spectrum, as shown in figure 4.1. Error bars representing the uncertainty in determining the interaction shifts and the 1D-lattice depths from the spectra are smaller than the marker size. For the measurements presented in panel a) the 2D-lattice was operated at $s_{2\mathrm{D}} = 16.971(15)\, E_{\mathrm{rec}}$, whereas for the measurements in panel b) it was operated at a depth of $s_{2\mathrm{D}} = 16.13(17)\, E_{\mathrm{rec}}$. The figure is adapted from the published version [2]. ©2021 American Physical Society.

Here and throughout this section the notation ${}^{171}_{173}X_{ij}$ corresponds to the quantity $X$ for an atom of $^{171}$Yb in orbital state $i$ and an atom of $^{173}$Yb in orbital state $j$. $U$ denotes the Hubbard on-site interaction given by [2]:

$$ {}^{171}_{173}U_{ij} = \frac{4\pi\, {}^{171}_{173}a_{ij}}{2\mu} \int d\boldsymbol{r} |w_0(s_{1\mathrm{D}}, s_{2\mathrm{D}}, \boldsymbol{r})|^4, \tag{4.3} $$

where ${}^{171}_{173}a_{ij}$ denotes the $s$-wave scattering length, $\mu$ the reduced mass of the atom pair and $w_0(s_{1\mathrm{D}}, s_{2\mathrm{D}})$ denotes the single particle Wannier function.
The single-particle resonance frequency for atoms trapped in a magic lattice is not affected by the lattice depth, whereas we observe a shift to higher resonance frequencies for the two-particle transition as the lattice depth increases. This is associated with an increasing Wannier integral and underlines the two-particle nature of the transition. To characterize the interaction, we perform spectroscopic measurements at different 1D-lattice depths. From the observed interaction-induced shift, we deduce the $s$-wave scattering length connected to the interorbital interisotope interaction using eq. 4.3.

Figure 4.2 shows interaction shifts measured in doubly polarized Fermi-Fermi mixtures in different spin configurations as a function of the 1D lattice depth. Panel a) shows data obtained exciting $^{171}$Yb whereas panel b) shows data obtained when exciting $^{173}$Yb. By fitting the lattice depth dependence of $\Delta^{171}_{173}U_{\mathrm{eg}}(s_{1\mathrm{D}})$ and $\Delta^{171}_{173}U_{\mathrm{ge}}(s_{1\mathrm{D}})$ according to eq. 4.3 we obtain the differential $s$-wave scattering lengths, $\Delta^{171}_{173}a_{\mathrm{e,-1/2;g,5/2}} = 498(1)\, a_0$ and

$\Delta^{171}_{173}a_{\mathrm{e,-1/2;g,3/2}} = 495.7(1.3)\,a_0$, when exciting $^{171}$Yb and $\Delta^{171}_{173}a_{\mathrm{g,-1/2;e,5/2}} = 481.3(1.8)\,a_0$ and $\Delta^{171}_{173}a_{\mathrm{g,1/2;e,5/2}} = 482.9(1.3)\,a_0$, when exciting $^{173}$Yb. (The measured differential interaction parameters are summarized in tab. 4.1.) Within experimental uncertainty the pairs of scattering lengths corresponding to $^{171}_{173}U_{\mathrm{eg}}$ and $^{171}_{173}U_{\mathrm{ge}}$ are equal, and indicate a symmetry of the interaction. For the $^{171}$Yb-$^{173}$Yb Fermi-Fermi mixture there are as many as twelve different combinations of atoms in different $m_F$ states, that in general could be characterized by different interorbital interisotope interactions. Due to the close-to-perfect decoupling of nuclear spin and electronic angular momentum in the involved states $^1S_0$ and $^3P_0$, however, we expect the interaction to obey an $SU(2) \otimes SU(6)$ symmetry and be equal for all $m_F$ configurations. In the following I will argue that it is sufficient to probe two different spin configurations to show the SU(2) $\otimes$ SU(6) symmetry of the interaction.

The Hamiltonian of the underlying rotationally symmetric $s$-wave interaction commutes with the total spin operator $F^2$. The total spin operator $\boldsymbol{F} = \boldsymbol{f}_1 + \boldsymbol{f}_2$ and the magnetization along the z-axis $M = m_1 + m_2$ are given by the sum of the total spins of the individual atoms $f_{1,2}$ and the spin components along the $z$-axis $m_{1,2}$. The interaction Hamiltonian hence can be written in terms of eigenfunctions $|F, M\rangle$ of the operator $F^2$ [91]:

$$\mathcal{H}_{\mathrm{int}} = \frac{2\pi\hbar}{2\mu}\delta\left(\boldsymbol{r}_1 - \boldsymbol{r_2}\right) \sum_{F=F_{\mathrm{min}}}^{F_{\mathrm{max}}} \sum_{M=-F}^{+F} a_F \left|F, M\right\rangle \left\langle F, M\right| . \tag{4.4}$$

Here $\delta\left(\boldsymbol{r}_1 - \boldsymbol{r_2}\right)$ denotes the Dirac $\delta$ functions for atoms at positions $\boldsymbol{r_1}$ and $\boldsymbol{r_2}$, while $a_F$ denotes the $s$-wave scattering wavelength corresponding to a scattering channel with quantum number $F$, that in general is different for different total spins $F$. In the experiment however we observe and prepare atoms in the magnetization basis $|m_1, m_2\rangle$ that is connected to the interaction basis by a basis transformation[2]:

$$\left|m_1, m_2\right\rangle = \sum_{m_1+m_2=M} c^{F,M}_{m_1,m_2} \left|F, M\right\rangle . \tag{4.5}$$

Here the summation is carried out over all states $|F, M\rangle$ with $M = m_1 + m_2$ and the coefficients $c^{F,M}_{m_1,m_2}$ denote the corresponding Clebsch-Gordan coefficients. For Fermi-Fermi mixtures of $^{171}$Yb and $^{173}$Yb with $f_1 = 1/2$ and $f_2 = 5/2$ there are only two possible scattering channels characterized by a total spin quantum number of $F = 2$ and $F = 3$. According to eq. 4.5 it is therefore sufficient to show that for two different spin configurations $|m_1, m_2\rangle$ and $|m_1', m_2'\rangle$ the interaction strength is equal, to prove the SU(2) $\otimes$ SU(6) symmetry. The two different spin configurations can be chosen almost arbitrarily, yet at least one spin configuration has to be a superposition of $F = 3$ and $F = 2$ states with two non-vanishing Clebsch-Gordan coefficients.

To probe the SU(2) $\otimes$ SU(6) symmetry for both interaction parameters $^{171}_{173}U_{\mathrm{eg}}$ and $^{171}_{173}U_{\mathrm{ge}}$ we therefore perform interaction spectroscopy on the clock transition of $^{171}$Yb for gases in the spin configurations:

$$\left|-1/2; 5/2\right\rangle = \sqrt{\frac{1}{6}}\left|3, 2\right\rangle - \sqrt{\frac{5}{6}}\left|2, 2\right\rangle \tag{4.6}$$

$$\left|-1/2; 3/2\right\rangle = \sqrt{\frac{1}{3}}\left|3, 1\right\rangle - \sqrt{\frac{2}{3}}\left|2, 1\right\rangle \tag{4.7}$$

| | $^{171}$Yb$_e$-$^{173}$Yb$_g$ | $^{171}$Yb$_g$-$^{173}$Yb$_e$ |
|---|---|---|
| $\Delta a_{-1/2,5/2}$ | 498(1) | 481.3(1.8) |
| $\Delta a_{-1/2,3/2}$ | 495.7(1.3) | |
| $\Delta a_{1/2,+5/2}$ | | 482.9(1.3) |
| $\Delta a_2$ | 501.2(2.5) | 481(2) |
| $\Delta a_3$ | 485(8) | 482.9(1.3) |
| $\Delta \bar{a}$ | 497.4(8) | 482(1) |
| $\bar{a}$ | -83(60) | -98(60) |

**Table 4.1.:** Summary of the elastic interaction parameters measured for $^{171}$Yb$_e$-$^{173}$Yb$_g$ and $^{171}$Yb$_g$-$^{173}$Yb$_e$ in different spin configurations in units of Bohr radii $a_0$.

and on the clock transition of $^{173}$Yb for gases in the spin configurations:

$$|-1/2;5/2\rangle = |3,3\rangle \tag{4.8}$$

$$|1/2;5/2\rangle = \sqrt{\frac{1}{6}}\,|3,2\rangle - \sqrt{\frac{5}{6}}\,|2,2\rangle \tag{4.9}$$

for various 1D lattice depths. Using eqs.4.6-4.7 and eqs. 4.8-4.9,respectively and the interaction shifts measured for the different spin configurations we compute the scattering lengths $a_2$ and $a_3$ that characterize the interorbital interisotope interactions. For the $^{171}$Yb$_e$-$^{173}$Yb$_g$ interaction we find: $\Delta a_2 = 501.2(2.5)\,a_0$ and $\Delta a_3 = 485(8)\,a_0$, whereas for the $^{171}$Yb$_g$-$^{173}$Yb$_e$ interaction we find: $\Delta a_2 = 481(2)\,a_0$ and $\Delta a_3 = 482.9(1.3)\,a_0$. For both interactions the values obtained for $a_2$ and $a_3$ are equal within experimental uncertainties, therefore proving the SU(2) $\otimes$ SU(6) symmetry of the interactions.
The mean scattering lengths for the two different interorbital interactions of $\Delta^{171}_{173}\bar{a}_{eg} = 497.4(8)\,a_0$ and $\Delta^{171}_{173}\bar{a}_{ge} = 482(1)\,a_0$ are similar but not identical. While the different ground state interisotope interactions for different ytterbium isotope pairs are well explained by a mass-scaling model[118], the observed differences of the interorbital interactions cannot be explained in this way, as the reduced mass is the same. Therefore, our measurements could prove valuable for further studies of the molecular potential, that go beyond mass scaling.
To underline the precision of our spectroscopic measurements we have given differential values for interaction shifts and $s$-wave scattering lengths. Using the literature value for the $s$-wave scattering length of the interisotope ground-state interaction $a_{gg} = -580(60)\,a_0$ [118], for the absolute values of the interorbital interisotope scattering lengths we obtain mean values of $^{171}_{173}\bar{a}_{eg} = -83(60)\,a_0$ and $^{171}_{173}\bar{a}_{ge} = -98(60)\,a_0$, corresponding to attractive interactions.

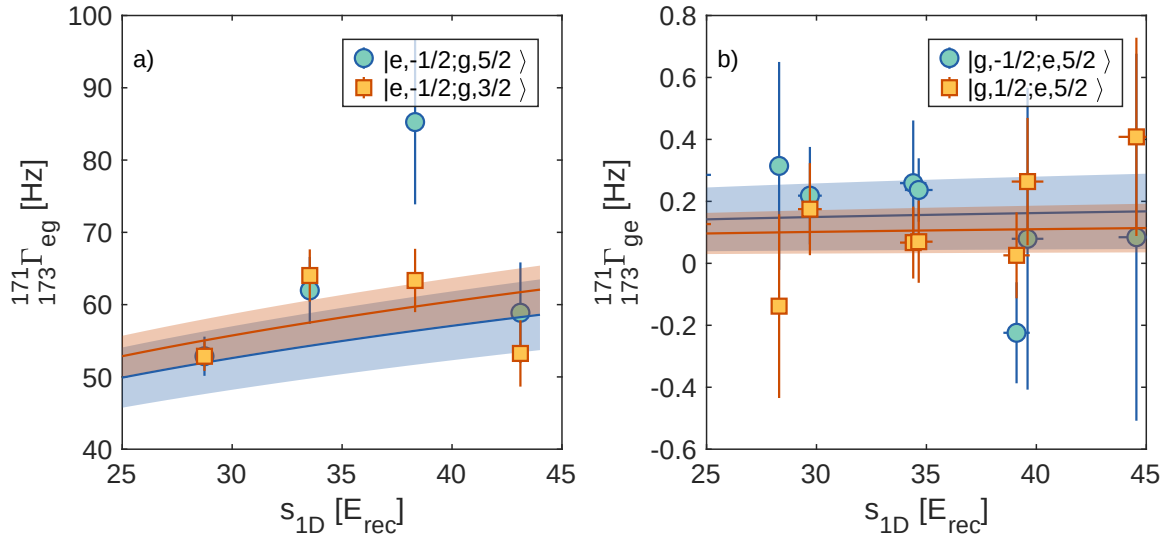


**Figure 4.3.:** Loss rates of the interorbital interisotope pairs. Panel a) shows the data obtained for $^{171}\mathrm{Yb_e} - ^{171}\mathrm{Yb_g}$, panel b) for $^{171}\mathrm{Yb_g} - ^{171}\mathrm{Yb_e}$. Different colors denote different spin configurations. Each data point is averaged several times and error bars indicate the propagated fit uncertainty. Solid lines indicate a fit to eq. 4.10. Shaded areas indicate 95% confidence intervalls. For the measurements presented in panel a) the lattices were operated at depths of $s_{1D} = 24.0(2)\, E_{rec}$ and $s_{2D} = 16.0(1)\, E_{rec}$. For the measurements presented in panel b) the lattices were operated at depths of $s_{1D} = 34.7(6)\, E_{rec}$ and $s_{2D} = 17.0(4)\, E_{rec}$. For the measurements The figure is adapted from the published version [2]. ©2021 American Physical Society.

### 4.1.2. Inelastic Interactions

To characterize the inelastic part of the different interorbital interisotope interactions, we excite atom pairs using pulses of clock laser light and observe the number of atoms in the excited state, that equals the number of doublons $N_d(t)$ as a function of hold time. The observed decay of $N_d(t)$ is fitted using an exponential ansatz: $N_d(t) = N_{d,0} \exp(-\Gamma_{int} t)$, leaving the initial number of doublons $N_d$ and the decay rate $\Gamma_{int}$ as free parameters. Analogue to the measurement of the elastic interactions, we repeat the measurement for different 1D lattice depths and obtain a decay rate $\Gamma_{int}$ for each lattice depth. To distinguish between one-body and two-body decay we characterize the one body decay rate by measuring the lifetime of excited-state atoms on singly occupied lattice sites $\Gamma_0$. The two body decay rate is then given by $^{171}_{173}\Gamma_{eg/ge} = \Gamma_{int} - \Gamma_0$ and is connected to the inelastic loss coefficient $^{171}_{173}\beta_{eg/ge}$ by:

$$^{171}_{173}\Gamma_{eg/ge} = ^{171}_{173}\beta_{eg/ge} \int d\boldsymbol{r} |w_0(s_{1D}, s_{2D})|^4. \tag{4.10}$$

We fit eq. 4.10 to the data and obtain the two inelastic loss coefficients $^{171}_{173}\beta_{eg} = 1.69(7) \times 10^{-12}\,\mathrm{cm^3 s^{-1}}$ and $^{171}_{173}\beta_{eg} = 1.79(5) \times 10^{-12}\,\mathrm{cm^3 s^{-1}}$ for the two different spin configurations $|e, -1/2; g, 5/2\rangle$ and $|e, -1/2; g, 3/2\rangle$. For the $^{171}\mathrm{Yb_g}$–$^{173}\mathrm{Yb_e}$ mixture in the configurations $|g, 1/2; e, 5/2\rangle$ and $|g, -1/2; e, 5/2\rangle$ we obtain $^{171}_{173}\beta_{ge} = 3(1) \times 10^{-15}\,\mathrm{cm^3 s^{-1}}$ and $^{171}_{173}\beta_{ge} = 4.6(7) \times 10^{-15}\,\mathrm{cm^3 s^{-1}}$. (To give an overview, the values are summarized in tab. 4.2.) The inelastic loss coefficients for different spin configurations of $^{171}\mathrm{Yb_e} - ^{171}\mathrm{Yb_g}$ and

| | $^{171}\mathrm{Yb_e}$-$^{173}\mathrm{Yb_g}$ | $^{171}\mathrm{Yb_g}$-$^{173}\mathrm{Yb_e}$ |
|---|---|---|
| $\beta_{-1/2,5/2}$ | $1.69(7) \times 10^{-12}$ | $3(1) \times 10^{-15}$ |
| $\beta_{-1/2,3/2}$ | $1.79(5) \times 10^{-12}$ | |
| $\beta_{1/2,+5/2}$ | | $4.6(7) \times 10^{-15}$ |

**Table 4.2.:** Summary of the inelastic loss coefficients measured for $^{171}\mathrm{Yb_e}$-$^{173}\mathrm{Yb_g}$ and $^{171}\mathrm{Yb_g}$-$^{173}\mathrm{Yb_e}$ in different spin configurations in units of $\mathrm{cm}^3\, s^{-1}$.

$^{171}\mathrm{Yb_g} - ^{171}\mathrm{Yb_e}$ are the same within experimental uncertainties, however, different from the case of elastic interactions this does not allow to infer the symmetry of the inelastic interactions. The loss coefficients for the orbital configuration $^{171}\mathrm{Yb_e} - ^{171}\mathrm{Yb_g}$ are larger than the loss coefficients of $^{171}\mathrm{Yb_g} - ^{171}\mathrm{Yb_e}$ by a factor of about 400. Which is in contrast to the elastic interactions that we have found to be similar. The reason for the large difference of the loss coefficients is currently unclear. Understanding the decay mechanism and the molecular potentials requires further experimental and theoretical work.

### 4.1.3. Coherent Addressing of Interisotope Pairs

In another set of experiments, we study the coherence properties of Rabi oscillations driven on the clock transition of single atoms and interisotope pairs. As discussed in chapter 3 the coupling of a two-level system to a (thermal) bath causes decoherence. In general, the specific origin of decoherence is hard to identify as possible sources are manifold. However, clock spectroscopy in the ytterbium Fermi-Fermi mixture allows comparing the coherence properties of two distinctly different systems: atoms at singly occupied lattice sites and interacting interisotope pairs.

For one-dimensional optical lattice clocks it has been shown that elastic interactions between ground and excited-state atoms cause a collisional shift of the clock transition and collisional dephasing decreases the coherence properties [178]. As interactions increase with increasing density for an optimal operation of a one-dimensional optical lattice clock, the atom number is limited [178].

Three-dimensional lattices allow to reduce the effect of interactions, increase the atomic density [216] and resolve frequency shifts between single atoms and interacting atom pairs residing at the same lattice site.

To probe the coherence properties of the clock transition for single atoms and interisotope pairs, we prepare a doubly spin-polarized Fermi-Fermi mixture as before and drive Rabi oscillations on the single-particle and the interaction-shifted transition of $^{171}$Yb as shown in fig. 4.4 a) and c). After each Rabi oscillation measurement, we take a spectrum of the transition under observation and determine the resonance frequency. This allows to perform an *a posteriori* drift compensation and obtain the clock laser's time dependent detuning with respect to the resonance frequency during the Rabi oscillation measurements.

While for single atoms on the timescale of the measurement of $t = 10\,\mathrm{ms}$ damping is small (see fig. 4.4 a)) for the interisotope pairs damping of the oscillation and thus

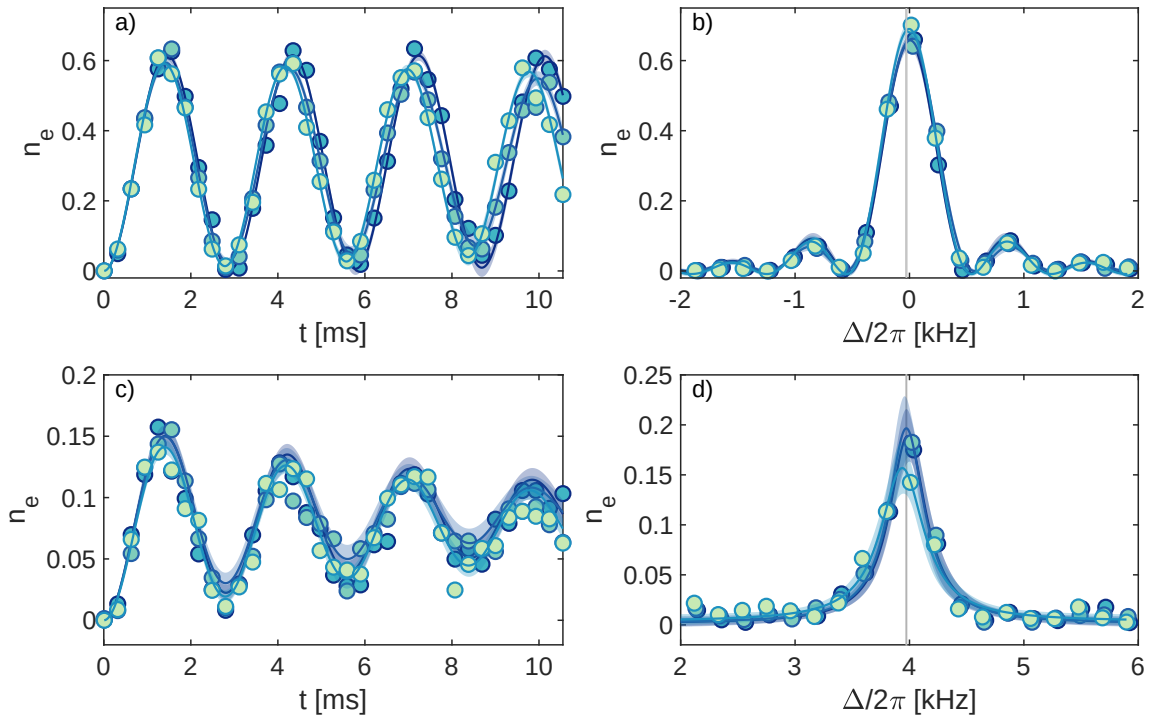


**Figure 4.4.:** Rabi oscillations of the ${}^1S_0 \rightarrow {}^3P_0$ transition of ${}^{171}$yb for atoms at singly occupied lattice sites a) and for lattice sites occupied by a pair of ${}^{171}$Yb and ${}^{173}$Yb. Each data point represents a single measurement. Different colors represent different runs of the experiment. After each Rabi oscillation measurement, we take a spectrum (as shown in panel b) and c)) to obtain the detuning of the clock laser during the Rabi oscillation measurement, indicated by a grey vertical line. We use the spectra shown in panel b) to perform an *aposteriori* drift compensation. Solid lines in panels a) and c) denote fits of a numerical solution of the optical Bloch equations, leaving the Rabi frequency and the transversal damping as free parameters. Solid lines in panel b) denote a fit of sinc$^2$ function in panel d) of a Lorentzian. Shaded areas represent 95% confidence intervals of the fits. Error bars indicating the uncertainty of the determination of the excited state fraction $n_e$ are smaller than the marker size. Lattices have been operated at depths of $S_{1D} = 30\,E_{rec}$ and $S_{1D} = 17\,E_{rec}$.

increased decoherence is clearly visible (see fig. 4.4 c)). To quantify the damping, we fit the numerically obtained solutions of the damped optical Bloch equations eqs. 3.42-3.45 for a given time dependent detuning $\Delta(t)$ to the data, leaving the Rabi frequency $\Omega$ and the transversal damping $\gamma_\perp$ as free parameters, while assuming negligible spontaneous decay $\Gamma_0 = 0$. The obtained Rabi frequencies for single atoms and interisotope pairs of $\Omega_{\text{singles}} = 2\pi \times 335(2)\,\text{Hz}$ and $\Omega_{\text{pairs}} = 2\pi \times 347.5(3.3)\,\text{Hz}$ are similar, whereas the transversal damping obtained from the fit differs by almost an order of magnitude, with $\gamma_{\perp,\text{singles}} = 2\pi \times 3.6(1.7)\,\text{Hz}$ and $\gamma_{\perp,\text{pairs}} = 2\pi \times 33(3)\,\text{Hz}$. (The values given here are the weighted averages of three measurements.) As discussed in chapter 3 transversal damping affects the spectroscopic lineshape, and for large damping the sinc$^2$ expected for a rectangular pulse transforms into a Lorentzian. While in the spectrum of the single-atom transition, one observes a sinc$^2$ for the interisotope pairs, side lobes are not visible indicating a significant transversal damping. Therefore, we fit the spectra of interacting

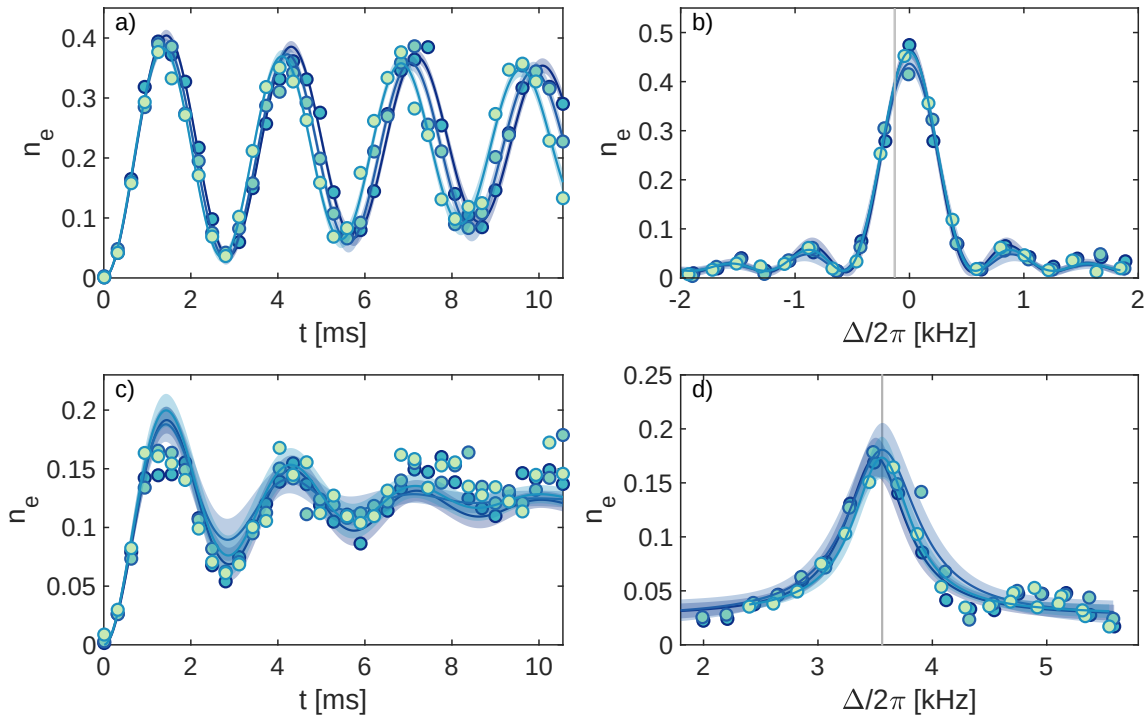


**Figure 4.5.:** Rabi Oscillations of the ${}^1S_0 \rightarrow {}^3P_0$ transition of ${}^{173}$yb for atoms at singly occupied lattice sites a) and for lattice sites occupied by a pair of ${}^{173}$Yb and ${}^{171}$Yb. After each Rabi oscillation measurement, we take a spectrum (as shown in panel b) and c)) to obtain the detuning of the clock laser during the Rabi oscillation measurement, indicated by a grey vertical line. We use the spectra shown in panel b) to perform an *a posteriori* drift compensation. Solid lines in panels a) and c) denote fits of a numerical solution of the optical Bloch equations, leaving the Rabi frequency and the transversal damping as free parameters. Solid lines in panel b) denote a fit of sinc$^2$ function in panel d) of a Lorentzian. Shaded areas represent 95% confidence intervals of the fits. Data points correspond to single measurements, error bars indicating the uncertainty of the determination of the excited state fraction $n_e$ are smaller than the marker size. Lattices were operated at depths of $S_{1D} = 26\,E_{rec}$ and $S_{2D} = 17\,E_{rec}$.

pairs by a Lorentzian that well describes the data.
We perform the same measurement but now excite ${}^{173}$Yb atoms, and observe a similar behavior, as shown in fig. 4.5. Fitting numerical solutions of the optical Bloch equations to the data, as described before, we obtain Rabi frequencies of $\Omega_{\text{single}} = 2\pi \times 322.7(1.6)\,\text{Hz}$ and $\Omega_{\text{pairs}} = 2\pi \times 349.8(4.9)\,\text{Hz}$, and transversal damping coefficients of $\gamma_{\perp,\text{singles}} = 2\pi \times 14(1)\,\text{Hz}$ and $\gamma_{\perp,\text{pairs}} = 2\pi \times 103(13)\,\text{Hz}$. The Rabi frequencies and transversal damping rates determined in both measurements are summarized in tab. 4.3.

Compared to the Rabi frequencies of the single-particle transition, the Rabi frequencies of the interisotope pairs are increased by 4% when exciting ${}^{171}$Yb and 8% when exciting ${}^{173}$Yb. At lowest order we expect the Rabi frequencies to be the same, however, an interaction-induced deformation of the single particle wave functions would lead to a different dipole matrix element and could explain the different Rabi frequencies. The problem of two interacting atoms in a harmonic trap can be solved analytically [217, 218] and the

| | $^{171}\mathrm{Yb_e}$-$^{173}\mathrm{Yb_g}$ | $^{171}\mathrm{Yb_g}$-$^{173}\mathrm{Yb_e}$ |
|---|---|---|
| $\Omega_{\mathrm{singles}}/2\pi$ | 335(2) | 322.7(1.6) |
| $\Omega_{\mathrm{pairs}}/2\pi$ | 347.5(3.3) | 349.8(4.9) |
| $\gamma_{\perp,\mathrm{singles}}/2\pi$ | 3.6(1.7) | 14(1) |
| $\gamma_{\perp,\mathrm{pairs}}/2\pi$ | 33(3) | 103(13) |

**Table 4.3.:** Summary of the Rabi frequencies and transversal damping parameters obtained for ytterbium Fermi-Fermi mixtures either exciting $^{171}$Yb or $^{173}$Yb, in units of Hz. The given values are the weighted mean of the values obtained in three individual measurements.

anharmonicities of an optical lattice potential can be treated perturbatively [219, 220]. A comparison of the measured Rabi frequencies with theory could yield a deeper understanding and possibly allow determining the interorbital interisotope interactions in an approach complementary to the spectroscopic measurements presented above.
However, the uncertainties of the determined Rabi frequencies might be underestimated. In Fig. 4.5 c) the fits systematically overestimate the first maximum of the Rabi oscillations indicating that the underlying model might not properly display the physics of the system under observation. The model is simplified and for example does not include inelastic losses. However, the direct measurement of the inelastic loss rates presented in the previous section suggests that for pairs in the $^{171}\mathrm{Yb_g} -^{173}\mathrm{Yb_e}$ configuration inelastic losses are negligible on the time scale of the measurement and therefore most likely do not explain the deviation of the fit. To definitely preclude systematic errors further measurements are necessary. For the interisotope pairs, the transversal damping is increased by about an order of magnitude, compared to the transversal damping of the corresponding single-particle transitions. Whereas the source of decoherence for the single-particle transition is hard to identify as possible sources are manifold, (including e.g., laser phase noise, lattice laser frequency noise, or magnetic field noise, to name only a few) we attribute the larger transversal damping obtained for the interacting pairs to two sources of decoherence the single atoms are not affected by. On the one hand, the interisotope interorbital transition frequency depends on the Wannier integral and thus is affected by lattice inhomogeneities, as well as shot to shot fluctuations of the lattice depth. On the other hand, interaction with the second atom might cause collisional dephasing, damping the Rabi oscillations.
Unfortunately, it is not possible to distinguish between interaction-induced and lattice-induced dephasing. To gain a deeper understanding of the underlying physics, it might be promising to compare the coherence properties of the two-particle transition to single-particle interband transitions as the interband transitions are sensitive to lattice depth and inhomogeneity as well. The spectroscopic band structure measurements presented in chapter 3 showed a rather good agreement with theory, which instead points into the direction of a high degree of homogeneity of the 1D-lattice. Based on a calculation that takes into account the Gaussian intensity profile of the lattice beams, the frequency broadening caused by the lattice inhomogeneity has been estimated to be very small [98], and hence most likely is negligible. Therefore we think that the damping of the Rabi oscilla-

tions is mainly caused by collisional dephasing. However, analyzing the homogeneity of the lattice remains and determining the source of decoherence remains an open task for the future.
Comparing transitions involving two- and three- or more-particles also might yield a better understanding of the dephasing mechanism. While in bosonic gases of $^{174}$Yb or fermionic gases of $^{87}$Sr multi-particle interactions have been observed [221], we have not been able to find a spectroscopic feature of triply occupied lattice sites in the ytterbium Fermi-Fermi mixtures - neither for mixtures of spin polarized $^{171}$Yb and two spin components of $^{173}$Yb nor for mixtures of spin polarized $^{173}$Yb and two spin components of $^{171}$Yb (for more details see ref.[98]) which could indicate strong three particle losses. Bose-Fermi mixtures of $^{174}$Yb and $^{171}$Yb or $^{174}$Yb and $^{173}$Yb featuring a repulsive interspecies interaction could be a promising candidates to study multi-particle interorbital interisotope interactions and different degrees of decoherence.

### 4.1.4. Conclusion and Outlook

We have characterized elastic and inelastic interorbital interisotope interactions in ytterbium Fermi-Fermi mixtures and directly proven the underlying $\mathrm{SU}(2) \otimes \mathrm{SU}(6)$ symmetry. The elastic interactions have been found to be attractive and similar for the $^{171}\mathrm{Yb_e}-^{171}\mathrm{Yb_g}$ and $^{171}\mathrm{Yb_g}-^{171}\mathrm{Yb_e}$ configuration which we attribute to the large degree of symmetry of the molecular potential. On the other hand the inelastic interactions measured in both electronic configurations differ by a factor of 400 hundred. The difference is currently not understood. And further experimental and theoretical work is required to get a deeper understanding of the molecular potential. We have compared Rabi oscillations on the clock transition for single atoms and interacting interisotope pairs in different configurations. For the interisotope pairs we found a transversal damping approximately eight times larger than for the single particle transition. This is most likely associated to collisional dephasing. The Rabi frequencies for the two-particle transition have been found to be increased by 4% and 8% respectively, which possibly could be an interaction-induced effect. To clarify this behavior a calculation of the analytical solution of two interacting atoms in an harmonic trap would be beneficial. Our measurements constitute an interesting starting point for further studies of the molecular potential of interisotope ytterbium pairs and could be complemented by studies of interorbital interactions in different mixtures including for example bosonic $^{174}$Yb in the future.

## 4.2. Interorbital Spin-Exchange Interaction in $^{171}$Yb

Over the last years, the interorbital spin-exchange interaction in gases of alkaline-earth (like) elements has gathered much attention. It has been proposed to be used for quantum simulation of orbital magnetism or the Kondo-lattice model [64–66] and has been characterized for gases of $^{173}$Yb and $^{87}$Sr some years ago [58, 184, 222]. In $^{173}$Yb the interorbital spin-exchange interaction has been found to be ferromagnetic and extraordinary large [58, 222]. The realization of the Kondo lattice model with ultracold atoms however, requires an antiferromagnetic spin-exchange interaction, and a vanishing ground-state interaction [64]. In the following we will characterize the interorbital spin-exchange interaction for gases of the other fermionic ytterbium isotope $^{171}$Yb, that features a vanishingly small ground-state interaction.

The interorbital spin-exchange interaction of $^{171}$Yb has also been characterized in refs. [62, 68].

### 4.2.1. Spectroscopy Hamiltonian

Here I discuss the spectroscopy Hamiltonian for $^{171}$Yb, following the detailed derivation of the spectroscopy Hamiltonian for $^{173}$Yb in refs. [82, 135].

Previously we have considered interactions between two atoms of different isotopes constituting two distinguishable particles. Now we consider two atoms of $^{171}$Yb, with spin $m_F = \pm 1/2$, that occupy the same lattice site, representing two indistinguishable fermionic particles. The two particle wave function can be written as a product state of an orbital wave function and a spin wave function. For both atoms in either the ground or excited state the antisymmetry of the wave function required for two indistinguishable fermionic particles is realized by a symmetric orbital state and an antisymmetric spin singlet state and can be written as:

$$|gg\rangle = |g,g\rangle \otimes \frac{1}{\sqrt{2}}(|\uparrow\downarrow\rangle - |\downarrow\uparrow\rangle) \tag{4.11}$$

$$|ee\rangle = |e,e\rangle \otimes \frac{1}{\sqrt{2}}(|\uparrow\downarrow\rangle - |\downarrow\uparrow\rangle) \tag{4.12}$$

If one atom is in the ground state and the other atom in the excited state $^3P_0$, the total antisymmetry of the wave function can be achieved in two different ways. Either by a symmetric orbital triplet and antisymmetric spin singlet wave function or the other way around by an antisymmetric orbital singlet and a symmetric spin triplet wave function. In the following we denote these states as $|\mathrm{eg}^+\rangle$ and $|\mathrm{eg}^-\rangle$ given by:

$$\left|\mathrm{eg}^+\right\rangle = \frac{1}{\sqrt{2}}(|e,g\rangle + |g,e\rangle) \otimes \frac{1}{\sqrt{2}}(|\uparrow\downarrow\rangle - |\downarrow\uparrow\rangle) \tag{4.13}$$

$$\left|eg^-\right\rangle = \frac{1}{\sqrt{2}}(|e,g\rangle - |g,e\rangle) \otimes \frac{1}{\sqrt{2}}(|\uparrow\downarrow\rangle + |\downarrow\uparrow\rangle). \tag{4.14}$$

Together with the states $(|e,g\rangle - |g,e\rangle)/\sqrt{2} \otimes |\uparrow\uparrow\rangle$ and $(|e,g\rangle - |g,e\rangle)/\sqrt{2} \otimes |\downarrow\downarrow\rangle$ these six states form the interaction basis. However in the following we restrict our considerations to the subspace formed by the four basis states given by eqs. 4.11-4.14, as the other two states are not accessible via excitation with $\pi$-polarized clock laser light as will be shown later. The two-particle Hamiltonian at vanishing magnetic field can be written as:

$$\mathcal{H} = \mathcal{H}_{\mathrm{el}} + \mathcal{H}_{\mathrm{int}} + \mathcal{H}_{L}, \tag{4.15}$$

and is comprised by the sum of the bare electronic Hamiltonian $\mathcal{H}_{\mathrm{el}}$ the atomic interaction Hamiltonian $\mathcal{H}_{\mathrm{int}}$ and the coupling Hamiltonian $\mathcal{H}_{\mathrm{L}}$ describing the atom light interaction. The bare electronic Hamiltonian $\mathcal{H}_{\mathrm{el}}$ is spin independent and in the frame rotating at the laser frequency it is given by:

$$\mathcal{H}_{\mathrm{el}} = \hbar\Delta \left( |gg\rangle \langle gg| - |ee\rangle \langle ee| \right). \tag{4.16}$$

Here $\Delta = \omega - \omega_0$ describes the detuning with respect to the atomic resonance. Each of the four states $|gg\rangle$ $|eg^+\rangle$ $|eg^-\rangle$ and $|ee\rangle$ is characterized by its own molecular potential and Hubbard on-site interaction $U_{gg}$, $U_{ee}$ and $U_{eg^\pm}$. The corresponding interaction Hamiltonian reads:

$$\mathcal{H}_{\mathrm{int}} = U_{gg} |gg\rangle\langle gg| + U_{ee} |ee\rangle\langle ee| + U_{eg^+} \left|eg^+\right\rangle\left\langle eg^+\right| + U_{eg^-} \left|eg^-\right\rangle\left\langle eg^-\right|. \tag{4.17}$$

The single particle Hamiltonian $\mathcal{H}_{\mathrm{L},\pi,1}$ describing the interaction of a single atom with $\pi$-polarized clock laser light is given by:

$$\mathcal{H}_{\mathrm{L},\pi,1} = \frac{\hbar\Omega}{2} \left( |e\uparrow\rangle\langle g\uparrow| - |e\downarrow\rangle\langle g\downarrow| + h.c. \right). \tag{4.18}$$

Here $h.c.$ denotes the hermitian conjugate. The two terms in eq. 4.18 have opposite sign due to the opposite signs of the Clebsch-Gordan coefficients for the transitions of the different $m_F$-states. The two-body Hamiltonian then reads :

$$\mathcal{H}_{\mathrm{L},\pi} = \mathcal{H}^{(1)}_{\mathrm{L},\pi,1} \otimes \mathbb{1}^{(2)} + \mathbb{1}^{(1)} \otimes \mathcal{H}^{(2)}_{\mathrm{L},\pi,1}. \tag{4.19}$$

Here $\mathbb{1}$ denotes the identity matrix and the superscripts (1) and (2) indicate that the operators act on the first or the second particle, respectively. Applying $\mathcal{H}_{\mathrm{L},\pi}$ to the interaction basis one finds only two non-vanishing matrix elements $\langle eg^-|\mathcal{H}_{\mathrm{L},\pi}|gg\rangle$ and $\langle ee|\mathcal{H}_{\mathrm{L},\pi}|eg^-\rangle$ and the two-particle Hamiltonian hence can be rewritten as[82]:

$$\mathcal{H}_{\mathrm{L},\pi} = \frac{\hbar\sqrt{2}\Omega}{2} \left( \left|eg^-\right\rangle \langle gg| - |ee\rangle \left\langle eg^-\right| + h.c. \right). \tag{4.20}$$

In particular, one finds that the ground state $|gg\rangle$ only couples to the spin triplet state $|eg^-\rangle$. Compared to the single particle transition the coupling is enhanced by a factor of $\sqrt{2}$, which is associated to superradiant behavior [223].
At finite magnetic field the energy levels of the atoms experience a Zeeman shift according to the orbital and $m_F$-state. The single particle Zeeman Hamiltonian $\mathcal{H}_{\mathrm{Z},1}$ reads [82]:

$$\mathcal{H}_{\mathrm{Z},1} = E_{\mathrm{Z},g\downarrow} |g\downarrow\rangle\langle g\downarrow| + E_{\mathrm{Z},g\uparrow} |g\uparrow\rangle\langle g\uparrow| + E_{\mathrm{Z},e\downarrow} |e\downarrow\rangle\langle e\downarrow| + E_{\mathrm{Z},e\uparrow} |e\uparrow\rangle\langle e\uparrow|. \tag{4.21}$$

Here the terms $E_{\mathrm{Z},g\downarrow}, E_{\mathrm{Z},g\uparrow}, E_{\mathrm{Z},e\downarrow}$ and $E_{\mathrm{Z},e\uparrow}$ denote the single particle Zeeman shifts at a certain magnetic field $B$. Applying the two-particle Zeeman Hamiltonian $\mathcal{H}_{\mathrm{Z}}$, given by [82]:

$$\mathcal{H}_{\mathrm{Z}} = \mathcal{H}_{\mathrm{Z},1}^{(1)} \otimes \mathbb{1}^{(2)} + \mathbb{1}^{(1)} \otimes \mathcal{H}_{\mathrm{Z},1}^{(2)}, \tag{4.22}$$

to the interaction basis, one finds that the Zeeman Hamiltonian is not diagonal in the interaction basis and by using the identities $E_{\mathrm{Z,g}\downarrow} = -E_{\mathrm{Z,g}\uparrow}$ and $E_{\mathrm{Z,e}\downarrow} = -E_{\mathrm{Z,e}\uparrow}$ it can be shown that[82]:

$$\mathcal{H}_{\mathrm{Z}} |gg\rangle = 0 \tag{4.23}$$

$$\mathcal{H}_{\mathrm{Z}} |ee\rangle = 0 \tag{4.24}$$

$$\mathcal{H}_{\mathrm{Z}} \left|eg^{+}\right\rangle = E_{\mathrm{Z}}(B) \left|eg^{-}\right\rangle \tag{4.25}$$

$$\mathcal{H}_{\mathrm{Z}} \left|eg^{-}\right\rangle = E_{\mathrm{Z}}(B) \left|eg^{+}\right\rangle. \tag{4.26}$$

Here $E_{\mathrm{Z}}(B)$ denotes the $B$-field dependent differential Zeeman shift between atoms of the same spin in the orbital state $^1S0$ and $^3P_0$. For $^{171}$Yb it is given by $E_{\mathrm{Z}}(B) = \delta g B m_F$, with $\delta g = -399.0(1)$Hz/G [68]. The atomic Hamiltonian $\mathcal{H}_{\mathrm{at}} = \mathcal{H}_{\mathrm{el}} + \mathcal{H}_{\mathrm{int}} + \mathcal{H}_{\mathrm{Z}}$ in the interaction basis thus can be written in matrix notation as [82]:

$$\mathcal{H}_{\mathrm{at}} = \begin{pmatrix} U_{gg} + \hbar\Delta & 0 & 0 & 0 \\ 0 & U_{eg^+} & E_{\mathrm{Z}}(B) & 0 \\ 0 & E_{\mathrm{Z}}(B) & U_{eg^-} & 0 \\ 0 & 0 & 0 & U_{ee} - \hbar\Delta \end{pmatrix} \tag{4.27}$$

The Zeeman interaction mixes the states $|eg^+\rangle$ and $|eg^-\rangle$. Diagonalizing the Hamiltonian eq. 4.27 yields new eigenstates $|+\rangle$ and $|-\rangle$ given by:

$$|+\rangle = c_1(B) \left|eg^{+}\right\rangle + c_2(B) \left|eg^{-}\right\rangle \tag{4.28}$$

$$|-\rangle = c_1(B) \left|eg^{-}\right\rangle - c_2(B) \left|eg^{+}\right\rangle, \tag{4.29}$$

with corresponding eigenenergies $E_\pm$ given by [2]:

$$E_\pm = V \pm V_{\mathrm{ex}} \sqrt{1 + \left(\frac{E_{\mathrm{Z}}(B)}{V_{\mathrm{ex}}}\right)^2}. \tag{4.30}$$

Here $V = (U_{eg^+} + U_{eg^-})/2$ denotes the direct and $V_{ex} = (U_{eg^+} - U_{eg^-})/2$ the spin-exchange part of the interaction. The mixing coefficients $c_1$ and $c_2$ are given by [2]:

$$c_1(B) = \frac{|V_{\mathrm{ex}}| + \sqrt{V_{\mathrm{ex}}^2 + E_{\mathrm{Z}}^2(B)}}{\sqrt{2V_{\mathrm{ex}}^2 + 2E_{\mathrm{Z}}^2(B) + 2|V_{\mathrm{ex}}|\sqrt{V_{\mathrm{ex}}^2 + E_{\mathrm{Z}}^2(B)}}} \tag{4.31}$$

$$c_2(B) = \frac{|E_{\mathrm{Z}}(B)|}{\sqrt{2V_{\mathrm{ex}}^2 + 2E_{\mathrm{Z}}^2(B) + 2|V_{\mathrm{ex}}|\sqrt{V_{\mathrm{ex}}^2 + E_{\mathrm{Z}}^2(B)}}}. \tag{4.32}$$

In the limit of $B \to \infty$ one finds $c_1 = c_2 = 1/\sqrt{2}$ while for $B = 0$ one finds $c_1 = 1$ and $c_2 = 0$.

Now we can write the complete Hamiltonian for an arbitrary magnetic field:

$$\mathcal{H} = \mathcal{H}_{\mathrm{el}} + \mathcal{H}_{\mathrm{int}} + \mathcal{H}_{\mathrm{Z}} + \mathcal{H}_{\mathrm{L}}, \tag{4.33}$$

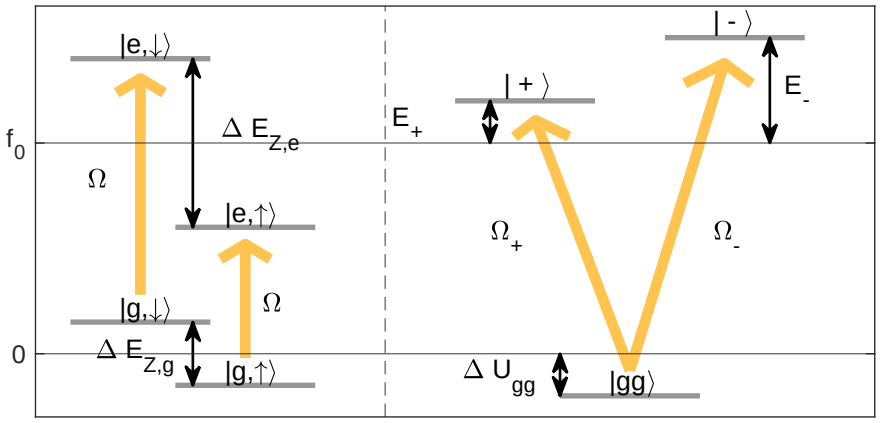


**Figure 4.6.:** Single particle (left) and two particle transitions (right) for a two component fermi gas of $^{171}$Yb. Shown are the relevant transitions and energy shifts caused by the Zeemann effect and two-body interactions. The frequency $f_0$ denotes the bare atomic resonance frequency. Distances are not to scale.

which in matrix notation reads:

$$\mathcal{H} = \begin{pmatrix} U_{\mathrm{gg}} + \hbar\Delta & \frac{\hbar\sqrt{2}\Omega}{2}c_2(B) & \frac{\hbar\sqrt{2}\Omega}{2}c_1(B) & 0 \\ \frac{\hbar\sqrt{2}\Omega}{2}c_2(B) & E_+ & 0 & \frac{\hbar\sqrt{2}\Omega}{2}c_2(B) \\ \frac{\hbar\sqrt{2}\Omega}{2}c_1(B) & 0 & E_- & \frac{\hbar\sqrt{2}\Omega}{2}c_1(B) \\ 0 & \frac{\hbar\sqrt{2}\Omega}{2}c_2(B) & \frac{\hbar\sqrt{2}\Omega}{2}c_1(B) & U_{\mathrm{ee}} - \hbar\Delta \end{pmatrix}. \tag{4.34}$$

At finite magnetic field the ground state $|gg\rangle$ couples to the state $|\pm\rangle$, as indicated in fig. 4.6. Note however, that the matrix transition elements $\langle eg^{\pm}|\mathcal{H}|gg\rangle$ scale with the mixing coefficients $c_1$ and $c_2$. Therefore the effective Rabi frequencies $\Omega_{\pm} = \sqrt{(2)}c_{2/1}\Omega_0$ of the optical transitions depend on the magnetic field and especially for small magnetic fields are different.

With these formulas at hand we are well equipped to understand the spectra of interacting two spin component gases of $^{171}$Yb.

### 4.2.2. Spectroscopic Characterizations of the Interorbital Spin-Exchange Interaction

To probe the interorbital spin-exchange interaction we prepare a spin balanced gas of $^{171}$Yb of $N_{171} \approx (15-35)\times 10^3$, load it into an magical optical lattice with $s_{1\mathrm{D}} = 50(2)E_{\mathrm{rec}}$ and $s_{2\mathrm{D}} = 25.0(3)\,E_{\mathrm{rec}}$ and perform clock spectroscopy with $\pi$-polarized clock laser light using a clock beam intensity that corresponds to a Rabi frequency of $\Omega_0 = 2\pi\times 345(2)$ Hz for the single particle transition. Figure 4.7 shows an exemplary spectrum taken at a

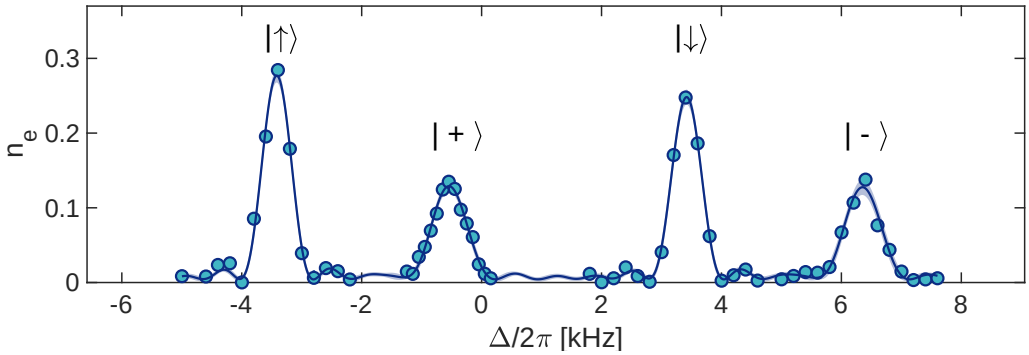


**Figure 4.7.:** Clock spectrum of an interacting two spin component gas of $^{171}$Yb at a magnetic field of $B = 13.1\,\mathrm{G}$. We find four spectroscopic features that can be attributed to single atoms in the states $m_\mathrm{F} = \pm 1/2$ and interacting atom pairs in the interorbital states $|+\rangle$ and $|-\rangle$. Shown is the excited state fraction $n_\mathrm{e}$ as a function of the clock laser detuning $\Delta$. For the single atom features labeled by $|\uparrow\rangle$ and $|\downarrow\rangle$ we used pulses of $t_\mathrm{pulse} = 1.45\,\mathrm{ms}$, corresponding to a Rabi frequency of $\Omega_0 = 2\pi \times 345(2)\,\mathrm{Hz}$. For the two particle features the pulse duration has been adapted to account for the sub- and superradiant properties of the states $|\pm\rangle$. The solid line denotes a fit of four sinc$^2$ functions used to find the resonance positions. The shaded area indicates the 95% confidence interval of the fit. Data points are the average of three measurements. Error bars indicating one standard deviation are typically smaller than the symbol size. The figure is adapted from the published version [2]. 

magnetic field of $B = 13.1\,\mathrm{G}$. We find four spectroscopic features. The most prominent two peaks can be attributed to single atoms in the spin states $m_\mathrm{F} = \pm 1/2$, while the two smaller peaks are associated to atom pairs in the interorbital states $|\pm\rangle$. By comparing the Rabi frequencies of the two interorbital features we identify the resonance at lower frequency as the transition $|gg\rangle \to |+\rangle$ and the resonance at the higher frequency as the $|gg\rangle \to |-\rangle$ transition as the Rabi frequency of the $|gg\rangle \to |+\rangle$ increases for an increasing magnetic field, while the Rabi frequency of the $|gg\rangle \to |-\rangle$ transition decreases for an increasing magnetic field, as shown in fig. 4.8. The one and two-particle transitions, are shifted with respect to the bare atomic transition frequency $f_0$, due to the Zeeman effect and the two-particle interactions, as schematically shown in fig. 4.6. The frequencies of the four spectroscopic features visible in fig. 4.7 are given by:

$$hf_\downarrow = hf_0 + E_{Z,\downarrow}(B) \tag{4.35}$$

$$hf_\uparrow = hf_0 + E_{Z,\uparrow}(B) \tag{4.36}$$

$$hf_+ = hf_0 + \Delta V + \Delta V_\mathrm{ex}\sqrt{1 + \left(\frac{E_Z(B)}{\Delta V_\mathrm{ex}}\right)^2} \tag{4.37}$$

$$hf_- = hf_0 + \Delta V - \Delta V_\mathrm{ex}\sqrt{1 + \left(\frac{E_Z(B)}{\Delta V_\mathrm{ex}}\right)^2}, \tag{4.38}$$

with $\Delta V = \left(U_{eg^+} + U_{eg^-}\right)/2 - U_{gg}$ and $\Delta V_\mathrm{ex} = \left(U_{eg^+} - U_{eg^-}\right)/2 - U_{gg}$. Here $E_{Z,\uparrow}(B)$ and $E_{Z,\downarrow}(B)$ denote the differential Zeeman shifts for atoms in the states $m_F = \pm 1/2$. As the differential Zeeman shift $E_\mathrm{Z}(B)$ and the ground state interaction $U_{gg}$ are known we

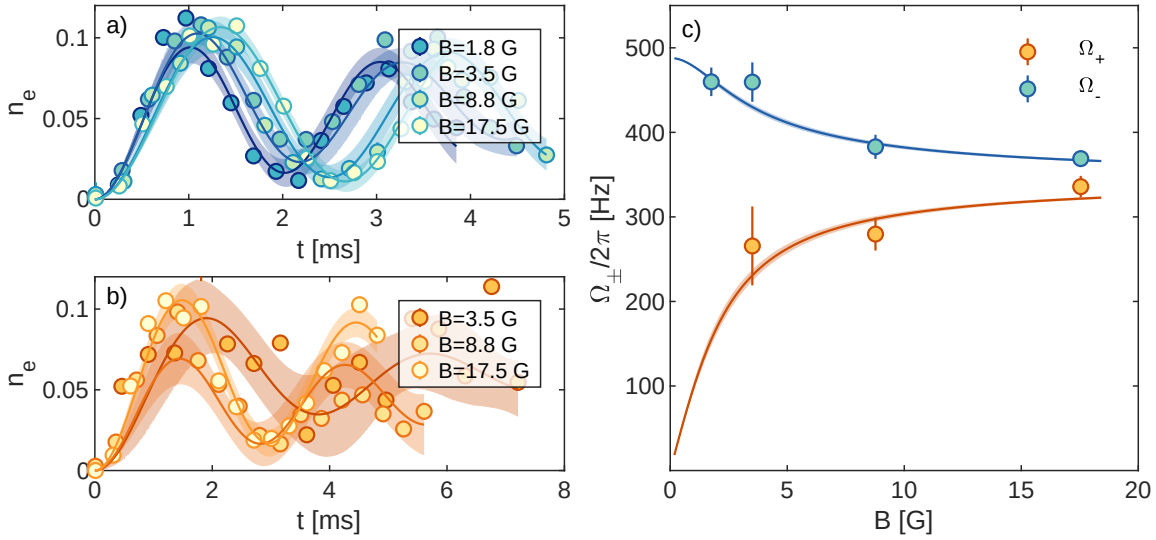


**Figure 4.8.:** Measurement of the Rabi frequencies $\Omega_{\pm}$. Panel a) and b) show Rabi oscillations on the interorbital transitions $|gg\rangle \rightarrow |-\rangle$ and $|gg\rangle \rightarrow |+\rangle$, for different magnetic fields. Solid lines indicate a fit of the numerical solutions of the optical Bloch equations, neglecting spontaneous emission as described in 3. To obtain the bare Rabi frequencies the maximum excited state fraction has been fixed to the value of $n_{\mathrm{e,max}} = 0.115(4)$, found in the spectroscopic measurement presented in fig. 4.9, while the detuning, the bare Rabi frequency and the transversal damping have been left as free parameters. Data points represent the average of two to three measurements with error bars (smaller than the marker size) denoting one standard deviation. Panel c) shows a comparison of the obtained Rabi frequencies $\Omega_{\pm}$ and the theoretical curves calculated using eq. 4.30 with the spectroscopically measured values of $V$ and $V_{\mathrm{ex}}$. Data points show the Rabi frequencies obtained from the fits shown in Panel a) and b) with errorbars indicating the uncertainty of the fit. Panel c) is adapted from the published version [2]. 

can use this system of equations to determine $f_0$, the magnetic field $B$ and obtain the quantities of interest $U_{\mathrm{eg}+}$ and $U_{\mathrm{eg}-}$ (see ref. [98] for more details).
To determine the interorbital interaction parameters we take spectra at different magnetic fields as shown in fig. 4.9 a). To achieve an optimal spectroscopic contrast we account for the different Rabi frequencies of the interorbital transitions caused by the magnetic field dependent state mixing by adapting the clock laser pulse length to fulfill the $\pi$ pulse condition.
We average the interaction parameters $\Delta U_{\mathrm{eg}^{\pm}} = U_{eg^{\pm}} - U_{gg}$ computed for each spectrum and find $\Delta U_{eg^-}/h = 3.53(4)\,\mathrm{kHz}$ and $\Delta U_{eg^+}/h = 2.32(3) kHz$, corresponding to a direct and spin-exchange interaction energy of$\Delta V/h = 2.896(11)\,\mathrm{kHz}$ and $\Delta V_{\mathrm{ex}}/h = -0.60(2)\,\mathrm{kHz}$. We compute the Wannier integrals for the used lattice depths of $s_{1\mathrm{D}} = 50\,E_{\mathrm{rec}}$ and $s_{2\mathrm{D}} = 25\,E_{\mathrm{rec}}$ and use eq. 1.14 to obtain the lattice depth independent $s$-wave scattering lengths. Using the literature value of the ground state $s$-wave scattering length $a_{gg} = -3(4)\,a_0$ obtained by two color photo association measurements [118], we find $s$-wave scattering lengths of $a_{eg^+} = 203(5)\,a_0$ and $a_{eg^-} = 308(6)\,a_0$. As a cross check we compare measured Rabi frequencies for the interorbital transitions and the expected values obtained from eq. 4.31 and eq. 4.32 using the measured values of $a_{eg^{\pm}}$ finding a

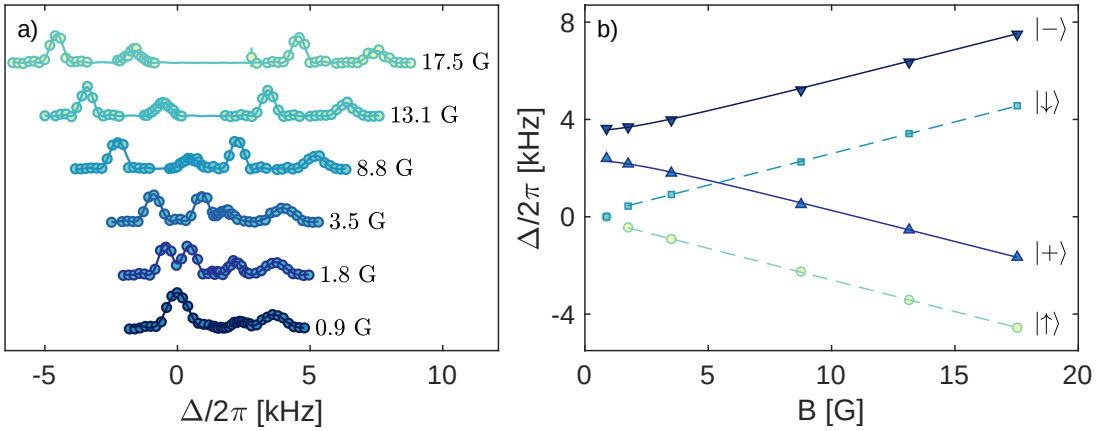


**Figure 4.9.:** Spectroscopic determination of the interorbital direct and spin-exchange interactions of $^{171}$Yb. Panel a) shows clock spectra of the two component Fermi gas of $^{171}$Yb at different magnetic fields, for clarity offset in the y-direction. Panel b) shows the resonance positions of the single particle and two-particle transitions obtained from fitting the sum of four sinc$^2$ functions to the spectra presented in panel a), as a function of the magnetic field. Solid lines show the energy branches $E_\pm$ according to eq. 4.30 computed with the weighted means of the values obtained for $V$ and $V_{\mathrm{ex}}$. Dashed lines show the Zeeman Shift of $E_z = -399.0(1)\,\mathrm{Hz/G}\,m_\mathrm{F}\,B$ as reported in [68]. The figure is adapted from the published version [2]. ©2021 American Physical Society.

good agreement (see fig. 4.8 c)).

### 4.2.3. Conclusion and Outlook

We have spectroscopically characterized interorbital interactions in two spin component gases of $^{171}$Yb and have determined the corresponding $s$-wave scattering lengths $a_{\mathrm{eg}^+} = 203(5)\,a_0$ and $a_{\mathrm{eg}^-} = 308(6)\,a_0$. The interorbital spin-exchange interaction in $^{171}$Yb has recently been characterized by the Kyoto and Munich groups finding values of $a_{\mathrm{eg}^+} = 225(13)\,a_0$ and $a_{\mathrm{eg}^-} = 355(6)\,a_0$ [62] and $a_{\mathrm{eg}^+} = 240(4)\,a_0$ and $a_{\mathrm{eg}^-} = 389(4)\,a_0$ [68], respectively. The here measured value of $a_{\mathrm{eg}^+} = 203(5)\,a_0$ is in agreement with the value measured by the Kyoto group but not with the value reported by the Munich group. The measured value of $a_{\mathrm{eg}^-} = 308(6)\,a_0$ deviates from the values measured by both groups. The difference between the value measured in our experiment and the value measured by the Kyoto group is, however, comparable to the difference between the values reported by the Kyoto and Munich groups. At the given moment it is unclear what causes the difference of the measured values. A difference between the measurements presented here and the measurements conducted by the Kyoto and the Munich groups are the lattice potentials. Whereas we use a combined lattice potential formed by a one-dimensional lattice and a triangular 2D-lattice, the Kyoto and Munich groups work with simple cubic lattices. However, the lattice geometry is taken into account in the calculation of the Wannier integrals, and hence this does not explain the deviation of the different measurements, which therefore remains an open question.
On the other hand, the findings of all three measurements correspond to an antiferro-

| $a_{gg}(a_0)$ | $a_{eg^+}(a_0)$ | $a_{eg^-}(a_0)$ | $\beta_{eg^\pm}(\mathrm{cm}^3 s^{-1})$ | $\beta_{ee}(\mathrm{cm}^3 s^{-1})$ | reference |
|---|---|---|---|---|---|
| $-3(4)$ | | | | | [226] |
| | 203(5) | 308(6) | | | This work [2] |
| | 225(13) | 355(6) | | | [62] |
| | 240(4) | 389(4) | $\leq 2.6(3) \times 10^{-16}$ | $4.8(2.1) \times 10^{-12}$ | [68] |

**Table 4.4.:** Summary of elastic and inelastic interorbital interaction parameters for $^{171}$Yb.

magnetic spin-exchange interaction $V_{\mathrm{ex}} < 0$ and therefore show a qualitative agreement. Elastic and inelastic interaction parameters for $^{171}$Yb measured in different experiments are summarized in tab. 4.4

The almost vanishing ground state interaction and the moderate antiferromagnetic spin-exchange interaction render $^{171}$Yb an ideal candidate for quantum simulation of the Kondo-lattice model[64, 65]. It would be beneficial to be able to tune the spin-exchange interaction, which could possibly be achieved employing confinement induced resonances 224, 225 but remains to be demonstrated. Therefore, studying the spin-exchange interaction as a function of the lateral confinement could be a reasonable next step.

# 5. Orbital Mixtures in a State Dependent Lattice

Over the last decades, ultracold gases in optical lattices have been used extraordinarily successfully for quantum simulation of Hubbard models [21, 227]. Ultracold atoms in combination with optical lattices constitute a versatile experimental toolbox as many system parameters such as interaction strength, lattice depth and geometry can be conveniently controlled, and therefore in many cases, allow to tailor Hamiltonians of interest. Though the $s$-wave interaction of ytterbium is fixed due to the lack of magnetic Feshbach resonances, which therefore restrict the utility of this element for quantum simulation applications, it offers other degrees of freedom. The SU($N$) symmetry of the $s$-wave interactions allows considering the spin degree of freedom as a synthetic dimension. Coupling multiple spin levels of $^{173}$Yb in a lattice system by Raman transitions has been used to create a finite lattice system, combining real and synthetic dimensions, and allowed to observe chiral edge currents, in analogy to quantum Hall systems [34]. In a similar approach the metastable state $^3P_0$ has been used to create a two-leg ladder and to observe chiral currents [169].

So far, most approaches to quantum simulation of lattice systems with cold atoms have been restricted to single-band models. However, it is known that in solid-state systems, interactions between itinerant band electrons and localized spins are of great importance. Related theories[228] developed by and named after P. W. Anderson [229] and J. Kondo [230] describe the interaction of conduction-band electrons with a single impurity. Perturbatively treating the interaction between conduction-band electrons and a magnetic impurity, J. Kondo obtained a logarithmic $\log(T)$ contribution for the electric resistivity, that could explain the minimum in resistivity observed for impure gold [231]. However, the divergence of the $\log(T)$ term at low temperatures fueled the search for a non-perturbative theory describing the system known as the Kondo problem [12]. In the following decades the Kondo problem was solved by K.G Wilson using numerical renormalization group theory [232] and by N. Andrei and P. Wiegmann using the Bethe Ansatz to diagonalize the Kondo Hamiltonian [233, 234]. The model, usually dealing with $d$-electrons, has been adapted by Coqblin and Schriefer [235] to describe Cerium impurities that are characterized by a $4f^1$ configuration.

The Kondo lattice model (KLM) and the periodic Anderson model extend the single impurity models to a lattice of impurities and are commonly used to describe intermetallic rare-earth and actinide compounds[12, 13]. These materials show low-temperature anomalies that are connected to the formation of $f$-bands characterized by a large effective mass. Therefore these systems are referred to as heavy-fermion materials [12, 13]. Heavy-fermion materials show a variety of low-temperature behaviors such as magnetic ordering, Kondo insulation or unconventional superconductivity [13]. To grasp the behavior

of heavy-fermion materials, a precise understanding of the interaction of conduction-band electrons and localized magnetic moments is necessary.
Ultracold alkaline-earth (-like) atoms in optical lattices have been proposed for quantum simulation of the Kondo lattice model [64–66]. The metastable state $^3P_0$ is conveniently accessible and radiatively stable on experimental timescales. State-dependent optical potentials allow to create optical lattices that feature tunneling coefficients different by orders of magnitude for ground- and excited-state atoms and are therefore feasible to create systems of mobile ground and localized excited-state atoms. The interorbital spin-exchange interaction between ground and excited-state atoms emulates the spin-exchange interaction between itinerant electrons and localized spin. Given these ingredients it is expected that engineering the Kondo lattice Hamiltonian $H_{\mathrm{KLM}}$ [64, 235]:

$$\mathcal{H}_{\mathrm{KLM}} = -\sum_{\langle i,j\rangle,m} J_g(c^\dagger_{igm}c_{jgm} + h.c.) + V_{\mathrm{ex}}\sum_{i,m,m'} c^\dagger_{igm}c^\dagger_{iem'}c_{igm}c_{iem'}, \tag{5.1}$$

in a system of ultracold atoms is feasible. Here $J_g$ denotes the tunneling energy for ground-state atoms and $V_{\mathrm{ex}}$ the interorbital spin-exchange energy. The fermionic creation and annihilation operators $c^\dagger_{igm}$ and $c_{igm}$ correspond to the creation and annihilation operators of a ground-state atom in the spin state $m$ at lattice site $i$, whereas $c^\dagger_{iem}$ and $c_{iem}$ denote operators corresponding to the creation and annihilation of an excited-state atom in the spin state $m$ at lattice site $i$. It has been shown by S. Doniach that in a one dimensional Kondo lattice, a second order phase transition from an antiferromagnetic ground state to a heavy-Fermi liquid characterized by Kondo singlet formation occurs, as the exchange coupling is increased above a critical value [11]. Below the critical value, in the antiferromagnetic phase the Ruderman-Kittel-Kasuya-Yosida (RKKY) interaction[236] is dominant, characterized by a temperature $T_{\mathrm{RKKY}}$ given by [11, 64]:

$$k_{\mathrm{B}}T_{\mathrm{RKKY}} \sim V_{\mathrm{ex}}^2/J_{\mathrm{g}}. \tag{5.2}$$

Above the critical value the relevant energy scale is given by the Kondo temperature:

$$k_{\mathrm{B}}T_{\mathrm{Kondo}} \sim J_{\mathrm{g}}e^{-cJ_{\mathrm{g}}/|V_{\mathrm{ex}}|}. \tag{5.3}$$

Here $c$ denotes a dimensionless constant on the order of one [64]. The corresponding phase diagram is known as the 'Doniach' phase diagram [11]. According to ref.[64] in the antiferromagnetic KLM ($V_{\mathrm{ex}} < 0$) heavy-Fermi liquid behavior is expected for $J_{\mathrm{g}} \lesssim |V_{\mathrm{ex}}|$ and temperatures below the Kondo temperature $T_{\mathrm{Kondo}}$, which for $J_{\mathrm{g}} \sim V_{\mathrm{ex}}$ is on the order of $V_{\mathrm{ex}}$. Though tuning the spin-exchange coupling using confinement induced resonances has been proposed [225, 237], reaching temperatures low enough to observe heavy-Fermion behavior might be challenging.

The Hamiltonian for a gas of atoms in the ground and the excited state in a state-dependent optical lattice is given by [64]:

$$\begin{aligned}\mathcal{H}_{\mathrm{SDL}} = &-\sum_{\langle i,j\rangle,m,\alpha} J_\alpha(c^\dagger_{i\alpha m}c_{j\alpha m} + h.c.) + \sum_{i,\alpha}\frac{U_{\alpha\alpha}}{2}n_{i\alpha}(n_{i\alpha}-1)\\ &+V\sum_i n_{ig}n_{ie} + V_{\mathrm{ex}}\sum_{i,m,m'} c^\dagger_{igm}c^\dagger_{iem'}c_{igm}c_{iem'}.\end{aligned} \tag{5.4}$$

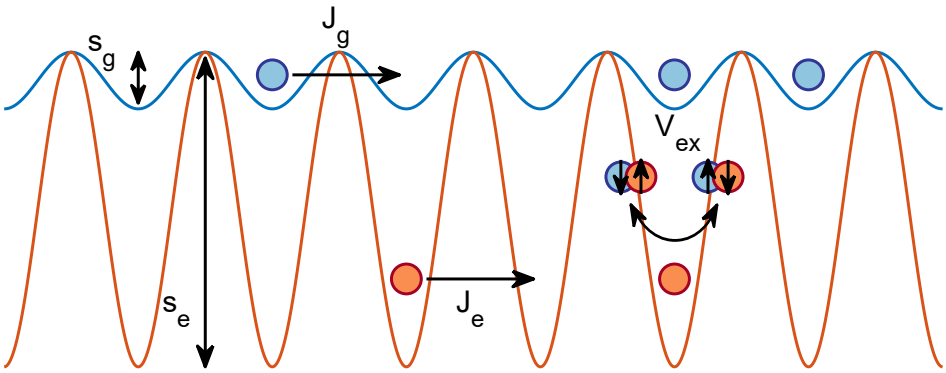


**Figure 5.1.:** Illustration of ground- and excited-state atoms depicted as blue and red spheres respectively in a state-dependent optical lattice. In the limit of $J_e \gg J_g$ it is possible to realize a system of localized excited-state and itinerant ground state-atoms. Interorbital pairs at a shared lattice site interact via the interorbital spin exchange interaction.

Here the $\alpha \in [g, e]$ describes the electronic state of the atom, $V$ and $V_{\mathrm{ex}}$ describe the direct and exchange part of the interorbital interactions, respectively, while $U_{\alpha\alpha}$ describes the on-site interaction between two ground- or excited-state atoms. The residual harmonic confinement caused by the intensity profile of the lattice laser beams has been neglected. Assuming one excited-state atom per lattice site and a strongly state-dependent lattice characterized by negligible tunneling for excited-state atoms $J_e \approx 0$ as well as a vanishing ground state on-site interaction $U_{gg} \approx 0$ the SDL Hamiltonian eq. 5.4 transforms into the Kondo lattice Hamiltonian eq. 5.1.

While for $^{173}$Yb the ground state $s$-wave scattering length is given by $^{173}a_{\mathrm{gg}} = 199(2)a_0$, for $^{171}$Yb it almost vanishes with $^{171}a_{\mathrm{gg}} = -3(4)a_0$ [118] (the non-interacting case $a = 0$ is within uncertainty). Hence neglecting the ground-state on-site interaction for $^{171}$Yb is well justified. The interorbital spin exchange interaction for $^{173}$Yb is ferromagnetic [58, 222] while it is antiferromagnetic for $^{171}$Yb (see sec. 4 and refs. [62, 68]) and hence closer to the solid state analogue. Therefore $^{171}$Yb constitutes an intriguing candidate for studying Kondo-lattice-type physics in state-dependent optical lattices. First inspiring studies of spin-exchange in one-dimensional state-dependent optical lattices with $^{173}$Yb [77] showed spin-exchange rates tunable by the perpendicular confinement and fueled theoretical interest [238].

In the ytterbium lab, we use light at 660 nm to create a state-dependent optical lattice for ytterbium atoms. The laser system setup has been set up by A. Skottke and is described in detail in ref.[90]. In the following, I will present characterization measurements of the state-dependent lattice and first experiments demonstrating interorbital spin-exchange in a gas of $^{171}$Yb in the state-dependent lattice. Similar measurements have been presented in a recent publication by the Kyoto group [78].

The experiments presented in this chapter have been conducted by K. Sponselee, M. Diem and mainly the author. Data analysis has been performed by the author.

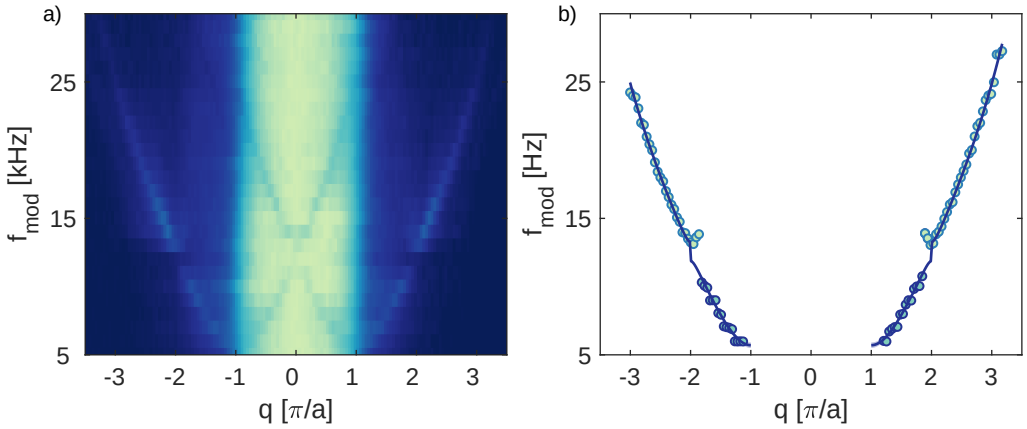


**Figure 5.2.:** Momentum-resolved modulation spectroscopy of a spin polarized gas of $^{171}$Yb ground-state atoms in the state-dependent optical lattice. Panel a) shows the momentum-resolved excitation spectrum. Each horizontal line represents the OD obtained from an absorption image after bandmapping and ToF, integrated along the direction perpendicular to the SDL and normalized to its maximum. Colors from dark to bright denote the optical density. The lattice-depth modulation induces a particle hole excitation. Particles appear in the second and third Brillouin zone while in the first Brillouin zone a reduced optical density indicates a hole. A fit of a 1D-lattice band structure to the particle excitation spectrum $f(q)$, extracted from the data shown in panel a) is shown in panel b) and yields a ground-state lattice depth of $s_{\mathrm{SDL,g}} = 4.33(8)\, E_{\mathrm{rec}}$. Data points shown in grey have been excluded from the fit.

## 5.1. Lattice Depth Calibration

Based on a calculation of the complex polarizabilities of the ground and excited state (see sec. 1) at a wavelength of $\lambda_{\mathrm{SDL}} = 660\,\mathrm{nm}$, we expect that the lattice depths for ground and excited state differ by a factor of$\alpha_{\mathrm{e}}/\alpha_{\mathrm{g}} = 5.5$ [84]. The magic wavelength predicted by this calculation significantly deviates from the actual magic wavelength as pointed out before, however it is expected to show better results in the proximity of resonances. Precise knowledge of the lattice potential is necessary to correctly predict the relevant timescales for dynamics in the optical lattice. Therefore we calibrate the lattice depth for both ground- and excited-state atoms utilizing momentum resolved lattice-modulation spectroscopy [239]. To do so, we prepare a spin polarized gas of ground- or excited-state atoms of $^{171}$Yb predominantly in the lowest band of the combined three dimensional lattice formed by the triangular magic 2D lattice and the state-dependent 1D lattice. We weakly modulate the intensity of the state-dependent lattice beam at a frequency $f_{\mathrm{mod}}$ and thereby drive a transition $\psi_n(q) \rightarrow \psi'_n(q)$ from the ground band $n = 0$ to a higher band $n'$. The transition frequency is determined by the band structure of the lattice and therefore the particle-hole excitation spectrum that is observed using band mapping[29, 240] is used to determine the lattice depth. Figure 5.2 a) shows the momentum-resolved lattice-modulation spectrum for a gas of ground-state atoms in a $s_{\mathrm{SDL,g}} = 4.33(8)\, E_{\mathrm{rec}}$ deep lattice. We observe particle hole pairs corresponding to the excitation in the lowest and the higher Brillouin zone. From the spectrum shown in panel a) we extract the particle excitation resonance frequencies and fit the differential band structure $\Delta E(q) = E_{n'}(s_{\mathrm{SDL}}, q) - E_0(s_{\mathrm{SDL}}, q)$ to determine the actual lattice depth $s_{\mathrm{SDL}}$ as

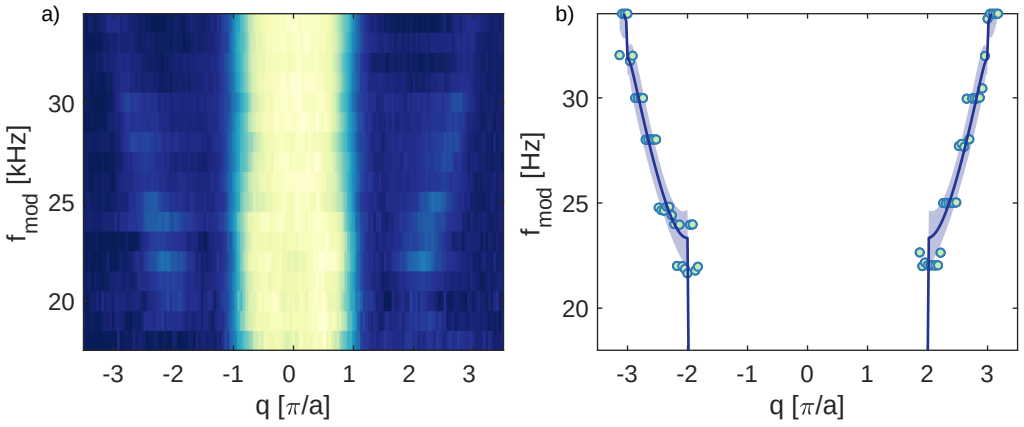


**Figure 5.3.:** Momentum-resolved modulation spectroscopy of a spin polarized gas of $^{171}$Yb atoms prepared in the metastable state $^3P_0$ in the state-dependent optical lattice. Panel a) shows the momentum-resolved excitation spectrum. Each horizontal line represents the the optical density obtained from an absorption image after bandmapping and ToF, integrated along the direction perpendicular to the SDL. Each row is normalized to its maximum. Colors from dark to bright denote the optical density. The lattice depth modulation induces a particle hole excitation. Particles appear in the third Brillouin zone. Corresponding holes in the first Brillouin zone are not visible. Panel b) shows a fit of a 1D-lattice band structure to the particle excitation spectrum $f(q)$, extracted from the data shown in panel a) that yields an excited-state lattice depth of $s_{\mathrm{SDL},e} = 11.7(5)\, E_{\mathrm{rec}}$.

shown in fig. 5.2 panel b). We perform the same measurement but with atoms prepared in the metastable state to determine the lattice depth for atoms in the excited state and the polarizability ratio $\alpha_{\mathrm{e}}/\alpha_{\mathrm{g}}$. Figure 5.3 shows the lattice-modulation spectrum obtained for excited-state atoms in a $s_{\mathrm{SDL},e} = 11.7(5)\, E_{\mathrm{rec}}$ deep lattice. Typically for excited-state atoms, the achieved data quality is worse than for ground-state atoms. However, the small relative uncertainty of the determined lattice depth of approximately 4% underlines the quality of the calibration method. To calibrate the intensity regulation used for the state-dependent lattice, we perform lattice modulation spectroscopy for excited- and ground-state atoms at different set levels of the intensity regulation. The obtained lattice depths are shown in fig. 5.4. We fit a coupled linear model:

$$s_{\mathrm{SDL,g}} = c\, U_{PD} \tag{5.5}$$

$$s_{\mathrm{SDL,e}} = \frac{\alpha_{\mathrm{e}}}{\alpha_{\mathrm{g}}}\, c\, U_{PD} \tag{5.6}$$

leaving the slope $c$ and the polarizability ratio as free parameters. The obtained polarizability ratio of $\alpha_{\mathrm{e}}/\alpha_{\mathrm{g}} = 5.5(3)$ is in excellent agreement with the expected value of $\alpha_{\mathrm{e}}/\alpha_{\mathrm{g}} = 5.5$. Figure 5.4 shows the Hubbard tunneling parameter $J$ calculated for ground- and excited-state atoms as a function of the ground-state lattice depth $s_{\mathrm{SDL,g}}$ for a polarizability ratio of $\alpha_{\mathrm{e}}/\alpha_{\mathrm{g}} = 5.5$. The tunneling rate for excited-state atoms quickly drops and for lattice depths $s_g \gtrsim 2\, E_{\mathrm{rec}}$ it is smaller by more than an order of magnitude. Hence we conclude that a system of localized excited state atoms and simultaneously itinerant ground state atoms is realizable at a lattice wavelength of 660 nm.

In the following the lattice depths of the state-dependent lattice will be given in terms

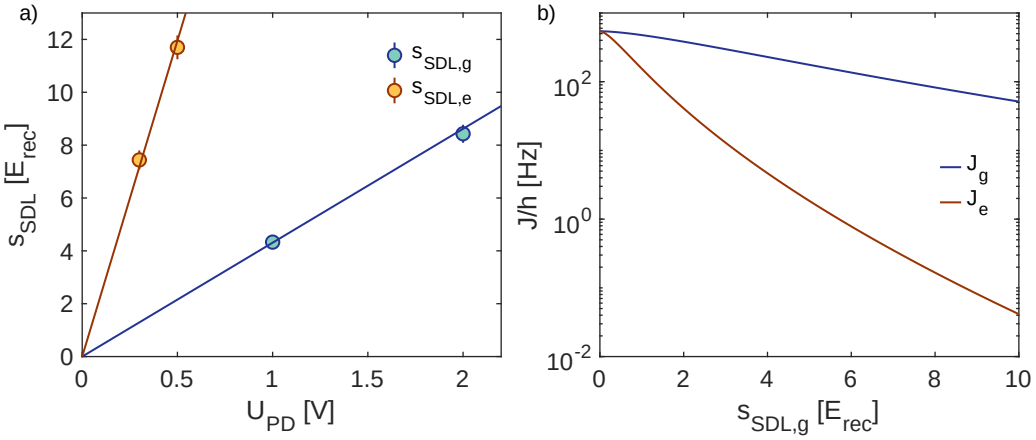


**Figure 5.4.:** Calibration of the SDL photodiode used for intensity regulation. Blue and red data points show the lattice depth obtained from lattice modulation spectroscopy as presented in fig. 5.2 and fog. 5.3 for ground- and excited-state atoms respectively. Solid lines show the calibration curves obtained from a shared fit that yields a polarizability ratio of $\alpha_e/\alpha_g = 5.5(3)$. Panel b) shows the tunneling energy $J$ calculated for the measured polarizability ratio as a function of the ground-state lattice, depth for atoms in the ground (blue line) and excited state (red line). For ground-state lattice depths of $s_g \gtrsim 2\,E_{rec}$ the tunneling energies differ by more than an order of magnitude.

of the ground-state lattice depth $s_{SDL,g}$, the excited state lattice depth is then given by $s_{SDL,e} = 5.5(3)\, s_{SDL,g}$.

## 5.2. Excited-State Preparation in the SDL

Whereas magic optical lattices allow to probe the clock transition with high resolution, in a state dependent lattice the transition is broadenend. In the following, I will present straightforward calculations to estimate the broadening and shift of the clock transition for atoms in the state-dependent lattice. The differential light shift is given by:

$$\Delta E(\lambda, I) = (\alpha_e(\lambda) - \alpha_g(\lambda))\, I. \tag{5.7}$$

At the magic wavelength the differential polarizability $\Delta\alpha = \alpha_e - \alpha_g$ vanishes and the frequency of the clock resonance is not affected by the light shift. Away from the magic wavelength this is explicitly not the case and the resonance frequency depends on the depth of the trapping potential. Therefore the Gaussian intensity profile of the lattice beams leads to a broadening of the transition as the potential depth becomes position dependent.
To estimate the effect of the broadening induced by the state-dependent lattice we assume a Gaussian intensity profile of the lattice beam given by [131]:

$$I_{SDL}(r,z) = I_0 \left(\frac{w_{0,SDL}}{w(z)}\right)^2 e^{\frac{-2r^2}{w^2(z)}} \tag{5.8}$$

where $w(z)$ denotes the waist at position $z$ and is given by [131]:

$$w(z) = w_{0,\mathrm{SDL}}\sqrt{1+\left(\frac{z}{z_\mathrm{R}}\right)^2}. \tag{5.9}$$

Here $w_0$ denotes the waist of the lattice beam, while $z_\mathrm{R}$ represents the Rayleigh range. The waist of the lattice beams has been determined to be $w_{0,\mathrm{SDL}} = 78\,\mu\mathrm{m}$ [90]. The potential is given by $V_{\mathrm{g/e}} = V_{0,\mathrm{g/e}}I(r,z)$, with $V_{0,\mathrm{g/e}} < 0$, and hence its position dependence is given by the intensity distribution of the lattice laser.
The combined three-dimensional lattice potential formed by the one-dimensional state-dependent lattice at $\lambda_\mathrm{SDL} = 660\,\mathrm{nm}$ and the triangular 2D lattice at $\lambda_\mathrm{2D} = 759\,\mathrm{nm}$ can be described by a Bravais lattice with lattice vectors $\boldsymbol{a}_1\ \boldsymbol{a}_2\ \boldsymbol{a}_3$ given by [129]:

$$\boldsymbol{a}_1 = a_\mathrm{2D}\begin{pmatrix}1\\0\\0\end{pmatrix},\quad \boldsymbol{a}_2 = \frac{a_\mathrm{2D}}{2}\begin{pmatrix}\sqrt{3}\\1\\0\end{pmatrix}\quad\text{and}\quad \boldsymbol{a}_3 = a_\mathrm{SDL}\begin{pmatrix}0\\0\\1\end{pmatrix}, \tag{5.10}$$

with $a_{2D} = 2\lambda_\mathrm{2D}/3$ and $a_\mathrm{SDL} = \lambda_\mathrm{SDL}/2$. Any lattice site position $\boldsymbol{R}_{i,j,k}$ can thus be written as $\boldsymbol{R}_{ijk} = i\boldsymbol{a}_1 + j\boldsymbol{a}_2 + k\boldsymbol{a}_3$ with $i,j,k \in \mathbb{N}$. The cylindrical coordinates used in eq. 5.8 thus can be parameterized by:

$$r = |i\boldsymbol{a}_1 + j\boldsymbol{a}_2| \tag{5.11}$$

$$z = k\boldsymbol{a}_3 \tag{5.12}$$

to compute the potential depths $V_{i,j,k}$ at a certain lattice site $\boldsymbol{R}_{ijk}$. In the limit of a deep lattice individual lattice sites can be approximated by harmonic oscillators with an oscillator frequency of:

$$\omega_\mathrm{ho}(R_{ijk}) = \sqrt{\frac{2V(\boldsymbol{R}_{ijk})k_\mathrm{SDL}}{m}}, \tag{5.13}$$

corresponding to a ground state energy of the harmonic oscillator of $E_0 = \hbar\omega_\mathrm{ho}(R_{ijk})/2$. The frequency shift of the clock-transition is then given by:

$$\Delta f = (V_\mathrm{e} + E_{0,\mathrm{e}}) - (V_\mathrm{g} + E_{0,\mathrm{g}})\,. \tag{5.14}$$

To compute the clock-transition frequency shift for every individual lattice site and estimate the broadening of the transition caused by the Gaussian intensity distribution we have to assume a certain lattice occupation. In a lowest order approximation we assume that due to the slow dynamics caused by the large atomic mass of ytterbium the spatial distribution determined by the dipole traps is mapped onto the lattice. Figure 5.5 a) shows the mean shift of the clock resonance $\bar{\Delta f}$ as a function of the ground-state lattice depth $s_{SDL,g}$ calculated for $10^5$ lattice sites inside a cigar-shaped volume with an aspect ratio of $\sqrt{1/3}$. Figure 5.5 b) shows the the spread of resonance frequencies caused by the intensity profile of the lattice beams at different lattice depths. At a lattice depth of $s_{\mathrm{SDl},g} = 20\,E_\mathrm{rec}$ for lattice parameters of $w_0 = 78\,\mu\mathrm{m}$, $\alpha_\mathrm{e}/\alpha_\mathrm{g} = 5.5$ and $10^5$ lattice sites the individual resonance frequencies are spread over $\Delta f_\mathrm{RMS} \approx 1\,\mathrm{kHz}$. According to the previous analysis of the excitation process in shallow lattices (see sec. 3), for efficient

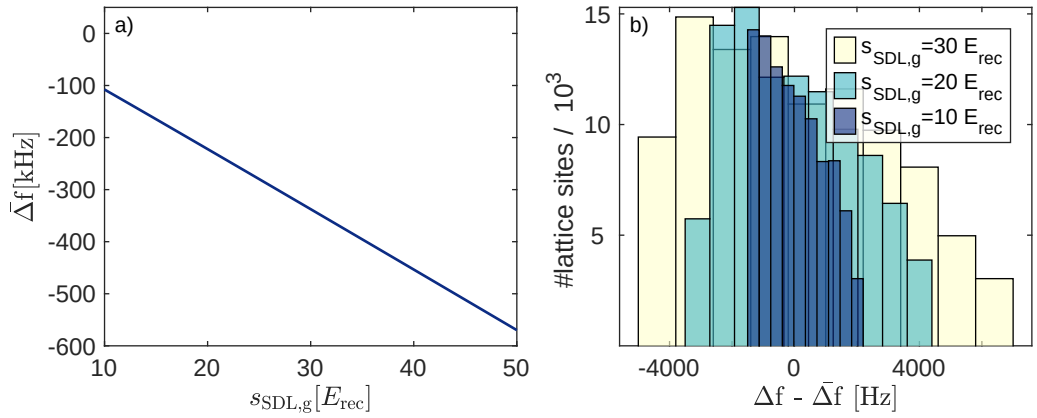


**Figure 5.5.:** Light shifts in the state-dependent lattice. Panel a) shows the mean light shift $\bar{\Delta f}$ as a function of the ground-state lattice depth. Panel b) shows a histogram of the light shifts calculated for $10^5$ lattice sites of our optical lattice assuming a polarizability ratio of $\alpha_{\mathrm{e}}/\alpha_{\mathrm{g}} = 5.5$. To compare the effective broadening for different lattice depths, the mean light shift $\bar{\Delta f}$is subtracted. For the computation, individual lattice sites are approximated by harmonic oscillators, which is a valid approximation in the limit of a deep lattice. Colors from dark to bright indicate an increasing ground-state lattice depth.

state transfer via $\pi$-pulses the Rabi frequency has to be larger than the broadening by at least one order of magnitude. For the $s_{\mathrm{SDL,g}} = 20\,E_{\mathrm{rec}}$ deep lattice this would require Rabi frequencies of $\Omega > 2\pi \times 50\,\mathrm{kHz}$ limiting the the achievable Fourier limited linewidth to $\Gamma > 80\,\mathrm{kHz}$. To resolve the spectroscopic features of the individual spin states of $^{171}$Yb the Zeeman splitting should be significantly larger than the linewidth (e.g. four times). The differential Zeeman shift between the ground- and excited state of $^{171}$Yb is given by $\Delta f_{\mathrm{Z}} = \delta g m_{\mathrm{F}} B$, with $\delta g = -399.0(1)\,\mathrm{Hz/G}$ [68]. Hence, a Zeeman splitting of $\delta f_{\mathrm{Z}} > 4\Gamma = 240\,\mathrm{kHz}$ requires a magnetic field of $B > 600\,\mathrm{G}$, which cannot be reached with the actual setup.

In the spin 1/2 system of $^{171}$Yb for a transition with $\Delta J = 0$, due to the selection rules, $\sigma^+$ and $\sigma^-$ polarized light only couples one transition each, allowing to address a certain spin state without the need of a particular Zeeman splitting. To do so, we change the polarization of the clock beam from linear to circular polarization and the main coils provide a quantization axis along the $z$-direction. Further we use a broad rapid adiabatic passage with $\Delta f_{\mathrm{chirp}} \gg \Delta f_{\mathrm{broadening}}$ to effectively transfer atoms from $|g,\downarrow\rangle \rightarrow |e,\uparrow\rangle$ or $|g,\uparrow\rangle \rightarrow |e,\downarrow\rangle$. As discussed in chapter 3 the transfer efficiency of a rapid adiabatic passage depends on the speed of the frequency chirp. Figure 5.6 b) shows the state transfer of a rapid adiabatic passage on the $\sigma^-$ transition, for different chirp speeds. According to sec. 3.4 varying the RAP chirp velocities or at a given RAP span the chirp time $t_{\mathrm{RAP}}$ allows to control the ratio of ground- and excited-state atoms. Due to the required large magnetic fields spin-resolved excitation of the clock state using $\pi$ pulses of $\pi$-polarized light is technically difficult implement. State preparation using $\sigma^+$ or $\sigma^-$ transitions benefits from the selection rules and constitutes a good alternative.

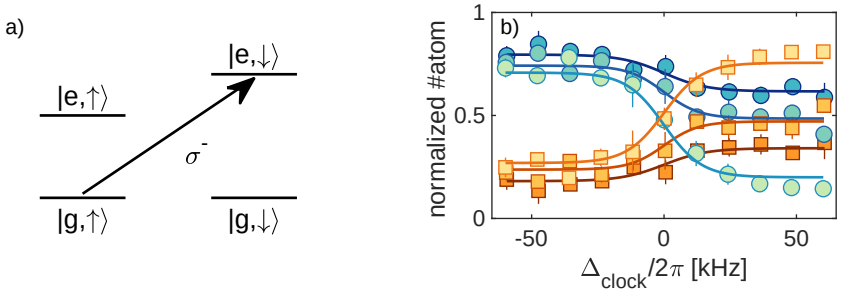


**Figure 5.6.:** Excited state preparation in the state-dependent lattice using a $\sigma^-$ polarized RAP. Panel a) shows the transition addressed by the $\sigma^-$ polarized clock laser. Panel b) shows the excited-state preparation with an adiabatic passage for increasing RAP times $t_{\mathrm{RAP}} = 2\,\mathrm{ms}$, $t_{\mathrm{RAP}} = 3\,\mathrm{ms}$ and $t_{\mathrm{RAP}} = 9\,\mathrm{ms}$, indicated by colors from dark to bright. Solid lines indicate fits to a sigmoid function to guide the eye. We associate the non-zero excited-state fraction at the beginning of the frequency ramp with excitation prior to the RAP that most likely is caused by incorrect switching and shuttering of the clock beam prior to the RAP.

## 5.3. Lattice Lifetimes

Quantum simulation applications involving the metastable state $^3P_0$ as a degree of freedom require a lattice lifetime of the excited-state atoms that exceeds the timescale dominating the dynamics of the system under investigation. Thus for the lattice experiments the lifetimes should be larger than the timescales associated to tunneling and super-exchange processes, at least by an order of magnitude, to achieve a separation of time scales. Figure 5.7 shows a previous measurement of lattice lifetimes in an all magical lattice for $^{173}$Yb[83]. While the $1/e$ lifetime of ground state atoms is found to be $\tau_{\mathrm{g}} \approx 18.5\,\mathrm{s}$, a sample initially prepared in the excited state shows a reduced lifetime of $\tau_e \approx 4.3\,\mathrm{s}$. After a hold time of $t_{\mathrm{hold}} = 8\,\mathrm{s}$ about 40% of the atoms that initially have been prepared in the metastable state decayed back into the ground state.

The wavelength of the state-dependent lattice is closer to the $^1S_0 \rightarrow {}^3P_1$ and $^3P_0 \rightarrow {}^3S_0$ transitions at 556 nm and 649 nm, respectively, than the magic lattice wavelength. As the off-resonant scattering rate scales as $\Gamma_{\mathrm{scat}} \propto I/\Delta^2$ [121], a shorter lattice lifetime, especially of the excited-state atoms is expected.

To characterize the lattice lifetimes of ground-state atoms in the SDL, we load spin-polarized gases of $^{171}$Yb into the combined lattice potential formed by the one-dimensional state-dependent lattice and the triangular magic lattice and observe the atom number decay as a function of the lattice hold time, as shown in fig. 5.8 a). We perform the same measurement for different lattice depths and fit the observed decrease of the atom number with an exponential decay. Figure 5.8 b) shows the extracted $1/e$ lifetimes $\tau_g$. We do not observe a significant lattice depth dependence of the atom number decay (yet the error bars are large). We conclude that lattice photon scattering induced losses for ground-state atoms are negligible, while back ground gas scattering probably is the dominant loss mechanism. We obtain an average lifetime of $\tau_{\mathrm{SDL,g}} = 24.4(1.2)\,\mathrm{s}$, that is comparable to the lifetime of $\tau_{\mathrm{mag,g}} \approx 18.5\,\mathrm{s}$ found for a gas of $^{173}$Yb in an all magical lattice.

We conduct the same experiment, but now prepare a spin-polarized gas in the metastable

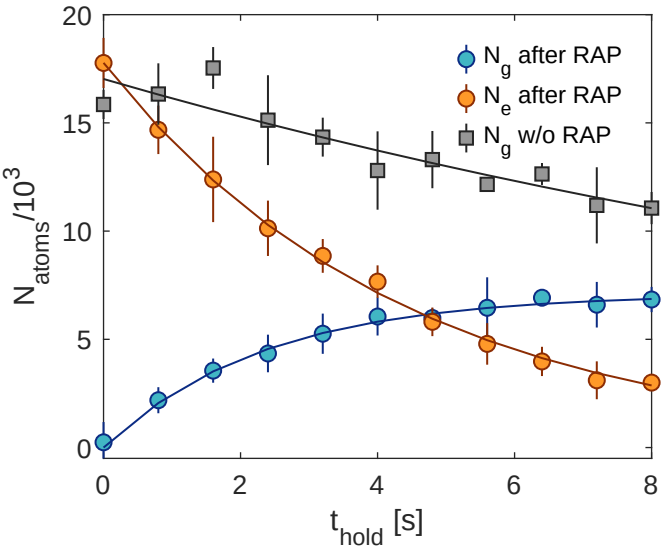


**Figure 5.7.:** Lifetime measurement for ground and excited state atoms of $^{173}$Yb in an all magic lattice, with $s_{1D} = 50\,E_{\text{rec}}$ and $s_{2D} = 18.8\,E_{\text{rec}}$. Grey squares show the particle number for a spin-polarized sample prepared in the ground state as a function of lattice hold time $t_{\text{hold}}$. Blue and orange circles indicate the time evolution of the particle numbers of ground and excited state atoms $N_{\text{g}}$ and $N_{\text{e}}$, respectively, for a sample initially prepared in the excited state using a rapid adiabatic passage. $N_{\text{e}}$ with RAP and $N_{\text{g}}$ without RAP are fitted by a decaying exponential whereas $N_{\text{g}}$ with RAP is fitted with $N(t) = N_0(1 - \exp(-t/\tau))$, respectively. The figure is adapted from [83].

state $^3P_0$ via a rapid adiabatic passage. Residual ground state atoms are removed by a pulse of resonant blue light. We detect the population of ground and excited state, and resolve the spin population of the ground state atoms using the OSG-technique 1.5. In addition to particle losses caused by background gas scattering and off-resonant lattice photon scattering, the metastable state naturally decays with a rate of $\Gamma_0$ into the ground state. However, as the linewidth is estimated to be smaller than 10 mHz [102] we expect spontaneous decay to be negligible on the experimental timescale. Yet as shown in fig. 5.7 even in the magic lattice we observe a decay of excited state atoms on timescales faster than the natural lifetime of the metastable state, which most likely is associated to a lattice light induced process. On the other hand the SDL is only detuned by 11 nm with the respect to the $^3P_0 \rightarrow {}^3S_1$ transition at 649 nm and therefore off-resonant scattering is expected to be more prominent compared to the magic lattice.
Figure 5.9 shows the ground- and excited-state population as a function of lattice hold time for different lattice depths. We observe a lattice-depth-dependent decay of the excited-state atom number and an increase of the ground-state population, which is faster than expected for spontaneous decay. According to ref. [241] this can be explained by off-resonant Raman scattering from $^3P_0 \rightarrow {}^3P_1$ with intermediate state $^3S_1$ and subsequent radiative decay from the $^3P_1$ state into the ground state $^1S_0$. The time evolution of the particle numbers for ground and excited state atoms $N_{\text{e}}$ and $N_{\text{g}}$ can be described by two

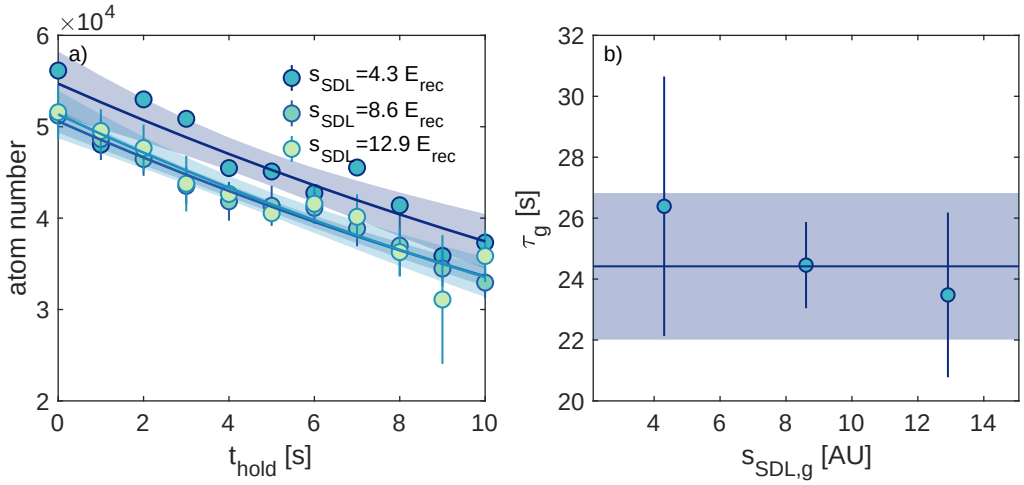


**Figure 5.8.:** Life times of ground state atoms in the SDL. Panel a) shows the atom number as a function of lattice hold time. Colors from dark to bright indicate an increasing 1D lattice depth $s_{1D}$. Data points for a lattice depths of $s_{1D} = 8.6$ and $s_{1D} = 12.9$ are the average of three measurements, with error bars indicating the standard deviation of the mean. Data points for a lattice depths of $s_{1D} = 4.3$ correspond to single measurements. Solid lines represents the fit of an exponential decay and shaded areas show the 95% confidence interval. The determined lifetimes shown in panel b) do not significantly differ. The solid line shows a weighted mean yielding an average lifetime of $\tau_\mathrm{g} = 24.4(1.2)\,\mathrm{s}$ with the shaded area representing the 95% confidence interval.

coupled differential equations:

$$\dot{N}_e = -\Gamma_{\mathrm{loss,e}} N_\mathrm{e} - (\Gamma_0 + \Gamma_\mathrm{lat}) N_e \tag{5.15}$$

$$\dot{N}_g = -\Gamma_{\mathrm{loss,g}} N_\mathrm{g} + (\Gamma_0 + \Gamma_\mathrm{lat}) N_\mathrm{e}, \tag{5.16}$$

here $\Gamma_{\mathrm{loss,g/e}}$ describes losses of ground and excited state atoms, respectively, while $\Gamma_\mathrm{lat}$ describes a lattice photon scattering induced decay of excited-state atoms into ground state atoms. The analytical solutions to equations 5.15 and 5.16 read [241]:

$$N_\mathrm{e}(t) = N_\mathrm{e}(0)\exp(-[\Gamma_{\mathrm{loss,e}} + \Gamma_0 + \Gamma_\mathrm{lat}]t) \tag{5.17}$$

$$N_\mathrm{g}(t) = \left(N_\mathrm{e}(0)\frac{1-\exp(-[\Gamma_{\mathrm{loss,e}} - \Gamma_{\mathrm{loss,g}} + \Gamma_0 + \Gamma_\mathrm{lat}]t)}{1 + (\Gamma_{\mathrm{loss,e}} - \Gamma_{\mathrm{loss,g}})/(\Gamma_0 + \Gamma_\mathrm{lat})} + N_\mathrm{g}(0)\right)\exp(-\Gamma_{\mathrm{loss,g}} t) \tag{5.18}$$

According to the expected linear scaling of the off-resonant photon scattering rate with the intensity [121], the lattice depth dependence of the lattice photon scattering is modeled using a linear ansatz for $\Gamma_\mathrm{lat}$:

$$\Gamma_\mathrm{lat}(s) = c_\mathrm{lat}\frac{\mathrm{Hz}}{E_\mathrm{rec}} s_{\mathrm{SDL,g}}. \tag{5.19}$$

Different from the results presented in [241], in our measurements we observe a lattice depth dependence of the loss rate $\Gamma_{\mathrm{loss,e}}$. This suggests that not all atoms which decay to the ground state via lattice-photon scattering are trapped. This behavior might be

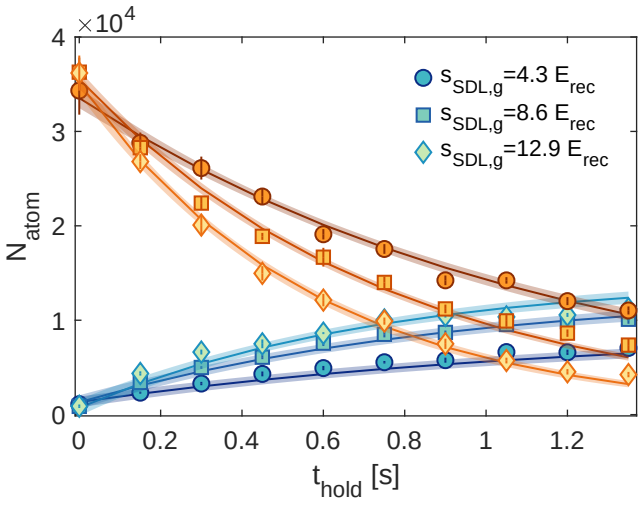


**Figure 5.9.:** State-dependent lattice lifetime measurement for atoms in the metastable state. The number of atoms in the excited state denoted by orange colors and ground-state atoms denoted by blue colors, is shown as a function of lattice hold time. Different symbols indicate different SDL lattice depths as denoted in the legend. Solid lines represent a combined fit of the complete data set using the solutions of the coupled equations eq. 5.17 and eq. 5.18. Shaded areas show 95% confidence intervals of the fit. Data points are the average of three individual measurements, with error bars indicating the standard deviation of the mean.

associated to the low value of the ground-state lattice depths which are smaller than the lattice depths used in ref. [241] by a factor of ten, and do not fulfill the Lamb-Dicke condition. At the low to moderate depths for ground state atoms due to tunneling processes, losses caused by inelastic *eg* collisions might play a role. To account for the lattice depth dependence of the excited-state atom loss we use a linear ansatz for $\Gamma_{\mathrm{loss,e}}$

$$\Gamma_{\mathrm{loss,e}}(s) = c_{\mathrm{loss,e}} \frac{\mathrm{Hz}}{E_{\mathrm{rec}}} s_{\mathrm{SDL,g}} + c_{\mathrm{loss,e,0}}. \tag{5.20}$$

Using the value of $\Gamma_{\mathrm{loss,g}} = 41.7(1.7)\,\mathrm{mHz}$ obtained from the ground-state lifetime measurement and assuming a spontaneous decay rate of $\Gamma_0 = 10\,\mathrm{mHz}$ the entire data set is fitted using, eq. 5.17-5.18 leaving the decay rates $\Gamma_{\mathrm{loss,e}}(s)$ and $\Gamma_{\mathrm{lat}}(s)$ as free parameters. From the fit we determine the lattice-photon scattering induced decay to be:

$$\Gamma_{\mathrm{lat}} = 0.041(2) \frac{\mathrm{Hz}}{E_{\mathrm{rec}}} s_{\mathrm{SDL,g}}. \tag{5.21}$$

Accordingly the excited-state loss is determined to be:

$$\Gamma_{\mathrm{loss}} = 0.065(7) \frac{\mathrm{Hz}}{E_{\mathrm{rec}}} s_{\mathrm{SDL,g}} + 0.39(5)\,\mathrm{Hz}. \tag{5.22}$$

Our finding indicates that about 65(7)% of the atoms that undergo lattice-photon induced decay are lost whereas about 41(1)% are trapped and appear as ground state atoms in fig. 5.9.

As the lattice-photon scattering-induced decay to the ground state involves radiative decay of an intermediate state, e.g. $^3P_1$, the decay process is not spin-preserving. Analysing

the spin population of the ground state atoms, we find that about 39.1(5)% of the atoms exhibit a spin-flip, whereas 60.9(5)% remain in the initial $m_F$ state, which we associate with different Clebsch-Gordan coefficients for spin-changing and spin-preserving decay channels. For the decay from ${}^3P_1, F = 3/2, m_F = \pm 1/2$ to the ${}^1S_0$ ground states these are given by $\sqrt{3}/3$ and $\sqrt{6}/3$ [92], respectively, and therefore are in qualitative agreement with the measured value. Further characterization of the losses in the optical lattice are beyond the scope of this thesis and are left for future work.
In conclusion, we have characterized the lattice lifetimes of ground and excited atoms in the state-dependent lattice. The lifetime of ground-state atoms does not depend on the lattice depths and is on the order of 20 s. Compared to the all magic lattice, the lifetime for excited state atoms on the order of $\tau_e \sim 1$s is significantly reduced, and crucially depends on the lattice depth. Yet the lifetimes are much larger than the experimental timescale and the ground-state tunneling times which are typically on the order of milliseconds. Therefore, we conclude that despite the reduced lattice lifetime in the SDL, the observation of spin-exchange dynamics in the state-dependent lattice should be possible.

## 5.4. Observation of Spin-Exchange Dynamics in a State Dependent Lattice

As a first step towards quantum simulation of multi-band systems with ${}^{171}$Yb, we aim to observe orbital spin-exchange dynamics in the state-dependent lattice. The experiments presented in the following were inspired by experiments conducted by the Munich group with ${}^{173}$Yb in a one-dimensional state-dependent lattice at $\lambda_{\mathrm{SDL}} = 670\,\mathrm{nm}$ [77], that show a spin-exchange rate, tunable by the 2D magic lattice confinement. Very recently, we became aware of a study similar to the measurements presented in the following with ${}^{171}$Yb in a state-dependent lattice at 650.7 nm [78].
We start with a spin-polarized gas of $25 - 35 \times 10^3$ ground state atoms prepared in the $|g, \uparrow\rangle$ state at a temperature of $T \approx 0.3\,T_F$ in a deep optical lattice. The 2D-lattice is operated at $s_{\mathrm{2D}} = 30\,E_{\mathrm{rec}}$ whereas the state-dependent lattice is operated at a depth of $s_{\mathrm{SDL,g}} = 17\,E_{\mathrm{rec}}$. A fast rapid adiabatic passage using $\sigma^-$ polarized light with $\Delta f_{\mathrm{RAP}} = 120\,\mathrm{kHz}$ and $t_{\mathrm{RAP}} = 2\,\mathrm{ms}$ is used to transfer approximately half of the atoms to the excited state $|e, \downarrow\rangle$ at a magnetic field of $B = 9\,\mathrm{G}$. Subsequently the state-dependent lattice is ramped down to a final value between $s_{\mathrm{SDL,g}} = 1.1\,E_{\mathrm{rec}}$ and $s_{\mathrm{SDL,g}} = 3.2\,E_{\mathrm{rec}}$ within 10 ms, to allow for tunneling and to initiate dynamics. The magnetic field is ramped down to a final value of $B = 2\,\mathrm{G}$. Interorbital spin-exchange processes are expected to decrease the spin polarization of the ground and excited state. We use absorption imaging combined with repumping and OSG techniques to detect the population of ground and excited state with spin resolution for ground-state atoms. To detect spin-exchange dynamics we observe the population of the different states as a function of the SDL hold time .
Figure 5.10 shows exemplary absorption images obtained for a final depth of the state-dependent lattice of $s_{\mathrm{SDL,g}} = 1.1\,E_{\mathrm{rec}}$ for different SDL hold times. Three different clouds correspond to atoms in the excited state, and in the different $m_F$-states of the ground state. Figure 5.11 shows atom numbers determined from the absorption images normal-

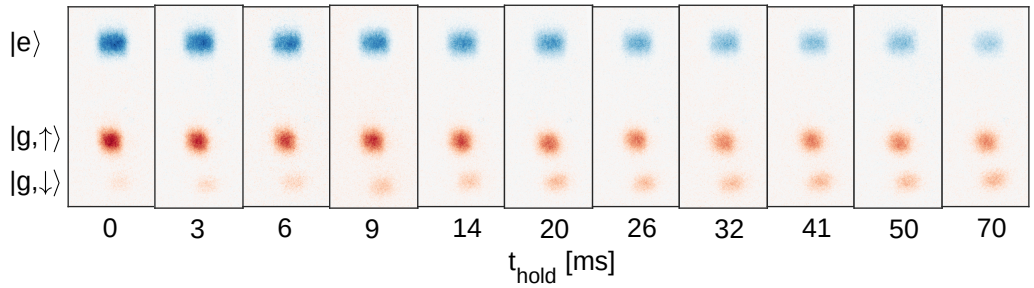


**Figure 5.10.:** Absorption images for different SDL hold times, $t_{\text{hold}}$, at a lattice depth of $s_{\text{SDL,g}} = 1.1\,E_{\text{rec}}$. Visible are three different clouds corresponding to ground-state atoms, indicated in red and excite-state atoms indicated in blue. The spin population for ground-state atoms is resolved using the OSG technique. As the SDL hold time increases the population of the states $|\text{e}\rangle$ and $|\text{g},\uparrow\rangle$ decreases, while the population of the state $|\text{g},\downarrow\rangle$ increases. Every image is the average of three individual images.

ized to the total number of atoms at $t_{\text{hold}} = 10\,\mu$s, for lattice depths of a) $s_{\text{SDL,g}} = 3.1\,E_{\text{rec}}$, b) $s_{\text{SDL,g}} = 2.2\,E_{\text{rec}}$ and c) $s_{\text{SDL,g}} = 1.1\,E_{\text{rec}}$. For all three lattice depths we observe a loss of excited state atoms and the number of atoms in the state $|\text{g},\uparrow\rangle$ decreases, while the number of atoms in the state $|\text{g},\downarrow\rangle$ increases.

In the prepared system many processes can drive particle number dynamics. In analogy to [78, 222] we use a simple rate-equation-based model to describe the dynamics of the system. We distinguish several processes that affect the particle number dynamics. Background losses ultimately limit the lifetime of ground and excited state atoms in the optical lattice. These losses have been characterized previously and correspond to decay rates $\Gamma_{\text{loss,g}}$ and $\Gamma_{\text{loss,e}}(s_{\text{SDL,g}})$. Lattice-photon scattering-induced decay of excited-state atoms to ground-state atoms increases the number of ground state atoms, and has been characterized by a rate of $\Gamma_{\text{lat}}(s_{\text{SDL,g}})$. Due to the different Clebsch-Gordan coefficients for the different radiative decay channels involved, the spin of the excited state atoms is not preserved. Based on Clebsch-Gordan coefficients for the decay of the state ${}^3P_1, F = 3/2, m_F = \pm 1/2$, we assume that 2/3 of the decay processes are spin-preserving while 1/3 is spin-changing (see e.g. ref. [92] for the Clebsch-Gordan coefficients). Inelastic collisions between excited-state atoms with different spins correspond to a loss rate of $\Gamma_{ee}$ while inelastic collisions of atoms in different orbitals correspond to a loss rate of $\Gamma_{eg}$. Interorbital spin-exchange processes reduce the spin polarization of ground- and excited-state and are described by a rate $\gamma_{\text{ex}}$.

Considering the four different states of the system $|g,\downarrow\rangle$, $|g,\uparrow\rangle$, $|e,\downarrow\rangle$ and $|e,\uparrow\rangle$ The

particle-number dynamics is modeled by four coupled differential equations:

$$\dot{N}_{\mathrm{g},\uparrow} = \gamma_{\mathrm{ex}}(N_{\mathrm{e},\uparrow}N_{\mathrm{g},\downarrow} - N_{\mathrm{e},\downarrow}N_{\mathrm{g},\uparrow}) - \Gamma_{\mathrm{eg}}N_{\mathrm{g},\uparrow}(N_{\mathrm{e},\uparrow} + N_{\mathrm{e},\downarrow}) + \Gamma_{\mathrm{lat}}(\frac{2}{3}N_{\mathrm{e},\uparrow} + \frac{1}{3}N_{\mathrm{e},\downarrow}) - \Gamma_{\mathrm{loss,g}}N_{\mathrm{g},\uparrow} \tag{5.23}$$

$$\dot{N}_{\mathrm{g},\downarrow} = \gamma_{\mathrm{ex}}(N_{\mathrm{e},\downarrow}N_{\mathrm{g},\uparrow} - N_{\mathrm{e},\uparrow}N_{\mathrm{g},\downarrow}) - \Gamma_{\mathrm{eg}}N_{\mathrm{g},\downarrow}(N_{\mathrm{e},\downarrow} + N_{\mathrm{e},\downarrow}) + \Gamma_{\mathrm{lat}}(\frac{1}{3}N_{\mathrm{e},\uparrow} + \frac{2}{3}N_{\mathrm{e},\downarrow}) - \Gamma_{\mathrm{loss,g}}N_{\mathrm{g},\downarrow} \tag{5.24}$$

$$\dot{N}_{\mathrm{e},\uparrow} = \gamma_{\mathrm{ex}}(N_{\mathrm{e},\downarrow}N_{\mathrm{g},\uparrow} - N_{\mathrm{e},\uparrow}N_{\mathrm{g},\downarrow}) - \Gamma_{\mathrm{eg}}N_{\mathrm{e},\uparrow}(N_{\mathrm{g},\uparrow} + N_{\mathrm{g},\downarrow}) - \Gamma_{\mathrm{ee}}N_{\mathrm{e},\uparrow}n_{\mathrm{e},\downarrow} - N_{\mathrm{e},\uparrow}(\Gamma_{\mathrm{loss,e}} + \Gamma_{\mathrm{lat}}) \tag{5.25}$$

$$\dot{N}_{\mathrm{e},\downarrow} = \gamma_{\mathrm{ex}}(N_{\mathrm{e},\uparrow}N_{\mathrm{g},\downarrow} - N_{\mathrm{e},\downarrow}N_{\mathrm{g},\uparrow}) - \Gamma_{\mathrm{eg}}N_{\mathrm{e},\downarrow}(N_{\mathrm{g},\uparrow} + N_{\mathrm{g},\downarrow}) - \Gamma_{\mathrm{ee}}N_{\mathrm{e},\uparrow}N_{\mathrm{e},\downarrow} - N_{\mathrm{e},\downarrow}(\Gamma_{\mathrm{loss,e}} + \Gamma_{\mathrm{lat}}). \tag{5.26}$$

We fit a numerically obtained solution of equations 5.23-5.26 to the data, leaving $\gamma_{\mathrm{ex}}$, $\Gamma_{\mathrm{ee}}$ and $\Gamma_{\mathrm{eg}}$ as well as the initial populations as fitting parameters, while for $\Gamma_{\mathrm{lat}}$, $\Gamma_{\mathrm{loss,f}}$ and $\Gamma_{\mathrm{loss,e}}$ we use the values obtained in the characterization measurements presented in sec. 5.3. The fits to equations 5.23-5.26 are shown in figure 5.11 and reasonably reproduce the observed dynamics. Figure 5.12 shows the loss and spin-exchange rates as well as the initial state populations as obtained from the fits. The extracted spin-exchange rates between $\gamma_{\mathrm{ex}} = 12(7)\,\mathrm{Hz}$ for $s_{\mathrm{SDL,g}} = 3.2\,E_{\mathrm{rec}}$ and $\gamma_{\mathrm{ex}} = 56(8)\,\mathrm{Hz}$ for $s_{\mathrm{SDL,g}} = 1.1\,E_{\mathrm{rec}}$ exceed the rates measured for lattice-photon induced decay by an order of magnitude. Therefore, we conclude that the depolarization of the ground state population is not caused by lattice-photon scattering induced decay of excited-state atoms but indeed is a direct consequence of interorbital spin-exchange processes.
As the experiments start with a spin-polarized sample due to the Pauli principle there is no initial double occupancy. The interorbital spin-exchange and the two-body losses considered in equations eqs. 5.23-5.26 therefore require tunneling and are supposed to be of super-exchange kind. As depicted in fig. 5.12 panel a) the rates for two-body losses and spin-exchange increase as tunneling times increase. Especially the increase of the excited-state pair losses as the lattice depth is decreased from $s_{\mathrm{SDL,g}} = 2.2\,E_{\mathrm{rec}}$ to $s_{\mathrm{SDL,g}} = 1.1\,E_{\mathrm{rec}}$, is noteworthy and to our understanding is connected to excited-state tunneling. At a lattice depth of $s_{\mathrm{SDL,g}} = 1.1\,E_{\mathrm{rec}}$ the tunneling times for ground- and excited state atoms becomes comparable and hence, for lattice depths below $s_{\mathrm{SDL,g}} < 2\,E_{\mathrm{rec}}$ excited-state atoms cannot be considered localized. Connecting the observed spin-exchange rates to the spin-exchange interaction measured in sec. 4.2, however, is difficult as it would require a mircoscopical model taking into account correlations, that are unknown. Initially, we assumed that prior to the start of the dynamics, the system is exclusively prepared in the states $|g,\uparrow\rangle$ and $|e,\downarrow\rangle$. However, the fit results presented in figure 5.12 b) suggest that $n_{\mathrm{e},\downarrow} = 20.5(1.6)\%$ of the atoms initially are prepared in the state $|e,\uparrow\rangle$. This could be caused by several reasons:

- The polarization of the clock laser is not set properly and thus during the rapid adiabatic passage we do not only drive the $\sigma^-$ but also the $\pi$ transition and hence the other spin state is populated as well.
- In this particular measurement we underestimate the loss rate $\Gamma_{\mathrm{loss,e}}$. During the fitting routine this is compensated for by overestimating $n_{\mathrm{e},\downarrow}$ and $\Gamma_{ee}$.

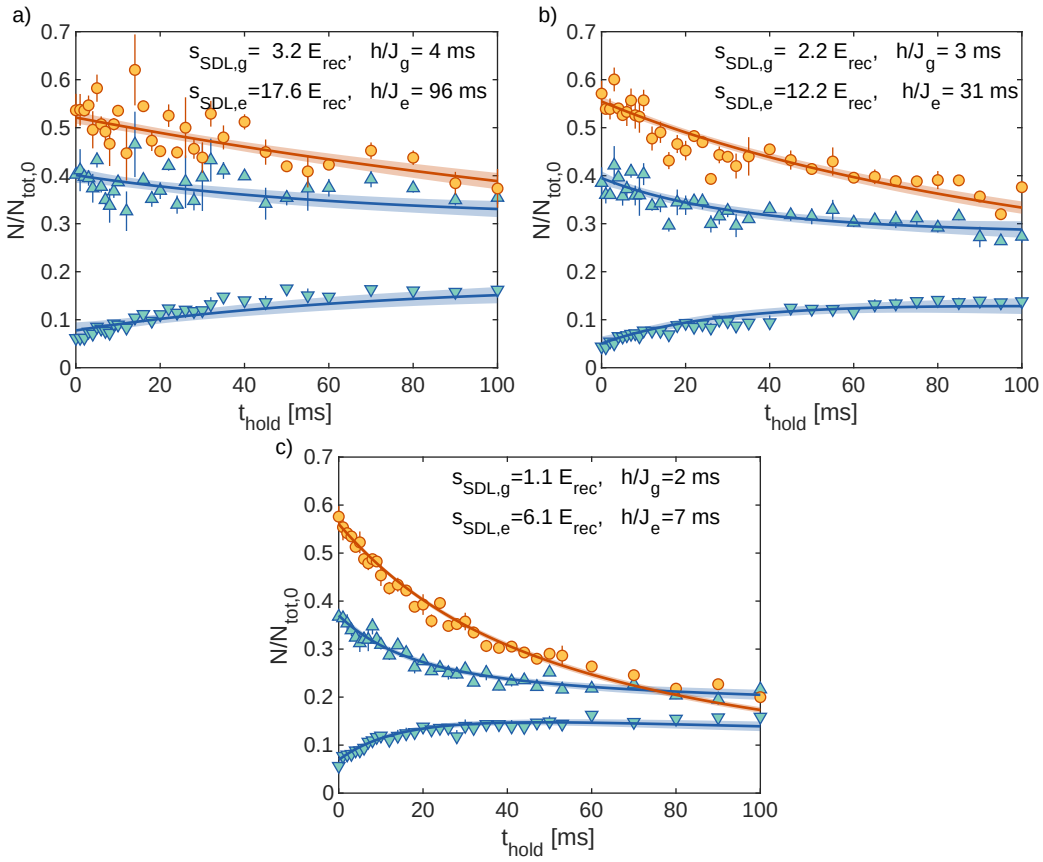


**Figure 5.11.:** Particle number dynamics in the SDL normalized to the total number of atoms at $t_{\text{hold}} = 10\,\mu$s. Panel a) to c) show data obtained for a set lattice depth of the state-dependent lattice of $s_{\text{SDL,g}} = 1.1\,E_{\text{rec}}$, $s_{\text{SDL,g}} = 2.2\,E_{\text{rec}}$ and $s_{\text{SDL,g}} = 3.2\,E_{\text{rec}}$. Orange circles show the number of atoms in the excited state, while blue downward pointing triangles represent the number of ground state atoms in $m_F = -1/2$. Upward pointing triangles show the number of ground state atoms in $m_F = 1/2$. Solid lines indicate fits to the differential equations 5.23-5.26. Data points are the weighted average of three individual images and error bars indicate one standard deviation. Shaded areas show the 95% confidence intervals of the fits.

- The all-classical model is not capable to properly describe the dynamics of the system as non-classical many-body effects play an important role (compare e.g. [1] for dissipative dynamics in a the Fermi-Hubbard model).

We tried fitting the data with a fixed initial population, however the data is significantly better described by leaving the initial population as a free parameter. Given the fact that with our current set-up we cannot access the spin population of the excited state this is well justified.

## 5.5. Conclusion and Outlook

In this chapter I have presented measurements with gases of $^{171}$Yb in a one-dimensional state-dependent lattice at $\lambda_{\text{SDL}} = 660\,$nm. I have characterized lattice lifetimes and the

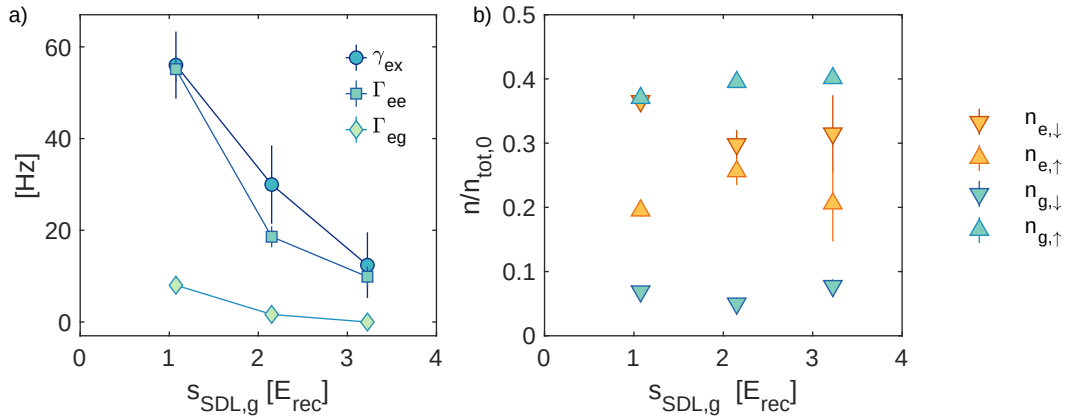


**Figure 5.12.:** Panel a) shows the loss and spin-exchange rates obtained from the fits shown in fig. 5.11. Data points are connected by lines as a guide to the eye. Panel b) shows the initial population of the different states as a function of the set lattice depth as obtained from the fits shown in fig. 5.11.

lattice-photon scattering-induced decay of excited-state atoms. The measured polarizability ratio of $\alpha_e/\alpha_g = 5.5(3)$ allows to create lattice potentials with vastly different mobility properties for atoms in ground and excited state. The differential light shift causes a lattice-depth dependent shift of the clock transition, while the Gaussian intensity distribution of the lattice beams cause a broadening of the transition for the atomic ensemble. For our currently reachable magnetic fields, the broadening prevents a spin-selective addressing of the clock transition using $\pi-$polarized light. Nevertheless combining optical pumping on the ${}^1S_0 \rightarrow {}^3P_1$ transition and excitation with $\sigma^{\pm}$ polarized light allows to prepare different interorbital spin configurations. However, as the spin population of the excited state is not accessible it is not possible to monitor the spin-state preparation for excited-state atoms. Finally, I presented first measurements showing spin-exchange dynamics in a state-dependent lattice. Our measurements show similar results to measurements recently reported by the Kyoto group [78] and represent an important step towards quantum simulation of Kondo lattice type physics. Heavy Fermion behavior is expected for temperatures well below the Kondo temperature $T_K$. According to ref. [78] the Kondo temperature can be estimated by:

$$k_B T_K = D\sqrt{2|V_{ex}|\rho}\exp\left(-\frac{1}{2|V_{ex}|\rho}\right), \tag{5.27}$$

where $D$ and $\rho$ denote the bandwidth and the density of states and are estimated to be $D = 2J_g$ and $\rho = 1/(2\pi J_g)$, respectively. Figure 5.13 a) shows the Hubbard parameters $J_g$, $V_{dir}$, and $V_{ex}$, for a 2D lattice depth of $s_{2D} = 30\,E_{rec}$ and a variable 1D lattice depth of the state dependent lattice[1]. Using eq. 5.27 and the values obtained for $J_g$ and $V_{ex}$ we can estimate the Kondo temperature for our experimental settings as shown in fig. 5.13 b). According

[1]To account for the state dependent confinement of the lattice the interaction parameters $V_{ex}$ and $V_{dir}$ have been computed using a Wannier integral of the form $\int w_g(\boldsymbol{r})^2 w_e(\boldsymbol{r})^2 d\boldsymbol{r}$, where $w_{g,e}(\boldsymbol{r})$ denotes the Wannier function for an atom in the ground or excited state, respectively [242].

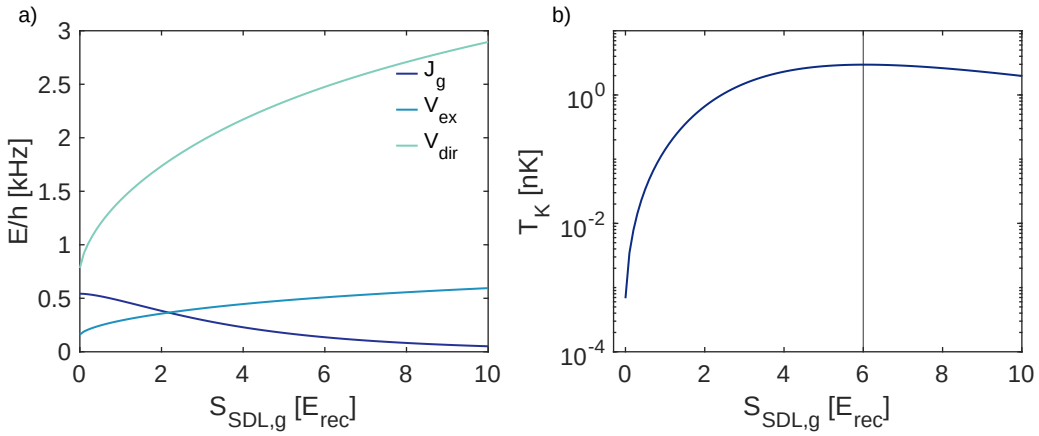


**Figure 5.13.:** Hubbard parameters in the state dependent lattice and the Kondo temperature calculated according to eq. 5.27 for a 2D lattice depth of $s_{2D} = 30\,E_{rec}$.

to ref. [78] the eq. 5.27 is only valid for $|V_{ex}|\rho < 0.6$. This is the region left of the vertical line in fig. 5.13. For our experimental settings we obtain a maximum Kondo temperature of $\sim 3\,\mathrm{nK}$. Experimentally reaching temperatures this low with the current setup is rather impossible, or might be at least extremely challenging. Yet, the experimentally measured temperatures of the gases are obtained for a bulk cloud in a dipole trap. In a lattice it is more reasonable to discuss temperatures rather in terms of entropy. In quantum gas microscopes entropy-engineering has been successfully used to enter the low temperature regime of the Fermi-Hubbard model and observe antiferromagnetic ordering, which requires very low temperatures as well [39]. Therefore, it cannot be excluded that there might be ways to reach the Kondo temperature as well. Other groups however, obtained larger values of the Kondo temperature, which experimentally might be better feasible: In ref. [78] the Kondo temperature is estimated to be on the order of 10 nK. Whereas in ref. [243] the authors argue that using confinement induced resonances for $^{173}$Yb on the one hand the spin-exchange interaction can be tuned to be antiferromagnetic and on the other hand the Kondo temperature is experimentally well within reach. For future work especially the preparation of a distinct initial state remains a challenging task. Emulation of the KLM Hamiltonian eq. 5.1 requires half filling for the localized spins/excited state atoms. Given the diminished degree of control over the orbital state caused by the differential light shift in the state-dependent lattice, developing precise preparation schemes for quantum simulation applications remains a challenging open task. The same holds for observables allowing to detect heavy Fermion behavior.
To gain more control over the spin population in the excited state, we plan to implement a spin-selective detection scheme, based on spin-selective repumping techniques. To this end, we plan to replace the current repumping laser by a frequency stabilized diode laser, to allow for spin selective addressing of the repumping transition. A PDH frequency stabilization of the new repumping laser has been setup by N. Pintul over the course of her master's thesis [123], that has been co-supervised by the author.

# 6. Outlook

In this thesis I presented a versatile apparatus that allows creating ytterbium quantum gases of fermionic $^{171}$Yb and $^{173}$Yb as well as Fermi-Fermi mixtures of both isotopes. Resonant optical pumping on the $^1S_0 \rightarrow {}^3P_1$ transition and coherent clock spectroscopy on the $^1S_0 \rightarrow {}^3P_0$ transition offer a great extent of control over spin and orbital degrees of freedom. Some $10^4$ atoms can be loaded into the lowest Bloch-band of a combined 3D optical lattice formed by a one-dimensional and a two-dimensional triangular lattice at the magic wavelength of $\lambda_{\mathrm{mag}} = 759\,\mathrm{nm}$. The $^1S_0 \rightarrow {}^3P_o$ clock transition is probed using a narrow linewidth laser at a wavelength of $\lambda_{\mathrm{clock}} = 578\,\mathrm{nm}$ which is stabilized to an ultrastable high-finesse resonator and characterized by a laser linewidth on the order of 1 Hz. In a deep magic lattice a maximal spectroscopic resolution, characterized by a spectroscopic linewidth of 26.7(2.4) Hz, has been reached. However, drifts of the clock laser frequency effectively hinder working at the highest resolution for extended periods. In the future, the long-term stability of the clock laser frequency could be improved by actively stabilizing the laser to the atomic resonance.

By the means of clock spectroscopy we characterized elastic and inelastic interorbital interisotope two-particle interactions in Fermi-Fermi mixtures of $^{171}$Yb and $^{173}$Yb and directly showed the $SU(2) \otimes \mathrm{SU}(6)$ symmetry of the elastic interactions. We find similar elastic interactions for pairs of $^{171}\mathrm{Yb}_e - {}^{171}\mathrm{Yb}_g$ and $^{171}\mathrm{Yb}_g - {}^{171}\mathrm{Yb}_e$, which is associated to a high degree of symmetry of the molecular potential. The inelastic interactions for the different electronic configurations differ, however, by a factor of roughly 400. Our measurement possibly can improve the understanding of the molecular potential of interisotope *eg*-pairs. In the future, our studies could be complemented by spectroscopic measurements of different ytterbium mixtures involving the bosonic isotope $^{174}$Yb. In contrast to the ytterbium Fermi-Fermi mixture, Bose-Fermi mixtures with $^{174}$Yb are characterized by a repulsive interisotope *s*-wave interaction [118]. Interorbital multi-body interactions have been studied previously in gases of $^{174}$Yb [221]. Therefore, ytterbium Bose-Fermi mixtures might pave the way towards the observation of interorbital interisotope multibody interactions. These systems might also be well suited to study interaction-induced decoherence in a well-controlled and distinctly different environment. Mixtures of $^{171}$Yb-$^{173}$Yb have also been proposed for the investigation of three-body bound states [244], or the simulation of two-flavor symmetry-locking phases [79, 80].

Furthermore the interorbital spin-exchange interaction in two spin-component gases of $^{171}$Yb has been studied and its previously measured [62, 68] antiferromagnetic nature has been confirmed. The antiferromagnetic spin-exchange interaction and the vanishing ground state interaction render $^{171}$Yb an intriguing candidate for quantum simulation of the Kondo-Lattice model in state-dependent optical potentials.

A state-dependent optical 1D lattice at a wavelength of $\lambda_{SDL} = 660\,\mathrm{nm}$ has been characterized, and in a step towards quantum simulation of multi-band Hubbard models interor-

bital spin-exchange dynamics in a gas of $^{171}$Yb in the state-dependent lattice have been observed. However, reaching temperatures well below the Kondo temperature with the current experimental setup will be very challenging and might instead require quantum-gas-microscope techniques. Yet, a system with distinctly different mobility properties for ground- and excited-state atoms can be realized. In a similar system of $^{171}$Yb in a state-dependent lattice at $\lambda = 671.5\,\mathrm{nm}$ transport properties altered by the interspecies interaction have been recently studied [245]. The current setup could be used to develop more advanced state preparation protocols, which are necessary because the state-dependent lattice diminishes the degree of control over the metastable state due to the non-vanishing light shift.
In previous measurements not described in this thesis (see refs. [1, 98]) we studied dissipative dynamics in a dissipative 1D-Fermi-Hubbard system of $^{173}$Yb atoms in the metastable state in a magic optical lattice. The observed particle number dynamics indicate the formation of a highly entangled Dicke-state [98]. $^{171}$Yb allows to study the dissipative Fermi-Hubbard model in a different parameter regime as the elastic and inelastic excited-state interactions are different. Studies of dissipative dynamics with $^{171}$Yb would therefore complement our previous studies.

# Bibliography


[1] K. Sponselee, L. Freystatzky, B. Abeln, M. Diem, B. Hundt, A. Kochanke, T. Ponath, B. Santra, L. Mathey, K. Sengstock, and C. Becker. Dynamics of ultracold quantum gases in the dissipative Fermi–Hubbard model. *Quantum Science and Technology*, 4(1):014002, (2018). doi: 10.1088/2058-9565/aadccd.

[2] B. Abeln, K. Sponselee, M. Diem, N. Pintul, K. Sengstock, and C. Becker. Interorbital interactions in an SU(2) $\bigotimes$ SU(6)-symmetric Fermi-Fermi mixture. *Phys. Rev. A*, 103:033315, (2021). doi: 10.1103/PhysRevA.103.033315.

[3] M. H. Anderson, J. R. Ensher, M. R. Matthews, C. E. Wieman, and E. A. Cornell. Observation of Bose-Einstein Condensation in a Dilute Atomic Vapor. *Science*, 269 (5221):198–201, (1995). doi: 10.1126/science.269.5221.198.

[4] K. B. Davis, M. O. Mewes, M. R. Andrews, N. J. van Druten, D. S. Durfee, D. M. Kurn, and W. Ketterle. Bose-Einstein Condensation in a Gas of Sodium Atoms. *Phys. Rev. Lett.*, 75:3969–3973, (1995). doi: 10.1103/PhysRevLett.75.3969.

[5] B. DeMarco and D. S. Jin. Onset of Fermi Degeneracy in a Trapped Atomic Gas. *Science*, 285(5434):1703–1706, (1999). doi: 10.1126/science.285.5434.1703.

[6] J. G. Bednorz and K. A. Müller. Possible high $T_c$ superconductivity in the Ba−La−Cu−O system. *Zeitschrift fur Physik B Condensed Matter*, 64:189–193, (1986). doi: 10.1007/BF01303701.

[7] P. A. Lee, N. Nagaosa, and X.-G. Wen. Doping a Mott insulator: Physics of high-temperature superconductivity. *Rev. Mod. Phys.*, 78:17–85, (2006). doi: 10.1103/RevModPhys.78.17.

[8] L. Balents. Spin liquids in frustrated magnets. *Nature*, 464(7286):199–208, (2010). doi: 10.1038/nature08917.

[9] C. Broholm, R. J. Cava, S. A. Kivelson, D. G. Nocera, M. R. Norman, and T. Senthil. Quantum spin liquids. *Science*, 367(6475), (2020). doi: 10.1126/science.aay0668.

[10] J. Hubbard and B. H. Flowers. Electron correlations in narrow energy bands. *Proceedings of the Royal Society of London. Series A. Mathematical and Physical Sciences*, 276(1365):238–257, (1963). doi: 10.1098/rspa.1963.0204.

[11] S. Doniach. The Kondo lattice and weak antiferromagnetism. *Physica B+C*, 91: 231–234, (1977). doi: https://doi.org/10.1016/0378-4363(77)90190-5.

[12] A. C. Hewson. *The Kondo Problem to Heavy Fermions*. Cambridge Studies in Magnetism. Cambridge University Press, (1993). doi: 10.1017/CBO9780511470752.

[13] P. Coleman. *Heavy Fermions: Electrons at the Edge of Magnetism*. J. Wiley and Sons, (2007). ISBN 9780470022184. doi: https://doi.org/10.1002/9780470022184.hmm105. URL `https://onlinelibrary.wiley.com/doi/abs/10.1002/9780470022184.hmm105`.

[14] R. P. Feynman. Simulating physics with computers. *International Journal of Theoretical Physics*, 21:467–488, (1982). doi: 10.1007/BF02650179.

[15] R. P. Feynman. Quantum Mechanical Computers. *Optics News*, 11(2):11–20, (1985). doi: 10.1364/ON.11.2.000011.

[16] R. P. Feynman. Quantum mechanical computers. *Foundations of Physics*, 16:507–531, (1986). doi: 10.1007/BF01886518.

[17] S. Lloyd. Universal Quantum Simulators. *Science*, 273(5278):1073–1078, (1996). doi: 10.1126/science.273.5278.1073.

[18] E. Altman, K. R. Brown, G. Carleo, L. D. Carr, E. Demler, C. Chin, B. DeMarco, S. E. Economou, M. A. Eriksson, K.-M. C. Fu, M. Greiner, K. R. Hazzard, R. G. Hulet, A. J. Kollár, B. L. Lev, M. D. Lukin, R. Ma, X. Mi, S. Misra, C. Monroe, K. Murch, Z. Nazario, K.-K. Ni, A. C. Potter, P. Roushan, M. Saffman, M. Schleier-Smith, I. Siddiqi, R. Simmonds, M. Singh, I. Spielman, K. Temme, D. S. Weiss, J. Vučković, V. Vuletić, J. Ye, and M. Zwierlein. Quantum Simulators: Architectures and Opportunities. *PRX Quantum*, 2:017003, (2021). doi: 10.1103/PRXQuantum.2.017003.

[19] I. M. Georgescu, S. Ashhab, and F. Nori. Quantum simulation. *Rev. Mod. Phys.*, 86:153–185, (2014). doi: 10.1103/RevModPhys.86.153.

[20] I. Bloch, J. Dalibard, and W. Zwerger. Many-body physics with ultracold gases. *Rev. Mod. Phys.*, 80:885–964, (2008). doi: 10.1103/RevModPhys.80.885.

[21] I. Bloch, J. Dalibard, and S. Nascimbène. Quantum simulations with ultracold quantum gases. *Nature Physics*, 8:267–276, (2012). doi: 10.1038/nphys2259.

[22] D. Jaksch, C. Bruder, J. I. Cirac, C. W. Gardiner, and P. Zoller. Cold Bosonic Atoms in Optical Lattices. *Phys. Rev. Lett.*, 81:3108–3111, (1998). doi: 10.1103/PhysRevLett.81.3108.

[23] M. P. A. Fisher, P. B. Weichman, G. Grinstein, and D. S. Fisher. Boson localization and the superfluid-insulator transition. *Phys. Rev. B*, 40:546–570, (1989). doi: 10.1103/PhysRevB.40.546.

[24] M. Greiner, T. Esslinger, T. W. Hänsch, and I. Bloch. Quantum phase transition from a superfluid to a Mott insulator in a gas of ultracold atoms. *Nature*, 415:39–44, (2002). doi: 10.1038/415039a.

[25] S. Fölling, S. Trotzky, P. Cheinet, M. Feld, R. Saers, A. Widera, T. Müller, and I. Bloch. Direct observation of second-order atom tunnelling. *Nature*, 448(7157): 1029–1032, (2007). doi: 10.1038/nature06112.

[26] C. Becker, P. Soltan-Panahi, J. Kronjäger, S. Dörscher, K. Bongs, and K. Sengstock. Ultracold quantum gases in triangular optical lattices. *New Journal of Physics*, 12 (6):065025, (2010). doi: 10.1088/1367-2630/12/6/065025.

[27] K. L. Lee, B. Grémaud, R. Han, B.-G. Englert, and C. Miniatura. Ultracold fermions in a graphene-type optical lattice. *Phys. Rev. A*, 80:043411, (2009). doi: 10.1103/PhysRevA.80.043411.

[28] G.-B. Jo, J. Guzman, C. K. Thomas, P. Hosur, A. Vishwanath, and D. M. Stamper-Kurn. Ultracold Atoms in a Tunable Optical Kagome Lattice. *Phys. Rev. Lett.*, 108:045305, (2012). doi: 10.1103/PhysRevLett.108.045305.

[29] M. Köhl, H. Moritz, T. Stöferle, K. Günter, and T. Esslinger. Fermionic Atoms in a Three Dimensional Optical Lattice: Observing Fermi Surfaces, Dynamics, and Interactions. *Phys. Rev. Lett.*, 94:080403, (2005). doi: 10.1103/PhysRevLett.94.080403.

[30] Y. J. Lin, R. L. Compton, K. Jiménez-García, J. V. Porto, and I. B. Spielman. Synthetic magnetic fields for ultracold neutral atoms. *Nature*, 462(7273):628–632, (2009). doi: 10.1038/nature08609.

[31] J. Struck, C. Ölschläger, R. Le Targat, P. Soltan-Panahi, A. Eckardt, M. Lewenstein, P. Windpassinger, and K. Sengstock. Quantum Simulation of Frustrated Classical Magnetism in Triangular Optical Lattices. *Science*, 333(6045):996–999, (2011). doi: 10.1126/science.1207239.

[32] G. Jotzu, M. Messer, R. Desbuquois, M. Lebrat, T. Uehlinger, D. Greif, and T. Esslinger. Experimental realization of the topological Haldane model with ultracold fermions. *Nature*, 515(7526):237–240, (2014). doi: 10.1038/nature13915.

[33] B. K. Stuhl, H.-I. Lu, L. M. Aycock, D. Genkina, and I. B. Spielman. Visualizing edge states with an atomic Bose gas in the quantum Hall regime. *Science*, 349 (6255):1514–1518, (2015). doi: 10.1126/science.aaa8515.

[34] M. Mancini, G. Pagano, G. Cappellini, L. Livi, M. Rider, J. Catani, C. Sias, P. Zoller, M. Inguscio, M. Dalmonte, and L. Fallani. Observation of chiral edge states with neutral fermions in synthetic Hall ribbons. *Science*, 349(6255):1510–1513, (2015). doi: 10.1126/science.aaa8736.

[35] M. E. Tai, A. Lukin, M. Rispoli, R. Schittko, T. Menke, D. Borgnia, P. M. Preiss, F. Grusdt, A. M. Kaufman, and M. Greiner. Microscopy of the interacting Harper–Hofstadter model in the two-body limit. *Nature*, 546(7659):519–523, (2017). doi: 10.1038/nature22811.

[36] N. Fläschner, B. S. Rem, M. Tarnowski, D. Vogel, D.-S. Lühmann, K. Sengstock, and C. Weitenberg. Experimental reconstruction of the Berry curvature in a Floquet Bloch band. *Science*, 352(6289):1091–1094, (2016). doi: 10.1126/science.aad4568.

[37] W. S. Bakr, J. I. Gillen, A. Peng, S. Fölling, and M. Greiner. A quantum gas microscope for detecting single atoms in a Hubbard-regime optical lattice. *Nature*, 462(7269):74–77, (2009). doi: 10.1038/nature08482.

[38] J. F. Sherson, C. Weitenberg, M. Endres, M. Cheneau, I. Bloch, and S. Kuhr. Single-atom-resolved fluorescence imaging of an atomic Mott insulator. *Nature*, 467 (7311):68–72, (2010). doi: 10.1038/nature09378.

[39] A. Mazurenko, C. S. Chiu, G. Ji, M. F. Parsons, M. Kanász-Nagy, R. Schmidt, F. Grusdt, E. Demler, D. Greif, and M. Greiner. A cold-atom Fermi–Hubbard antiferromagnet. *Nature*, 545(7655):462–466, (2017). doi: 10.1038/nature22362.

[40] M. Endres, H. Bernien, A. Keesling, H. Levine, E. R. Anschuetz, A. Krajenbrink, C. Senko, V. Vuletic, M. Greiner, and M. D. Lukin. Atom-by-atom assembly of defect-free one-dimensional cold atom arrays. *Science*, 354(6315):1024–1027, (2016). doi: 10.1126/science.aah3752.

[41] D. Barredo, S. de Léséleuc, V. Lienhard, T. Lahaye, and A. Browaeys. An atom-by-atom assembler of defect-free arbitrary two-dimensional atomic arrays. *Science*, 354(6315):1021–1023, (2016). doi: 10.1126/science.aah3778.

[42] A. Omran, H. Levine, A. Keesling, G. Semeghini, T. T. Wang, S. Ebadi, H. Bernien, A. S. Zibrov, H. Pichler, S. Choi, J. Cui, M. Rossignolo, P. Rembold, S. Montangero, T. Calarco, M. Endres, M. Greiner, V. Vuletić, and M. D. Lukin. Generation and manipulation of Schrödinger cat states in Rydberg atom arrays. *Science*, 365(6453): 570–574, (2019). doi: 10.1126/science.aax9743.

[43] S. de Léséleuc, V. Lienhard, P. Scholl, D. Barredo, S. Weber, N. Lang, H. P. Büchler, T. Lahaye, and A. Browaeys. Observation of a symmetry-protected topological phase of interacting bosons with Rydberg atoms. *Science*, 365(6455):775–780, (2019). doi: 10.1126/science.aav9105.

[44] G. Semeghini, H. Levine, A. Keesling, S. Ebadi, T. T. Wang, D. Bluvstein, R. Verresen, H. Pichler, M. Kalinowski, R. Samajdar, A. Omran, S. Sachdev, A. Vishwanath, M. Greiner, V. Vuletic, and M. D. Lukin. Probing Topological Spin Liquids on a Programmable Quantum Simulator. (2021), arXiv:2104.04119 [quant-ph].

[45] K.-K. Ni, S. Ospelkaus, M. H. G. de Miranda, A. Pe'er, B. Neyenhuis, J. J. Zirbel, S. Kotochigova, P. S. Julienne, D. S. Jin, and J. Ye. A High Phase-Space-Density Gas of Polar Molecules. *Science*, 322(5899):231–235, (2008). doi: 10.1126/science.1163861.

[46] A. Griesmaier, J. Werner, S. Hensler, J. Stuhler, and T. Pfau. Bose-Einstein Condensation of Chromium. *Phys. Rev. Lett.*, 94:160401, (2005). doi: 10.1103/PhysRevLett.94.160401.

[47] M. Lu, N. Q. Burdick, S. H. Youn, and B. L. Lev. Strongly Dipolar Bose-Einstein Condensate of Dysprosium. *Phys. Rev. Lett.*, 107:190401, (2011). doi: 10.1103/PhysRevLett.107.190401.

[48] K. Aikawa, A. Frisch, M. Mark, S. Baier, A. Rietzler, R. Grimm, and F. Ferlaino. Bose-Einstein Condensation of Erbium. *Phys. Rev. Lett.*, 108:210401, (2012). doi: 10.1103/PhysRevLett.108.210401.

[49] M. Schmitt, M. Wenzel, F. Böttcher, I. Ferrier-Barbut, and T. Pfau. Self-bound droplets of a dilute magnetic quantum liquid. *Nature*, 539(7628):259–262, (2016). doi: 10.1038/nature20126.

[50] L. Chomaz, S. Baier, D. Petter, M. J. Mark, F. Wächtler, L. Santos, and F. Ferlaino. Quantum-Fluctuation-Driven Crossover from a Dilute Bose-Einstein Condensate to a Macrodroplet in a Dipolar Quantum Fluid. *Phys. Rev. X*, 6:041039, (2016). doi: 10.1103/PhysRevX.6.041039.

[51] S. G. Porsev and A. Derevianko. Hyperfine quenching of the metastable $^3P_{0,2}$ states in divalent atoms. *Phys. Rev. A*, 69:042506, (2004). doi: 10.1103/PhysRevA.69.042506.

[52] H. Katori, M. Takamoto, V. G. Pal'chikov, and V. D. Ovsiannikov. Ultrastable Optical Clock with Neutral Atoms in an Engineered Light Shift Trap. *Phys. Rev. Lett.*, 91:173005, (2003). doi: 10.1103/PhysRevLett.91.173005.

[53] T. Fortier and E. Baumann. 20 years of developments in optical frequency comb technology and applications. *Communications Physics*, 2(1), (2019). doi: 10.1038/s42005-019-0249-y.

[54] A. D. Ludlow, M. M. Boyd, J. Ye, E. Peik, and P. O. Schmidt. Optical atomic clocks. *Rev. Mod. Phys.*, 87:637–701, (2015). doi: 10.1103/RevModPhys.87.637.

[55] N. Hinkley, J. A. Sherman, N. B. Phillips, M. Schioppo, N. D. Lemke, K. Beloy, M. Pizzocaro, C. W. Oates, and A. D. Ludlow. An Atomic Clock with $10^{-18}$ Instability. *Science*, 341(6151):1215–1218, (2013). doi: 10.1126/science.1240420.

[56] B. J. Bloom, T. L. Nicholson, J. R. Williams, S. L. Campbell, M. Bishof, X. Zhang, W. Zhang, S. L. Bromley, and J. Ye. An optical lattice clock with accuracy and stability at the $10^{-18}$ level. *Nature*, 506(7486):71–75, (2014). doi: 10.1038/nature12941.

[57] F. Scazza, C. Hofrichter, M. Höfer, P. C. De Groot, I. Bloch, and S. Fölling. Observation of two-orbital spin-exchange interactions with ultracold SU(N)-symmetric fermions. *Nature Physics*, 10(10):779–784, (2014). doi: 10.1038/nphys3061.

[58] G. Cappellini, M. Mancini, G. Pagano, P. Lombardi, L. Livi, M. Siciliani de Cumis, P. Cancio, M. Pizzocaro, D. Calonico, F. Levi, C. Sias, J. Catani, M. Inguscio, and L. Fallani. Direct Observation of Coherent Interorbital Spin-Exchange Dynamics. *Phys. Rev. Lett.*, 113:120402, (2014). doi: 10.1103/PhysRevLett.113.120402.

[59] X. Zhang, M. Bishof, S. L. Bromley, C. V. Kraus, M. S. Safronova, P. Zoller, A. M. Rey, and J. Ye. Spectroscopic observation of SU(N)-symmetric interactions in Sr orbital magnetism. *Science*, 345(6203):1467–1473, (2014). doi: 10.1126/science.1254978.

[60] R. Bouganne, M. B. Aguilera, A. Dareau, E. Soave, J. Beugnon, and F. Gerbier. Clock spectroscopy of interacting bosons in deep optical lattices. *New Journal of Physics*, 19(11):113006, (2017). doi: 10.1088/1367-2630/aa8c45.

[61] A. Goban, R. B. Hutson, G. E. Marti, S. L. Campbell, M. A. Perlin, P. S. Julienne, J. P. D'Incao, A. M. Rey, and J. Ye. Emergence of multi-body interactions in a fermionic lattice clock. *Nature*, 563:369–373, (2018). doi: 10.1038/s41586-018-0661-6.

[62] K. Ono, J. Kobayashi, Y. Amano, K. Sato, and Y. Takahashi. Antiferromagnetic interorbital spin-exchange interaction of $^{171}$Yb. *Phys. Rev. A*, 99:032707, (2019). doi: 10.1103/PhysRevA.99.032707.

[63] O. Bettermann, N. D. Oppong, G. Pasqualetti, L. Riegger, I. Bloch, and S. Fölling. Clock-line photoassociation of strongly bound dimers in a magic-wavelength lattice. (2020), arXiv:2003.10599 [cond-mat.quant-gas].

[64] A. V. Gorshkov, M. Hermele, V. Gurarie, C. Xu, P. S. Julienne, J. Ye, P. Zoller, E. Demler, M. D. Lukin, and A. M. Rey. Two-orbital S U(N) magnetism with ultracold alkaline-earth atoms. *Nature Physics*, 6(4):289–295, (2010). doi: 10.1038/nphys1535.

[65] M. Foss-Feig, M. Hermele, and A. M. Rey. Probing the Kondo lattice model with alkaline-earth-metal atoms. *Phys. Rev. A*, 81:051603, (2010). doi: 10.1103/PhysRevA.81.051603.

[66] M. Foss-Feig, M. Hermele, and A. M. Rey. Probing the Kondo lattice model with alkaline-earth-metal atoms. *Phys. Rev. A*, 81:051603, (2010). doi: 10.1103/PhysRevA.81.051603.

[67] M. A. Cazalilla and A. M. Rey. Ultracold Fermi gases with emergent SU(N) symmetry. *Reports on Progress in Physics*, 77(12):124401, (2014). doi: 10.1088/0034-4885/77/12/124401.

[68] O. Bettermann, N. D. Oppong, G. Pasqualetti, L. Riegger, I. Bloch, and S. Fölling. Clock-line photoassociation of strongly bound dimers in a magic-wavelength lattice. (2020), arXiv:2003.10599 [cond-mat.quant-gas]. arXiv:2003.10599.

[69] M. Höfer, L. Riegger, F. Scazza, C. Hofrichter, D. R. Fernandes, M. M. Parish, J. Levinsen, I. Bloch, and S. Fölling. Observation of an Orbital Interaction-Induced Feshbach Resonance in $^{173}$Yb. *Phys. Rev. Lett.*, 115:265302, (2015). doi: 10.1103/PhysRevLett.115.265302.

[70] G. Pagano, M. Mancini, G. Cappellini, L. Livi, C. Sias, J. Catani, M. Inguscio, and L. Fallani. Strongly Interacting Gas of Two-Electron Fermions at an Orbital Feshbach Resonance. *Phys. Rev. Lett.*, 115:265301, (2015). doi: 10.1103/PhysRevLett.115.265301.

[71] G. Cappellini, L. F. Livi, L. Franchi, D. Tusi, D. Benedicto Orenes, M. Inguscio, J. Catani, and L. Fallani. Coherent Manipulation of Orbital Feshbach Molecules of Two-Electron Atoms. *Phys. Rev. X*, 9:011028, (2019). doi: 10.1103/PhysRevX.9.011028.

[72] J. Xu, R. Zhang, Y. Cheng, P. Zhang, R. Qi, and H. Zhai. Reaching a Fermi-superfluid state near an orbital Feshbach resonance. *Phys. Rev. A*, 94:033609, (2016). doi: 10.1103/PhysRevA.94.033609.

[73] M. Iskin. Two-band superfluidity and intrinsic Josephson effect in alkaline-earth-metal Fermi gases across an orbital Feshbach resonance. *Phys. Rev. A*, 94:011604, (2016). doi: 10.1103/PhysRevA.94.011604.

[74] L. He, J. Wang, S.-G. Peng, X.-J. Liu, and H. Hu. Strongly correlated Fermi superfluid near an orbital Feshbach resonance: Stability, equation of state, and Leggett mode. *Phys. Rev. A*, 94:043624, (2016). doi: 10.1103/PhysRevA.94.043624.

[75] T. Tomita, S. Nakajima, Y. Takasu, and Y. Takahashi. Dissipative Bose-Hubbard system with intrinsic two-body loss. *Phys. Rev. A*, 99:031601, (2019). doi: 10.1103/PhysRevA.99.031601.

[76] M. Foss-Feig, A. J. Daley, J. K. Thompson, and A. M. Rey. Steady-State Many-Body Entanglement of Hot Reactive Fermions. *Phys. Rev. Lett.*, 109:230501, (2012). doi: 10.1103/PhysRevLett.109.230501.

[77] L. Riegger, N. Darkwah Oppong, M. Höfer, D. R. Fernandes, I. Bloch, and S. Fölling. Localized Magnetic Moments with Tunable Spin Exchange in a Gas of Ultracold Fermions. *Phys. Rev. Lett.*, 120:143601, (2018). doi: 10.1103/PhysRevLett.120.143601.

[78] K. Ono, Y. Amano, T. Higomoto, Y. Saito, and Y. Takahashi. Observation of spin-exchange dynamics between itinerant and localized $^{171}$Yb atoms. *Phys. Rev. A*, 103:L041303, (2021). doi: 10.1103/PhysRevA.103.L041303.

[79] L. Lepori, A. Trombettoni, and W. Vinci. Simulation of two-flavor symmetry-locking phases in ultracold fermionic mixtures. *EPL (Europhysics Letters)*, 109(5):50002, (2015). doi: 10.1209/0295-5075/109/50002.

[80] J. C. Pinto Barros, L. Lepori, and A. Trombettoni. Phase diagram and non-Abelian symmetry locking for fermionic mixtures with unequal interactions. *Phys. Rev. A*, 96:013603, (2017). doi: 10.1103/PhysRevA.96.013603.

[81] S. Dörscher. *Creation of ytterbium quantum gases with a compact 2D-/3D-MOT setup*. PhD thesis, Universität Hamburg, (2013).

[82] A. Thobe. *Ultracold Yb Gases with Control over Spin and Orbital Degree of Freedom*. PhD thesis, Universität Hamburg, (2014).

[83] B. Hundt. *Optical Potentials for the Realization of Dissipative Fermi-Hubbard Models with Ultracold Ytterbium Atoms*. PhD thesis, Universität Hamburg, (2016).

[84] A. Kochanke. *Towards Quantum Simulation of the Kondo-Lattice-Model*. PhD thesis, Universität Hamburg, (2017).

[85] T. Ponath. *Probing Ytterbium Quantum Gases in an Optical Lattice using the Clock Transition*. PhD thesis, Universität Hamburg, (2018).

[86] S. Dörscher, A. Thobe, B. Hundt, A. Kochanke, R. Le Targat, P. Windpassinger, C. Becker, and K. Sengstock. Creation of quantum-degenerate gases of ytterbium in a compact 2D-/3D-magneto-optical trap setup. *Review of Scientific Instruments*, 84(4):043109, (2013). doi: 10.1063/1.4802682.

[87] T. Rützel. Konzeption und Aufbau eines hochstabilen Lasers für Präzisionsmessungen an ultrakalten Quantengasen. Master's thesis, Universität Hamburg, (2010).

[88] J.-H. Carstens. Stabilization of a Clock Laser for High Precision Spectroscopy on Ultracold Quantum Gases. Master's thesis, Universität Hamburg, (2011).

[89] H. Keßler. Aufbau eines blauen Lasersystems als Lichtquelle für eine Ytterbium 2D-MOT. Master's thesis, Universität Hamburg, (2011).

[90] A. Skottke. Aufbau eines zustandsabhängigen Gitters für die Realisierung des 1D-Kondo-Gitter-Modells mit ultrakalten Ytterbium-Atomen. Master's thesis, Universität Hamburg, (2016).

[91] B. Abeln. Design, Implementation and Characterization of a new Laser System for Mixtures of Ytterbium Quantum Gases. Master's thesis, Universität Hamburg, (2016).

[92] L. Hilbig. Künstliche Eichfelder und Synthetische Dimensionen. Master's thesis, Universität Hamburg, (2019).

[93] A. Skottke. Aufbau spektroskopischer Komponenten zur Laserstabilisierung für ein Quantengasexperiment. Master's thesis, Universität Hamburg, (2013).

[94] K. L. Heinze. Optimierung des Designs und Konstruktion eines 399nm External Cavity Diodelasers. Master's thesis, Universität Hamburg, (2016).

[95] T. Sobottke. Design und Realisierung eines hochauflösenden Detektionssystems für Ytterbium-Quantengase. Master's thesis, Universität Hamburg, (2014).

[96] L. Hilbig. Simulation zur Optimierung einer 2 dimensionalen magneto-otpischen Falle mit Ytterbium. Master's thesis, Universität Hamburg, (2017).

[97] L. Hilbig. Optische Resonatoren zur Frequenzstabilisierung von Lasern. Master's thesis, Universität Hamburg, (2018).

[98] K. Sponselee. *Lattice Clock Experiments with Interacting Fermionic Quantum Gases.* PhD thesis, Universität Hamburg, (2021).

[99] M. Diem. *To be appear.* PhD thesis.

[100] A. Kramida, Yu. Ralchenko, J. Reader, and NIST ASD Team. NIST Atomic Spectra Database (ver. 5.8), [Online]. Available: `https://physics.nist.gov/asd` [2021, May 16]. National Institute of Standards and Technology, Gaithersburg, MD., (2020).

[101] Y. Takasu, K. Komori, K. Honda, M. Kumakura, T. Yabuzaki, and Y. Takahashi. Photoassociation Spectroscopy of Laser-Cooled Ytterbium Atoms. *Phys. Rev. Lett.*, 93:123202, (2004). doi: 10.1103/PhysRevLett.93.123202.

[102] S. G. Porsev, A. Derevianko, and E. N. Fortson. Possibility of an optical clock using the $6^1S_0 \rightarrow 6^3P_0^o$ transition in $^{171,173}$Yb atoms held in an optical lattice. *Phys. Rev. A*, 69:021403, (2004). doi: 10.1103/PhysRevA.69.021403.

[103] J. E. Golub, Y. S. Bai, and T. W. Mossberg. Radiative and dynamical properties of homogeneously prepared atomic samples. *Phys. Rev. A*, 37:119–124, (1988). doi: 10.1103/PhysRevA.37.119.

[104] K. Beloy, J. A. Sherman, N. D. Lemke, N. Hinkley, C. W. Oates, and A. D. Ludlow. Determination of the $5d6s\ ^3D_1$ state lifetime and blackbody-radiation clock shift in Yb. *Phys. Rev. A*, 86:051404, (2012). doi: 10.1103/PhysRevA.86.051404.

[105] J. Meija, T. B. Coplen, M. Berglund, W. A. Brand, P. D. Bièvre, M. Gröning, N. E. Holden, J. Irrgeher, R. D. Loss, T. Walczyk, and T. Prohaska. Isotopic compositions of the elements 2013 (IUPAC Technical Report). *Pure and Applied Chemistry*, 88 (3):293–306, (2016). doi: doi:10.1515/pac-2015-0503.

[106] M. M. Boyd, T. Zelevinsky, A. D. Ludlow, S. Blatt, T. Zanon-Willette, S. M. Foreman, and J. Ye. Nuclear spin effects in optical lattice clocks. *Phys. Rev. A*, 76: 022510, (2007). doi: 10.1103/PhysRevA.76.022510.

[107] A. V. Taichenachev, V. I. Yudin, C. W. Oates, C. W. Hoyt, Z. W. Barber, and L. Hollberg. Magnetic Field-Induced Spectroscopy of Forbidden Optical Transitions with Application to Lattice-Based Optical Atomic Clocks. *Phys. Rev. Lett.*, 96: 083001, (2006). doi: 10.1103/PhysRevLett.96.083001.

[108] Z. W. Barber, J. E. Stalnaker, N. D. Lemke, N. Poli, C. W. Oates, T. M. Fortier, S. A. Diddams, L. Hollberg, C. W. Hoyt, A. V. Taichenachev, and V. I. Yudin. Optical Lattice Induced Light Shifts in an Yb Atomic Clock. *Phys. Rev. Lett.*, 100: 103002, (2008). doi: 10.1103/PhysRevLett.100.103002.

[109] M. Pizzocaro, F. Bregolin, P. Barbieri, B. Rauf, F. Levi, and D. Calonico. Absolute frequency measurement of the $^1S_0$–$^3P_0$ transition of 171Yb with a link to international atomic time. *Metrologia*, 57(3):035007, (2020). doi: 10.1088/1681-7575/ab50e8.

[110] M. Yasuda, H. Inaba, T. Kohno, T. Tanabe, Y. Nakajima, K. Hosaka, D. Akamatsu, A. Onae, T. Suzuyama, M. Amemiya, and F.-L. Hong. Improved Absolute Frequency Measurement of the $^{171}$Yb Optical Lattice Clock towards a Candidate for the Redefinition of the Second. *Applied Physics Express*, 5(10):102401, (2012). doi: 10.1143/apex.5.102401.

[111] J. P. D'Incao and B. D. Esry. Mass dependence of ultracold three-body collision rates. *Phys. Rev. A*, 73:030702, (2006). doi: 10.1103/PhysRevA.73.030702.

[112] Y. Takasu, K. Maki, K. Komori, T. Takano, K. Honda, M. Kumakura, T. Yabuzaki, and Y. Takahashi. Spin-Singlet Bose-Einstein Condensation of Two-Electron Atoms. *Phys. Rev. Lett.*, 91:040404, (2003). doi: 10.1103/PhysRevLett.91.040404.

[113] T. Fukuhara, Y. Takasu, S. Sugawa, and Y. Takahashi. Quantum Degenerate Fermi Gases of Ytterbium Atoms. *Journal of Low Temperature Physics*, 148:441–445, (2007). doi: 10.1007/s10909-007-9411-0.

[114] T. Fukuhara, S. Sugawa, Y. Takasu, and Y. Takahashi. All-optical formation of quantum degenerate mixtures. *Phys. Rev. A*, 79:021601, (2009). doi: 10.1103/PhysRevA.79.021601.

[115] S. Taie, Y. Takasu, S. Sugawa, R. Yamazaki, T. Tsujimoto, R. Murakami, and Y. Takahashi. Realization of a SU(2) × SU(6) System of Fermions in a Cold Atomic Gas. *Phys. Rev. Lett.*, 105:190401, (2010). doi: 10.1103/PhysRevLett.105.190401.

[116] T. Bourdel, L. Khaykovich, J. Cubizolles, J. Zhang, F. Chevy, M. Teichmann, L. Tarruell, S. J. J. M. F. Kokkelmans, and C. Salomon. Experimental Study of the BEC-BCS Crossover Region in Lithium 6. *Phys. Rev. Lett.*, 93:050401, (2004). doi: 10.1103/PhysRevLett.93.050401.

[117] M. Bartenstein, A. Altmeyer, S. Riedl, S. Jochim, C. Chin, J. H. Denschlag, and R. Grimm. Collective Excitations of a Degenerate Gas at the BEC-BCS Crossover. *Phys. Rev. Lett.*, 92:203201, (2004). doi: 10.1103/PhysRevLett.92.203201.

[118] M. Kitagawa, K. Enomoto, K. Kasa, Y. Takahashi, R. Ciuryło, P. Naidon, and P. S. Julienne. Two-color photoassociation spectroscopy of ytterbium atoms and the precise determinations of *s*-wave scattering lengths. *Phys. Rev. A*, 77:012719, (2008). doi: 10.1103/PhysRevA.77.012719.

[119] K. Dieckmann, R. J. C. Spreeuw, M. Weidemüller, and J. T. M. Walraven. Two-dimensional magneto-optical trap as a source of slow atoms. *Phys. Rev. A*, 58: 3891–3895, (1998). doi: 10.1103/PhysRevA.58.3891.

[120] M. R. Tarbutt. Magneto-optical trapping forces for atoms and molecules with complex level structures. *New Journal of Physics*, 17(1):015007, (2015). doi: 10.1088/1367-2630/17/1/015007.

[121] R. Grimm, M. Weidemüller, and Y. B. Ovchinnikov. Optical Dipole Traps for Neutral Atoms. volume 42 of *Advances In Atomic, Molecular, and Optical Physics*, pages 95–170. Academic Press, (2000). doi: https://doi.org/10.1016/S1049-250X(08)60186-X.

[122] W. Ketterle, D. Durfee, and D. Stamper-Kurn. Making, probing and understanding Bose-Einstein condensates. *arXiv: Condensed Matter*, (1999).

[123] N. Pintul. Ytterbium Fermi-Fermi Mixtures in Optical Lattices. Master's thesis, Universität Hamburg, (2020).

[124] T. Sleator, T. Pfau, V. Balykin, O. Carnal, and J. Mlynek. Experimental demonstration of the optical Stern-Gerlach effect. *Phys. Rev. Lett.*, 68:1996–1999, (1992). doi: 10.1103/PhysRevLett.68.1996.

[125] S. Stellmer, R. Grimm, and F. Schreck. Detection and manipulation of nuclear spin states in fermionic strontium. *Phys. Rev. A*, 84:043611, (2011). doi: 10.1103/PhysRevA.84.043611.

[126] K. Pandey, A. K. Singh, P. V. K. Kumar, M. V. Suryanarayana, and V. Natarajan. Isotope shifts and hyperfine structure in the 555.8-nm $^1S_0 \rightarrow {}^3P_1$ line of Yb. *Phys. Rev. A*, 80:022518, (2009). doi: 10.1103/PhysRevA.80.022518.

[127] T. Li, L. Duca, M. Reitter, F. Grusdt, E. Demler, M. Endres, M. Schleier-Smith, I. Bloch, and U. Schneider. Bloch state tomography using Wilson lines. *Science*, 352(6289):1094–1097, (2016). doi: 10.1126/science.aad5812.

[128] A. Mazurenko, C. S. Chiu, G. Ji, M. F. Parsons, M. Kanász-Nagy, R. Schmidt, F. Grusdt, E. Demler, D. Greif, and M. Greiner. A cold-atom Fermi–Hubbard antiferromagnet. *Nature*, 545(7655):462–466, (2017). doi: 10.1038/nature22362.

[129] P. Windpassinger and K. Sengstock. Engineering novel optical lattices. *Reports on Progress in Physics*, 76(8):086401, (2013). doi: 10.1088/0034-4885/76/8/086401.

[130] C. Kittel. *Introduction to solid state physics*. Wiley,Hoboken, NJ, 8. ed. edition, (2005).

[131] S. A. Self. Focusing of spherical Gaussian beams. *Appl. Opt.*, 22(5):658–661, (1983). doi: 10.1364/AO.22.000658.

[132] G. H. Wannier. The Structure of Electronic Excitation Levels in Insulating Crystals. *Phys. Rev.*, 52:191–197, (1937). doi: 10.1103/PhysRev.52.191.

[133] D. Jaksch and P. Zoller. The cold atom Hubbard toolbox. *Annals of Physics*, 315(1):52–79, (2005). doi: 10.1016/j.aop.2004.09.010.

[134] N. D. Lemke, A. D. Ludlow, Z. W. Barber, T. M. Fortier, S. A. Diddams, Y. Jiang, S. R. Jefferts, T. P. Heavner, T. E. Parker, and C. W. Oates. Spin-1/2 Optical Lattice Clock. *Phys. Rev. Lett.*, 103:063001, (2009). doi: 10.1103/PhysRevLett.103.063001.

[135] F. Scazza. *Probing SU(N)-symmetric orbital interactions with ytterbium fermi gases in optical lattices*. PhD thesis, Ludwig-Maximilian-Universität München, (2015).

[136] V. A. Dzuba and A. Derevianko. Dynamic polarizabilities and related properties of clock states of the ytterbium atom. *Journal of Physics B: Atomic, Molecular and Optical Physics*, 43(7):074011, (2010). doi: 10.1088/0953-4075/43/7/074011.

[137] N. I. Petersen. Aufbau und Charakterisierung eines optischen Dreiecksgitters für Ytterbium. Master's thesis, Universität Hamburg, (2014).

[138] D. Das, S. Barthwal, A. Banerjee, and V. Natarajan. Absolute frequency measurements in Yb with 0.08 ppb uncertainty: Isotope shifts and hyperfine structure in the 399−nm $^1S_0 \rightarrow^1 P_1$ line. *Phys. Rev. A*, 72:032506, (2005). doi: 10.1103/PhysRevA.72.032506.

[139] N. Poli, Z. W. Barber, N. D. Lemke, C. W. Oates, L. S. Ma, J. E. Stalnaker, T. M. Fortier, S. A. Diddams, L. Hollberg, J. C. Bergquist, A. Brusch, S. Jefferts, T. Heavner, and T. Parker. Frequency evaluation of the doubly forbidden $^1S_0 \rightarrow^3 P_0$ transition in bosonic $^{174}$Yb. *Phys. Rev. A*, 77:050501, (2008). doi: 10.1103/PhysRevA.77.050501.

[140] C. W. Hoyt, Z. W. Barber, C. W. Oates, T. M. Fortier, S. A. Diddams, and L. Hollberg. Observation and Absolute Frequency Measurements of the $^1S_0-^3P_0$ Optical Clock Transition in Neutral Ytterbium. *Phys. Rev. Lett.*, 95:083003, (2005). doi: 10.1103/PhysRevLett.95.083003.

[141] W. Demtröder. *Nonlinear Spectroscopy*, pages 83–147. Springer Berlin Heidelberg, Berlin, Heidelberg, (2015). ISBN 978-3-662-44641-6. doi: 10.1007/978-3-662-44641-6_2. URL `https://doi.org/10.1007/978-3-662-44641-6_2`.

[142] R. V. Pound. Electronic Frequency Stabilization of Microwave Oscillators. *Review of Scientific Instruments*, 17(11):490–505, (1946). doi: 10.1063/1.1770414.

[143] R. W. P. Drever, J. L. Hall, F. V. Kowalski, J. Hough, G. M. Ford, a. J. Munley, and H. Ward. Laser phase and frequency stabilization using an optical resonator. *Appl. Phys. B Photophysics Laser Chem.*, 31(2):97–105, (1983). doi: 10.1007/BF00702605.

[144] E. D. Black. An introduction to Pound–Drever–Hall laser frequency stabilization. *American Journal of Physics*, 69(1):79–87, (2001). doi: 10.1119/1.1286663.

[145] K. F. Klein, P. Schließmann, E. Smolka, G. Hillrichs, M. Belz, W. J. Boyle, and K. T. Grattan. UV-stabilized silica-based fibre for applications around 200 nm wavelength. *Sensors and Actuators B: Chemical*, 39(1):305–309, (1997). doi: https:

//doi.org/10.1016/S0925-4005(97)80224-9. 3rd European Conference on Optical Chemical Sensors and Biosensors.

[146] J. Appel, A. MacRae, and A. I. Lvovsky. A versatile digital GHz phase lock for external cavity diode lasers. *Measurement Science and Technology*, 20(5):055302, (2009). doi: 10.1088/0957-0233/20/5/055302.

[147] N. Pintul. Towards the Creation of Artificial Gauge Fields in Synthetic Dimensions for Fermionic Ytterbium. Master's thesis, Universität Hamburg, (2020).

[148] U. Schünemann, H. Engler, R. Grimm, M. Weidemüller, and M. Zielonkowski. Simple scheme for tunable frequency offset locking of two lasers. *Review of Scientific Instruments*, 70(1):242–243, (1999). doi: 10.1063/1.1149573.

[149] G. D. Domenico, S. Schilt, and P. Thomann. Simple approach to the relation between laser frequency noise and laser line shape. *Appl. Opt.*, 49(25):4801–4807, (2010). doi: 10.1364/AO.49.004801.

[150] D. G. Matei, T. Legero, C. Grebing, S. Häfner, C. Lisdat, R. Weyrich, W. Zhang, L. Sonderhouse, J. M. Robinson, F. Riehle, J. Ye, and U. Sterr. A second generation of low thermal noise cryogenic silicon resonators. *Journal of Physics: Conference Series*, 723:012031, (2016). doi: 10.1088/1742-6596/723/1/012031.

[151] D. G. Matei, T. Legero, S. Häfner, C. Grebing, R. Weyrich, W. Zhang, L. Sonderhouse, J. M. Robinson, J. Ye, F. Riehle, and U. Sterr. 1.5 $\mu$m Lasers with Sub-10 mHz Linewidth. *Phys. Rev. Lett.*, 118:263202, (2017). doi: 10.1103/PhysRevLett.118.263202.

[152] D. Vogel. *Measuring Geometry and Topologyof Floquet-Bloch Statesin and out of Equilibriumwith ultracold fermions*. PhD thesis, Universität Hamburg, (2018).

[153] J. I. Thorpe, K. Numata, and J. Livas. Laser frequency stabilization and control through offset sideband locking to optical cavities. *Opt. Express*, 16(20):15980–15990, (2008). doi: 10.1364/OE.16.015980.

[154] R. Houtz, C. Chan, and H. Müller. Wideband, Efficient Optical Serrodyne Frequency Shifting with a Phase Modulator and a Nonlinear Transmission Line. *Opt. Express*, 17(21):19235–19240, (2009). doi: 10.1364/OE.17.019235.

[155] D. M. S. Johnson, J. M. Hogan, S. w. Chiow, and M. A. Kasevich. Broadband optical serrodyne frequency shifting. *Opt. Lett.*, 35(5):745–747, (2010). doi: 10.1364/OL.35.000745.

[156] R. Kohlhaas, T. Vanderbruggen, S. Bernon, A. Bertoldi, A. Landragin, and P. Bouyer. Robust laser frequency stabilization by serrodyne modulation. *Opt. Lett.*, 37(6):1005–1007, (2012). doi: 10.1364/OL.37.001005.

[157] L.-S. Ma, P. Jungner, J. Ye, and J. L. Hall. Delivering the same optical frequency at two places: accurate cancellation of phase noise introduced by an optical fiber or

other time-varying path. *Opt. Lett.*, 19(21):1777–1779, (1994). doi: 10.1364/OL.19.001777.

[158] S. Stellmer, R. Grimm, and F. Schreck. Detection and manipulation of nuclear spin states in fermionic strontium. *Phys. Rev. A*, 84:043611, (2011). doi: 10.1103/PhysRevA.84.043611.

[159] H. F. Hess. Evaporative cooling of magnetically trapped and compressed spin-polarized hydrogen. *Phys. Rev. B*, 34:3476–3479, (1986). doi: 10.1103/PhysRevB.34.3476.

[160] C. J. Myatt, E. A. Burt, R. W. Ghrist, E. A. Cornell, and C. E. Wieman. Production of Two Overlapping Bose-Einstein Condensates by Sympathetic Cooling. *Phys. Rev. Lett.*, 78:586–589, (1997). doi: 10.1103/PhysRevLett.78.586.

[161] F. Schreck, G. Ferrari, K. L. Corwin, J. Cubizolles, L. Khaykovich, M.-O. Mewes, and C. Salomon. Sympathetic cooling of bosonic and fermionic lithium gases towards quantum degeneracy. *Phys. Rev. A*, 64:011402, (2001). doi: 10.1103/PhysRevA.64.011402.

[162] W. Ketterle and M. Zwierlein. Making, probing and understanding ultracold Fermi gases. *Rivista del Nuovo Cimento*, 164, (2008). doi: 10.1393/ncr/i2008-10033-1.

[163] H. J. Metcalf and P. van der Straten. *Laser Cooling and trapping*. Springer science + Business Media New York, (1999).

[164] D. A. Steck. *Quantum and Atom Optics*. (2020). available online at http://steck.us/teaching (revision 0.13.4, 24 September 2020).

[165] F. Schwabl. *Quantenmechanik*. Springer-Verlag, (2002).

[166] S. Matsuo, T. Fujii, N. Kosugi, and N. Hatakenaka. Theory of damped Rabi oscillations at finite temperatures. *Journal of Physics: Conference Series*, 150(2):022056, (2009). doi: 10.1088/1742-6596/150/2/022056.

[167] Z. Barber. *Ytterbium Optical Lattice Clock*. PhD thesis, Montana State University,, (2003). URL `https://www.proquest.com/docview/304868454?accountid=11262`.

[168] O. Svelto. *Principles of Lasers*. Springer, (2010). doi: 10.1007/978-1-4419-1302-9.

[169] L. F. Livi, G. Cappellini, M. Diem, L. Franchi, C. Clivati, M. Frittelli, F. Levi, D. Calonico, J. Catani, M. Inguscio, and L. Fallani. Synthetic Dimensions and Spin-Orbit Coupling with an Optical Clock Transition. *Phys. Rev. Lett.*, 117:220401, (2016). doi: 10.1103/PhysRevLett.117.220401.

[170] P. Lemonde and P. Wolf. Optical lattice clock with atoms confined in a shallow trap. *Phys. Rev. A*, 72:033409, (2005). doi: 10.1103/PhysRevA.72.033409.

[171] S. Kolkowitz, S. L. Bromley, T. Bothwell, M. L. Wall, G. E. Marti, A. P. Koller, X. Zhang, A. M. Rey, and J. Ye. Spin–orbit-coupled fermions in an optical lattice clock. *Nature*, 542(7639):66–70, (2016). doi: 10.1038/nature20811.

[172] E. Condon. A Theory of Intensity Distribution in Band Systems. *Phys. Rev.*, 28: 1182–1201, (1926). doi: 10.1103/PhysRev.28.1182.

[173] M. L. Wall, A. P. Koller, S. Li, X. Zhang, N. R. Cooper, J. Ye, and A. M. Rey. Synthetic Spin-Orbit Coupling in an Optical Lattice Clock. *Phys. Rev. Lett.*, 116: 035301, (2016). doi: 10.1103/PhysRevLett.116.035301.

[174] D. Wineland, C. Monroe, W. M. Itano, D. Leibfried, B. E. King, and D. M. Meekhof. Experimental Issues in Coherent Quantum-State Manipulation of Trapped Atomic Ions. *Journal of Research of the National Institute of Standards and Technology*, 103(3), (1998). doi: 10.6028/jres.103.019.

[175] D. M. Meekhof, C. Monroe, B. E. King, W. M. Itano, and D. J. Wineland. Generation of Nonclassical Motional States of a Trapped Atom. *Phys. Rev. Lett.*, 76: 1796–1799, (1996). doi: 10.1103/PhysRevLett.76.1796.

[176] F. Bloch. Nuclear Induction. *Phys. Rev.*, 70:460–474, (1946). doi: 10.1103/PhysRev.70.460.

[177] N. Kosugi, S. Matsuo, K. Konno, and N. Hatakenaka. Theory of damped Rabi oscillations. *Phys. Rev. B*, 72:172509, (2005). doi: 10.1103/PhysRevB.72.172509.

[178] C. Lisdat, J. S. R. V. Winfred, T. Middelmann, F. Riehle, and U. Sterr. Collisional Losses, Decoherence, and Frequency Shifts in Optical Lattice Clocks with Bosons. *Phys. Rev. Lett.*, 103:090801, (2009). doi: 10.1103/PhysRevLett.103.090801.

[179] P. Dubé, A. Madej, J. E. Bernard, L. Marmet, and A. D. Shiner. A narrow linewidth and frequency-stable probe laser source for the $^{88}Sr^{+}$ single ion optical frequency standard. *Applied Physics B*, 95:43–54, (2009). doi: 10.1007/s00340-009-3390-6.

[180] C. Hagemann, C. Grebing, C. Lisdat, S. Falke, T. Legero, U. Sterr, F. Riehle, M. J. Martin, and J. Ye. Ultrastable laser with average fractional frequency drift rate below $5 \times 10^{-19}$ /s. *Opt. Lett.*, 39(17):5102–5105, (2014). doi: 10.1364/OL.39.005102.

[181] E. Benkler. Erik Benkler (2021). Allan and modified Allan deviation estimation from phase-time data comprising gaps (https://www.mathworks.com/matlabcentral/fileexchange/53395-allan-and-modified-allan-deviation-estimation-from-phase-time-data-comprising-gaps), MATLAB Central File Exchange. Retrieved July 13, 2021.

[182] W. Riley and D. Howe. Handbook of Frequency Stability Analysis, (2008). URL `https://tsapps.nist.gov/publication/get_pdf.cfm?pub_id=50505`.

[183] N. Hinkley, J. A. Sherman, N. B. Phillips, M. Schioppo, N. D. Lemke, K. Beloy, M. Pizzocaro, C. W. Oates, and A. D. Ludlow. An Atomic Clock with 10–18 Instability. *Science*, 341(6151):1215–1218, (2013). doi: 10.1126/science.1240420.

[184] X. Zhang, M. Bishof, S. L. Bromley, C. V. Kraus, M. S. Safronova, P. Zoller, A. M. Rey, and J. Ye. Spectroscopic observation of SU(N)-symmetric interactions in Sr orbital magnetism. *Science*, 345(6203):1467–1473, (2014). doi: 10.1126/science.1254978.

[185] C. J. Myatt, E. A. Burt, R. W. Ghrist, E. A. Cornell, and C. E. Wieman. Production of Two Overlapping Bose-Einstein Condensates by Sympathetic Cooling. *Phys. Rev. Lett.*, 78:586–589, (1997). doi: 10.1103/PhysRevLett.78.586.

[186] D. S. Hall, M. R. Matthews, J. R. Ensher, C. E. Wieman, and E. A. Cornell. Dynamics of Component Separation in a Binary Mixture of Bose-Einstein Condensates. *Phys. Rev. Lett.*, 81:1539–1542, (1998). doi: 10.1103/PhysRevLett.81.1539.

[187] J. Stenger, S. Inouye, D. M. Stamper-Kurn, H.-J. Miesner, A. P. Chikkatur, and W. Ketterle. Spin domains in ground-state Bose–Einstein condensates. *Nature*, 396 (6709):345–348, (1998). doi: 10.1038/24567.

[188] C. A. Regal, C. Ticknor, J. L. Bohn, and D. S. Jin. Creation of ultracold molecules from a Fermi gas of atoms. *Nature*, 424(6944):47–50, (2003). doi: 10.1038/nature01738.

[189] A. G. Truscott, K. E. Strecker, W. I. McAlexander, G. B. Partridge, and R. G. Hulet. Observation of Fermi Pressure in a Gas of Trapped Atoms. *Science*, 291 (5513):2570–2572, (2001). doi: 10.1126/science.1059318.

[190] F. Schreck, L. Khaykovich, K. L. Corwin, G. Ferrari, T. Bourdel, J. Cubizolles, and C. Salomon. Quasipure Bose-Einstein Condensate Immersed in a Fermi Sea. *Phys. Rev. Lett.*, 87:080403, (2001). doi: 10.1103/PhysRevLett.87.080403.

[191] S. B. Papp, J. M. Pino, and C. E. Wieman. Tunable Miscibility in a Dual-Species Bose-Einstein Condensate. *Phys. Rev. Lett.*, 101:040402, (2008). doi: 10.1103/PhysRevLett.101.040402.

[192] Z. Hadzibabic, C. A. Stan, K. Dieckmann, S. Gupta, M. W. Zwierlein, A. Görlitz, and W. Ketterle. Two-Species Mixture of Quantum Degenerate Bose and Fermi Gases. *Phys. Rev. Lett.*, 88:160401, (2002). doi: 10.1103/PhysRevLett.88.160401.

[193] C. A. Stan, M. W. Zwierlein, C. H. Schunck, S. M. F. Raupach, and W. Ketterle. Observation of Feshbach Resonances between Two Different Atomic Species. *Phys. Rev. Lett.*, 93:143001, (2004). doi: 10.1103/PhysRevLett.93.143001.

[194] S. Inouye, J. Goldwin, M. L. Olsen, C. Ticknor, J. L. Bohn, and D. S. Jin. Observation of Heteronuclear Feshbach Resonances in a Mixture of Bosons and Fermions. *Phys. Rev. Lett.*, 93:183201, (2004). doi: 10.1103/PhysRevLett.93.183201.

[195] C. Ospelkaus, S. Ospelkaus, K. Sengstock, and K. Bongs. Interaction-Driven Dynamics of $^{40}$K$-^{87}$Rb Fermion-Boson Gas Mixtures in the Large-Particle-Number Limit. *Phys. Rev. Lett.*, 96:020401, (2006). doi: 10.1103/PhysRevLett.96.020401.

[196] M. Taglieber, A.-C. Voigt, T. Aoki, T. W. Hänsch, and K. Dieckmann. Quantum Degenerate Two-Species Fermi-Fermi Mixture Coexisting with a Bose-Einstein Condensate. *Phys. Rev. Lett.*, 100:010401, (2008). doi: 10.1103/PhysRevLett.100.010401.

[197] E. Wille, F. M. Spiegelhalder, G. Kerner, D. Naik, A. Trenkwalder, G. Hendl, F. Schreck, R. Grimm, T. G. Tiecke, J. T. M. Walraven, S. J. J. M. F. Kokkelmans, E. Tiesinga, and P. S. Julienne. Exploring an Ultracold Fermi-Fermi Mixture: Interspecies Feshbach Resonances and Scattering Properties of $^6$Li and $^{40}$K. *Phys. Rev. Lett.*, 100:053201, (2008). doi: 10.1103/PhysRevLett.100.053201.

[198] H. Hara, Y. Takasu, Y. Yamaoka, J. M. Doyle, and Y. Takahashi. Quantum Degenerate Mixtures of Alkali and Alkaline-Earth-Like Atoms. *Phys. Rev. Lett.*, 106:205304, (2011). doi: 10.1103/PhysRevLett.106.205304.

[199] G. Cappellini, M. Mancini, G. Pagano, P. Lombardi, L. Livi, M. Siciliani de Cumis, P. Cancio, M. Pizzocaro, D. Calonico, F. Levi, C. Sias, J. Catani, M. Inguscio, and L. Fallani. Direct Observation of Coherent Interorbital Spin-Exchange Dynamics. *Phys. Rev. Lett.*, 113:120402, (2014). doi: 10.1103/PhysRevLett.113.120402.

[200] S. Ospelkaus, C. Ospelkaus, O. Wille, M. Succo, P. Ernst, K. Sengstock, and K. Bongs. Localization of Bosonic Atoms by Fermionic Impurities in a Three-Dimensional Optical Lattice. *Phys. Rev. Lett.*, 96:180403, (2006). doi: 10.1103/PhysRevLett.96.180403.

[201] M. H. G. de Miranda, A. Chotia, B. Neyenhuis, D. Wang, G. Quéméner, S. Ospelkaus, J. L. Bohn, J. Ye, and D. S. Jin. Controlling the quantum stereodynamics of ultracold bimolecular reactions. *Nature Physics*, 7(6):502–507, (2011). doi: 10.1038/nphys1939.

[202] A. Chotia, B. Neyenhuis, S. A. Moses, B. Yan, J. P. Covey, M. Foss-Feig, A. M. Rey, D. S. Jin, and J. Ye. Long-Lived Dipolar Molecules and Feshbach Molecules in a 3D Optical Lattice. *Phys. Rev. Lett.*, 108:080405, (2012). doi: 10.1103/PhysRevLett.108.080405.

[203] C. Kohstall, M. Zaccanti, M. Jag, A. Trenkwalder, P. Massignan, G. M. Bruun, F. Schreck, and R. Grimm. Metastability and coherence of repulsive polarons in a strongly interacting Fermi mixture. *Nature*, 485(7400):615–618, (2012). doi: 10.1038/nature11065.

[204] M. Koschorreck, D. Pertot, E. Vogt, B. Fröhlich, M. Feld, and M. Köhl. Attractive and repulsive Fermi polarons in two dimensions. *Nature*, 485(7400):619–622, (2012). doi: 10.1038/nature11151.

[205] P. Massignan, M. Zaccanti, and G. M. Bruun. Polarons, dressed molecules and itinerant ferromagnetism in ultracold Fermi gases. *Reports on Progress in Physics*, 77(3):034401, (2014). doi: 10.1088/0034-4885/77/3/034401.

[206] N. Darkwah Oppong, L. Riegger, O. Bettermann, M. Höfer, J. Levinsen, M. M. Parish, I. Bloch, and S. Fölling. Observation of Coherent Multiorbital Polarons in a Two-Dimensional Fermi Gas. *Phys. Rev. Lett.*, 122:193604, (2019). doi: 10.1103/PhysRevLett.122.193604.

[207] K. Günter, T. Stöferle, H. Moritz, M. Köhl, and T. Esslinger. Bose-Fermi Mixtures in a Three-Dimensional Optical Lattice. *Phys. Rev. Lett.*, 96:180402, (2006). doi: 10.1103/PhysRevLett.96.180402.

[208] S. Taie, R. Yamazaki, S. Sugawa, and Y. Takahashi. An SU(6) Mott insulator of an atomic Fermi gas realized by large-spin Pomeranchuk cooling. *Nature Physics*, 8(11):825–830, (2012). doi: 10.1038/nphys2430.

[209] Z. Xu and S. Chen. Topological Mott insulators of ultracold atomic mixtures induced by interactions in one-dimensional optical superlattices. *Phys. Rev. B*, 88:045110, (2013). doi: 10.1103/PhysRevB.88.045110.

[210] P. Nataf, M. Lajkó, A. Wietek, K. Penc, F. Mila, and A. M. Läuchli. Chiral Spin Liquids in Triangular-Lattice SU($N$) Fermionic Mott Insulators with Artificial Gauge Fields. *Phys. Rev. Lett.*, 117:167202, (2016). doi: 10.1103/PhysRevLett.117.167202.

[211] F. T. Lisandrini, A. M. Lobos, A. O. Dobry, and C. J. Gazza. Topological Kondo insulators in one dimension: Continuous Haldane-type ground-state evolution from the strongly interacting to the noninteracting limit. *Phys. Rev. B*, 96:075124, (2017). doi: 10.1103/PhysRevB.96.075124.

[212] D. Greif, T. Uehlinger, G. Jotzu, L. Tarruell, and T. Esslinger. Short-Range Quantum Magnetism of Ultracold Fermions in an Optical Lattice. *Science*, 340(6138):1307–1310, (2013). doi: 10.1126/science.1236362.

[213] M. F. Parsons, A. Mazurenko, C. S. Chiu, G. Ji, D. Greif, and M. Greiner. Site-resolved measurement of the spin-correlation function in the Fermi-Hubbard model. *Science*, 353(6305):1253–1256, (2016). doi: 10.1126/science.aag1430.

[214] J. S. Krauser, J. Heinze, N. Fläschner, S. Götze, O. Jürgensen, D.-S. Lühmann, C. Becker, and K. Sengstock. Coherent multi-flavour spin dynamics in a fermionic quantum gas. *Nature Physics*, 8(11):813–818, (2012). doi: 10.1038/nphys2409.

[215] J. S. Krauser, U. Ebling, N. Fläschner, J. Heinze, K. Sengstock, M. Lewenstein, A. Eckardt, and C. Becker. Giant Spin Oscillations in an Ultracold Fermi Sea. *Science*, 343(6167):157–160, (2014). doi: 10.1126/science.1244059.

[216] S. L. Campbell, R. B. Hutson, G. E. Marti, A. Goban, N. Darkwah Oppong, R. L. McNally, L. Sonderhouse, J. M. Robinson, W. Zhang, B. J. Bloom, and J. Ye. A

Fermi-degenerate three-dimensional optical lattice clock. *Science*, 358(6359):90–94, (2017). doi: 10.1126/science.aam5538.

[217] T. Busch, B.-G. Englert, K. Rzażewski, and M. Wilkens. Two Cold Atoms in a Harmonic Trap, (1998). URL `https://www.sciencedirect.com/science/article/pii/S0925400597802249`.

[218] Z. Idziaszek and T. Calarco. Two atoms in an anisotropic harmonic trap. *Phys. Rev. A*, 71:050701, (2005). doi: 10.1103/PhysRevA.71.050701.

[219] F. Deuretzbacher, K. Plassmeier, D. Pfannkuche, F. Werner, C. Ospelkaus, S. Ospelkaus, K. Sengstock, and K. Bongs. Heteronuclear molecules in an optical lattice: Theory and experiment. *Phys. Rev. A*, 77:032726, (2008). doi: 10.1103/PhysRevA.77.032726.

[220] J. Mentink and S. Kokkelmans. Two interacting atoms in an optical lattice site with anharmonic terms. *Phys. Rev. A*, 79:032709, (2009). doi: 10.1103/PhysRevA.79.032709.

[221] L. Franchi, L. F. Livi, G. Cappellini, G. Binella, M. Inguscio, J. Catani, and L. Fallani. State-dependent interactions in ultracold174Yb probed by optical clock spectroscopy. *New Journal of Physics*, 19(10):103037, (2017). doi: 10.1088/1367-2630/aa8fb4.

[222] F. Scazza, C. Hofrichter, M. Höfer, P. C. De Groot, I. Bloch, and S. Fölling. Observation of two-orbital spin-exchange interactions with ultracold SU(N)-symmetric fermions. *nature Physics*, 10:779–784, (2014). doi: 10.1038/nphys3061.

[223] R. H. Dicke. Coherence in Spontaneous Radiation Processes. *Phys. Rev.*, 93:99–110, (1954). doi: 10.1103/PhysRev.93.99.

[224] R. Zhang, D. Zhang, Y. Cheng, W. Chen, P. Zhang, and H. Zhai. Kondo effect in alkaline-earth-metal atomic gases with confinement-induced resonances. *Phys. Rev. A*, 93:043601, (2016). doi: 10.1103/PhysRevA.93.043601.

[225] Y. Cheng, R. Zhang, P. Zhang, and H. Zhai. Enhancing Kondo coupling in alkaline-earth-metal atomic gases with confinement-induced resonances in mixed dimensions. *Phys. Rev. A*, 96:063605, (2017). doi: 10.1103/PhysRevA.96.063605.

[226] M. Kitagawa, K. Enomoto, K. Kasa, Y. Takahashi, R. Ciuryło, P. Naidon, and P. S. Julienne. Two-color photoassociation spectroscopy of ytterbium atoms and the precise determinations of $s$-wave scattering lengths. *Phys. Rev. A*, 77:012719, (2008). doi: 10.1103/PhysRevA.77.012719.

[227] C. Gross and I. Bloch. Quantum simulations with ultracold atoms in optical lattices. *Science*, 357(6355):995–1001, (2017). doi: 10.1126/science.aal3837.

[228] J. R. Schrieffer and P. A. Wolff. Relation between the Anderson and Kondo Hamiltonians. *Phys. Rev.*, 149:491–492, (1966). doi: 10.1103/PhysRev.149.491.

[229] P. W. Anderson. Localized Magnetic States in Metals. *Phys. Rev.*, 124:41–53, (1961). doi: 10.1103/PhysRev.124.41.

[230] J. Kondo. Resistance Minimum in Dilute Magnetic Alloys. *Progress of Theoretical Physics*, 32(1):37–49, (1964). doi: 10.1143/PTP.32.37.

[231] W. de Haas, J. de Boer, and G. van dën Berg. The electrical resistance of gold, copper and lead at low temperatures. *Physica*, 1(7):1115–1124, (1934). doi: https://doi.org/10.1016/S0031-8914(34)80310-2.

[232] K. G. Wilson. The renormalization group: Critical phenomena and the Kondo problem. *Rev. Mod. Phys.*, 47:773–840, (1975). doi: 10.1103/RevModPhys.47.773.

[233] N. Andrei, K. Furuya, and J. H. Lowenstein. Solution of the Kondo problem. *Rev. Mod. Phys.*, 55:331–402, (1983). doi: 10.1103/RevModPhys.55.331.

[234] P. B. Wiegmann. Exact solution of the s-d exchange model (Kondo problem). *Journal of Physics C: Solid State Physics*, 14(10):1463–1478, (1981). doi: 10.1088/0022-3719/14/10/014.

[235] B. Coqblin and J. R. Schrieffer. Exchange Interaction in Alloys with Cerium Impurities. *Phys. Rev.*, 185:847–853, (1969). doi: 10.1103/PhysRev.185.847.

[236] M. A. Ruderman and C. Kittel. Indirect Exchange Coupling of Nuclear Magnetic Moments by Conduction Electrons. *Phys. Rev.*, 96:99–102, (1954). doi: 10.1103/PhysRev.96.99.

[237] R. Zhang, D. Zhang, Y. Cheng, W. Chen, P. Zhang, and H. Zhai. Kondo effect in alkaline-earth-metal atomic gases with confinement-induced resonances. *Phys. Rev. A*, 93:043601, (2016). doi: 10.1103/PhysRevA.93.043601.

[238] M. Kanász-Nagy, Y. Ashida, T. Shi, C. u. u. u. u. P. m. c. Moca, T. N. Ikeda, S. Fölling, J. I. Cirac, G. Zaránd, and E. A. Demler. Exploring the anisotropic Kondo model in and out of equilibrium with alkaline-earth atoms. *Phys. Rev. B*, 97:155156, (2018). doi: 10.1103/PhysRevB.97.155156.

[239] J. Heinze, S. Götze, J. S. Krauser, B. Hundt, N. Fläschner, D.-S. Lühmann, C. Becker, and K. Sengstock. Multiband Spectroscopy of Ultracold Fermions: Observation of Reduced Tunneling in Attractive Bose-Fermi Mixtures. *Phys. Rev. Lett.*, 107:135303, (2011). doi: 10.1103/PhysRevLett.107.135303.

[240] A. Kastberg, W. D. Phillips, S. L. Rolston, R. J. C. Spreeuw, and P. S. Jessen. Adiabatic Cooling of Cesium to 700 nK in an Optical Lattice. *Phys. Rev. Lett.*, 74:1542–1545, (1995). doi: 10.1103/PhysRevLett.74.1542.

[241] S. Dörscher, R. Schwarz, A. Al-Masoudi, S. Falke, U. Sterr, and C. Lisdat. Lattice-induced photon scattering in an optical lattice clock. *Phys. Rev. A*, 97:063419, (2018). doi: 10.1103/PhysRevA.97.063419.

[242] L. Riegger. *Interorbital spin exchange in a state-dependent optical lattice*. PhD thesis, Ludwig-Maximilians-Universität München, (2019).

[243] I. Kuzmenko, T. Kuzmenko, Y. Avishai, and G.-B. Jo. Coqblin-Schrieffer model for an ultracold gas of ytterbium atoms with metastable state. *Phys. Rev. B*, 93: 115143, (2016). doi: 10.1103/PhysRevB.93.115143.

[244] A. Sanayei and L. Mathey. Three-body bound states of an atom in a Fermi mixture. (2020), arXiv:2007.13511 [physics.atom-ph].

[245] N. D. Oppong, G. Pasqualetti, O. Bettermann, P. Zechmann, M. Knap, I. Bloch, and S. Fölling. Probing transport and slow relaxation in the mass-imbalanced Fermi-Hubbard model. (2020), arXiv:2011.12411 [cond-mat.quant-gas].

# A. Momentum Resolved Clock Spectra

Figures A.2 to A.8 show momentum resolved spectra for ground and excited state atoms (see sec. 3.2.1 for a detailed explanation). Figure A.1 shows spectra calculated using eq. 3.20 for a lattice depth of $s_{1D} = 5\,E_{rec}$.

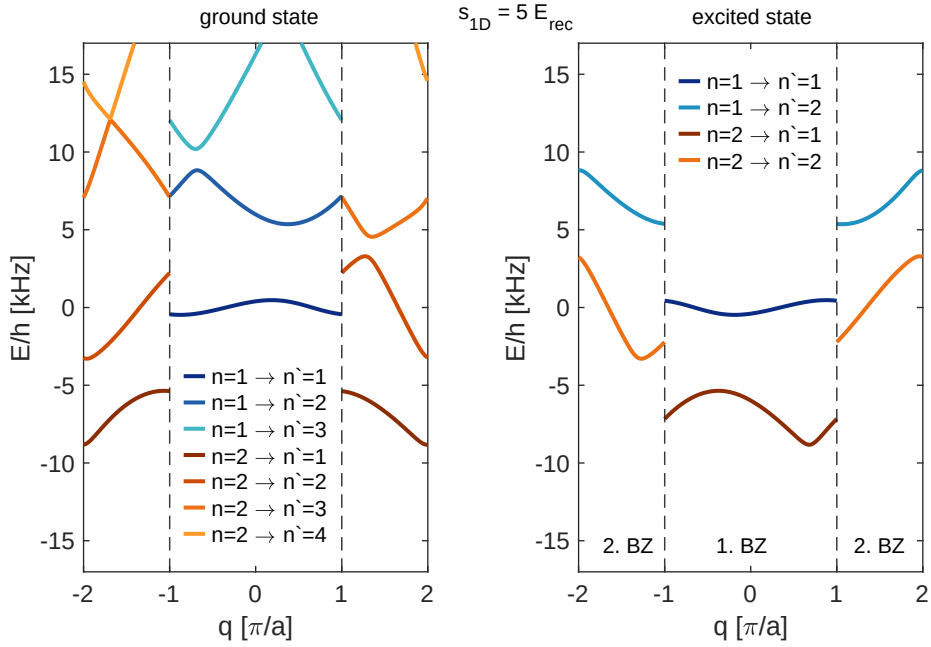


**Figure A.1.:** Momentum resolved spectra of the lowest lying transitions for ground and excited state atoms calculated for a lattice depth of $s_{1D} = 5\,E_{rec}$ assuming a quasimomentum transfer $\delta q = -1.31$ and taking into account transitions from the lowest and the second Bloch Band.

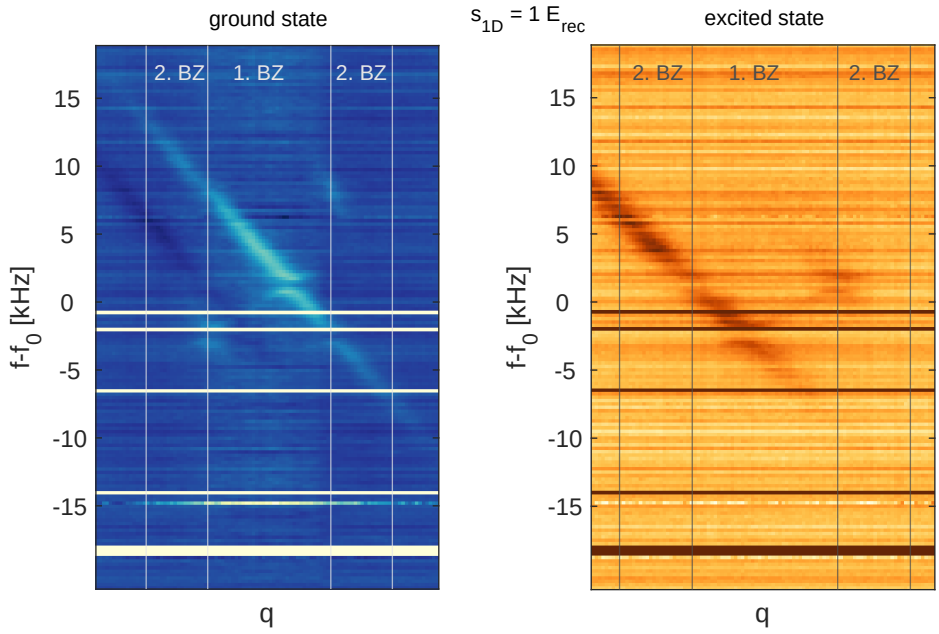


**Figure A.2.:** Momentum resolved clock spectra for a lattice depth of $s_{1D} = 1\,E_{rec}$ for ground- and excited-state atoms. Horizontal lines correspond to absorption images after time of flight and bandmapping, integrated along the direction perpendicular to the 1D lattice. The average of six images without clock excitation is subtracted.

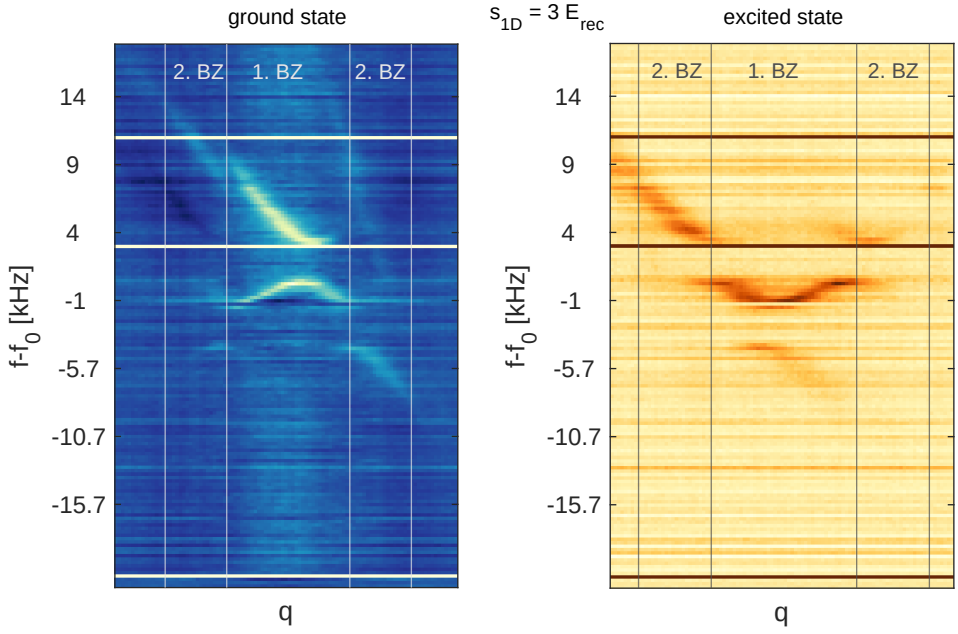


**Figure A.3.:** Momentum resolved clock spectra for a lattice depth of $s_{1D} = 3\,E_{rec}$ for ground- and excited-state atoms. Horizontal lines correspond to absorption images after time of flight and bandmapping, integrated along the direction perpendicular to the 1D lattice. The average of six images without clock excitation is subtracted.

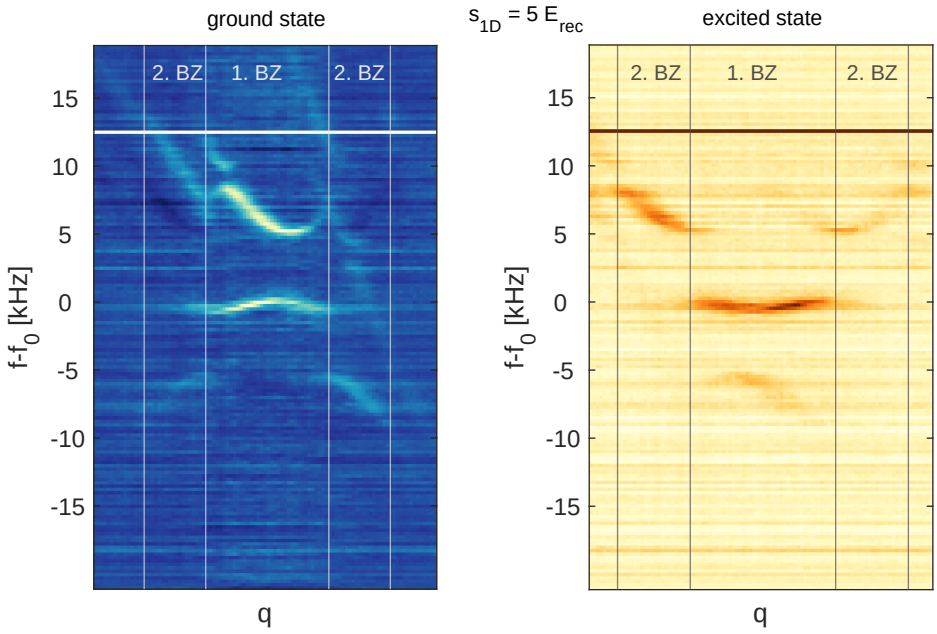


**Figure A.4.:** Momentum resolved clock spectra for a lattice depth of $s_{1D} = 5\,E_{rec}$ for ground- and excited-state atoms. Horizontal lines correspond to absorption images after time of flight and bandmapping, integrated along the direction perpendicular to the 1D lattice. The average of six images without clock excitation is subtracted.

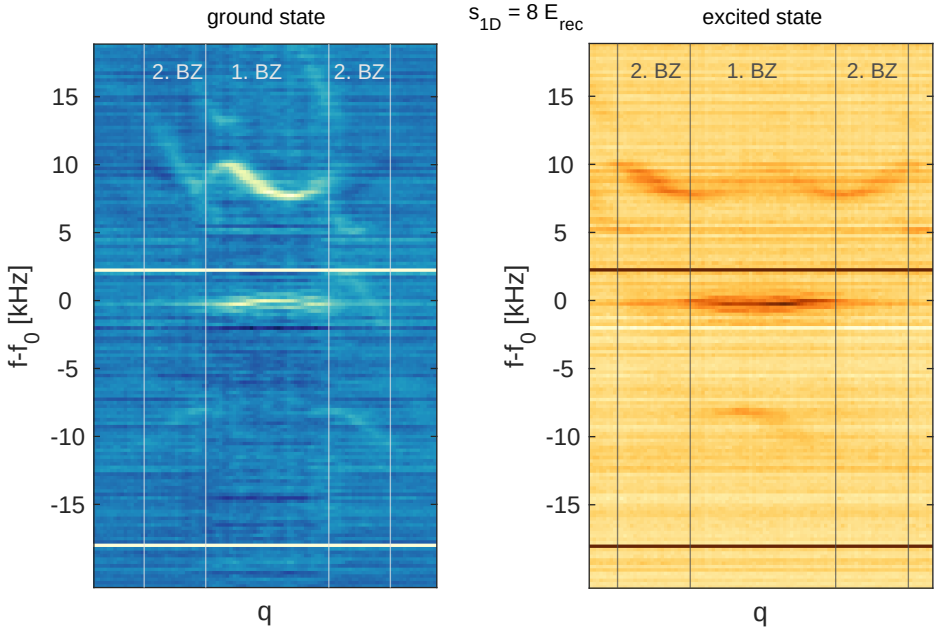


**Figure A.5.:** Momentum resolved clock spectra for a lattice depth of $s_{1D} = 8\,E_{rec}$ for ground- and excited-state atoms. Horizontal lines correspond to absorption images after time of flight and bandmapping, integrated along the direction perpendicular to the 1D lattice. The average of six images without clock excitation is subtracted.

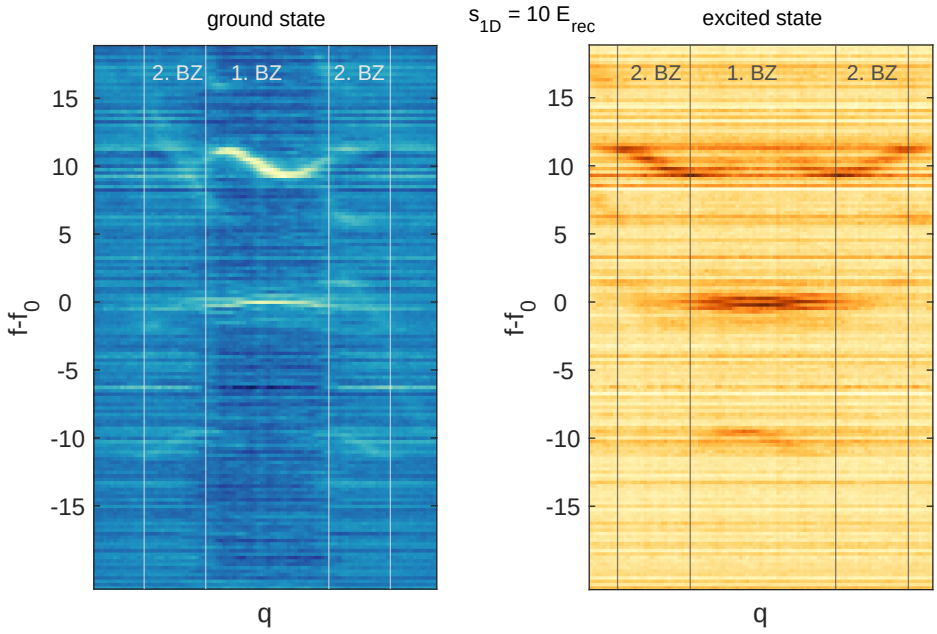


**Figure A.6.:** Momentum resolved clock spectra for a lattice depth of $s_{1D} = 10\,E_{rec}$ for ground- and excited-state atoms. Horizontal lines correspond to absorption images after time of flight and bandmapping, integrated along the direction perpendicular to the 1D lattice. The average of six images without clock excitation is subtracted.

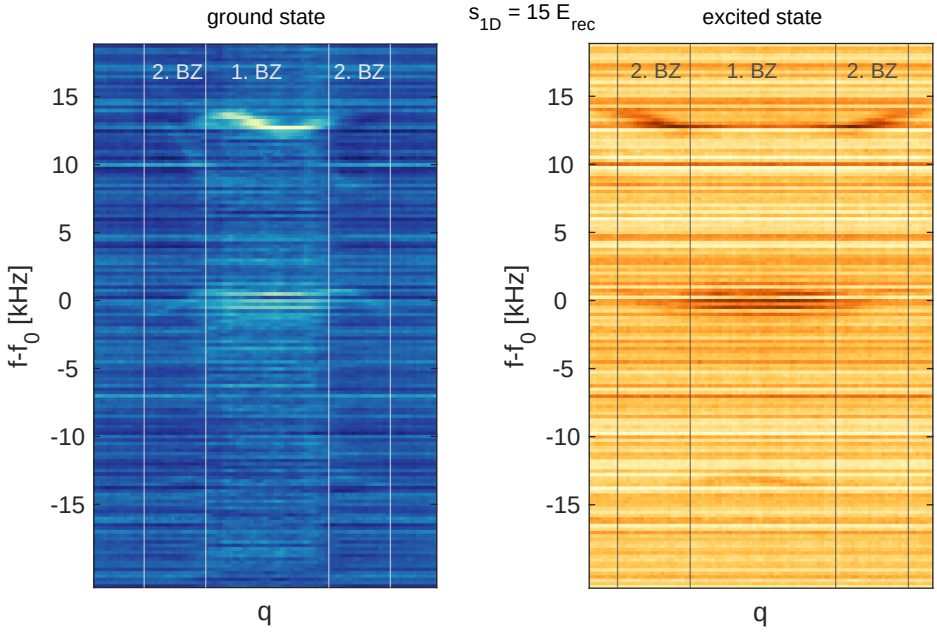


**Figure A.7.:** Momentum resolved clock spectra for a lattice depth of $s_{1D} = 15\,E_{rec}$ for ground- and excited-state atoms. Horizontal lines correspond to absorption images after time of flight and bandmapping, integrated along the direction perpendicular to the 1D lattice. The average of six images without clock excitation is subtracted.

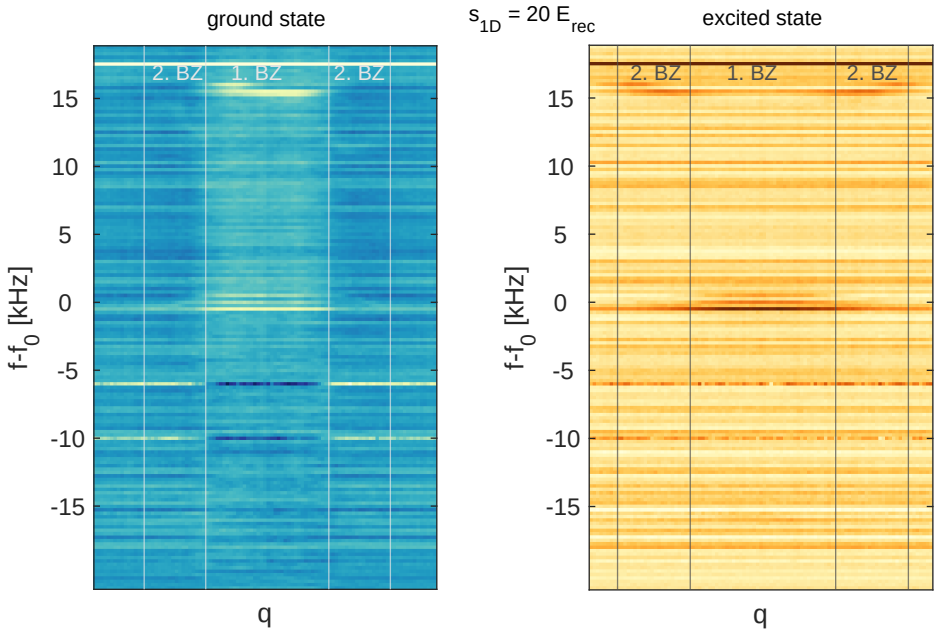


**Figure A.8.:** Momentum resolved clock spectra for a lattice depth of $s_{1D} = 20\,E_{rec}$ for ground- and excited-state atoms. Horizontal lines correspond to absorption images after time of flight and bandmapping, integrated along the direction perpendicular to the 1D lattice. The average of six images without clock excitation is subtracted.

# Danksagung

Diese Arbeit wäre ohne die Hilfe und Unterstützung vieler Menschen, denen ich an dieser Stelle danken möchte, nicht möglich gewesen.

2014 kam ich als Bachelorstudent der Arbeitsgruppe Sengstock ans Institut für Laserphysik. In den vergangenen sieben Jahren bin ich als HiWi, Masterstudent und schließlich als Doktorand Teil der Gruppe gewesen. Dieses natürlich nicht ohne Grund: Neben den spannenden Projekten, der exzellenten Ausstattung und den hervorragenden Forschungsbedingungen ist es das außergewöhnlich kollegiale Arbeitsklima, welches diese Arbeitsgruppe so besonders macht. Ich danke Klaus Sengstock dafür, dass ich Teil dieser Arbeitsgruppe sein durfte und für die Chance, die faszinierende Welt der Quantengase zu entdecken.
Über die Jahre hinweg haben viele Menschen das Ytterbium-Experiment vorangetrieben, geprägt und bereichert, so dass ich während meiner Zeit als Doktorand von deren Arbeit profitieren konnte. Neben den ehemaligen Doktoranden Sören Dörscher und Alexander Thobe, Bastian Hundt, André Kochanke und Thomas Ponath. gilt mein Dank auch den vielen Studierenden, die im Rahmen von Diplom-, Bachelor- und Masterarbeiten an dem Projekt beteiligt waren. Besonders nennen möchte ich Maximilian Hagenah, Lars Hilbig, Nejira Pintul, Donika Imeri, Fabian Gropp und Timo Eikelmann.
Zu Beginn meiner Promotion hat Bodhaditya Santra als Post-Doc am Projekt gearbeitet und mir den Start ins Doktorandenleben erleichtert. Dafür ein herzliches Dankeschön! Ein besonderer Dank gilt Christoph Becker, der mich in den vergangenen Jahren als Betreuer begleitet hat. Seine Tür stand immer offen und es fand sich stets Zeit, um anstehende Fragen und Probleme zu klären und physikalische Fragen zu diskutieren. Ohne meine beiden Mitdoktoranden Marcel Diem und Koen Sponselee wäre diese Arbeit nicht möglich gewesen. In den vergangenen Jahren haben wir zusammen die verschiedenen Hürden des experimentellen Alltags gemeistert. Dafür, für die gemeinsame Zeit und für die gute Zusammenarbeit möchte ich mich ganz herzlich bedanken. Darüberhinaus möchte ich mich bei der ganzen Arbeitsgruppe für die überaus kollegiale Zusammenarbeit und die große Hilfsbereitschaft bedanken. Ein besonderer Dank geht hier an Ortwin Hellmig, der uns oft mit seinem Wissen und Können ausgeholfen hat. Außerdem geht mein Dank an Reinhard Mielck, Ralf Lühr, Dieter Barlösius, Ellen Gloy und Janina Neubert, die mir an verschiedenen Stellen sehr geholfen haben.
Andreas Hemmerich danke ich für die Übernahme des Zweitgutachtens.
Zu guter Letzt möchte ich mich bei meinen Freund:innen, meiner Familie und Wiebke bedanken: eure Unterstützung war und ist großartig!

# Eidesstattliche Versicherung/ Declaration on Oath

Hiermit versichere ich an Eides statt, die vorliegende Dissertationsschrift selbst verfasst und keine anderen als die angegebenen Hilfsmittel und Quellen benutzt zu haben.

Hamburg, den 26.07.2021

Benjamin Abeln